Technical Physics, Vol. 50, No. 9, 2005, pp. 1105–1111. Translated from Zhurnal Tekhnicheskoĭ Fiziki, Vol. 75, No. 9, 2005, pp. 1–7.

THEORETICAL AND MATHEMATICAL PHYSICS

Absorption of Electrical Energy by a Fine Cylindrical Metal Particle

É. V. Zavitaev and A. A. Yushkanov

Moscow State University of Forest, Mytishchi, Moscow Oblast, 141005 Russia

e-mail: yushkanov@mtu-net.ru

Received October 4, 2004

Abstract—The absorption cross section for the energy of an electric field aligned with the symmetry axis of a cylindrical metal particle is calculated. The radius of the particle is assumed to be much smaller than its length. As the boundary condition of the problem, diffuse reflection of electrons from the inner surface of the particle is taken. Limiting cases are considered, and the results obtained are discussed. © *2005 Pleiades Publishing, Inc.*

INTRODUCTION

The electromagnetic properties of fine metal particles may differ substantially from those of bulk metal [1]. If linear size R of a metal is comparable to electron free path Λ, $R < \Lambda$, or smaller than Λ, $R < \Lambda$, interaction of electrons with the metal boundary has a significant effect on the response of the electrons to an applied magnetic field. This circumstance is responsible for specific optical properties of metal particles. When $R < \Lambda$, a basic optical characteristic, absorption cross section, depends on ratio R/Λ in a nontrivial manner. In highly conductive metals (aluminum, copper, silver, and others), electron free path Λ ranges from 1 to 100 nm at room temperature. Particles studied in experiments are usually several nanometers across; that is, the condition $R < \Lambda$ holds.

The response of the electrons to an applied electromagnetic field with allowance for electron–boundary interaction may be treated in terms of the conventional kinetic theory of conduction electrons in metals [2], which does not impose restrictions on ratio R/Λ.

The equations of macroscopic electrodynamics are applicable to "bulk" samples, for which $R \gg \Lambda$. Therefore, the well-known Mie theory, which describes interaction of electromagnetic waves with metallic bodies in terms of macroscopic electrodynamics, fails in treating the size effect mentioned above.

A theory of interaction between electromagnetic radiation and a spherical particle was elaborated in [3, 4]. Somewhat earlier, Trodahl [5, 6], considering the limiting case $R \ll \Lambda$ at low frequencies (far infrared), came to the same result as in [3]. In all the works cited, the approach to the problem was based on solving the kinetic Boltzmann equation for conduction electrons in metals. An alternative approach was developed by Bondar' [7, 8].

Particles encountered in nature and used in applications are frequently nonspherical. Because of this, interest in interaction between electromagnetic radiation and nonspherical particles has greatly increased in recent years [9–13]. Interaction of electromagnetic radiation with ellipsoidal particles was considered in [9] and with cylindrical particles in [10–13]. However, works [3–6, 10–13] analyze only the magnetic dipole absorption of fine metal particles. Of interest are also works [14, 15], where relevant quantum-mechanical effects, which become significant at low temperatures, are touched upon.

In this work, a distribution function describing the linear response of conduction electrons in a homogeneous cylindrical particle to the variable electric field of a plane electromagnetic wave is calculated using the kinetic approach. From this distribution function, the absorption cross section as a function of the frequency and particle radius is determined. Also, the case of a low-frequency external field and a low electron–electron collision rate inside the particle is discussed.

1. MATHEMATICAL MODEL AND CALCULATION

Let a metal nonmagnetic cylindrical particle of radius R and length L (with $L \gg R$) be placed in the field of a plane electromagnetic wave with frequency ω that is much lower than plasma resonance frequency ω_p in metals ($\omega_p \sim 10^{16}$ s^{-1}). The particle is considered to be small; that is, $R \ll 2\pi c/\omega$ (c is the speed of light in free space). The applied field is assumed to be uniform, and the skin effect is disregarded (it is assumed that $R < \delta$, where δ is the skin depth).

Consider the case when this particle interacts with linearly polarized electromagnetic radiation, the symmetry axis of the particle being orthogonal to the propagation direction of the radiation.

Let field strength $\mathbf{E}$ make angle γ with the axis of the cylindrical particle. Then, the projection of the field

1063-7842/05/5009-1105$26.00

strength vector onto the cylinder axis is $E_1 = E\cos\gamma$ and onto the direction perpendicular to the axis, $E_n = E\sin\gamma$.

The absorption cross section of the particle can be represented as

$$\sigma = \sigma_1\cos^2\gamma + \sigma_n\sin^2\gamma.$$

Quantity σ_1 is related to projection E_1 of the field strength vector; σ_n, to projection E_n.

In this work, we calculate σ_1 (subscript 1 is hereafter omitted). If electric field strength **E** of the electromagnetic wave runs normally to the cylinder axis, magnetic field strength **H** is aligned with the axis. In this case, the magnetic dipole absorption by the particle, which is due to eddy currents, makes a major contribution to the absorption cross section. This type of absorption was discussed in [10–13].

In the cylinder is sufficiently long, the electric field of the wave is unscreened in most of the cylinder. To estimate the parameters corresponding to such conditions, we turn to the well-known solution for a prolate ellipsoid in an electric field [16] by recognizing that a sufficiently long cylinder can be approximated by a prolate ellipsoid. The electric field of a prolate ellipsoid of revolution with semiaxes a, b, and d ($a > b = d$) that is placed in a uniform electric field aligned with its symmetry axis is given by [16]

$$E_{\text{int}} = \frac{E_{\text{ext}}}{1 + (\varepsilon_{\text{int}} - 1)n(e)},$$

where

$$n(e) = \frac{1-e^2}{2e^3}\left[\ln\left(\frac{1+e}{1-e}\right) - 2e\right]$$

is a coefficient depending on eccentricity e of the ellipsoid ($e = \sqrt{1 - b^2/a^2}$), E_{ext} is the external electric field, E_{int} is the internal electric field (the electric field inside the ellipsoid), and ε_{int} is the permittivity of the ellipsoid.

In the absence of screening, $E_{\text{int}} \approx E_{\text{ext}}$ and, hence, $1 + (\varepsilon_{\text{int}} - 1)n(e) \approx 1$. This approximate equality is valid if $|\varepsilon_{\text{int}}n(e)| \ll 1$ (the unity in the parentheses may be ignored, since the permittivity of metals is very high).

Then, using the Drude formulas for the frequency dependence of the permittivity, $\varepsilon(\omega)$, and conductivity, $\Sigma(\omega)$, of metals [17] (we assume that the frequency of the applied field is much lower than the frequency of electron–electron collisions inside the particle; that is, $\omega\tau \ll 1$),

$$\varepsilon(\omega) = 1 + i(4\pi\Sigma(\omega)/\omega), \quad \Sigma(\omega = \Sigma(0)/(1 - i\omega\tau),$$

where

$$\Sigma(0) = e^2 n\tau/m,$$

e and m are the electron charge and mass, respectively; n is the concentration of conduction electrons; and τ is the electron relaxation time), and also the definition of eccentricity (if a prolate ellipsoid is identified with an infinite cylinder, semiaxes b and a are identified with the radius and half-length of the cylinder; that is, $b = R$ and $a = L/2$; note also that $e \longrightarrow 1$ for an infinite cylinder), we obtain, by the method of successive approximations, a limiting relationship between the radius and length of the particle ($\Gamma = R/L$),

$$\Gamma \ll \sqrt{\frac{\omega}{8\pi\Sigma(0)}} \Big/ \sqrt{\ln\left(\frac{4\pi\Sigma(0)}{\omega}\right)}.$$

Additionally, we make conventional physical assumptions: conduction electrons are viewed as a degenerate Fermi gas, and their response to an applied magnetic field is described with the Boltzmann equation in the relaxation time approximation. It is remembered that diffuse reflection of electrons by the inner surface of the particle is taken to be the boundary condition.

Absorption of the electromagnetic wave energy by a cylindrical particle can be described as follows: the uniform time-periodic electric field of the wave,

$$\mathbf{E} = \mathbf{E}_0\exp(-i\omega t), \tag{1}$$

acts on conduction electrons in the particle and causes deviation f_1 of their distribution function f from equilibrium Fermi distribution function f_0. That is,

$$f(\mathbf{r}, \mathbf{v}) = f_0(\varepsilon) + f_1(\mathbf{r}, \mathbf{v}), \quad \varepsilon = \frac{m\mathbf{v}^2}{2},$$

where **r** is the radius vector (the origin is placed on the axis of the particle) and **v** is the electron velocity.

The field–electron interaction generates a high-frequency current,

$$\mathbf{j} = e\int \mathbf{v} f \frac{2d^3(mv)}{h^3} = 2e\left(\frac{m}{h}\right)^3 \int \mathbf{v} f_1 d^3v, \tag{2}$$

where h is the Planck constant, and also causes dissipation inside the particle. Energy $\bar{Q}$ dissipated per unit time (dissipated power) is given by [16]

$$\bar{Q} = \int \overline{(\text{Re}\mathbf{E}) \cdot (\text{Re}\mathbf{j})} d^3r = \frac{1}{2}\text{Re}\int \mathbf{j} \cdot \mathbf{E}^* d^3r. \tag{3}$$

Here, the bar means time averaging and the asterisk, the complex conjugate.

In (2), distribution function is normalized in a standard manner so that the density of electron states is $2/h^3$. For equilibrium distribution function $f_0(\varepsilon)$, we use the step approximation

$$f_0(\varepsilon) = \theta(\varepsilon_F - \varepsilon) = \begin{cases} 1, & 0 \le \varepsilon \le \varepsilon_F \\ 0, & \varepsilon_F < \varepsilon, \end{cases}$$

where $\varepsilon_F = mv_F^2/2$ is the Fermi energy and v_F is the Fermi velocity.

It is assumed that the Fermi surface is spherical.

The problem is reduced to finding deviation f_1 of the electron distribution function from equilibrium function f_0 (f_1 is induced by high-frequency field (1)). In an approximation linear in electric field, function f_1 satisfies the kinetic equation [2, 17]

$$-i\omega f_1 + \mathbf{v}\frac{\partial f_1}{\partial \mathbf{r}} + e(\mathbf{v}\cdot\mathbf{E})\frac{\partial f_0}{\partial \varepsilon} = -\frac{f_1}{\tau}, \qquad (4)$$

where it is assumed that $f_1 \sim \exp(-i\omega t)$ and the collision integral is taken in the relaxation time approximation,

$$(df_1/dt)_s = -\frac{f_1}{\tau}.$$

Solving Eq. (4) by the method of characteristics [18], we arrive at

$$f_1 = A(\exp(-\nu t') - 1)/\nu, \quad t' \geq 0, \qquad (5)$$

where

$$\nu = 1/\tau - i\omega, \quad A = e(\mathbf{v}\cdot\mathbf{E})\frac{\partial f_0}{\partial \varepsilon} \qquad (6)$$

and parameters ν and A (characteristics) are invariable along the trajectory. Parameter t' in (5) is the time an electron takes to move along the trajectory from the boundary where it reflects to point $\mathbf{r}$ with velocity $\mathbf{v}$.

To uniquely determine f_0, it is necessary to set a boundary condition for it on the cylindrical surface. Such a condition is taken to be diffuse reflection of electrons from this surface [2],

$$f_1(\mathbf{r}, \mathbf{v}) = 0 \quad \text{at} \quad \begin{cases} |\mathbf{r}_\perp| = R \\ \mathbf{r}_\perp \cdot \mathbf{v}_\perp < 0, \end{cases} \qquad (7)$$

where $\mathbf{r}_\perp$ and $\mathbf{v}_\perp$ are the components of radius vector $\mathbf{r}$ and velocity $\mathbf{v}$ of an electron in the plane normal to the axis of the inhomogeneous cylinder.

When the electron reflects from the boundary of the particle, parameter t' in (5) is defined as

$$t' = \{\mathbf{r}_\perp \cdot \mathbf{v}_\perp + [(\mathbf{r}_\perp \cdot \mathbf{v}_\perp)^2 + (R^2 - r_\perp^2)v_\perp^2]^{1/2}\}/v_\perp^2. \qquad (8)$$

The above expression results from the following geometric considerations. Projecting the obvious vector equality $\mathbf{r} = \mathbf{r}_0 + \mathbf{v}t'$ (where $\mathbf{r}_0$ is the radius vector of the electron at the time it reflects from the boundary of the particle) onto the plane normal to the cylinder axis gives $\mathbf{r}_\perp = \mathbf{r}_{0\perp} + \mathbf{v}_\perp t'$, where vectors $\mathbf{r}_\perp$ and $\mathbf{r}_{0\perp}$, and $\mathbf{v}_\perp$ are the components of the starting vectors in the projection plane. Squaring both sides of the latter equality and solving the resulting expression for t' yields expression (8).

Relationships (5), (6), and (8) completely define solution f_1 to Eq. (4) with boundary condition (7). So, we can now calculate current (2) and dissipated power (3).

To take integrals (2) and (3), it is convenient to pass to the cylindrical coordinates both in the coordinate space ($r_\perp$, φ, z; z is the polar axis aligned with vector $\mathbf{E}_0$) and in the velocity space ($v_\perp$, α, v_z; here, v_z is the polar axis). The cylinder axis coincides with the z axis. In the cylindrical coordinates, field (1) has only the z component,

$$\mathbf{E} = E_z\mathbf{e}_z; \quad E_z = E_0\exp(-i\omega t). \qquad (9)$$

Accordingly, so does current (2) (the current lines are straight lines parallel to the z axis),

$$j_z = \frac{3ne^2}{4\pi v_F^3 \nu}\int v_z^2 \delta(\varepsilon - \varepsilon_F)(1 - \exp(-\nu t'))d^3v. \qquad (10)$$

Above, we took into account that the concentration of conduction electrons in metals is given by

$$n = 2\left(\frac{m}{h}\right)^3 \int f_0 d^3v = 2\left(\frac{m}{h}\right)^3 \frac{4}{3}\pi v_F^3.$$

Electromagnetic radiation absorption cross section σ is found by dividing dissipated power $\bar{Q}$ (see (3)) by the mean energy flux in the wave equal to $cE_0^2/8\pi$,

$$\sigma = \frac{1}{2}\frac{8\pi}{cE_0^2}\mathrm{Re}\{\int j_z E_z^* d^3r\},$$

or, in view of (10),

$$\sigma = \frac{1}{2}\frac{8\pi}{cE_0^2}\mathrm{Re}\left\{\int \frac{3ne^2E_z}{4\pi v_F^3 \nu} \times [\int v_z^2 \delta(\varepsilon - \varepsilon_F)(1 - \exp(-\nu t'))d^3v]E_z^* d^3r\right\}.$$

Taking advantage of the properties of the δ function, we can write

$$\delta(\varepsilon - \varepsilon_F) = \frac{2}{m}\delta(v_z^2 + v_\perp^2 - v_F^2) = \frac{2}{m}\delta[v_z^2 - (v_F^2 - v_\perp^2)]$$

$$= \frac{2}{m}\delta[(v_z - \sqrt{v_F^2 - v_\perp^2})(v_z + \sqrt{v_F^2 - v_\perp^2})]$$

$$= \frac{1}{m\sqrt{v_F^2 - v_\perp^2}}[\delta(v_z - \sqrt{v_F^2 - v_\perp^2}) + \delta(v_z + \sqrt{v_F^2 - v_\perp^2})].$$

Owing to the symmetry of the problem, we integrate over the positive range of velocities v_z (rather than over

the entire range) and double the result to obtain

$$\sigma = \frac{1}{2}\frac{8\pi}{cE_0^2}\mathrm{Re}\left\{\int\frac{3ne^2E_z}{4\pi v_F^3\nu}\left[\frac{2}{m}\right.\right.$$
$$\left.\left.\times\int\frac{v_z^2\delta(v_z-\sqrt{v_F^2-v_\perp^2})}{\sqrt{v_F^2-v_\perp^2}}(1-\exp(-\nu t'))d^3v\right]E_z^*d^3r\right\}.$$

Then, in view of (9), we have

$$\sigma = \frac{1}{2}\frac{8\pi}{cE_0^2}\mathrm{Re}\left\{\frac{3ne^2}{4\pi v_F^3\nu}\frac{2}{m}\int E_0\exp(-\omega t)\right.$$
$$\left[\int\frac{v_z^2\delta(v_z-\sqrt{v_F^2-v_\perp^2})}{\sqrt{v_F^2-v_\perp^2}}(1-\exp(-\nu t'))d^3v\right]$$
$$\left.\times E_0\exp(i\omega t)d^3r\right\},$$

or, upon straightforward transformations,

$$\sigma = \mathrm{Re}\left\{\frac{6ne^2}{mcv_F^3\nu}\int\left[\int\frac{v_z^2\delta(v_z-\sqrt{v_F^2-v_\perp^2})}{\sqrt{v_F^2-v_\perp^2}}\right]\right.$$
$$\left.\times(1-\exp(-\nu t'))d^3v\right]d^3r\right\}.$$

With the limits of integration in the inner integral taken into account, we come to

$$\sigma = \mathrm{Re}\left\{\frac{6ne^2\omega^2}{mcv_F^3\nu}\int\left[\int_0^{v_F}\int_0^{2\pi}\int_0^{\infty}\frac{v_z^2v_\perp}{\sqrt{v_F^2-v_\perp^2}}\right.\right.$$
$$\left.\left.\times\delta(v_z-\sqrt{v_F^2-v_\perp^2})(1-\exp(-\nu t'))dv_\perp d\alpha dv_z\right]d^3r\right\}.$$

Integrating over variable v_z and substituting the limits of integration into the outer integral yields

$$\sigma = \mathrm{Re}\left\{\frac{6ne^2}{mcv_F^3\nu}\int_0^R\int_0^{2\pi}\int_0^L\left[\int_0^{v_F}\int_0^{2\pi}v_\perp\sqrt{v_F^2-v_\perp^2}\right.\right.$$
$$\left.\left.\times(1-\exp(-\nu t'))dv_\perp d\alpha\right]r_\perp dr_\perp d\varphi dz\right\}.$$

The integrals over variables φ and z are elementary ones; therefore,

$$\sigma = \mathrm{Re}\left\{\frac{6ne^2}{mcv_F^3\nu}2\pi L\int_0^R r_\perp dr_\perp\right.$$
$$\left.\times\int_0^{v_F}\int_0^{2\pi}v_\perp\sqrt{v_F^2-v_\perp^2}(1-\exp(-\nu t'))dv_\perp d\alpha\right\}.$$

Eventually, we have

$$\sigma = \mathrm{Re}\left\{\frac{12\pi ne^2L}{mcv_F^3\nu}\int_0^R r_\perp dr_\perp\right.$$
$$\left.\times\int_0^{v_F}\int_0^{2\pi}v_\perp\sqrt{v_F^2-v_\perp^2}(1-\exp(-\nu t'))dv_\perp d\alpha\right\}. \quad (11)$$

For further computation and analysis, expression (11) for the cross section of applied field energy absorption is convenient to recast in the form

$$\sigma = \mathrm{Re}\left\{\frac{24\pi ne^2L}{mcv_F^3\nu}\int_0^R r_\perp dr_\perp\right.$$
$$\left.\times\int_0^{v_F}\int_0^{2\pi}v_\perp\sqrt{v_F^2-v_\perp^2}(1-\exp(-\nu t'))dv_\perp d\alpha\right\} \quad (12)$$

(the motion of electrons is symmetric about any diametral plane where the point of their position on the trajectory lies; therefore, we may assume that angle α varies from 0 to π in the velocity space and double the result of integration over this variable).

Introducing new variables,

$$\xi = \frac{r_\perp}{R}, \quad \rho = \frac{v_\perp}{v_F},$$
$$z = \nu\frac{R}{v_F} = \left(\frac{1}{\tau}-i\omega\right)\frac{R}{v_F} = x-iy$$

we rearrange expression (8) to

$$t' = \frac{R}{v_\perp}\eta,$$

where

$$\eta = (\xi\cos\alpha+\sqrt{1-\xi^2\sin^2\alpha}).$$

Here, we took into consideration that $\mathbf{r}_\perp\cdot\mathbf{v}_\perp = r_\perp v_\perp\cos\alpha$ (all electrons on the Fermi surface inside the particle

move with velocity v_F). Formula (12) can then be represented as

$$\sigma = \mathrm{Re}\left\{\frac{24\pi ne^2R^3L}{mcv_F}\int_0^1 \xi d\xi \times \int_0^1\int_0^\pi \rho\sqrt{1-\rho^2}\frac{(1-\exp(-z\eta/\rho))}{z}d\rho d\alpha\right\}. \quad (13)$$

Absorption cross section (13) is recast in the form

$$\sigma = \sigma_0 F(x, y), \quad (14)$$

where

$$\sigma_0 = \frac{24\pi ne^2R^3L}{mcv_F},$$

$$F(x, y) = \mathrm{Re}\left\{\int_0^1 \xi d\xi \times \int_0^1\int_0^\pi \rho\sqrt{1-\rho^2}\frac{(1-\exp(-z\eta/\rho))}{z}d\rho d\alpha\right\}. \quad (15)$$

Let us make change of variables $\alpha \longrightarrow \eta$ in the inner integral; then,

$$\cos\alpha = (\eta^2+\xi^2-1)/2\eta\xi,$$

$$\alpha = \arccos((\eta^2+\xi^2-1)/2\eta\xi),$$

$$d\alpha = \left[1-\frac{(\eta^2+\xi^2-1)^2}{4\eta^2\xi^2}\right]^{-\frac{1}{2}}\left[\frac{\xi^2-\eta^2-1}{2\eta^2\xi}\right]d\eta.$$

Now, the dimensionless absorption cross section takes the form

$$F(x, y) = \mathrm{Re}\left\{\int_0^1 d\rho\int_0^1\int_0^\pi (\ldots)d\xi d\alpha\right\} = \mathrm{Re}\left\{-\int_0^1 d\rho\int_0^1\int_{1-\xi}^{1+\xi}(\ldots)d\xi d\eta\right\}.$$

Next, changing the order of integration, we have

$$F(x, y) = \mathrm{Re}\left\{\int_0^1 -d\rho\left[\int_0^1 d\eta\int_{1-\eta}^1(\ldots)d\xi + \int_1^2 d\eta\int_{\eta-1}^1(\ldots)d\xi\right]\right\}.$$

Since

$$\int_{1-\eta}^1\left[1-\frac{(\eta^2+\xi^2-1)^2}{4\eta^2\xi^2}\right]^{-\frac{1}{2}}\left[\frac{\xi^2-\eta^2-1}{2\eta^2\xi}\right]\xi d\xi = \int_{\eta-1}^1\left[1-\frac{(\eta^2+\xi^2-1)^2}{4\eta^2\xi^2}\right]^{-\frac{1}{2}}\left[\frac{\xi^2-\eta^2-1}{2\eta^2\xi}\right]\xi d\xi = -\frac{1}{2}\sqrt{4-\eta^2},$$

the dimensionless cross section of absorption by the cylindrical particle becomes

$$F(x, y) = \mathrm{Re}\left\{\frac{1}{2}\int_0^1 \rho\sqrt{1-\rho^2}d\rho \times \int_0^2\frac{(1-\exp(-z\eta/\rho))}{z}\sqrt{4-\eta^2}d\eta\right\}.$$

Integrating by parts in the inner integral, we obtain

$$F(x, y) = \mathrm{Re}\left\{\frac{1}{2z}\left[\int_0^1 -\frac{2\rho^2}{z}\sqrt{1-\rho^2}d\rho + \int_0^1\int_0^2 \rho\sqrt{1-\rho^2}\frac{\eta}{\sqrt{4-\eta^2}}\left[\eta+\frac{\rho}{z}\exp(-z\eta/\rho)\right]d\rho d\eta\right\}.$$

Integrating this expression yields

$$F(x, y) = \mathrm{Re}\left\{\frac{1}{2z}\left[\frac{\pi}{3}-\frac{\pi}{8z} + \int_0^1\int_0^2\frac{\rho^2}{z}\sqrt{1-\rho^2}\frac{\eta}{\sqrt{4-\eta^2}}[\exp(-z\eta/\rho)]d\rho d\eta\right]\right\}. \quad (16)$$

The frequency dependences of dimensionless cross section $F(x, y)$ numerically calculated for the extended cylindrical particle are shown in Figs. 1 and 2.

2. ABSORPTION AT HIGH AND LOW FREQUENCIES

Let us concentrate on the case when frequency ω of the applied field and the frequency of electron–electron collisions $(1/\tau)$ in the bulk of the metal are low compared with the frequency of electron collisions with the inner surface of the cylindrical particle. In other words, the case at hand is $|z| \ll 1$.

The exponential entering into (15) may then be expanded in the Taylor series. Leaving the first two

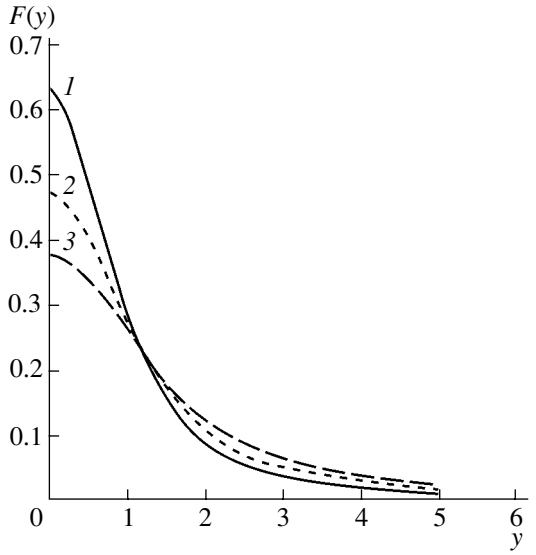

Fig. 1. Dimensionless absorption cross section F vs. dimensionless frequency y at x = (*1*) 0.3, (*2*) 0.6, and (*3*) 0.9.

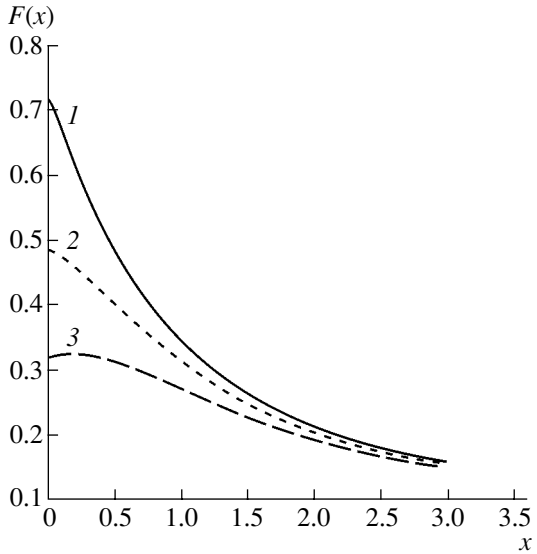

Fig. 2. Dimensionless absorption cross section F vs. dimensionless reciprocal electron free path x at y = (*1*) 0.3, (*2*) 0.6, and (*3*) 0.9.

terms in the series, we get

$$F(x, y) = \int_0^1 \xi d\xi \times \int_0^1 \int_0^\pi \sqrt{1-\rho^2}(\xi\cos\alpha + \sqrt{1-\xi^2\sin^2\alpha})d\rho d\alpha = \frac{\pi}{3}.$$

Hence, the cross section of "low-frequency" absorption is given by

$$\sigma = \frac{8\pi^2 ne^2 R^3 L}{mcv_F}. \quad (17)$$

If $|z| \gg 1$, expression (16) has an asymptote. Ignoring the term containing the exponential (it quickly decays) and the term proportional to $1/z^2$, we arrive at an expression for dimensionless absorption cross section $F(z)$,

$$F(z) = \mathrm{Re}\left\{\frac{\pi}{6}\frac{1}{z(x, y)}\right\}.$$

Upon algebraic transformations, cross section (14) for "high-frequency" absorption takes the form

$$\sigma(z) = \sigma_0 \mathrm{Re}\left\{\frac{\pi}{6}\frac{1}{z(x, y)}\right\} = \sigma_0\frac{\pi}{6}\frac{x}{x^2 + y^2}.$$

This expression corresponds to the Drude classical formula for electric absorption by a homogeneous extended cylindrical metal particle. It implies that, when the free path of electrons in the particle is small ($x \gg 1$, $x > y$), the absorption cross section decays as $1/x$. In the opposite case ($x \ll 1$, which is valid for pure metals), the absorption cross section for the extended particle varies as ratio x/y^2.

3. DISCUSSION

Work [9] was also concerned with electrical absorption by a prolate ellipsoid of revolution (in essence, by an infinite cylinder). In the case of low-frequency ($x \ll 1$, $y \gg 1$) surface scattering of electrons (free-electron regime), formula (17) coincides with the result obtained in that work,

$$\sigma_{el} = \frac{8\pi ne^2 R}{mcv_F}V$$

(where V is the volume of the ellipsoid), in terms of the specific (per unit volume) absorption cross sections of the cylinder and ellipsoid. However, in the case of high-frequency surface scattering ($x < 1$, $y \gg 1$, and $x \ll y$), the result of [9],

$$\sigma_{el} = \frac{9}{16}\frac{\pi^2 ne^2 R}{mcv_F y^2}V, \quad (18)$$

differs noticeably from the exact kinetic calculation.

To compare the results obtained in our work and work [9], let us find the asymptotics of dimensionless absorption cross section (16) for an infinite cylinder. Ignoring the term containing the exponential, we have

$$F(z) = \frac{\pi}{6}\mathrm{Re}\left\{\left[\frac{1}{z} - \frac{3}{8z^2}\right]\right\}.$$

Consequently,

$$\sigma(z) = \sigma_0\frac{\pi}{6}\mathrm{Re}\left\{\left[\frac{1}{z} - \frac{3}{8z^2}\right]\right\}$$
$$= \sigma_0\frac{\pi}{6}\left[\frac{x}{x^2+y^2} - \frac{3(x^2-y^2)}{8(x^2+y^2)^2}\right]. \quad (19)$$

Now we find the ratio of specific (per unit volume) cross sections (18) and (19) in the high-frequency limit (under the above conditions, the term proportional to $-1/y^2$ prevails in (19)),

$$\frac{\sigma_{el}}{\sigma(z)} = \frac{9}{4} = 2.25.$$

Thus, the result for electric absorption by an extended cylindrical particle obtained in [9] is highly overstated in comparison with that found by the exact kinetic calculation.

Figure 1 plots dimensional absorption cross section F versus dimensionless applied electric field frequency y at different dimensionless reciprocal electron free paths x. From these curves, it follows that, when the dimensionless frequency is low ($y < 1.3$), the particles with the longest free path of electrons (i.e., with smallest x) have the highest dimensionless absorption cross section F (provided that the particles have an equal size). At higher dimensionless frequencies of the applied field ($y > 1.3$), the situation is reverse. As the frequency grows further ($y \gg 1$), the dimensionless absorption cross section of the particles declines. This is because conduction electrons inside the particle have no time to be significantly accelerated for the period of the applied field.

Figure 2 shows the dependences of dimensionless absorption cross section F on dimensionless reciprocal electron free path x at three values of y. Here, high dimensionless absorption cross sections are observed for pure-metal particles ($x \ll 1$), the particles subjected to the lowest frequency electric field having a maximal absorption cross section. As x grows, the curves merge together, following the macroscopic asymptotics.

REFERENCES

1. Yu. I. Petrov, *The Physics of Small Particles* (Nauka, Moscow, 1984), Chap. 7 [in Russian].
2. J. M. Ziman, *Electrons and Phonons* (Clarendon, Oxford, 1960; Inostrannaya Literatura, Moscow, 1962), Chap. 11.
3. A. G. Lesskis, V. E. Pasternak, and A. A. Yushkanov, Zh. Éksp. Teor. Fiz. **83**, 310 (1982) [Sov. Phys. JETP **56**, 170 (1982)].
4. A. G. Lesskis, A. A. Yushkanov, and Yu. I. Yalamov, Poverkhnost, No. 11, 115 (1987).
5. H. J. Trodahl, Phys. Rev. **19**, 1316 (1979).
6. H. J. Trodahl, J. Phys. C **15**, 7245 (1982).
7. E. A. Bondar', Opt. Spektrosk. **75**, 837 (1993) [Opt. Spectrosc. **75**, 496 (1993)].
8. E. A. Bondar', Opt. Spektrosk. **80**, 89 (1996) [Opt. Spectrosc. **80**, 78 (1996)].
9. P. M. Tomchuk and B. P. Tomchuk, Zh. Éksp. Teor. Fiz. **112**, 661 (1997) [JETP **85**, 360 (1997)].
10. E. V. Zavitaev, A. A. Yushkanov, and Yu. I. Yalamov, Zh. Tekh. Fiz. **71** (11), 114 (2001) [Tech. Phys. **46**, 1460 (2001)].
11. E. V. Zavitaev, A. A. Yushkanov, and Yu. I. Yalamov, Opt. Spektrosk. **92**, 851 (2002) [Opt. Spectrosc. **92**, 784 (2002)].
12. E. V. Zavitaev, A. A. Yushkanov, and Yu. I. Yalamov, Zh. Tekh. Fiz. **73** (3), 16 (2003) [Tech. Phys. **48**, 290 (2003)].
13. E. V. Zavitaev, A. A. Yushkanov, and Yu. I. Yalamov, Zh. Éksp. Teor. Fiz. **124**, 1112 (2003) [JETP **97**, 996 (2003)].
14. R. J. Kubo, J. Phys. Soc. Jpn. **17**, 975 (1962).
15. E. A. Manykin, P. P. Poluektov, and Yu. G. Rubezhnyĭ, Zh. Éksp. Teor. Fiz. **70**, 2117 (1976) [Sov. Phys. JETP **43**, 1105 (1976)].
16. L. D. Landau and E. M. Lifshitz, *Course of Theoretical Physics*, Vol. 8: *Electrodynamics of Continuous Media* (Nauka, Moscow, 1992; Pergamon, New York, 1984).
17. W. A. Harrison, *Solid State Theory* (McGraw-Hill, New York, 1970; Mir, Moscow, 1972).
18. R. Courant, *Methods of Mathematical Physics*, Vol. 2: *Partial Differential Equations* (Interscience Publ., New York, 1962; Mir, Moscow, 1964).

Translated by V. Isaakyan

Technical Physics, Vol. 50, No. 9, 2005, pp. 1112–1118. Translated from Zhurnal Tekhnicheskoĭ Fiziki, Vol. 75, No. 9, 2005, pp. 8–14.

GASES AND LIQUIDS

Measurement of the Water Jet Velocity at the Outlet of Nozzles with Different Profiles

L. S. Kotousov

St. Petersburg State Electrotechnical University, ul. Prof. Popova 5, St. Petersburg, 197376 Russia

e-mail: root@post.spb.ru

Received December 2, 2004

Abstract—Water jets accelerated by differently configured convergent nozzles of diameters ranging from 4.5 to 5.0 mm are studied. The excess pressure at the nozzle inlet varies from 5×10^3 to 3.5×10^6 Pa. Velocity measurements are carried out with a spring dynamometer and a free-running Pelton microturbine. The jet strength at the outlet of the nozzle is found to increase by a factor of 4.0–4.5 compared with the water flow strength at the inlet, which depends on the excess pressure and volume flow at the inlet. Reasons for such an effect and a possible source of the additional energy are considered. The 2D Bernoulli equation used instead of the 1D equation routinely applied in nozzle analysis leads to a negative value of the excess pressure at the nozzle exit section and in the jet. Gas evolution and cavitation enhance this effect because of a decrease in the jet density. As a result, the jet is accelerated not only by the inlet pressure but also due to the fact that the potential energy of the flowing medium decreases because of a decrease in its absolute pressure down to the technical vacuum level. The contraction of the jet by the atmospheric air and the establishment of the equilibrium (in air) pressure in the water jet eventually raise its kinetic energy through the internal energy of the air. © *2005 Pleiades Publishing, Inc.*

In all the nozzles studied, the inlet sections by 10–20 times exceeded the outlet sections in area. Therefore, the static inlet pressure differed from the total pressure by no more than 1%. The static pressure was measured with a precision manometer; at low relative dynamic pressures, a water manometer was used.

Designate the ratio between the specific kinetic energy of the jet at the outlet to the excess specific potential energy of the flowing medium at the inlet as q,

$$q = \frac{\bar{u}^2}{2p_1 v_1} = \frac{\rho_1 \bar{u}^2}{2p_1} = \frac{\dot{m}\bar{u}^2}{2p_1 Q}. \quad (1)$$

Here, p_1 is the excess static inlet pressure; v_1 and $\rho_1 = 1/v_1$ are the specific volume and density of the medium at the inlet, respectively; $\dot{m}$ is the mass flow; $\bar{u}$ is the mean velocity of streams and flow inside the nozzle; and $Q = \dot{m}/\rho_1$ is the volume flow of the water. Quantity q can be considered as the flow energy (power) conversion efficiency of a nozzle. This quantity also has the meaning of the relative dynamic pressure of the jet, since it formally involves the density of the jet at the inlet rather than the density of the medium.

A total of more than a hundred different nozzles were studied: circular conical and rectangular; direct and curved; with a constant and stepwise varying inner diameter; and with circular, oval, and annular outlet channels. The outlet sections were varied from 0.1 to 5 cm^2. For wide nozzles, measurements were made at an inlet pressure excess of 0.6 MPa. Under these conditions, quantity q invariably turned out to be higher than unity (this value is commonly accepted for ideal liquids in hydraulics and fluid mechanics), sometimes reaching 4.5. It was also found in these experiments that circular conical nozzles are the most efficient if their length is roughly equal to the inlet diameter. Note also that curved nozzles may be more efficient than direct ones, all other things being the same.

Following are the systematic results obtained for circular nozzles of diameter ranging from 4.5 to 4.9 mm at excess inlet pressures of up to 3.6×10^5 Pa.

The mean velocity of the jet was measured with two new techniques: by means of a spring dynamometer with allowance for partially inelastic impact of the jet on the disk of the dynamometer and also by means of a free-running Pelton microturbine. As a reference method, we used the well-known technique of calculating the jet velocity from its diameter and flow rate.

The measuring device (Fig. 1) was placed on a support mounted under the tray. One end of a 3.5-m-long Dyurit tube of diameter 25 mm was connected to the water supply system of the hydraulic room through a controlling valve and its other end, to a three-way pipe of diameter 22 mm with its horizontal and vertical branches either connected to the nozzle or plugged. The inlet diameter of the nozzles was about 16 mm. The precision manometer scaled for 4 atm was connected to the vertical branch 5 cm below the axis of the horizontal branch, this axis being on a level with the entrance to the manometer. The nozzles were mounted on the hor-

1063-7842/05/5009-1112$26.00

izontal branch when the measurements were taken with the spring dynamometer and when the jet diameter was measured or on the vertical branch in measurements with the free-running turbine. Figure 1 shows the dynamometer on an enlarged scale. Its disk is slightly concave in order for small jets reflected from it to fly apart approximately normally to the direction of the impinging jet.

The mean velocity of the jet near the disk of the dynamometer was calculated by the formula that follows from the momentum conservation law,

$$\bar{u} = \frac{F}{\dot{m}}1.4, \qquad (2)$$

where F is the force exerted by the jet and $\dot{m}$ is the mass flow rate of the water, which is determined from volume flow Q. Quantity Q was measured by collecting the water in a wide-necked (a neck cross-sectional area of about 5 dm^2) high (about 70-cm) reservoir over a certain time interval under steady-state conditions.

When taking the measurements, we placed the dynamometer at various distances from the nozzle section and so small deviations of the disk from the position normal to the jet insignificantly influenced the force being measured. The springs of the dynamometers were of a different elasticity, making it possible to measure the dynamic pressure at different inlet pressures. With such an approach, the spread of measurements did not exceed 10% and the confidence interval for a random error in mean jet velocity $\bar{u}$ was within 5%. The latter value was obtained with random samples of three or more observations. The dynamometers were graduated using weights with allowance for a systematic error arising when they were placed horizontally.

The factor 1.4 in formula (2) takes into account the inelastic component of jet–disk interaction. This value was found by comparing the velocities measured with the dynamometers and microturbine at low pressures p_1, $p_1 = (0.5–3.0) \times 10^4$ Pa. When jets with a diameter ranging from 3.5 to 4.7 mm were incident on the turbine having a mean radius of 5.0 cm at the site of incidence, it set in rotation a stroboscopic disk with which the rate of revolution of the turbine's shaft could be determined. The error of a single frequency measurement (no more than 3%) depended on inlet pressure fluctuations. The correction coefficient 1.4 was taken to be the same throughout the inlet pressure range studied (from 0.5×10^4 to 36×10^4 Pa). For the mean velocity of the jet, we took the circumferential velocity of the turbine at points of radius 5.0 cm. The true velocity is always somewhat higher, especially at high rotation frequencies, because of free-running losses. This means that the numerical coefficient in (2) may also be slightly higher. The simplicity and reliability of the velocity measurement method suggested and its applicability to nozzles of different shape and cross-sectional area are noteworthy; therefore, it was also used in other experiments.

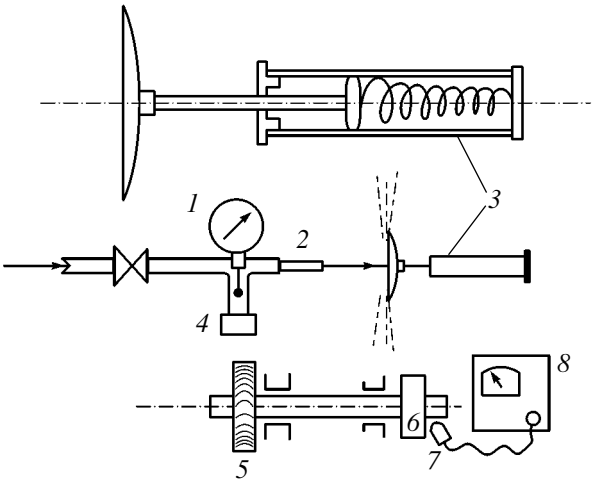

Fig. 1. Experimental setup: (*1*) standard precision manometer, (*2*) nozzle, (*3*) dynamometer, (*4*) plug, (*5*) turbine, (*6*) stroboscopic disk, (*7*) LED, and (*8*) G3-102 audio-frequency generator.

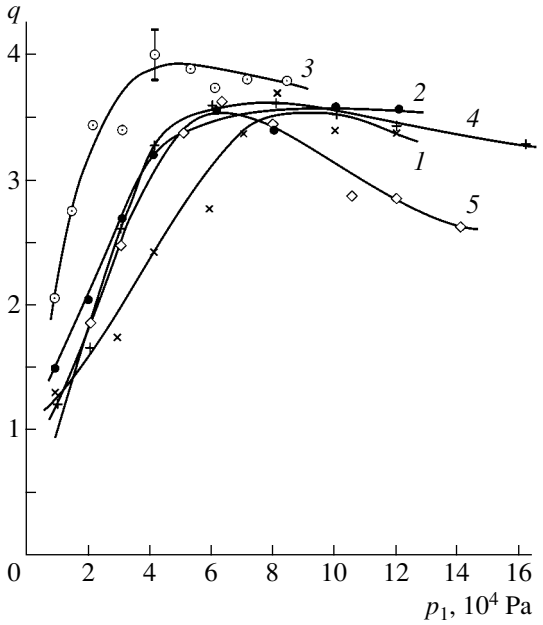

Fig. 2. Relative dynamic pressure of the water jet vs. inlet excess pressure according to formula (1) for direct conical nozzles with apex angle θ = (*1*) 180°, (*2*) 130.4°, (*3*) 90°, (*4*) 34°, and (*5*) 16.6°.

The experimental data were verified with a well-known device that sets the nozzle inlet pressure by means of a water column open to the environment. The height and diameter of the column were 3.4 m and 85 mm, respectively. For the time of measuring the force exerted by the jet or the flow rate, the water level lowered by only 2 cm. Note that both ways of inlet pressure setting showed close results.

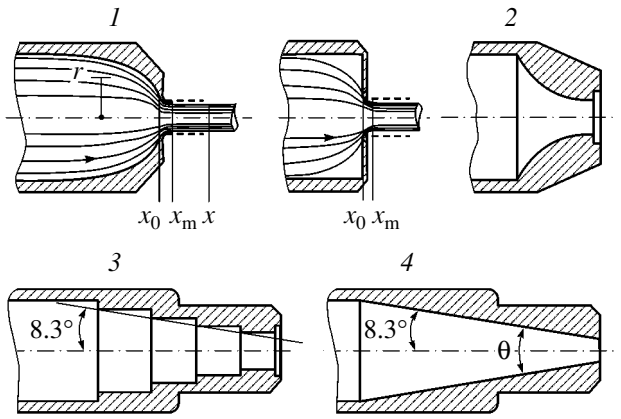

Fig. 3. Nozzles used in the experiments. r is the radial coordinate; x is the axial coordinate; and x_0 and x_m are the coordinates of the outlet section and minimal cross section, respectively. The dashed portion shows the wall of the nozzle with outlet diameter d_0.

Figure 2 demonstrates the data for nozzles in the form of direct circular cones with varying apex angle θ (including θ = 180°; this experiment is akin to the famous Torricelli run with a hole in a thin wall). For these nozzles, the values of force F were virtually identical for the disk of the dynamometer placed at distances of 5–40 cm from the nozzle section. As the disk–nozzle spacing shrinks down to 1 cm, the force gradually decreases by 20–30%. Figure 2 shows the data only for distances exceeding 5 cm.

Figures 3–5 illustrate how different configurations of circular nozzles with the same diameter (see Fig. 3) influence the jet velocity. In nozzle *1*, the curvature of the profile increases toward the outlet; nozzle *2* is a short conoidal nozzle; nozzle *3* has a stepwise decreasing inner diameter; and nozzle *4* is conical. Nozzles *3* and *4* have the same length-averaged apex angle. Shown also are the streamlines for nozzle *1* and for the hole in the thin wall that follow from the measured static pressure distributions along the radius and length of the nozzles.

The jet velocity versus inlet pressure for nozzles *1* and *2* is plotted in Fig. 4. Here, curves *4* are constructed by calculating the mean velocity in the minimal cross section of the jet according to the Bernoulli equation under the assumption routinely used in hydraulics that the static pressure in the jet equals the atmospheric pressure. Another common assumption is that the pressure in and the velocity of the medium vary only along the longitudinal axis of the nozzle (1D statement).

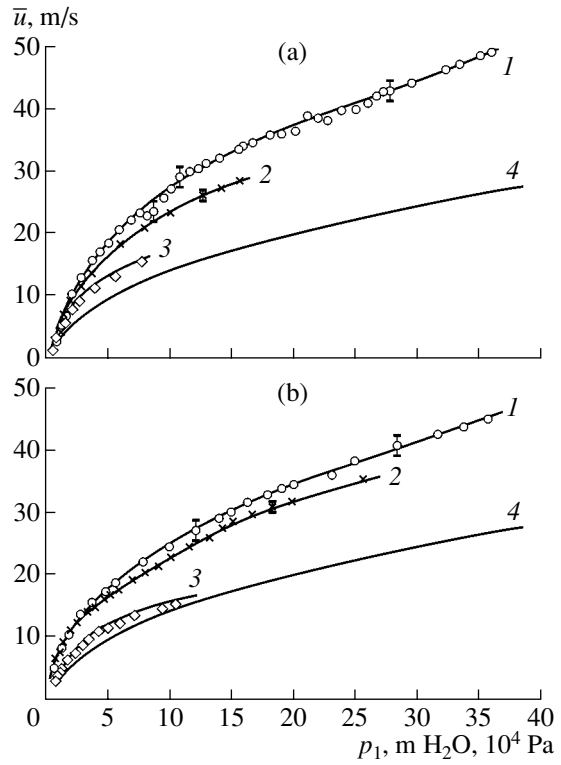

Fig. 4. Mean velocity of the jet at distance L from the nozzle vs. inlet pressure for (a) nozzle *1* and (b) nozzle *2*. (*1*) Method of dynamometer, L = 5–50 cm; (*2*) method of microturbine, L = 10 cm; (*3*) velocity measured from the mean diameter of the jet in the minimal cross section; and (*4*) velocity measured by the 1D Bernoulli equation for ideal water.

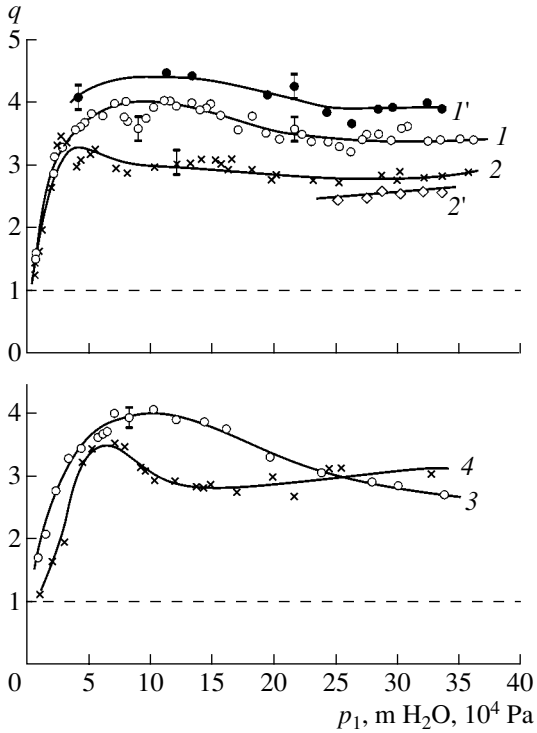

Fig. 5. Relative dynamic pressure of the jet vs. inlet pressure at distance L from the nozzle. L = 5–50 cm: (*1*) nozzle *1*, (*2*) nozzle *2*, (*3*) nozzle *3*, and (*4*) nozzle *4*. L = 70–120 cm: (*1*') nozzle *1* and (*2*') nozzle *2*.

For nozzles of diameter 5 mm or below, the minimal cross section of the jet is within 3 mm from the outlet section; for nozzle *1* and for the hole in the wall, within 1.5–2.0 mm. For nozzle *1* of diameter $d_0 = 4.6$ mm, the minimal cross section has a diameter of 3.6 mm at low inlet pressures and 3.8 mm at elevated inlet pressures. At the given inlet pressure, the mean diameter of the jet remains nearly constant over a distance of 70 cm from the minimal cross section. Then, the jet starts emitting fine sprays, which remain adjacent to it up to the water collector used to measure the flow rate. The core of the jet seems slightly contracted over a length from 0.7 to 1.2 m; then, it gradually expands.

Air–jet friction and air ejection by the jet affect jet velocity measurements. In these experiments, force F remained constant when the diameter of the disk was larger than 3 cm. For disk diameters of 2.2 and 1.3 cm, force F decreased by 5–6% and 10–12%, respectively.

Figure 5 plots relative dynamic pressure q against inlet pressure for these nozzles. The dashed line $q = 1$ corresponds to the related value for an ideal liquid. Remarkably, for real (viscous) water, q lies above this line, while it is customary to assume that, with regard to losses, the values of q lie below this curve.

BASIC RESULTS FOLLOWING FROM FIGURES 2–5

(1) It is found that, for the nozzles corresponding to Fig. 2, the value of q is virtually independent of the water temperature on the range 8–40°C.

(2) In the experiments the result of which are shown in Figs. 3–5, the water temperature was within 8–10°C. The disk of the dynamometer was placed at a distance of 5–150 cm from the nozzle outlet section. A few measurements were made at horizontal distances of up to 3 m. Over a distance of 50 cm, the jet velocity remains constant up to the measurement error for all the nozzles. Next, over the still horizontal portion of the jet trajectory up to 1.2 m (at increased inlet pressures), the velocity slightly rises for nozzles *1* and *3* or declines for nozzles *2* and *4*. Then, both the horizontal component and the total dynamic pressure fall for all the nozzles.

(3) Relative dynamic pressure q has a diffuse maximum at a level of 3.3–4.5 for inlet pressures between 5×10^4 and 15×10^4 Pa depending on the nozzle. Then, it slightly decreases to 2.5–4.0.

(4) The profile of nozzle *1* implies that the hydrodynamic drag of this nozzle is higher than that of nozzle *2*; however, the former turns out to be energetically more efficient. Similarly, nozzle *3* is bound to have a higher drag compared with smooth-channel nozzle *4*, which has the same angle between the profile generatrix and the nozzle axis. Nevertheless, nozzle *3* is more efficient.

(5) At inlet pressures below 3×10^4 Pa, determination of the jet velocity by measuring the jet diameter and water flow rate is valid if the measurement error does not exceed 20%.

(6) The value of the coefficient of dynamic pressure loss when a jet encounters a normally placed barrier, 0.92–0.96, which appears in handbooks on hydraulics (see, e.g., [1]) seems questionable without reference to relevant experimental data. The assumption that jets impinging on and leaving the disk have the same velocities, which is usually adopted in considering the jet dynamics [2], appears to be still more implausible. When measuring the velocities of these jets with the dynamometric method, we found that the velocity of the jet reflected is, on average, 1.5 times lower than the velocity of the impinging jet. This factor agrees well with that appearing in formula (2).

REASONS FOR A HIGH DYNAMIC PRESSURE OF OUTGOING WATER JETS

(1) Actually, the absolute static pressure in the flow inside the nozzle and in the jet near the nozzle outlet section drops below the atmospheric pressure because of a rotation of the flow, as well as of the acceleration and velocity vectors of elementary streams (filaments) everywhere in the medium except for the near-axial region. Consequently, when dealing with tubes of variable cross-sectional area, one should take into account the radial component of the static pressure gradient, which may even exceed the axial component (it should be noted here that flow–wall friction and an increase in the curvature of the nozzle profile generatrix toward the outlet section may also increase the radial component of this gradient).

Handbooks on hydraulics and applied or theoretical fluid mechanics [1, 3–6] consider the flow in tubes of variable cross-sectional area in the Cartesian coordinates. This makes it difficult to estimate the contribution of cross terms in the projections of the equation of motion onto the coordinate axes. For our circular nozzles, we take the cylindrical coordinates and place the origin on the symmetry axis of the nozzle so that coordinate x is aligned with this axis. For a steady-state flow in a small-diameter horizontal nozzle, the Euler equation for an ideal liquid has the form

$$\rho\frac{d\mathbf{u}}{dt} = \rho(\mathbf{u}\cdot\nabla)\mathbf{u} = -\nabla p, \qquad (3)$$

where $\mathbf{u}$ is the velocity of a given (constant) elementary mass of the flowing medium.

Under such conditions, Eq. (3) is exact irrespective of whether the density of the medium is constant or variable. We also take into account the equality

$$(\mathbf{u}\cdot\nabla)\mathbf{u} = \nabla\left(\frac{u^2}{2}\right) + \mathrm{curl}\,\mathbf{u}\times\mathbf{u}. \qquad (4)$$

If the parameters of the medium are azimuth-independent, we get

$$\mathrm{curl}\mathbf{u}\times\mathbf{u} = \mathbf{e}_r u_x\left(\frac{\partial u_r}{\partial x}-\frac{\partial u_x}{\partial r}\right)+\mathbf{e}_x u_r\left(\frac{\partial u_x}{\partial r}-\frac{\partial u_r}{\partial x}\right). \quad (5)$$

From (3)–(5), we have

$$\begin{aligned}-\frac{1}{\rho}\frac{\partial p}{\partial x} &= u_x\frac{\partial u_x}{\partial x}+u_r\frac{\partial u_x}{\partial r},\\ -\frac{1}{\rho}\frac{\partial p}{\partial r} &= u_r\frac{\partial u_r}{\partial r}+u_x\frac{\partial u_r}{\partial x}.\end{aligned} \quad (6)$$

Figure 3 shows the trajectory of filaments for nozzle *1* and for the hole in the thin wall. The shape of the jet can be directly observed. The trajectories of the filaments inside the nozzle are consistent with our measurements of the radial and longitudinal static pressure distributions that were taken with small sensors made of thin-walled capillaries 0.8 mm in diameter. The sensors were both stationary and movable in either of the directions both inside and outside the nozzle. In-jet measurements can be made only if the capillaries are inserted into the jet from the side of the nozzle. Simultaneously, we measured the pressure above the jet at the outlet, surrounding the jet by a chamber (as in a water-jet pump) and introducing a standard static pressure sensor into the wall of the chamber. In this paper, details of these measurements are omitted. It is essential here that a negative excess pressure may be observed both in the jet and in the flow inside the nozzle at its outlet.

The trajectories in Fig. 3 also comply with the fact that the measured static pressure equals the inlet pressure in stagnation zones at the wall of the hole and that the excess pressure tends to zero or becomes negative near the center of the hole in the same section.

From Fig. 3, it follows that

$$u_x,\ \frac{\partial u_x}{\partial x}>0,\quad u_r,\ \frac{\partial u_r}{\partial r}<0;$$

$$\frac{\partial u_x}{\partial r}<0,\quad \frac{\partial u_r}{\partial x}\leqslant 0,$$

for any x and r both inside and outside the nozzle except for axial points.

The last derivative above is negative upstream of the nozzle outlet and positive downstream. The static pressure diminishes even inside the nozzle, since u_x depends on x and u_r depends on r. The cross terms are also a factor: near the outlet, $\partial u_r/\partial x \longrightarrow 0$ and $u_r\partial u_x/\partial r$ significantly reduce the pressure in the longitudinal direction.

To calculate the pressure decrease, we combine Eqs. (3) and (4) to get

$$\nabla\left(\frac{u^2}{2}\right)+\mathrm{curl}\mathbf{u}\times\mathbf{u} = -\frac{\nabla p}{\rho}. \quad (7)$$

Scalarly multiplying the left- and right-hand sides of (7) by streamline unit vector $\mathbf{u}/u$ [5] yields

$$\frac{1}{\rho}\frac{dp}{ds}+\frac{1}{2}\frac{d(u^2)}{ds} = 0. \quad (8)$$

If the density of the medium is constant along streamline s, Eq. (8) turns into the Bernoulli equation for an ideal liquid. It strictly holds only for a streamline provided that $\rho = \mathrm{const}(s)$,

$$\Delta p = -\frac{1}{2}\rho\Delta(u^2). \quad (9)$$

For water, we may put $\rho = 1$ kg/dm^3. By way of example, let us consider nozzle *1* (Fig. 3) with diameter $d_0 = 4.6$ mm and outlet cross-sectional area $\Omega_0 = 0.167$ cm^2. At an inlet excess pressure of 10^5 Pa and corresponding volume flow rate $Q = 198$ cm^3/s, mean velocity component $\bar{u}_{x_0}$ is equal to $Q/\Omega_0 = 12$ m/s. Taking into account that the streamlines in the major part of the outlet section are inclined to the x axis at an angle of 20°–50° according to the nozzle profile, we find that $\bar{u}_{r_0} \cong 10$ m/s. Then, from (9), the pressure excess is $p_0 = (\Delta p)_0 + p_1 = -2.2\times10^4$ Pa. Similarly, in minimal cross section x_m diameter d_m of which equals 3.7 mm at this p_1, the value of $\bar{u}_{x_\mathrm{m}}$ calculated from the cross-sectional area is 18.6 m/s and the pressure excess $p_\mathrm{m} = -7.4\times10^4$ Pa. It is adopted here that $\bar{u}_{r_\mathrm{m}} = 0$ in the minimal cross section. Actually, however, this is not the case, since the ambient air not only disturbs the jet through friction and ejection but also tends to squeeze it because of a high static pressure drop.

(2) If the mass flow, mean velocity of the jet, and its mean diameter are known from experiments (for the nozzles studied, the jet is especially stable over a length between the minimal cross section and the point 1 m distant from the outlet), the mean density of the jet is found by the formula

$$\bar{\rho} = \frac{\dot{m}}{\Omega\bar{u}}. \quad (10)$$

For the example considered above, $\bar{\rho} = 0.62$ kg/dm^3 over the jet portion between 5 and 50 cm at velocity $\bar{u} = 28.3$ m/s (Fig. 4). Assuming that the jet velocities in section x_m and over the portion 5–50 cm are roughly the same, we find from (9) that, for ideal water, the excess pressure is $p_\mathrm{m} = -1.5\times10^5$ Pa (or, in other words, the absolute pressure is -0.5×10^5 Pa). The jet density in section x_m calculated by formula (10) is also close to 0.62 kg/dm^3. However, rigorous calculation by formula (9) involves not the final density of water but its mean integral density, which is higher than ρ_m. Therefore, the calculated value of p_m is still lower.

For nozzles *1* and *2*, one can trace the jet density variation by comparing curves *1* and *3* in Fig. 4 and contrasting them with formula (10). It turns out that,

even for excess inlet pressures above 2×10^4 Pa, the jet velocity determined from the volume flow involves a significant error if the jet density is assumed to be the same as in the water collector (i.e., close to 1.0 kg/dm^3).

(3) Let us also discuss the effect of gas evolution and cavitation on the water acceleration in the nozzle and jet. Since the water solubility of oxygen and nitrogen is low, it seems reasonable to take into consideration the effect of CO_2 and Cl_2 gases, which are usually dissolved in tap water. A reduction of the absolute static pressure along the streamline from p_1 to p_0 or from p_m to a value much lower than the atmospheric pressure (up to technical vacuum), which is observed in the dynamic regime for a short time the water takes to pass through the nozzle, is bound to cause gas evolution. Data for water solubility of gases [7] suggest that, if at least one-tenth of the equilibrium amount (according to the Henry law) of the dissolved gas evolves in water, its mean density decreases by 10–20% compared with the density of homogeneous water or water solution of gases. As a result, the actual flow velocity increases, in accordance with formula (10), and the pressure markedly drops in accordance with (9).

Cavitation is evaporation of a flowing liquid. Acceleration alone may cause water molecules (clusters) to be detached from each other. However, at reduced static pressures (close to a technical vacuum), which were observed in our experiments, this phenomenon is intensified by locally equilibrium phase transformations. It seems that, for the very short time (on the order of several hundredths or thousandths of a second) taken for the water to pass through the nozzle in the precavitation and cavitation conditions, only an extremely small part of the liquid can evaporate because of the phase transition resistance. However, even a millionth part of the water mass that evaporates in the volume of the medium may noticeably change the water density. Consider the real case when the water temperature is 8°C. At this temperature, the saturation vapor pressure equals 1070 Pa. Evaporation takes place at a lower pressure. In the experiments, the absolute pressure in the jet varied from 500 to 1500 Pa at excess inlet pressures of 10^5 Pa or higher.

Let one-millionth part of the water mass turn into steam at a certain section of the jet near the outlet. Neglecting clustering in the steam and considering specific volume v as the volume of a mechanical mixture of the liquid and steam (i.e., digressing from the concepts of partial volume and mixture nonideality), we get

$$v = v_{st}10^6 + v_{liq}(1–10^6), \quad (11)$$

where v_{st} is the specific volume of the steam, which is considered as a perfect gas. At 281 K and 540 Pa, v_{st} = 240 m^3/kg. Hence, v = 0.00124 m^3/kg and $\rho = 1/v$ = 0.80 kg/dm^3. If two millionths of water evaporates, ρ = 0.68 kg/dm^3.

Thus, gas evolution and cavitation result in "swelling" of the flow in the nozzle and water jet.

(4) A small decrease in the temperature of the medium due to cavitation leads to a further significant decrease in the pressure and, thereby, sustains cavitation. Assuming that the flow regime is adiabatic and that local thermostatic equilibrium in a first approximation is possible, we use the relationship

$$\Delta p_c = \frac{\rho c_p}{\alpha T}\Delta T_c, \quad (12)$$

which follows from the first law of thermodynamics. Here, α is the isobaric expansion coefficient, c_p is the specific heat at constant pressure, ΔT_c is the cavitation-related decrease in temperature due to removal of the heat of evaporation, and Δp_c is the decrease in pressure. If, as in the previous example, 0.001 g per 1 kg of water evaporates, then ΔT_c = –0.0006 K at water temperature T = 282 K. Here, the value of α is taken to be that for pure water, $\alpha = 6 \times 10^{-5}$ 1/K, since this quantity for the water–steam heterogeneous system at its density of 0.80 kg/dm^3 is unknown. Accordingly, $\Delta p_c = -1.2 \times 10^5$ Pa.

Of course, the nonadiabaticity of the medium, the time the medium takes to relax to a new thermodynamic state, and an increase in α with decreasing density of the medium should be taken into account. Furthermore, the virtual constancy of the jet diameter over a distance of 0.7 m from the nozzle outlet means that the normal component of the stress acting on the jet in motion through the air counterbalances the disturbance of the jet due to the shear component. The latter component will prevail where the jet expands noticeably, i.e., at distances of 1.2–1.5 m from the outlet. Equalization of the pressure over the cross section of the jet occurs relatively slowly, because the velocity of the sound wave in the water–air and water–steam two-phase system is low (the well-known Wood effect [5]).

Even if the value of Δp_c is overestimated, an additional decrease in the static pressure due to the evaporation-related temperature effect is a key factor enhancing cavitation and raising the jet velocity.

(5) Thus, the air tends to contract the reduced-pressure jet downstream of the nozzle. This increases the velocity of the jet, sustains gas evolution and cavitation in its axial region, etc. The static pressure in the jet approaches the air pressure over some portion of the jet. Complete equalization is likely to be observed where the jet noticeable expands. It should be noted here that conoidal nozzle *2* with its cylindrical part shortened to 2 mm does not have a clear-cut minimal cross section. The jet from this nozzle starts markedly expanding well before than in the other nozzles.

Converging filaments leaving nozzle *1* and the hole in the wall collide with each other, i.e., exchange the normal components of the momentum. Inside the nozzle up the outlet, these components are quenched by the wall of the nozzle; outside the nozzle, by the pressure difference between the air and jet. It should be borne in

mind that filament–filament collisions are partially inelastic.

ENERGY BALANCE AT WATER ACCELERATION IN A NOZZLE

The contributors to the kinetic energy of the jet are as follows: (1) a decrease in the potential energy of the water flow in the homogeneous and heterogeneous states according to Bernoulli equation (9), where the density should be meant as the integral density averaged over the distance from the inlet to the minimal cross section ($\langle\rho\rangle$), and (2) a decrease in the internal energy of the surrounding air, which is spent on (i) quenching the momentum normal components of filaments colliding with each other over the portion from x_0 to x_m; (ii) contracting the jet over the portion from x_0 to x_m; and (iii) recovering the static pressure of the jet to the atmospheric level.

Within the practically important portion of the jet (from 5 to 50 cm from the outlet), its kinetic energy is nearly constant for all the nozzles considered. Here, air–jet energy exchange may be ignored; however, it should be taken into account in the final result. For example, for nozzle *1* at excess pressure $p_1 = 10^5$ Pa, the measurements gave the following results: $\dot{m} = 0.198$ kg/s, $d_0 = 4.6$ mm, $d_m = 3.7$ mm, $\rho_1 = 1.00$ kg/dm^3, $\rho_m = 0.62$ kg/dm^3, and $p_m = -0.995 \times 10^5$ Pa. The jet power equals $N = \dot{m}\bar{u}^2/2 = 80$ W. The contributions to the jet power are as follows: $N_1 = \dot{m}(p_1 - p_m)/\langle\rho\rangle = 50$ W (if we put $\langle\rho\rangle = 0.8$ kg/dm^3) and $N_{2i} \cong (\tan 30^\circ)\dot{m}\bar{u}^2/4 = 13.2$ W (here, allowance is made for momentum losses due to filament–filament collisions). The mean half-angle of convergence of the filaments is set equal to 30°. If this half-angle equals 35°, then $N_{2ii} = 19.5$ W. For air pressure $p_a = 10^5$ Pa,

$$N_{2ii} \cong \frac{\pi(d_0^2 - d_m^2)}{4}\frac{\bar{u}_m + \bar{u}_0}{2}p_a.$$

The contraction resistance of the jet depends on the normal component of its dynamic pressure, since the absolute static pressure in the jet is very low within this portion.

The values of N_1, N_{2i}, and N_{2ii} add up to 75.2–81.5 W. Thus, our qualitative reasoning is supported numerically: the energy balance holds. The same is true for other parameters of nozzle *1* and the parameters of nozzles *2–4*.

Of interest is the recoil force propeling the water jet from the nozzle into the air. In experiments, it is close to a value calculated using the 1D Bernoulli equation under the assumption that the static pressure in the jet at the outlet is close to the atmospheric pressure. However, the deeper insight into the jet dynamics made it possible to raise the recoil force with a simple mouthpiece attached to the nozzle. This point will be discussed elsewhere.

Significantly, the seemingly high intrinsic efficiency of the Pelton turbine in comparison with an air turbine is related to the increase in the power of the water flow in the nozzle that drives the turbine. The velocity of the water jet leaving this nozzle was calculated by the 1D Bernoulli equation but in no case was verified experimentally.

It should be emphasized in conclusion that we are not aware of publications where the directly measured mean velocity of water jets several millimeters across exceeded 10 m/s. The data reported in [8] refer to ducted flows in large power stations. We failed in measuring the jet velocity with a Pitot tube, since insertion of a capillary against the jet causes the atmospheric-pressure air to escape into the capillary (because the excess pressure in the jet is negative) and, thereby, introduces an error into local parameters of the jet.

Nozzle flows, as well as flows at mouthpiece or at hole in wall, are usually treated in terms of the 1D Bernoulli equation. Based on this study, we can argue that such an approach as applied to variable-section liquid flows fails and also that the static pressure in the minimal cross section is always lower than the atmospheric or environmental pressure.

In similar studies with the air flow, the flow and jet velocities were measured with a Pitot tube. For the air, power conversion efficiency q is also larger than unity and may exceed 1.3 at critical parameters of the flow and in a supersonic flow. Yet, this efficiency is significantly lower than for water.

ACKNOWLEDGMENTS

The author thanks A.D. Girgidov and V.P. Troitskiĭ for assistance in the experiments with water jets.

REFERENCES

1. I. I. Agroskin, G. T. Dmitriev, and F. I. Pikalov, *Hydraulics* (Énergiya, Leningrad, 1964) [in Russian].
2. Yu. U. Édel', *Pelton-Type Turbines* (Mashgiz, Leningrad, 1963) [in Russian].
3. R. R. Chugaev, *Hydraulics* (Kolos, Moscow, 2004) [in Russian].
4. I. L. Povkh, *Technical Hydromechanics* (Mashinostroenie, Leningrad, 1976) [in Russian].
5. D. G. Loitsyanskii, *Fluid Mechanics* (Nauka, Moscow, 1987) [in Russian].
6. A. D. Girgidov, *Technical Fluid Mechanics* (St. Peterb. Gos. Tekh. Univ., St. Petersburg, 1999) [in Russian].
7. A. I. Brodskiĭ, *Physical Chemistry* (Roskhimizdat, Moscow, 1948), Vol. 2 [in Russian].
8. L. Bergmann, *Der Ultraschall und Seine Anwendung in Wissenschaft und Technik* (Hirzel, Zürich, 1954; Inostrannaya Literatura, Moscow, 1956).

Translated by V. Isaakyan

Technical Physics, Vol. 50, No. 9, 2005, pp. 1119–1123. Translated from Zhurnal Tekhnicheskoĭ Fiziki, Vol. 75, No. 9, 2005, pp. 15–19.

GASES AND LIQUIDS

Simulation of Nonstationary Electrohydrodynamic Flows in a Symmetric System of Electrodes of the Wire–Wire Type

Yu. K. Stishkov and I. A. Elagin

Research Institute of Radiophysics, St. Petersburg State University, St. Petersburg, 198504 Russia
e-mail: pelab@niirf.spbu.ru

Received December 15, 2004

Abstract—Computer simulation is carried out for the process of formation of electrohydrodynamic flows emerging in a system of two parallel wires as a result of symmetric injection from each electrode (2D case). Simulation is performed using the ANSYS system. A simulation algorithm is developed for nonstationary electrohydrodynamic flows. The results of simulation are presented. Analysis of the results shows that the evolution of electrohydrodynamic flows is accompanied by the formation of thin oppositely charged liquid streams moving in opposite direction from near-electrode charged layers. © *2005 Pleiades Publishing, Inc.*

INTRODUCTION

The formation of electrohydrodynamic flows in the case when a stepwise voltage is supplied to electrodes was considered by several authors. The results of experimental investigation of the formation of electrohydrodynamic (EHD) flows upon the application of a voltage were reported in [1, 2]. The main results of these works can be formulated as follows: (i) EHD flows emerge with a certain delay relative to the instant of voltage application and (ii) the evolution of the flow occurs via alternating outbursts of a thin trickle of charged liquid from the electrode surface. The former effect can be explained by the formation of a charged layer at the electrode surface prior to the formation of the EHD flow. Subsequent investigations showed [3] that if the charged layer has a symmetric annular structure, it can give rise only to local flows. The formation of a directional flow requires that the primary near-electrode charge structure be asymmetric (e.g., in the shape of an oval ring).

This study is devoted to computer simulation of the process of formation of EHD flows in a symmetric system of wire-wire electrodes in the 2D case, when the length of the wires is much larger than the distance between them. In the electrostatic approximation, such a system is symmetric relative to the central plane.

The modeling algorithm was constructed under the following assumptions: (i) after the application of voltage, a layer of charged liquid in the form of an oval ring extended towards the opposite electrode is formed around each electrode, (ii) the electric charge density distribution within the ring is uniform, and (iii) the EHD flow formed from the stationary charged layer under the action of Coulomb forces carries the electric charge along the current line. The electric charge density distribution in the new region is also assumed to be uniform. These assumptions are justified if the ions forming the volume charge cloud are frozen in the liquid; i.e., the electric Reynolds number is much greater than unity. Indeed, the charge conservation law under the above assumptions can be written in the form

$$\frac{\partial \rho}{\partial t} + \mathrm{div}(\rho \mathbf{v}) = 0 \qquad (1)$$

or, in the case of incompressible liquid,

$$\frac{\partial \rho}{\partial t} = -\mathbf{v}\mathrm{grad}\rho, \qquad (2)$$

where ρ is the volume charge density and $\mathbf{v}$ is the velocity of the liquid.

Simulation was carried out using the finite-element software package ANSYS. We worked out a method for solving nonstationary problems in electrohydrodynamics, which involves consistent solution of electrostatic and hydrodynamic problems; this method will be described below.

DESCRIPTION OF THE MODEL AND MODELING ALGORITHM

The model is similar to that used in experiments [1] and consists of a cuvette with a square cross section (of side 10 cm) with two parallel wires of diameter 0.14 cm spaced by a distance of 1 cm at the center of the cuvette. The liquid under study is transformer oil with a conductivity of $10^{-12}\ \Omega^{-1}\ \mathrm{m}^{-1}$ and a permittivity of 2.2.

The modeling algorithm is based on an iterative process with several steps in each iteration.

1063-7842/05/5009-1119$26.00

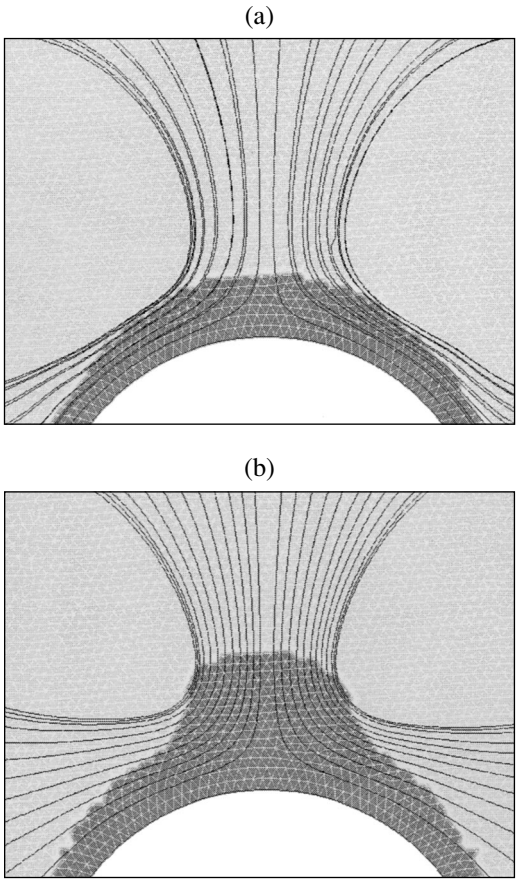

Fig. 1. (a) Initial region of the volume charge of a density of 0.01 C/m^3 (darker region) and corresponding streamlines; (b) region of the volume charge of a density of 0.01 C/m^3 (darker region) after the fourth iteration and corresponding streamlines.

(1) At the first step, the electrostatic problem is solved with a volume charge of ±0.01 C/m^3 (Fig. 1a) defined within an oval ring having a thickness of 0.1 of the electrode radius, enveloping each electrode, and displaced towards the opposite electrode (i.e., having the shape of an oval ring). In Fig. 1, a part of an electrode is represented by a white region bounded by a semicircle. Figure 1a shows the initial charge structure at the lower electrode. The boundary conditions are as follows: potentials at the electrodes are ±12 kV; the normal electric field component is zero at the outer walls. The Coulomb force distribution in the charged region is determined from the solution obtained at the first step.

(2) At the second step, the nonstationary hydrodynamic problem with a distributed load in the form of the Coulomb forces calculated at the first step is solved. The boundary conditions are as follows: both velocity components at the walls are zero. The velocity and pressure fields of EHD flows formed in this case are calculated. After the emergence of EHD flows, the charge is carried from their initial oval structure by an EHD flow along the streamlines of the liquid, forming a charged jet. Proceeding from these considerations, the new region of volume charge distribution is calculated from the obtained distributions of velocities and streamlines. For this purpose, streamlines passing through the boundary of the region of the initial charge distribution are constructed from the obtained solution of the hydrodynamic problem (Fig. 1a) and the displacement of this boundary over a certain time interval is calculated with allowance for the change in the velocity of the liquid along a streamline. We assume that the charge moves with the liquid. To attain a satisfactory accuracy, the time interval for the next iteration is calculated so that the boundary of the charge region is displaced by less than half the ring thickness. Figure 1b shows the region of the volume charge density distribution after the fourth iteration.

(3) At the third step, the electrostatic problem is solved with a new region of charge distribution and a new distribution of electric forces is calculated.

(4) At the fourth step, the hydrodynamic problem is solved with the volume load calculated at the third step and new streamlines are plotted (see Fig. 1b).

After this, the iterative process is repeated until the charged region reaches the middle of the electrode gap, where the jet from the opposite electrode is encountered.

Thus, the EHD flow in the above model emerges as a result of formation of a charged central jet carrying the charge to the electrode gap. The central jet in turn is formed by the displacement of the charge from the initially formed annular charge region by the EHD flow. In all, we performed 17 cycles, as a result of which two counterpropagating jets of the EHD flow are formed. We assumed that the charge density emerging at each electrode is the same and equal to 0.01 C/m^3 and has the polarity corresponding to the sign of the charge on the electrode.

RESULTS OF SIMULATION

The results of simulation include the dynamics of the displacement of the volume charge density distribution region, as well as the distribution of electric field, Coulomb forces, and corresponding contour lines of velocity and pressure distributions in the emerging EHD flows at instants of 0.006, 0.024, 0.036, 0.048, 0.060, 0.078, and 0.102 s after the application of voltage. All quantities represented on the curves are given in SI units.

Figure 2 shows velocity isolines for the EHD flow at the instant of 0.102 s, which corresponds to the meeting of two charged jets propagating from the opposite electrodes. As expected from the results of

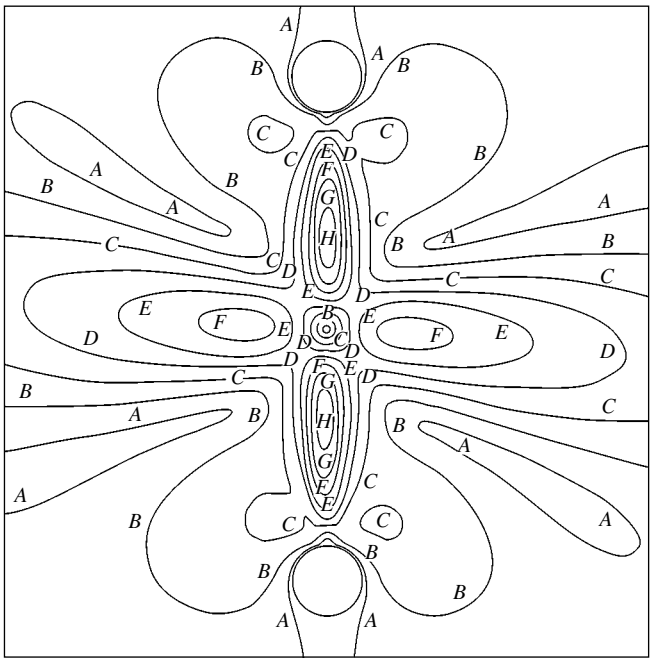

ANSYS 7.0

$A = 0.012401$ $C = 0.062007$ $E = 0.111612$ $G = 0.161217$
$B = 0.037204$ $D = 0.086809$ $F = 0.136415$ $H = 0.18602$

Fig. 2. Velocity isolines.

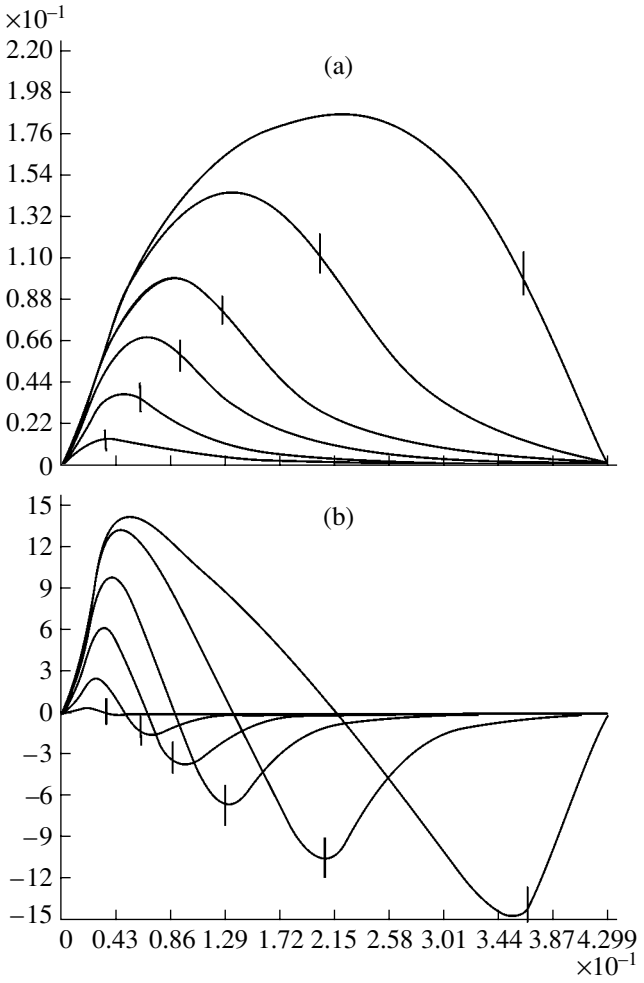

Fig. 3. (a) Velocity distribution at instants of 0.024, 0.036, 0.048, 0.06, 0.078, and 0.102 s; (b) dynamics of the formation of acceleration and stagnation zones in the liquid.

experiments [1, 2], two counterpropagating EHD flows forming a four-cell structure are formed in the cuvette.

Analysis of the results shows that each of the counterpropagating jets of the EHD flow exhibits a typical zone structure described earlier on the basis of analysis of experimental data. In a thin layer of liquid formed at the surface of each electrode, the velocity of the flow is very low. The next is the acceleration zone followed by the zone of weakly varying flow and the stagnation zone of the liquid. At the middle of the electrode gap, there is a region of stationary liquid of circular shape. Since the pattern of EHD flows is symmetric about the middle of the electrode gap, we will henceforth analyze only the lower half-plane.

Figure 3a shows consecutive distributions of the EHD flow velocity along the central axis of the flow from the lower electrode to the middle of the electrode gap. Vertical segments in the figure mark the corresponding positions of the boundary of the charged jet. The acceleration zone followed by the stagnation zone can be clearly seen. As the charge jet propagates, the peak of the EHD flow is displaced to the bulk of the liquid. At all stages, the hump of the velocity is slightly displaced towards the electrode relative to the boundary of the charged region.

Figure 3b shows the acceleration distributions in the liquid, corresponding to the same instants. These distributions have a clearly manifested two-hump structure. The acceleration zone has a peak at a certain distance from the electrode surface, which depends on time only slightly. The liquid stagnation zone also has an extremum, i.e., a negative acceleration peak propagating to the bulk of the liquid together with the boundary of the charged jet. The presence of this zone determines the cellular nature of the EHD flow and its structure.

Figure 4a shows the contour lines of the pressure distribution in the electrode gap. The evolution of the EHD flow is accompanied by the formation of two pressure zones located at the opposite ends of the charged jet, i.e., the low-pressure zone lying in the near-electrode region and concentrated mainly in the upper part of the charged ring and the high-pressure zone having a semicircular structure and a flattened lower boundary. The lower boundary of the high-pressure zone is determined by the upper boundary of the charge jet and propagates with it to the middle of the electrode gap, where it merges with the analogous zone propagating from the opposite electrode. At instant 0.06 s corre-

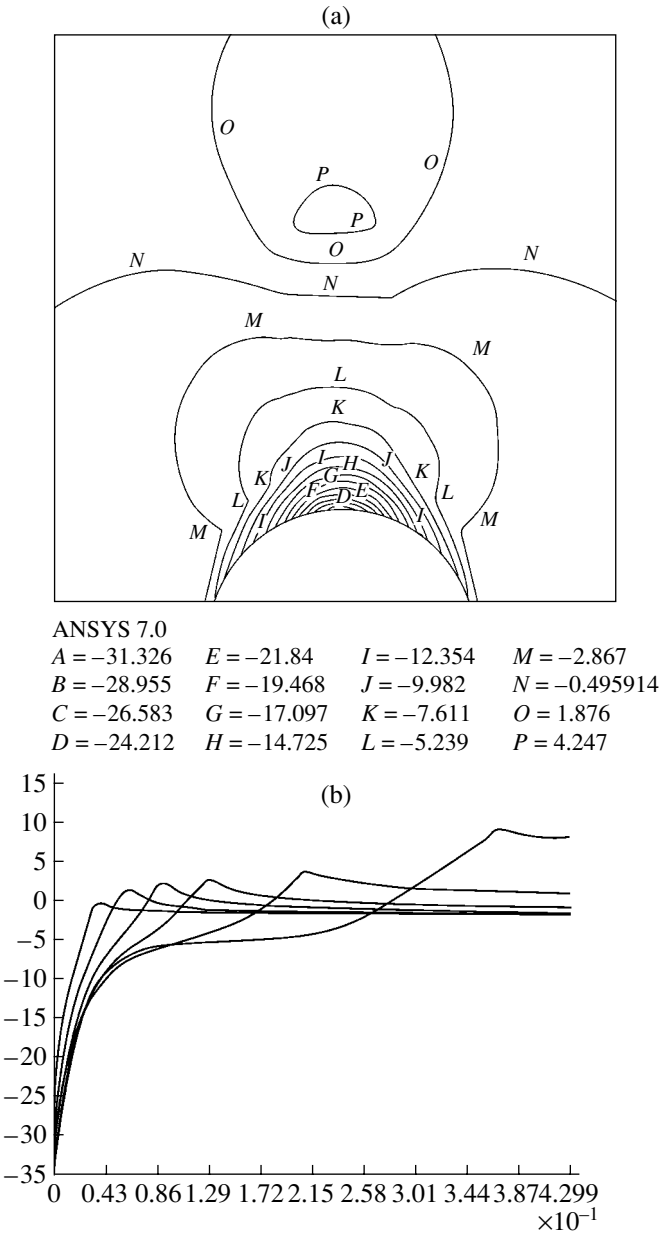

Fig. 4. (a) Contour lines of pressure distribution; (b) pressure distribution at instants of 0.024, 0.036, 0.048, 0.06, 0.078, and 0.102 s.

sponding to Fig. 4a, the high-pressure zone lies at a level of 0.3 of the electrode gap.

Figure 4b shows the curves describing the pressure distribution in the liquid along the central axis of the flow from the lower electrode to the middle of the electrode gap. As the charged jet propagates to the bulk of the electrode gap, the low- and high-pressure zones are formed. The low-pressure zone has a peak near the electrode surface and the value of pressure increases with time. Negative pressure rapidly decreases in the direction from the electrode surface to the bulk of the liquid, while the low-pressure zone is localized in the near-electrode region. The high-pressure region has a peak located at the outer surface of the charged jet and propagating with it to the center of the electrode gap. The peaks of the acceleration zones shown in Fig. 3b approximately correspond to the regions of localization of low pressure, while the extrema of the stagnation zones correspond to the regions of localization of high pressure.

Analysis of the charts of acceleration level lines shows that, at the initial stage (when the charged structure has the shape of a ring), the acceleration zone of EHD flows formed in the cuvette is bifurcated and lies along the lateral surfaces of the electrode. As the charged jet propagates to the bulk of the electrode gap, the acceleration zone of the liquid moves along the axis of the flow to the region located under the electrode, and the flow acquires the structure typical of a developed EHD flow [4, 5]: in the central jet zone formed behind the acceleration zone, acceleration is virtually absent and the velocity vector is directed along the line connecting the electrodes.

Thus, an exotic mechanism is realized in the EHD flow: liquid flows from the region of lower pressure to the region of elevated pressure. Such a flow is possible owing to the volume nature of driving Coulomb forces. It is this flow that determines the original structure of the dynamics of propagation of acceleration and stagnation zones, which is shown in Fig. 3b.

The dynamics of variation of Coulomb forces is characterized by propagation of the region of their localization to the middle of the electrode gap together with a charged liquid jet. The forces decrease monotonically from the electrode surface to the bulk of the liquid and have no extrema in contrast to acceleration. Coulomb forces produce a low-pressure zone immediately in the near-electrode region and set the liquid in motion only at a certain distance from the electrode surface.

CONCLUSIONS

Thus, we have developed a modeling algorithm for processes of formation of EHD flows in a symmetric system of electrodes of the wire-wire type, to which a voltage is applied. The algorithm is determined by propagation of two charged jets from the two electrodes to the bulk of the electrode gap. The computations revealed that, at the same charge density in the near-electrode zones, symmetric four-cellular EHD counterflows are formed in the near-electrode zones of both electrodes. Such flows were repeatedly observed in experiments. The process of formation of a typical zone structure of symmetric EHD counterflows is determined by the flow of a charged jet from each electrode. This process leads to the formation of spatially distributed Coulomb forces decreasing monotonically in the direction from the electrode to the bulk of the liquid. In this case, the low-pressure zone is formed in the near-

electrode regions predominantly in the narrow near-electrode layer, while elevated pressure zones propagate to the bulk of the liquid together with the charged jet boundary. These features determine the characteristic zone structure of EHD flows, i.e., the acceleration zone with an extremum in the near-electrode region and the stagnation zone leading to the formation of a cellular flow.

REFERENCES

1. Yu. K. Stishkov and A. A. Ostapenko, *Electrohydrodynamic Flows in Liquid Insulators* (Leningr. Gos. Univ., Leningrad, 1989) [in Russian].
2. Yu. K. Stishkov, N. A. Zhmaev, and A. V. Yarunichev, Magn. Gidrodin., No. 2, 93 (1989).
3. A. V. Buyanov, A. S. Lazarev, and Yu. K. Stishkov, in *Proceedings of the 5th International Electrohydrodynamics (EHD) Workshop, Poitiers, 2004*, pp. 262–267.
4. Yu. K. Stishkov and M. A. Pavleĭno, Elektron. Obrab. Mater., No. 1, 14 (2000).
5. A. V. Buyanov and Yu. K. Stishkov, Zh. Tekh. Fiz. **73** (8), 34 (2003) [Tech. Phys. **48**, 972 (2003)].

Translated by N. Wadhwa

Technical Physics, Vol. 50, No. 9, 2005, pp. 1124–1131. Translated from Zhurnal Tekhnicheskoĭ Fiziki, Vol. 75, No. 9, 2005, pp. 20–26.

GASES AND LIQUIDS

Properties of Expansions in Legendre Polynomial Derivatives that Show Up in Analysis of Nonlinear Vibrations of a Viscous Liquid Drop

A. N. Zharov, A. I. Grigor'ev, and S. O. Shiryaeva

Demidov State University, Sovetskaya ul. 14, Yaroslavl, 150000 Russia

e-mail: grig@uniyar.ac.ru

Received December 30, 2004

Abstract—Analytical expressions for the coefficients of expansions of Legendre polynomial products in the first and second derivatives of the polynomials with respect to polar angles, as well as for the coefficients of expansions of derivative products in Legendre polynomials and their first derivatives, are derived. An interrelation between these expansion coefficients and a relationship between these coefficients and the Clebsch–Gordan coefficients are found. When axisymmetric nonlinear vibrations of a viscous liquid drop are investigated analytically, the toroidal component of the velocity field can be ignored, which significantly cuts the body of computation. © *2005 Pleiades Publishing, Inc.*

(1) The charged drop is an object of both scientific and applied research. In the 20th century, hundreds of publications were concerned with theoretical and experimental investigation of this object in the approximation linear in vibration amplitude [1–4]. Studies of the drop in terms of a hydrodynamic approach taking into consideration its actual nonlinearity were begun at the end of the last century (see, e.g., [5–7] and Refs. cited therein). Contrary to the linear approximation, which was used to advantage for solving problems stated for both ideal and viscous liquids, the nonlinear investigations performed to date dealt with the ideal liquid alone. The reason for such a situation is the extremely involved mathematics used to solve the nonlinear problem. In this work, we consider a number of local mathematical problems of independent interest appearing in analytical asymptotic studies of a nonlinearly vibrating viscous liquid drop.

(2) It is known [8–11] that, in the approximation linear in amplitude of disturbance of the equilibrium free surface of the drop, the flow velocity field in it can generally be represented as a superposition of three fields: potential, vortex toroidal, and vortex poloidal. The scalarization method allows one to expand the flow velocity field of a viscous liquid in the drop in three mutually orthogonal vector operators $\mathbf{N}_1 \equiv \nabla$, $\mathbf{N}_2 \equiv \mathbf{N}_1 \times \mathbf{r} \equiv \nabla \times \mathbf{r}$, and $\mathbf{N}_3 \equiv \mathbf{N}_1 \times \mathbf{N}_2 \equiv \nabla \times (\nabla \times \mathbf{r})$ as follows [12, 13]:

$$\begin{aligned}\mathbf{V}(\mathbf{r}, t) &= \nabla\Psi_1(\mathbf{r}, t) + \nabla \times (\nabla \times \mathbf{r})\Psi_3(\mathbf{r}, t) \\ &\quad + (\nabla \times \mathbf{r})\Psi_2(\mathbf{r}, t),\end{aligned} \tag{1}$$

where $\Psi_i(\mathbf{r}, t)$ (i = 1–3) are unknown scalar functions to be determined from a specific linearized system of hydrodynamic equations with relevant boundary conditions.

In (1), the first term is the potential part of the velocity field; the second, the vortex poloidal part; and the third, the vortex toroidal part. In the most common case of axisymmetric vibrations of the drop, the potential and poloidal components of the velocity field have projections onto unit vectors $\mathbf{e}_r$ and $\mathbf{e}_\vartheta$, while the toroidal component is projected only on unit vector $\mathbf{e}_\varphi$ of the spherical coordinate system with the origin at the center of mass of the drop.

It was shown [8–11] that hydrodynamic determination of the toroidal component of the velocity field is unrelated to determination of its potential and poloidal components and that the toroidal component does not contribute to the flow-induced deformation of the shape of the drop. The reverse statement is also true: the axisymmetric vibration of the free surface of the drop generates potential and vortex poloidal flows of the liquid in the drop but does not cause toroidal vortex flows. This circumstance was included in all the analyses of vibration of a viscous liquid drop that were made in the linear-in-amplitude approximation [8–12]. Namely, first the potential and vortex poloidal components were calculated; then, a dispersion relation of the problem was derived on their basis, the solution and study of which is the basic goal of linear analysis. In the case of nonlinear vibrations of a liquid viscous drop, the vortex toroidal component should be considered separately, since it is unclear *a priori* whether or not this component will affect the solution through the nonlinear convective term in the Navier–Stokes equation.

In [13, 14], the problem of finding the vortex toroidal component in the linear approximation was considered in explicit form. It was shown that the properties of this velocity field component depend on initial con-

1063-7842/05/5009-1124$26.00

ditions. In particular, it was noted [13, 14] that, if the axisymmetric deformation initially lacks the velocity toroidal component ($\Psi_2(\mathbf{r}, t) \equiv 0$), this component can be set identically equal to zero at any subsequent time instant without loss of generality. It is known that, when nonlinear problems are solved with regular asymptotic techniques based on expansions in small parameter, the initial nonlinear problem is split into a set of linear inhomogeneous subproblems (interrelated through inhomogeneity functions) by means of which the solution components in different orders of smallness are found. Taken together, these components asymptotically approximate a solution to the general nonlinear problem. When a first-order solution to the problem of nonlinear axisymmetric vibrations of a viscous liquid drop lacks vortex toroidal liquid flows, one can argue that these flows will not appear in higher order calculations as well, since inhomogeneity functions in higher order problems are found from solutions to lower order ones, which, as was mentioned above, will not contain the toroidal component of the velocity field.

In view of the aforesaid, the flow velocity field in a viscous axisymmetrically vibrating drop in the approximation linear in vibration amplitude can be represented through scalar functions $\Psi_i(\mathbf{r}, t)$ (i = 1–3) projected onto the axes of the spherical coordinate system [12–15],

$$\mathbf{V}(\mathbf{r}, t) = \left[\frac{\partial \Psi_1}{\partial r} - \frac{1}{r}\Delta_\Omega \Psi_3\right]\mathbf{e}_r + \frac{\partial}{\partial \vartheta}\left[\frac{1}{r}\Psi_1 + \frac{1}{r}\frac{\partial}{\partial r}(r\Psi_3)\right]\mathbf{e}_\vartheta; \quad \Delta_\Omega \equiv \frac{1}{\sin\vartheta}\frac{\partial}{\partial\vartheta}\left(\sin\vartheta\frac{\partial}{\partial\vartheta}\right). \tag{2}$$

As is known [12–15], scalar functions $\Psi_i(\mathbf{r}, t)$ must satisfy the Laplace equations in the spherical coordinate system placed inside the volume bounded by the free surface of the drop, which has a near-spherical shape; hence, these functions are representable as expansions in spherical polynomials $Y_m^l(\vartheta, \varphi)$,

$$\Psi_i(\mathbf{r}, t) = \sum_{m=2}^{\infty} A_{ml}^{(i)}(r, t) Y_m^l(\vartheta, \varphi), \quad i = 1, 3. \tag{3}$$

Since the drop vibrates axisymmetrically (in (3), l = 0 in the spherical functions), it is reasonable to replace expansions in spherical functions by expansions in Legendre polynomials, since $Y_m^0(\vartheta, \varphi) \equiv P_m(\cos\vartheta)$.

Then, from (2) and (3), it follows that the radial part of the flow velocity field in a viscous liquid drop can be represented in the form of a series in Legendre polynomials $P_m(\cos\vartheta)$ that constitute a complete orthogonal set and the vortex poloidal part, as a series in Legendre polynomial first derivatives with respect to polar angle ϑ. Thus, by virtue of (2) and (3), the Legendre polynomial first derivatives with respect to polar angle ϑ, as well as the Legendre polynomials themselves, constitute a complete orthogonal set for functions of the class considered. This is scarcely surprising, since the Legendre polynomial first derivatives are expressed through associated Legendre polynomials with the superscript equal to unity,

$$\frac{d}{d\vartheta}P_m(\cos\vartheta) = P_m^1(\cos\vartheta).$$

Associated Legendre polynomials with a fixed superscript form a complete orthogonal set of eigenfunctions in the interval $-1 \le \cos\vartheta \le 1$, in which any continuous doubly differentiable function of polar angle ϑ is expanded into an absolutely and uniformly convergent series [16, pp. 612–613]. Thus, in analytical calculations of nonlinear axisymmetric vibrations of a viscous liquid drop, there arises the need and simultaneously possibility to expand desired functions in both Legendre polynomials and their first derivatives. The norm of the Legendre polynomial first derivatives with respect to the polar angle is given by

$$\int_0^\pi \partial_\vartheta P_k(\cos\vartheta)\partial_\vartheta P_m(\cos\vartheta)\sin\vartheta d\vartheta = \frac{2\delta_{km}}{2m+1}m(m+1).$$

(3) Let us have a spherical drop of a perfectly conducting incompressible viscous liquid of density ρ, kinematic viscosity ν, and surface tension coefficient σ. The drop, executing nonlinear axisymmetric vibrations, has radius r_0 and carries charge Q. In the spherical coordinate system with the origin at the center of mass of the drop, the equation for its free surface at any time t has the form

$$F(r, \vartheta, t) = r - r_0 - \xi(\vartheta, t).$$

The general problem of nonlinear axisymmetric vibrations of the drop is then mathematically stated as

$$\partial_t \mathbf{U} + (\mathbf{U}\cdot\nabla)\mathbf{U} = -\frac{1}{\rho}\mathrm{grad}\,p + \nu\Delta\mathbf{U};$$

$$\mathrm{div}\mathbf{U} = 0; \quad \Delta\phi = 0;$$

$$t = 0: \mathbf{U} = 0; \quad \xi = \varepsilon\sum_{m\in\Omega} h_m P_m(\mu); \quad \mu \equiv \cos(\vartheta);$$

$$r \longrightarrow 0: \mathbf{U} < \infty; \quad r \longrightarrow +\infty: \nabla\phi \longrightarrow 0;$$

$$r = r_0 + \xi(\vartheta, t): \phi = \phi_S(t); \int_S \mathbf{n}\cdot\nabla\phi dS = -4\pi Q; \tag{4}$$

$$S = \{r, \vartheta, \varphi | r = r_0 + \xi; 0 \le \vartheta \le \pi; 0 \le \varphi \le 2\pi\};$$

$$\int_V r^2 \sin\vartheta dr d\vartheta d\varphi = \frac{4\pi}{3}r_0^3;$$

$$V = \{r, \vartheta, \varphi | 0 \le r \le r_0 + \xi; 0 \le \vartheta \le \pi; 0 \le \varphi \le 2\pi\};$$

$$\int_V \mathbf{r} r^2 \sin\vartheta dr d\vartheta d\varphi = 0;$$

$$\partial_t F + (\mathbf{U}\cdot\nabla)F = 0; \quad \boldsymbol{\tau}(\mathbf{n}\cdot\nabla)\mathbf{U} + \mathbf{n}(\boldsymbol{\tau}\cdot\nabla)\mathbf{U} = 0;$$

$$-p + 2\rho\nu\mathbf{n}(\mathbf{n}\cdot\nabla)\mathbf{U} - \frac{1}{8\pi}(\nabla\phi)^2 + \sigma(\nabla\cdot\mathbf{n}) = 0.$$

Here, ε is a small parameter characterizing the initial disturbance amplitude; Ω is the set of subscripts for initially excited modes; h_m are constants describing the contribution of an mth mode to the initial shape (deformation) of the drop, $\sum_{m\in\Omega} h_m = 1$; $\mathbf{n}$ and $\boldsymbol{\tau}$ are the unit normal and tangent vectors, respectively, relative to the surface of the drop; $\mathbf{U}(r, \vartheta, t)$ is the flow velocity field in the drop; $p(r, \vartheta, t)$ is the pressure field; and $\phi(r, \vartheta, t)$ and $\phi_S(t)$ are the electric field potential near the drop and on its surface, respectively. Symbol ∂_t means the partial derivative with respect to t, and Δ is the Laplacian.

A solution to this nonlinear set of equations will be sought asymptotically by the direct expansion method. To this end, following the general idea of the method of expansion in small parameter, we represent all the desired quantities as series in ε,

$$\begin{aligned}
\xi(\vartheta, t) &= \varepsilon\xi^{(1)}(\vartheta, t) + \varepsilon^2\xi^{(2)}(\vartheta, t) + O(\varepsilon^3);\\
\mathbf{U}(r, \vartheta, t) &= \varepsilon U_r^{(1)}(r, \vartheta, t)\mathbf{e}_r + \varepsilon^2 U_r^{(2)}(r, \vartheta, t)\mathbf{e}_r\\
&+ \varepsilon U_\vartheta^{(1)}(r, \vartheta, t)\mathbf{e}_\vartheta + \varepsilon^2 U_\vartheta^{(2)}(r, \vartheta, t)\mathbf{e}_\vartheta + O(\varepsilon^3);\\
p(r, \vartheta, t) &= p^{(0)}(r, \vartheta, t) + \varepsilon p^{(1)}(r, \vartheta, t)\\
&+ \varepsilon^2 p^{(2)}(r, \vartheta, t) + O(\varepsilon^3);\\
\phi(r, \vartheta, t) &= \phi^{(0)}(r, t) + \varepsilon\phi^{(1)}(r, \vartheta, t)\\
&+ \varepsilon^2\phi^{(2)}(r, \vartheta, t) + O(\varepsilon^3);\\
\phi_S(t) &= \phi_S^{(0)}(t) + \varepsilon\phi_S^{(1)}(t) + \varepsilon^2\phi_S^{(2)}(t) + O(\varepsilon^3).
\end{aligned} \tag{5}$$

In view of the aforesaid, functions $\xi^{(j)}(\vartheta, t)$, $U_r^{(j)}(r, \vartheta, t)$, $U_\vartheta^{(j)}(r, \vartheta, t)$, $p^{(j)}(r, \vartheta, t)$, and $\phi^{(j)}(r, \vartheta, t)$ ($j = 1, 2, 3, \ldots$) are sought in the form of series in Legendre polynomials or Legendre polynomial derivatives,

$$\begin{aligned}
\xi^{(j)}(\vartheta, t) &= \sum_{n\in\Omega} \xi_n^{(j)}(t)P_n(\mu);\\
U_r^{(j)}(r, \vartheta, t) &= \sum_{n\in\Omega} U_{rn}^{(j)}(r, t)P_n(\mu);\\
U_\vartheta^{(j)}(r, \vartheta, t) &= \sum_{n\in\Omega} U_{\vartheta n}^{(j)}(r, t)\partial_\vartheta P_n(\mu);\\
p^{(j)}(r, \vartheta, t) &= \sum_{n\in\Omega} p_n^{(j)}(r, t)P_n(\mu);\\
\phi^{(j)}(r, \vartheta, t) &= \sum_{n\in\Omega} \phi_n^{(j)}(r, t)P_n(\mu);\\
\phi_S^{(j)}(r, \vartheta, t) &= \sum_{n\in\Omega} \phi_{nS}^{(j)}(r, t)P_n(\mu).
\end{aligned} \tag{6}$$

Let us substitute (5) into system (4). Equating the coefficients multiplying different powers of the small parameter yields sets of equations from which solutions in different orders of smallness can be found. The zeroth- and first-order equations will be homogeneous; in higher-than-first orders, we will have sets of inhomogeneous equations where inhomogeneity functions are specified by the nonlinear terms of the equations through solutions to lower order sets. For example, in the second order of smallness, we have

$$\partial_t U_r^{(2)} + \frac{1}{\rho}\partial_r p^{(2)} - \nu\left(\frac{1}{r^2}\partial_{\vartheta\vartheta}U_r^{(2)} + \frac{\cot\vartheta}{r^2}\partial_\vartheta U_r^{(2)} - \frac{1}{r}\partial_{r\vartheta}U_\vartheta^{(2)} - \frac{\cot\vartheta}{r}\partial_r U_\vartheta^{(2)} - \frac{1}{r^2}\partial_\vartheta U_\vartheta^{(2)} - \frac{\cot\vartheta}{r^2}U_\vartheta^{(2)}\right)$$

$$= -U_r^{(1)}\partial_r U_r^{(1)} - \frac{1}{r}U_\vartheta^{(1)}\partial_\vartheta U_r^{(1)} + \frac{1}{r}(U_\vartheta^{(1)})^2;$$

$$\partial_t U_\vartheta^{(2)} + \frac{1}{\rho}\frac{1}{r}\partial_\vartheta p^{(2)} - \nu\left(\partial_{rr}U_\vartheta^{(2)} + \frac{2}{r}\partial_r U_\vartheta^{(2)} - \frac{1}{r}\partial_{r\vartheta}U_r^{(2)}\right)$$

$$= -U_r^{(1)}\partial_r U_\vartheta^{(1)} - \frac{1}{r}U_\vartheta^{(1)}\partial_\vartheta U_\vartheta^{(1)} - \frac{1}{r}U_r^{(1)}U_\vartheta^{(1)};$$

$$\partial_r U_r^{(2)} + \frac{2}{r}U_r^{(2)} + \frac{1}{r}\partial_\vartheta U_\vartheta^{(2)} + \frac{\cot\vartheta}{r}U_\vartheta^{(2)} = 0, \quad \Delta\phi^{(2)} = 0;$$

$$t = 0\colon \mathbf{U}^{(2)} = 0; \quad \xi^{(2)} = -\frac{1}{r_0}\sum_{m\in\Omega}\frac{h_m^2}{2m+1}P_0(\mu)$$

$$-\frac{9}{r_0}\sum_{m\in\Omega}\frac{(m+1)h_m h_{m+1}}{(2m+1)(2m+3)}P_1(\mu);$$

$$r \longrightarrow 0\colon \mathbf{U}^{(2)} < \infty; \quad r \longrightarrow +\infty\colon \nabla\phi^{(2)} \longrightarrow 0;$$

$$r = r_0\colon \phi^{(2)} + \xi^{(2)}\partial_r\phi^{(0)} - \phi_S^{(2)}(t)$$

$$= -\frac{1}{2}(\xi^{(1)})^2\partial_{rr}\phi^{(0)} - \xi^{(1)}\partial_r\phi^{(1)};$$

$$\int_{-1}^{1}\Big[r_0^2\partial_r\phi^{(2)} + r_0\xi^{(1)}(r_0\partial_{rr}\phi^{(1)} + 2\partial_r\phi^{(1)})$$

$$+ r_0\xi^{(2)}(r_0\partial_{rr}\phi^{(0)} + 2\partial_r\phi^{(0)})$$

$$+ (\xi^{(1)})^2\left(\frac{1}{2}r_0^2\partial_{rrr}\phi^{(0)} + 2r_0\partial_{rr}\phi^{(0)}\right) + \partial_r\phi^{(0)}\Big)$$

$$-\partial_\vartheta\xi^{(1)}\partial_\vartheta\phi^{(1)}\Big]d\mu = 0;$$

$$\int_{-1}^{1}(r_0\xi^{(2)} + (\xi^{(1)})^2)d\mu = 0; \quad (7)$$

$$\int_{-1}^{1}(2r_0\xi^{(2)} + 3(\xi^{(1)})^2)P_1(\mu)d\mu = 0;$$

$$-\partial_t\xi^{(2)}(\vartheta, t) + U_r^{(2)}$$

$$= -\partial_t U_r^{(1)}\xi^{(1)}(\vartheta, t) + \frac{1}{r_0}U_\vartheta^{(1)}\partial_\vartheta\xi^{(1)}(\vartheta, t);$$

$$\frac{1}{r_0}\partial_\vartheta U_r^{(2)} + \partial_r U_\vartheta^{(2)} - \frac{1}{r_0}U_\vartheta^{(2)} = -\Big(\frac{1}{r_0}\partial_{r\vartheta}U_r^{(1)} - \frac{1}{r_0^2}\partial_\vartheta U_r^{(1)}$$

$$+ \partial_{rr}U_\vartheta^{(1)} - \frac{1}{r_0}\partial_r U_\vartheta^{(1)} + \frac{1}{r_0^2}U_\vartheta^{(1)}\Big)\xi^{(1)}(\vartheta, t)$$

$$+ 2\Big(\frac{1}{r_0^2}\partial_\vartheta U_\vartheta^{(1)} + \frac{1}{r_0^2}U_r^{(1)} - \frac{1}{r_0}\partial_r U_r^{(1)}\Big)\partial_\vartheta\xi^{(1)}(\vartheta, t);$$

$$-p^{(2)} - \frac{\sigma}{r_0^2}(2 + \Delta_\Omega)\xi^{(2)} + \frac{2\sigma}{r_0^3}\xi^{(1)}(1 + \Delta_\Omega)\xi^{(1)}$$

$$-\frac{1}{8\pi}[2\xi^{(2)}\partial_{rr}\phi^{(0)}\partial_r\phi^{(0)} + (\xi^{(1)})^2((\partial_{rr}\phi^{(0)})^2$$

$$+ \partial_{rrr}\phi^{(0)}\partial_r\phi^{(0)}) + \frac{1}{r_0^2}(\partial_\vartheta\phi^{(1)})^2 + (\partial_r\phi^{(1)})^2$$

$$+ 2\partial_r\phi^{(2)}\partial_r\phi^{(0)} + 2\xi^{(1)}(\partial_{rr}\phi^{(0)}\partial_r\phi^{(1)} + \partial_{rr}\phi^{(1)}\partial_r\phi^{(0)})]$$

$$+ 2\rho\nu\partial_r U_r^{(2)} - (\partial_r p^{(1)} - 2\rho\nu\partial_{rr}U_r^{(1)})\xi^{(1)}(\vartheta, t)$$

$$-2\rho\nu\Big(\frac{1}{r_0^2}\partial_\vartheta U_r^{(1)} + \frac{1}{r_0}\partial_r U_\vartheta^{(1)} - \frac{1}{r_0^2}U_\vartheta^{(1)}\Big)\partial_\vartheta\xi^{(1)}(\vartheta, t) = 0.$$

Substituting (7) into (5) and (6), we obtain inhomogeneity functions containing the products of the Legendre polynomials and their derivatives, namely, $P_k(\cos\vartheta)P_m(\cos\vartheta)$, $\partial_\vartheta P_k(\cos\vartheta)\partial_\vartheta P_m(\cos\vartheta)$, $P_k(\cos\vartheta)\partial_\vartheta P_m(\cos\vartheta)$, and $\partial_\vartheta P_k(\cos\vartheta)\partial_{\vartheta\vartheta}P_m(\cos\vartheta)$. Since, in this case, the right-hand sides of the equations will be represented by series in Legendre polynomials or in their first derivatives, these products should also be represented by the same series,

$$P_k(\cos\vartheta)P_m(\cos\vartheta) = \sum_{n=0}^{\infty}K_{kmn}P_n(\cos\vartheta);$$

$$\partial_\vartheta P_k(\cos\vartheta)\partial_\vartheta P_m(\cos\vartheta) = \sum_{n=0}^{\infty}\alpha_{kmn}P_n(\cos\vartheta);$$

$$P_k(\cos\vartheta)\partial_\vartheta P_m(\cos\vartheta) = \sum_{n=0}^{\infty}\Gamma_{kmn}\partial_\vartheta P_n(\cos\vartheta); \quad (8)$$

$$\partial_\vartheta P_k(\cos\vartheta)\partial_{\vartheta\vartheta}P_m(\cos\vartheta) = \sum_{n=0}^{\infty}\Lambda_{kmn}\partial_\vartheta P_n(\cos\vartheta).$$

The set of eigenfunctions (Legendre polynomials or their derivatives) in which one or another of these products is expanded depends on the expansion standing on the left of a specific inhomogeneous equation.

For relationships (8) to be more convenient to use, it is necessary to find coefficients K_{kmn}, α_{kmn}, Γ_{kmn}, and Λ_{kmn} in explicit form.

(4a) It is known that, for Legendre polynomials defined by the Rodrigues formula

$$P_n(\cos\vartheta) = \frac{(-1)^n}{2^n n!}\frac{d^n}{d(\cos\vartheta)^n}\sin^{2n}\vartheta, \quad n \geq 0, \quad (9)$$

the orthogonality condition

$$\int_0^\pi P_k(\cos\vartheta)P_m(\cos\vartheta)\sin\vartheta d\vartheta = \frac{2\delta_{km}}{2m+1}; \quad (10)$$

$$k, m \geq 0$$

(where δ_{km} is the Kronecker delta) holds.

Let us expand the product $P_k(\cos\vartheta)P_m(\cos\vartheta)$ into a series in Legendre polynomials $P_n(\cos\vartheta)$. To this end, we multiply the relationship

$$P_k(\cos\vartheta)P_m(\cos\vartheta) = \sum_{n=0}^{+\infty}K_{kmn}P_n(\cos\vartheta)$$

by $Pg(\cos\vartheta)\sin\vartheta$ ($g \geq 0$) and integrate the result over ϑ from 0 to π. We (10), we find that

$$K_{kmn} = \frac{2n+1}{2}\int_0^\pi P_k(\cos\vartheta)P_m(\cos\vartheta)P_n(\cos\vartheta)\sin\vartheta d\vartheta. \quad (11)$$

As follows from (9)–(11), coefficients K_{kmn} have the following properties: (i) they are symmetric with respect to the first two subscripts; (ii) at $n = 0$, $K_{km0} = \delta_{km}/(2m + 1)$; (iii) if the first or second subscript is zero, $K_{0mn} = \delta_{mn}$ or $K_{k0n} = \delta_{kn}$, respectively; and (iv) at any k, m, $n \geq 0$,

$$K_{kmn} = (C_{k0m0}^{n0})^2, \quad (12)$$

where C_{k0m0}^{n0} are the Clebsch–Gordan coefficients [17].

At $n = 1$, in view of (11) and (9), we have

$$K_{km1} = \frac{3}{2}\int_0^\pi P_k(\cos\vartheta)\cos\vartheta P_m(\cos\vartheta)\sin\vartheta d\vartheta.$$

Applying the recurrent formula

$$\cos\vartheta P_m(\cos\vartheta) = \frac{m+1}{2m+1}P_{m+1}(\cos\vartheta) + \frac{mn}{2m+1}P_{m-1}(\cos\vartheta)$$

to this expression and using orthogonality condition (10), we easily arrive at an expression for coefficients K_{km1},

$$K_{km1} = \frac{3m\delta_{k,m-1}}{(2m-1)(2m+1)} + \frac{3(m+1)\delta_{k,m+1}}{(2m+1)(2m+3)}.$$

Note that the explicit form of coefficients K_{1mn} and K_{k1n} can be obtained in a similar manner,

$$K_{1mn} = \frac{m}{2m+1}\delta_{m-1,n} + \frac{m+1}{2m+1}\delta_{m+1,n},$$

$$K_{k1n} = \frac{k}{2k+1}\delta_{k-1,n} + \frac{k+1}{2k+1}\delta_{k+1,n}.$$

(4b) Prior to expanding the product $\partial_\vartheta P_k(\cos\vartheta)\partial_\vartheta P_m(\cos\vartheta)$ in Legendre polynomials $P_n(\cos\vartheta)$, we write the relationship

$$\partial_\vartheta P_k(\cos\vartheta)\partial_\vartheta P_m(\cos\vartheta) = \sum_{n=0}^{+\infty}\alpha_{kmn}P_n(\cos\vartheta), \quad (13)$$

multiply it by $P_g(\cos\vartheta)\sin\vartheta$ ($s_g \geq 0$), and integrate the result over ϑ from 0 to π to find, in view of (10),

$$\alpha_{kmn} = \frac{2n+1}{2}\times\int_0^\pi \partial_\vartheta P_k(\cos\vartheta)\partial_\vartheta P_m(\cos\vartheta)P_n(\cos\vartheta)\sin\vartheta d\vartheta. \quad (14)$$

Using (9) and the formula of integration by parts, we find that

$$\alpha_{km0} = \frac{1}{2}\int_0^\pi P_k(\cos\vartheta)(\partial_{\vartheta\vartheta}P_m(\cos\vartheta) + \cot\vartheta\partial_\vartheta P_m(\cos\vartheta))\sin\vartheta d\vartheta. \quad (15)$$

Legendre polynomials are known to satisfy the differential equation

$$\partial_{\vartheta\vartheta}P_m(\cos\vartheta) + \cot\vartheta\partial_\vartheta P_m(\cos\vartheta) + m(m+1)P_m(\cos\vartheta) = 0. \quad (16)$$

Expressing the combination $\partial_{\vartheta\vartheta}P_m(\cos\vartheta) + \cot\vartheta\,\partial_\vartheta P_m(\cos\vartheta)$ from (16), substituting the result into (15), and using orthogonality condition (10), we obtain coefficients α_{km0} in the form

$$\alpha_{km0} = \frac{m(m+1)}{2m+1}\delta_{km}. \quad (17)$$

As follows from (14), coefficients α_{kmn} are (i) symmetric with respect to the first two subscripts; (ii) equal to zero when the first or second subscript equals zero, $\alpha_{0mn} = \alpha_{k0n} = 0$; and (iii) expressed through the Clebsch–Gordan coefficients as [17]

$$\alpha_{kmn} = -C^{n0}_{k0m0}C^{n0}_{k(-1)m1}\sqrt{k(k+1)m(m+1)}. \quad (18)$$

At $n = 1$, in view of (14) and (9), we find that

$$\alpha_{km1} = \frac{3}{2}\int_0^\pi \partial_\vartheta P_k(\cos\vartheta)\cos\vartheta\partial_\vartheta P_m(\cos\vartheta)\sin\vartheta d\vartheta.$$

Applying the recurrent formula

$$\cos\vartheta\partial_\vartheta P_m(\cos\vartheta) = \frac{m}{2m+1}\partial_\vartheta P_{m+1}(\cos\vartheta) + \frac{m+1}{2m+1}\partial_\vartheta P_{m-1}(\cos\vartheta),$$

to this expression, we easily find, with (10), (13), and (17), that

$$\alpha_{km1} = \frac{3m(m-1)(m+1)}{(2m-1)(2m+1)}\delta_{k,m-1} + \frac{3m(m+1)(m+2)}{(2m+1)(2m+3)}\delta_{k,m+1}.$$

(4c) Let us expand the product $P_k(\cos\vartheta)\partial_\vartheta P_m(\cos\vartheta)$ in Legendre polynomial derivatives $\partial_\vartheta P_n(\cos\vartheta)$,

$$P_k(\cos\vartheta)\partial_\vartheta P_m(\cos\vartheta) = \sum_{n=1}^{+\infty}\Gamma_{kmn}\partial_\vartheta P_n(\cos\vartheta). \quad (19)$$

Multiplying (19) by $\partial_\vartheta P_g(\cos\vartheta)\sin\vartheta$ ($g \geq 1$) and integrating the result over ϑ from 0 to π, we find, in view of (10), (13), and (17), that

$$\Gamma_{kmn} = \frac{2n+1}{2n(n+1)}\times\int_0^\pi P_k(\cos\vartheta)\partial_\vartheta P_m(\cos\vartheta)\partial_\vartheta P_n(\cos\vartheta)\sin\vartheta d\vartheta. \quad (20)$$

Substituting expansion (13) into (20) in view of (10) yields

$$\Gamma_{kmn} = \frac{2n+1}{n(n+1)}\frac{\alpha_{nmk}}{2k+1} \quad (21)$$

or, in view of (18),

$$\Gamma_{kmn} = \frac{2n+1}{n(n+1)}\frac{\alpha_{nmk}}{2k+1} \equiv -\frac{(2n+1)}{(2k+1)}\sqrt{\frac{m(m+1)}{n(n+1)}}C^{k0}_{n0m0}C^{k0}_{n(-1)m1}. \quad (21a)$$

Taking into account (20), we can write

$$\Gamma_{kmn} + \Gamma_{mkn} = \frac{2n+1}{2n(n+1)} \times \int_0^\pi \partial_\vartheta (P_k(\cos\vartheta)P_m(\cos\vartheta))\partial_\vartheta P_n(\cos\vartheta)\sin\vartheta d\vartheta. \quad (22)$$

Integration of (22) by parts yields

$$\Gamma_{kmn} + \Gamma_{mkn} = -\frac{2n+1}{2n(n+1)}\int_0^\pi P_k(\cos\vartheta)P_m(\cos\vartheta) \times (\partial_{\vartheta\vartheta}P_n(\cos\vartheta) + \cot\vartheta\partial_\vartheta P_n(\cos\vartheta))\sin\vartheta d\vartheta. \quad (23)$$

Expressing the combination $\partial_{\vartheta\vartheta}P_n(\cos\vartheta) + \cot\vartheta\,\partial_\vartheta P_n(\cos\vartheta)$ from (16) and substituting the result into (23), we get

$$\Gamma_{kmn} + \Gamma_{mkn} = \frac{2n+1}{2} \times \int_0^\pi P_k(\cos\vartheta)P_m(\cos\vartheta)P_n(\cos\vartheta)\sin\vartheta d\vartheta = K_{kmn}. \quad (24)$$

(4d) Let us expand the product $\partial_\vartheta P_k(\cos\vartheta)\partial_{\vartheta\vartheta}P_m(\cos\vartheta)$ in Legendre polynomial derivatives $\partial_\vartheta P_n(\cos\vartheta)$,

$$\partial_\vartheta P_k(\cos\vartheta)\partial_{\vartheta\vartheta}P_m(\cos\vartheta) = \sum_{n=1}^{+\infty}\Lambda_{kmn}\partial_\vartheta P_n(\cos\vartheta). \quad (25)$$

Multiplying identity (25) by $\partial_\vartheta P_g(\cos\vartheta)\sin\vartheta$ and integrating the result over ϑ from 0 to π, we find, in view of (10), (13), and (17), that

$$\Lambda_{mkn} = \frac{2n+1}{2n(n+1)} \times \int_0^\pi \partial_\vartheta P_k(\cos\vartheta)\partial_{\vartheta\vartheta}P_m(\cos\vartheta)\partial_\vartheta P_n(\cos\vartheta)\sin\vartheta d\vartheta. \quad (26)$$

Expressing derivative $\partial_{\vartheta\vartheta}P_m(\cos\vartheta)$ from (16) and applying the recurrent formula

$$-\cot\vartheta\partial_\vartheta P_m(\mu) = \partial_\mu P_{m-1}(\mu) + mP_m(\mu); \quad \mu \equiv \cos\vartheta,$$

we obtain

$$\partial_{\vartheta\vartheta}P_m(\mu) = \partial_\mu P_{m-1}(\mu) - m^2 P_m(\mu). \quad (27)$$

Substituting (27) into (26) in view of the expansion

$$\partial_\mu P_{m-1}(\mu) = \sum_{j=1}^{[m/2]}(2m-4j+1)P_{m-2j}(\mu)$$

(the bracketed quantity in the upper limit of the sum is the integer part of the number), we find that

$$\Lambda_{kmn} = \frac{2n+1}{2n(n+1)}\sum_{j=1}^{[m/2]}(2m-4j+1) \times \int_0^\pi \partial_\vartheta P_n(\cos\vartheta)\partial_\vartheta P_k(\cos\vartheta)P_{m-2j}(\cos\vartheta)\sin\vartheta d\vartheta - \frac{(2n+1)m^2}{2n(n+1)} \times \int_0^\pi \partial_\vartheta P_n(\cos\vartheta)\partial_\vartheta P_k(\cos\vartheta)P_m(\cos\vartheta)\sin\vartheta d\vartheta.$$

In view of (14), this expression can be recast as

$$\Lambda_{kmn} \equiv \frac{2n+1}{n(n+1)}\left(-\frac{m^2}{2m+1}\alpha_{nkm} + \sum_{j=1}^{[m/2]}\alpha_{n,k,m-2j}\right) \quad (28)$$

or, in view of (18),

$$\Lambda_{kmn} \equiv (2n+1)\sqrt{\frac{k(k+1)}{n(n+1)}} \times \left(\frac{m^2}{2m+1}C^{m0}_{n0k0}C^{m0}_{n(-1)k1} - \sum_{j=1}^{[m/2]}C^{(m-2j)0}_{n0k0}C^{(m-2j)0}_{n(-1)k1}\right). \quad (28a)$$

Using (26), we can write the sum

$$\Lambda_{kmn} + \Lambda_{mkn} = \frac{2n+1}{2n(n+1)} \times \int_0^\pi \partial_\vartheta(\partial_\vartheta P_k(\cos\vartheta)\partial_\vartheta P_m(\cos\vartheta))\partial_\vartheta P_n(\cos\vartheta)\sin\vartheta d\vartheta.$$

Integrating this expression by parts gives

$$\Lambda_{kmn} + \Lambda_{mkn} = -\frac{2n+1}{2n(n+1)}\int_0^\pi \partial_\vartheta P_k(\cos\vartheta)\partial_\vartheta P_m(\cos\vartheta) \times (\partial_{\vartheta\vartheta}P_n(\cos\vartheta) + \cot\vartheta\partial_\vartheta P_n(\cos\vartheta))\sin\vartheta d\vartheta.$$

Expressing the combination $\partial_{\vartheta\vartheta}P_n(\cos\vartheta) + \cot\vartheta\,\partial_\vartheta P_n(\cos\vartheta)$ from (16) and substituting it into this

relationship, we get

$$\Lambda_{kmn} + \Lambda_{mkn} = \frac{2n+1}{2} \times \int_0^\pi \partial_\vartheta P_k(\cos\vartheta)\partial_\vartheta P_m(\cos\vartheta)P_n(\cos\vartheta)\sin\vartheta\, d\vartheta = \alpha_{kmn}. \quad (29)$$

Thus, in (8), coefficients Γ_{kmn} of the expansions in Legendre polynomial derivatives are expressed through coefficients α_{kmn} and K_{kmn} of the expansions in Legendre polynomials, according to (21) and (24). The same is true for coefficients Λ_{kmn}, according to (28) and (29). Since α_{kmn} and K_{kmn}, in turn, are expressed through the products of the Clebsch–Gordan coefficients, according to (12) and (18), coefficients Γ_{kmn} and Λ_{kmn} are also expressed though the Clebsch–Gordan coefficients, according to (21a) and (28a). In solving the problem of nonlinear vibrations of a viscous liquid drop, the found relationship between the coefficients may significantly cut the body of computation by means of convolution of the coefficients.

(5) Relationships (24) and (29) can be found in another way, i.e., directly from expansions (8).

(5a) Differentiation of the first expansion in (8) with respect to the polar angles gives

$$P_k(\cos\vartheta)\partial_\vartheta P_m(\cos\vartheta) + P_m(\cos\vartheta)\partial_\vartheta P_k(\cos\vartheta) = \sum_{n=0}^{\infty} K_{kmn}\partial_\vartheta P_n(\cos\vartheta).$$

Now, we apply the third of the expansions in (8) to the left of this relationship and combine all the terms under the sum to get

$$\sum_{n=1}^{\infty} (\Gamma_{kmn} + \Gamma_{mkn} - K_{kmn})\partial_\vartheta P_n(\cos\vartheta) = 0. \quad (30)$$

From this equality, relationship (24) follows immediately, since this expansion in the infinite orthogonal set of the Legendre polynomial first derivatives vanishes iff all the coefficients in (30) equal zero.

(5b) Differentiation of the second expansion in (8) with respect to the polar angle yields

$$\partial_\vartheta P_k(\cos\vartheta)\partial_{\vartheta\vartheta} P_m(\cos\vartheta) + \partial_\vartheta P_m(\cos\vartheta)\partial_{\vartheta\vartheta} P_k(\cos\vartheta) = \sum_{n=0}^{\infty} \alpha_{kmn}\partial_\vartheta P_n(\cos\vartheta).$$

Now, we apply the fourth of the expansions in (8) to the left of this relationship and combine all the terms under the sum to get

$$\sum_{n=1}^{\infty} (\Lambda_{kmn} + \Lambda_{mkn} - \alpha_{kmn})\partial_\vartheta P_n(\cos\vartheta) = 0$$

from whence relationship (29) follows.

(6) The found relationship between the expansion coefficients in (8) and the Clebsch–Gordan coefficients allows us to derive new relationships between second-degree products of the Clebsch–Gordan coefficients, which cannot be derived from the known formulas (see, e.g., [17]). For example, substituting (18) and (28) into (29) yields

$$\sum_{j=1}^{[m/2]} \frac{1}{\sqrt{m(m+1)}} C_{n0,\,k0}^{(m-2j)0} C_{n(-1),\,k1}^{(m-2j)0} \times \sum_{j=1}^{[k/2]} \frac{1}{\sqrt{k(k+1)}} C_{n0,\,m0}^{(k-2j)0} C_{n(-1),\,m1}^{(k-2j)0} = \frac{1}{(2n+1)\sqrt{n(n+1)}} \times \frac{[n(n+1)-(k-m)^2][n-(k+m)](1-n+m+k)}{[n(n+1)-k(k+1)-m(m+1)]} \times C_{k0,\,m0}^{n0} C_{k(-1),\,m1}^{n0}.$$

Another relationship between the second-degree products of the Clebsch–Gordan coefficients can be found from (24) in view of (12) and (21). However, this relationship can also be deduced from the relationships for the Clebsch–Gordan coefficients that were presented in [17] and is therefore omitted here.

CONCLUSIONS

Thus, problem (7) of finding quadratic-in-amplitude solution components appearing in calculation of nonlinear vibrations of a viscous liquid drop can be represented in a solvable form. In any case, the inhomogeneity functions on the right-hand sides of problem (7) can be expanded in the same single series in Legendre polynomials or in their first derivatives as the desired quantities of the problem, which stand on the left-hand sides of Eqs. (7). Using expressions (21), (24), (28), and (29), which relate coefficients Γ_{kmn}, Λ_{kmn}, K_{kmn}, and α_{kmn} in expansions (8), one can significantly simplify the mathematics and analytical form of the final result.

ACKNOWLEDGMENTS

This work was supported by a grant of the President of the Russian Federation (grant no. MK-2946-2004-1) and the Russian Foundation for Basic Research (grant no. 03-01-00760).

REFERENCES

1. A. I. Grigor'ev, Elektrokhim. Obrab. Met., No. 6, 23 (1990).
2. A. I. Grigor'ev and S. O. Shiryaeva, Izv. Ross. Akad. Nauk, Mekh. Zhidk. Gaza, No. 3, 3 (1994).
3. D. F. Belonozhko and A. I. Grigor'ev, Elektrokhim. Obrab. Met., No. 4, 17 (2000).
4. A. I. Grigor'ev, Zh. Tekh. Fiz. **70** (6), 22 (2000) [Tech. Phys. **45**, 543 (2000)].

5. J. A. Tsamopolous and R. A. Brown, J. Fluid Mech. **147**, 373 (1984).
6. Z. C. Feng, J. Fluid Mech. **333**, 1 (1997).
7. S. O. Shiryaeva, A. N. Zharov, and A. I. Grigor'ev, Zh. Tekh. Fiz. **74** (1), 10 (2004) [Tech. Phys. **49**, 8 (2004)].
8. S. Chandrasekhar, Proc. London Math. Soc. **3** (9), 141 (1959).
9. C. A. Miller and L. E. Scriven, J. Fluid Mech. **32**, 417 (1968).
10. D. A. Saville, Phys. Fluids **17**, 54 (1974).
11. R. W. Hasse, Ann. Phys. **93**, 68 (1975).
12. A. I. Grigor'ev and A. E. Lazaryants, Zh. Tekh. Fiz. **63** (10), 12 (1993) [Tech. Phys. **38**, 840 (1993)].
13. S. O. Shiryaeva, A. E. Lazaryants, A. I. Grigor'ev, *et al.*, Preprint No. 27, IM RAN (Institute of Microelectronics, Russian Academy of Sciences, Yaroslavl, 1994).
14. S. O. Shiryaeva, D. F. Belonozhko, V. B. Svetovoĭ, and A. I. Grigor'ev, Preprint No. 31, IM RAN (Institute of Microelectronics, Russian Academy of Sciences, Yaroslavl, 2001).
15. A. N. Zharov and A. I. Grigor'ev, Zh. Tekh. Fiz. **75** (1), 22 (2005) [Tech. Phys. **50**, 19 (2005)].
16. A. N. Tikhonov and A. A. Samarskii, *Equations of Mathematical Physics* (Nauka, Moscow, 1977; Pergamon, Oxford, 1964).
17. D. A. Varshalovich, A. N. Moskalev, and V. K. Khersonskiĭ, *Quantum Theory of Angular Momentum* (Nauka, Leningrad, 1975; World Sci., Singapore, 1988).

Translated by V. Isaakyan

Technical Physics, Vol. 50, No. 9, 2005, pp. 1132–1138. Translated from Zhurnal Tekhnicheskoĭ Fiziki, Vol. 75, No. 9, 2005, pp. 27–33.

GASES AND LIQUIDS

Characteristics of a Magnetogasdynamic Diffuser under Different Modes of Electric Current Switching

R. V. Vasil'eva*, A. V. Erofeev*, T. A. Lapushkina*, S. A. Poniaev*, S. V. Bobashev*, and D. M. van Wie**

** Ioffe Physicotechnical Institute, Russian Academy of Sciences, Politekhnicheskaya ul. 26, St. Petersburg, 194021 Russia*

e-mail: tanyusha@mail.ioffe.ru

*** John Hopkins University, Laurel, Maryland, 20723 United States*

Received January 26, 2005

Abstract—This paper elaborates upon a previous investigation into the influence of external electric and magnetic fields on a flow through a supersonic diffuser. The aim of the present study is to correlate a change in the configuration of a shock wave emerging near the diffuser inlet at magnetohydrodynamic interaction with the amount of force and energy actions and with total pressure losses. For this purpose, the main parameters of the shock wave structure and the total pressure are measured at the diffuser outlet when the flow is subjected to magnetic and electric fields of various strengths at different routes of current passage. In the experiments, a shock tube with a supersonic nozzle is employed. The shock tube forms a flow behind the shock wave reflecting from the end of the tube, which terminates in the nozzle. The diffuser is located directly downstream of the nozzle. The investigation is carried out in xenon. The flow is subjected to external fields at the inlet of the diffuser. The shock wave structure is visualized by frame sweeping of Schlieren patterns of the flow. The total pressure is measured with a piezoelectric transducer located at the end of the channel. The results obtained make it possible to optimize the action on the flow in terms of power consumption and total pressure losses for a given design of the diffuser. © *2005 Pleiades Publishing, Inc.*

INTRODUCTION

This work was favored by the furiously debated concept of shock control in the diffusers of hypersonic vehicles with the magnetohydrodynamic (MHD) approach [1–7].

The objects of experimental investigation are a diffuser with total internal compression of the flow and a shock wave in the form of two attached shocks arising at the inlet of the diffuser. With magnetic and electric fields applied, the flow through the diffuser is subjected to the Lorentz force, which decelerates or accelerates the flow, depending on the direction of the current, and Joule heating, which slows down the supersonic flow. In addition, the flow through the diffuser is noticeably affected by the boundary layer. The region and duration of the field action on the flow depend on the time of electric current passage.

In this paper, we study the effect of magnetic and electric fields on the flow at the diffuser inlet. Our aim is (i) to see how various modes of current passage influence the basic characteristics of the attached shocks and total pressure losses, (ii) to correlate the changes observed with the amount of force and energy actions causing these changes, and (iii) to optimize the external action on the flow by analyzing the data obtained. It also seems useful to compare our experimental data with the available analytical calculations.

EXPERIMENTAL

As a working gas, we used thermally preionized inert gas xenon. Simulation was performed in terms of the basic similarity criteria.

The experimental setup was described in detail elsewhere [8, 9]. It comprises a gasdynamic channel, a system generating a quasi-static magnetic field, and a system generating quasi-static and pulsed–periodic electric currents. Figure 1 shows the basic components of the gasdynamic channel: a shock tube, a nozzle, and a diffuser. When the flow at the end of the shock tube

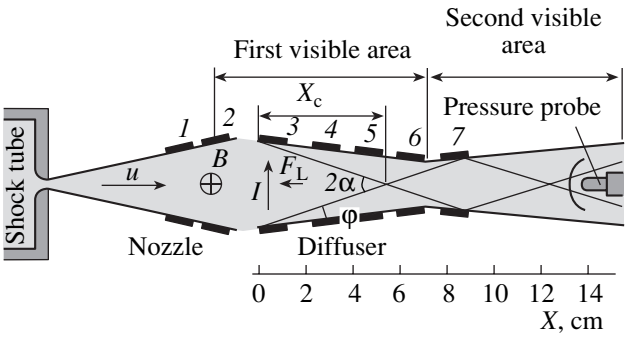

Fig. 1. Schematic of the setup. u is the flow velocity, B is the magnetic induction, I is the electric current, and F_L is the Lorentz force. (*1–7*) Electrodes.

1063-7842/05/5009-1132$26.00 © 2005 Pleiades Publishing, Inc.

slows down, the gas strongly heats up with subsequent thermal ionization. The resulting plasma issues into the accelerating nozzle, where the degree of ionization decreases appreciably; however, it remains sufficient for MHD interaction because of a slow recombination of charged particles in xenon. Then, the accelerated flow enters the diffuser with electrodes mounted on its wall (the electrodes are numbered in Fig. 1). Figure 1 also shows the directions of flow velocity u, magnetic induction B, electric current I, and Lorentz force F_L, together with the basic parameters of the shock wave at the inlet: distance X_c between the diffuser inlet and the point of crossing of the attached shocks, angle φ between the attached shock and the diffuser wall, and angle 2α at which the attached shocks meet.

The investigation techniques used in the experiments were the following: optical methods (a tailored optical scheme for visualizing gasdynamic inhomogeneities in the first or second area of observation (see Fig. 1) and high-speed Schlieren photography of the flow [8, 9]); recording of I–V characteristics [10] and potential spatial distribution; and measurement of the volume and effective conductivity of the plasma [11], as well as of the concentration and temperature of electrons based on radiation in recombination continuum [11, 12]. A new (previously unused) procedure in this experiment is measurement of total pressure [13]. To this end, using the calibrated piezoelectric probe shown in Fig. 1, we measured stagnation pressure p_{20} behind the shock wave detached from the probe. Then, the probe was replaced by a notched plate. From the inclination of the contours of weak flow perturbations due to the notches, we determined local Mach number M_1 of the flow. With these two values, total pressure p_{10} in the flow was calculated using the well-known relationship [14].

A magnetic field was generated by discharging a capacitor bank through Helmholtz coils. Compared with plasma flow duration Δt, the magnetic field can be considered as stationary. An electric field was produced by discharging a circuit consisting of a set of LC cells through the plasma gap and loading resistor. It should be noted that, in the experiment discussed, the application of an external electric field is the necessary condition for operation of the setup; namely, it is applied to compensate for a high near-electrode potential drop, which prevents the passage of a magnetically induced current [10]. The electric field generation circuit used in the experiments makes it possible to study both steady-state and pulsed–periodic processes. To form short single current pulses and a train of current pulses, time-separated voltages from several LC circuits were applied to the electrodes. Each of the LC cells was fed by closing a controllable switch (a TCh-25 thyristor). To close the switch at a given time instant and control the time delay between current pulses, we designed a special switch-controlling device consisting of synchronization and delay control units. The equivalent

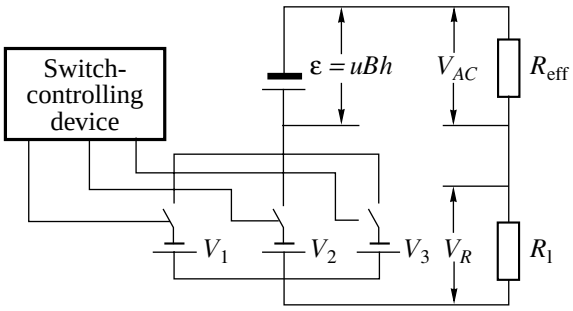

Fig. 2. Equivalent electric diagram.

electric circuit for a pair of electrodes is shown in Fig. 2. Here, the MHD generator is represented as a source of emf $\varepsilon = uBh$ with internal resistance R_{eff} series-connected to three sources of time-shifted external voltages (V_1, V_2, and V_3) and loading resistor R_l. For the circuit consisting of the MHD generator and external voltage source connected in series, Ohm's law has the form

$$IR_{eff} = (1 - k)(uBh + V),$$

where $k = R_l/(R_l + R_{eff})$ is the load ratio, h is the electrode gap, and V is the voltage at the output of the LC circuit.

The experiments were carried out for a Mach number at the shock wave front in the shock tube of 8 and an initial gas pressure in the low-pressure channel of 30 Torr. The calculated flow parameters at the diffuser inlet were Mach number $M_0 = 4.3$, gas density $\rho_{in} = 0.127$ kg/m^3, flow velocity $u_{in} = 1.55 \times 10^3$ m/s, plasma conductivity $\sigma_0 = 600$ S/m, and flow duration $\Delta t \approx 600$ μs.

Interaction with the external fields was accomplished at the inlet of the diffuser, because, as was shown earlier [9, 15, 16], such a local action provides an energetically more favorable control of attached shocks.

The flow through the diffuser was studied for three modes of current switching: (i) the steady-state transverse current passes between the third pair of electrodes facing each other in the inlet part of the diffuser, the inlet operating like a Faraday channel; (ii) the current is of the same configuration, but the channel operates in the pulsed–periodic regime; and (iii) the steady-state longitudinal current flows in a narrow near-wall region between adjacent electrodes *3* and *4*.

THE FIRST MODE OF CURRENT SWITCHING

The influence of external fields on the diffuser flow appreciably depends on the current density distribution in the electrode gap. This distribution was deduced theoretically [17, 18]. Figure 3 shows the current distribution numerically simulated under the conditions of the

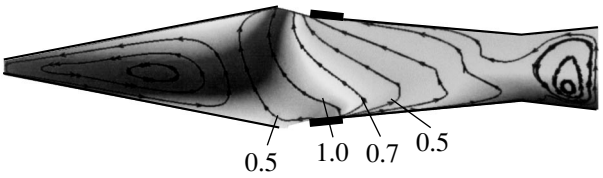

Fig. 3. Numerically simulated current density isolines at I = 390 A and B = 1.3 T. The figures indicate the relative current density.

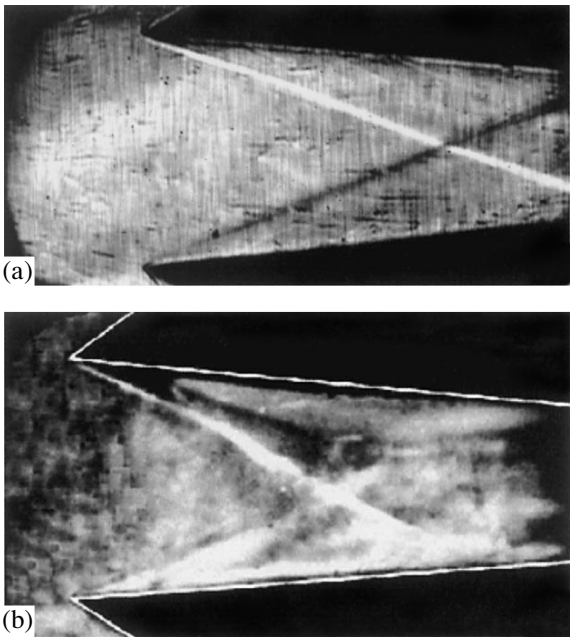

Fig. 4. Schlieren pattern of the flow. (a) I = 0, B = 0 and (b) I = 390 A, B = 1.3 T.

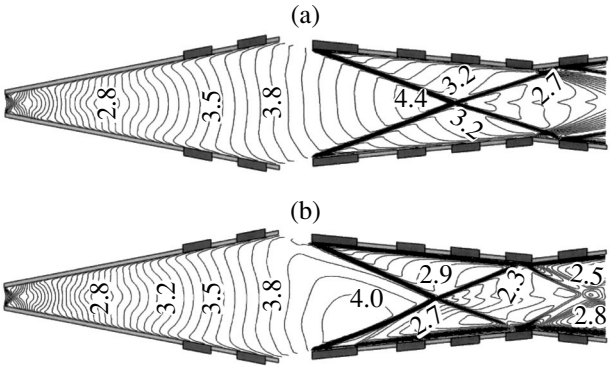

Fig. 5. Numerically simulated distribution of the flow Mach number and the positions of the attached shocks. (a) I = 0, B = 0 and (b) I = 390 A, B = 1.45 T.

given experiment (courtesy of the authors of [17, 18]). The distribution is asymmetric due to the Hall effect. A high current density near the remote edge of the anode, which results in a considerably wide temperature layer near the wall, stands out. We assume that range L of interaction equals approximately two electrode lengths along the flow. The closed current lines in the nozzle and at the end of the channel (Fig. 3) are due to flow and field nonuniformities. The calculation shows that these currents are weak and, therefore, affect the flow pattern little.

Figure 4a (Schlieren patterns of the flow) shows the positions of the attached and reflected shocks in the absence of external fields. The reflection of the attached shocks from one another is regular. In the Schlieren pattern, one can also see the boundary layer and weak gasdynamic perturbations at the electrode–insulator interfaces. Figure 4b shows the Schlieren pattern for the case when the flow stagnates in the magnetic and electric fields. The switch-on attached shocks are seen to became slightly concave, possibly because of the presence of Hall currents. The most noticeable changes are that angle φ increased and the point of interaction of these shocks approached the diffuser inlet, since the external fields slowed down the flow and decreased its Mach number. The Schlieren pattern also shows that the near-wall layer widened considerably: it originates at the remote edges of the electrodes and accommodates weak shocks.

Figure 5a displays the pattern of gasdynamic inhomogeneities calculated at the same initial conditions with no regard to viscosity [17] at I = 0, and Fig. 5b shows the shock configuration when the flow is affected by the Lorentz force and Joule heat. It is seen that the positions of the attached shocks obtained by numerical simulation change more weakly than in the physical experiment. To elucidate the reason for this observation, let us estimate the amounts of the force and energy actions that affect the flow in the numerical and physical experiments.

In the calculation, the initial conditions were identical and the values of the electric current and magnetic field were nearly identical to those used in the experiment. The difference showed up in the value of the conductivity. The calculation results showed that the voltage drop over the electrode gap is approximately twice as small as in the experiment. This means that the calculated conductivity (σ = 650 S/m) is higher than the experimental value in the flow core (σ = 300 S/m) determined in [11]. This, probably, is due to the fact that, once the Lavsan[1] diaphragm at the end of the shock tube breaks down, a large amount of organic impurities enter the channel, decreasing the selective heating of electrons and nonequilibrium ionization of the gas. A lower conductivity leads to an increase in the Joule heating of the gas and, consequently, to greater changes in the positions of the attached shocks, which we observe in the experiment.

Another sign that the flow is affected from the outside are total pressure losses. The total pressure was

[1] Russian equivalent of Dacron.

measured and calculated at the diffuser end. In the absence of external actions, the experimental and calculated values of the total pressure were $p_{10}^0 = 9.4$ and 12.3 atm, respectively. In the presence of current I = 330 A and magnetic induction B = 1.3 T, the respective values of the total pressure equaled $p_{10} = 5.9$ and 9.13 atm. Consequently, a weaker change in the positions of the attached shocks in the numerical experiment is accompanied by a lower relative loss in the total pressure.

The changes in the positions of the attached shocks and total pressure losses are the responds of the flow to the force and energy actions. The force action is defined by the Stuart parameter (St), which is the ratio of the work done by the Lorentz force over the length of the interaction zone to the doubled kinetic energy of the gas [19]. Energy action N is defined as the ratio of the Joule heat being released in the gas due to external and magnetically induced fields for the time of flight to the doubled kinetic energy of the gas [19]. We express these parameters as follows:

$$\mathrm{St} = \frac{jBL}{\rho_{in}u_{in}^2}, \quad N = \frac{j^2}{\sigma_0}\frac{L}{u_{in}}\frac{1}{\rho_{in}u_{in}^2}.$$

Here, $j = I/S$ is the current density; S is the sum of the areas of the electrode and electrode gap; σ_0 is the plasma scalar conductivity; and ρ_{in} and u_{in} are the gas density and flow velocity at the diffuser inlet, respectively. The table lists the experimental and calculated amounts of the actions and their attendant changes in the flow at I = 350 A and B = 1.3 T (namely, relative change $\frac{\Delta\alpha}{\alpha^0}$ in the angle between the attached shocks at the point of crossing, relative change $\frac{\Delta X_c}{X_c^0}$ in the position of this point, and relative change $\frac{\Delta p_{10}}{p_{10}^0}$ in the total pressure; the values in the denominators are the respective parameters in the absence of external actions).

As seen from the data presented, the weaker changes in the flow parameters in the numerical experiment are associated with weaker Joule heating.

The impression of how the flow parameters are affected by various external effects can be gained using the one-dimensional approximation [19, 20]. It has been shown that various factors (the channel geometry, Lorentz force, heat supply or removal) act additively, their relative contributions being different. For example, with St and N being the same, the Lorentz force influences the flow velocity 2.5 times more strongly than the heating, irrespective of the flow Mach number. The influence of the Stuart and energy parameters on flow Mach number M depends on the value of M. For example, at M close to unity, the Lorentz force also acts

Table

	I, A	$\frac{\Delta\alpha}{\alpha^0}$	$\frac{\Delta X_c}{X_c^0}$	$\frac{\Delta p_{10}}{p_{10}^0}$	St	N
Experiment	330	0.4	0.27	0.38	0.037	0.047
Calculation	360	0.05	0.12	0.245	0.04	0.022

2.5 times more effectively than the heating. At M > 5, the Lorentz force and Joule heating equally influence number M. As applied to the given experiment, these two factors seem to have comparable effects on the flow Mach number, which is the chief parameter specifying the positions of the attached shocks.

Thus, one reason for the discrepancy between the experimental and numerical data is that, in the experiment, the plasma conductivity is lower than that used in the calculation; accordingly, the Joule heating is more intense and the flow stagnates more rapidly. The second reason is the formation of the near-wall layer in the diffuser in the experiment.

The experiment was carried out in a wide range of the current at B = 1.3 T. Figure 6 shows the main geometric parameters of the attached shocks, as well as the total pressure on the flow axis at the diffuser outlet and the relative amounts of the force and energy actions, at various current strengths. It follows from Fig. 6 that the shock wave configuration changes appreciably as the action gets stronger. For example, at the maximum current, angle 2α approaches 90°; that is, under these conditions, regular reflection of the attached shocks changes to Mach reflection with the formation of local subsonic zones. In this regime, the total pressure drops most significantly (by a factor of five) and approximately 10% of the flow kinetic energy is spent.

Since this work was aimed at studying the feasibility of correcting the shock wave characteristics at small deviations of the flight Mach number from the rated values, it is of interest to know conditions under which the shock characteristics change insignificantly (about 10%) in the given diffuser. The corresponding data are $\frac{\Delta\alpha}{\alpha^0} = 0.1$, $\frac{\Delta X_c}{X_c^0} = 0.1$, $\frac{\Delta p_{10}}{p_{10}^0} = 0.25$, and St = 0.011, N = 0.0055.

THE SECOND MODE OF CURRENT SWITCHING

To reduce the level of force and energy actions, we used pulsed–periodic current signals and accomplished the so-called relaxation–periodic action. The essence of such an approach is that there exist a finite relaxation time for which the shock wave takes a new configuration after the action has been switched on and a finite relaxation time for which the shock returns to the former configuration after the action has been switched

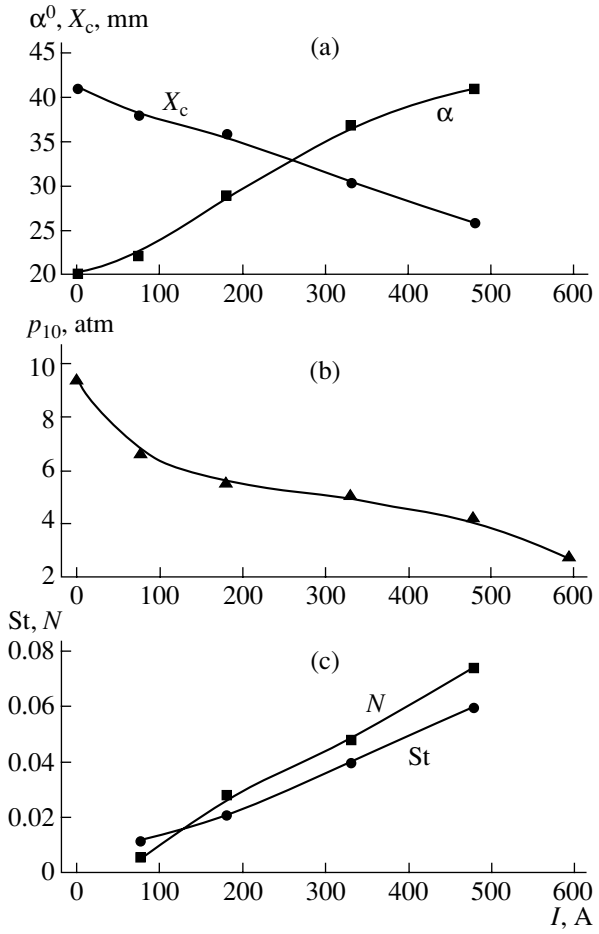

Fig. 6. (a) Half-angle between the shocks at the point of crossing and the position of this point, (b) total pressure, and (c) parameters of the force (St) and energy (N) actions vs. the current strength at $B = 1.3$ T.

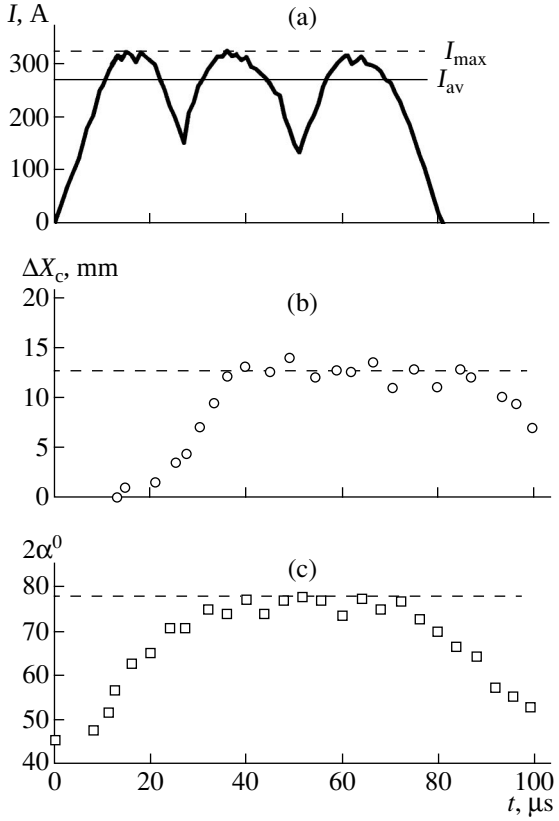

Fig. 7. Pulsed–periodic regime at $B = 1.3$ T. The time variations of the (a) current, (b) difference between the positions of the point of crossing of the shocks in the absence and presence of the interaction, and (c) angle between the intersecting attached shocks. The dashed lines in panels (b) and (c) show the steady-state values of ΔX_c and 2α at $I = I_{max}$.

off [21–23]. The shape of current pulses is shown in Fig. 7a. The first pulse rises more slowly. It may be assumed that the second and third pulses are fragments of the pulsed–periodic current. Figures 7b and 7c show that the angle between the shocks and the distance to the point of their crossing reach the steady-state values, which correspond to a maximum current, within 30–40 μs from the beginning of the first pulse and then remain virtually insensitive to the current oscillations. The pulsed–periodic current needed to produce a given shock configuration is approximately 10% lower than the direct current. Thus, there is reason to think that, in the former case, the force and energy actions are 10 and 20%, respectively, lower than in the latter. The total pressure remains nearly the same.

The numerical simulation of the problem indicates the same tendencies [23]. Figure 8 shows the variation of geometric parameter X_c with current oscillation. During the first pulse, X_c increases but does not reach the steady-state value. Then, the value of X_c varies weakly with time and, when the current drops most significantly (between the second and third pulses), becomes appreciably higher than its value for the same value of the stationary current.

From the experiments with pulsed–periodic interaction, one can find the amount of external actions causing small changes in the geometric parameters of the attached shocks and an insignificant drop of the total pressure. The related data are as follows: $\frac{\Delta\alpha}{\alpha^0} = 0.1$, $\frac{\Delta X_c}{X_c^0} = 0.1$, $\frac{\Delta p_{10}}{p_{10}^0} = 0.75$, St = 0.01, and $N = 0.0045$.

The force and energy cost in this case are lower than in the previous one.

THE THIRD MODE OF CURRENT SWITCHING

This mode of interaction is shown in Fig. 9 [16, 20]. Here, near-wall longitudinal current I passes through the pair of electrodes *3* and *4*. In this case, Lorentz force

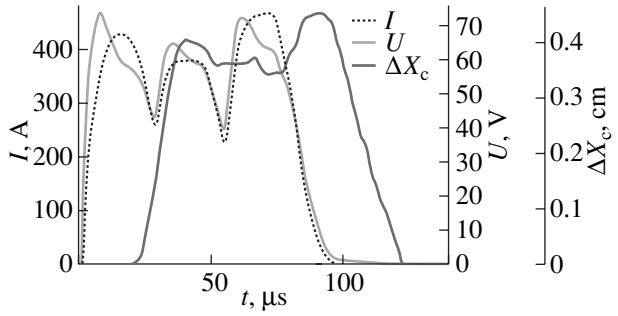

Fig. 8. Numerically simulated time variations of the electric current, voltage applied to the electrodes, and shift of the point of crossing of the attached shocks at $B = 1.3$ T.

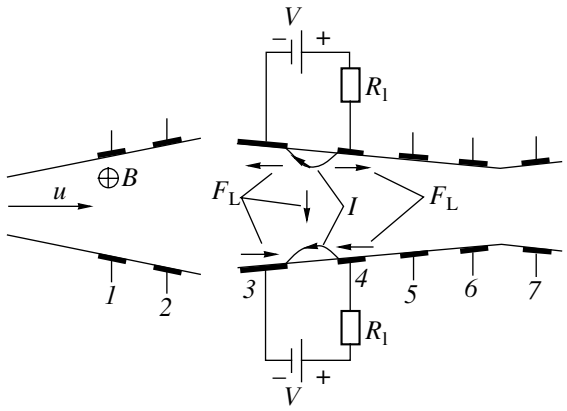

Fig. 9. The third mode of current switching: I is the electric current and F_L is the Lorentz force.

(a)

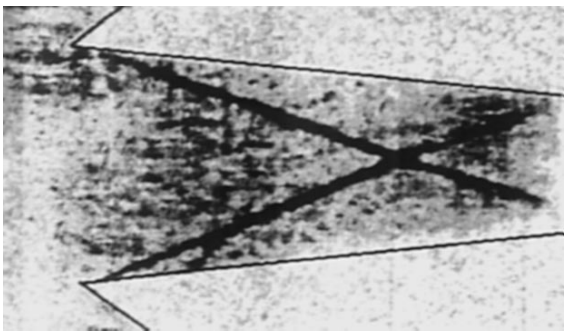

(b)

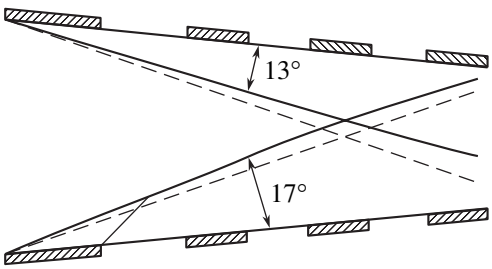

Fig. 10. (a) Schlieren pattern of the shocks and (b) the values of angle φ.

F_L both compresses (expands) the gas volume and decelerates (accelerates) the flow. Figure 10a shows the Schlieren pattern of the flow at an average current of 450 A and $B = 1.3$ T, and Fig. 10b clarifies the related values of angle φ. It is seen that the inclinations of the attached shocks changed by 2° as a result of the interaction: the upper shock approached the wall, while the lower moved away from it. Within the accuracy of the measurements, the total pressure in the absence and presence of the external actions remained the same.

In this mode of current switching, the power of volume forces P is defined as

$$P = \int \mathbf{F}_L \cdot \mathbf{u} d\tau,$$

where $\mathbf{F}_L = \mathbf{j} \times \mathbf{B}$ is the Lorentz force, $\mathbf{u}$ is the flow velocity, and τ is the volume.

The average work of the Lorentz force is $\langle A \rangle = \langle P \rangle (L/u_{in})$. The value of $\langle \mathrm{St} \rangle = \langle A \rangle / \rho_{in} u_{in}^2$ is estimated accurate to a factor of two.

Here, the main parameters of the shocks and flow change noticeably when $\frac{\Delta\varphi}{\varphi_0} = 0.13$, $\frac{\Delta p_{10}}{p_{10}^0} = 0$, St = 0.02, and $N = 0.1$.

This mode seems attractive in that the flow core is disturbed weakly; however, it is energy-hungry.

CONCLUSIONS

Analysis of the configuration of the shock wave at the inlet of the diffuser that appears under the action of magnetic and electric fields suggests that the pulse–periodic regime is optimal in terms of energy consumption and total pressure losses.

Generalizing the experience gained in this area of research, we argue that the place and mode of action application can always be found in such a way that small changes in the position of the attached shocks require low energy costs and are accompanied by low losses in the total pressure. The MHD approach to controlling shocks in a diffuser seems very promising in this respect.

ACKNOWLEDGMENTS

This work was supported by the Russian Academy of Sciences (program no. 20) and the EOARD (ISTC project no. 2009).

REFERENCES

1. E. P. Gurijanov and P. T. Harsha, in *Proceedings of the 7th Aerospace Planes and Hypersonic Technology Conference, Norfolk, 1996*; AIAA Pap. No. 96-4609.
2. V. L. Fraishtadt, A. L. Kuranov, and E. G. Sheikin, Zh. Tekh. Fiz. **68** (11), 43 (1998) [Tech. Phys. **43**, 1309 (1998)].

3. Yu. P. Golovachev and S. Yu. Sushchikh, Zh. Tekh. Fiz. **70** (2), 28 (2000) [Tech. Phys. **45**, 168 (2000)].
4. A. Vatazhin, V. Kopchenov, and O. Gouskov, AIAA Pap. No. 99-4972 (1999).
5. S. O. Macheret, V. N. Shneider, and R. V. Miles, AIAA Pap. No. 2001-2880 (2001).
6. V. A. Bityurin, J. T. Lineberry, V. G. Potebnia, *et al.*, in *Proceedings of the 28th AIAA Plasmadynamics and Lasers Conference, Atlanta, 1997*; AIAA Pap. No. 97-2393.
7. Yu. P. Golovachev, S. Yu. Sushchikh, and D. V. van Wie, AIAA Pap. No. 2000-2666 (2000).
8. S. V. Bobashev, R. V. Vasil'eva, E. A. D'yakonova, *et al.*, Pis'ma Zh. Tekh. Fiz. **27** (2), 63 (2001) [Tech. Phys. Lett. **27**, 71 (2001)].
9. T. A. Lapushkina, S. V. Bobashev, R. V. Vasil'eva, *et al.*, Zh. Tekh. Fiz. **72** (4), 23 (2002) [Tech. Phys. **47**, 397 (2002)].
10. S. V. Bobashev, A. V. Erofeev, T. A. Lapushkina, *et al.*, in *Proceedings of the 32nd AIAA Plasmadynamics and Lasers Conference & 4th Weakly Ionized Gases Workshop, Anaheim, 2001;* AIAA Pap. No. 2001-2878.
11. S. V. Bobashev, A. V. Erofeev, T. A. Lapushkina, *et al.*, in *Proceedings of the 41st Aerospace Meeting and Exhibition, Reno, 2003;* AIAA Pap. No. 2003-0169.
12. T. A. Lapushkina, R. V. Vasil'eva, A. V. Erofeev, *et al.*, Pis'ma Zh. Tekh. Fiz. **30** (17), 33 (2004) [Tech. Phys. Lett. **30**, 724 (2004)].
13. R. V. Vasil'eva, A. V. Erofeev, T. A. Lapushnika, *et al.*, in *Proceedings of the International Scientific and Technical Conference on Fundamental Problems of Fast Flows, Zhukovskii, 2004*, pp. 237–238.
14. D. G. Loitsyanskii, *Fluid Mechanics* (Nauka, Moscow, 1978) [in Russian].
15. S. V. Bobashev, A. V. Erofeev, T. A. Lapushkina, *et al.*, in *Proceedings of the 11th AIAA/AAAF International Conference on Space Planes and Hypersonic Systems and Technologies, Orleans, 2002*; AIAA Pap. No. 2002-5183.
16. S. V. Bobashev, R. V. Vasil'eva, A. V. Erofeev, *et al.*, in *Proceedings of the 4th Workshop on Magnetoplasma Aerodynamics for Aerospace Applications, Moscow, 2002*, pp. 169–175.
17. Yu. P. Golovachev, Yu. A. Kurakin, A. A. Schmidt, *et al.*, AIAA Pap. No. 2001-2883.
18. S. V. Bobashev, Yu. P. Golovachov, and D. M. Van Wie, J. Propul. Power **19**, 4658 (2003).
19. L. A. Vulis, A. L. Genkin, and V. A. Fomenko, *The Theory and Analysis of Channel Magnetohydrodynamic Flows* (Atomizdat, Moscow, 1971) [in Russian].
20. S. V. Babashev, R. V. Vasil'eva, A. V. Erofeev, *et al.*, Zh. Tekh. Fiz. **73** (2), 43 (2003) [Tech. Phys. **48**, 177 (2003)].
21. S. V. Bobashev, A. V. Erofeev, T. A. Lapushkina, *et al.*, in *Proceedings of the 33rd AIAA Plasmadynamics and Lasers Conference & 14th International Conference on MHD Power Generation and High Temperature Technologies, Maui (Hawaii), 2002*; AIAA Pap. No. 2002-2164.
22. S. A. Poniaev, A. V. Erofeev, T. A. Lapushkina, *et al.*, in *Proceedings of the 5th International Workshop on Magnetoplasma Aerodynamics for Aerospace Applications, Moscow, 2003*, pp. 284–288.
23. Yu. P. Golovachev, Yu. A. Kurakin, A. A. Shmidt, *et al.*, in *Proceedings of the International Scientific and Technical Conference on Fundamental Problems of Fast Flows, Zhukovskii, 2004*, pp. 235–236.

Translated by N. Mende

Technical Physics, Vol. 50, No. 9, 2005, pp. 1139–1144. Translated from Zhurnal Tekhnicheskoĭ Fiziki, Vol. 75, No. 9, 2005, pp. 34–39.

GAS DISCHARGES, PLASMA

Vacuum Discharge Instability at Laser Initiation of a Cathode Spot

Yu. V. Korobkin, I. V. Romanov, A. A. Rupasov, and A. S. Shikanov

Lebedev Physics Institute, Russian Academy of Sciences, Leninskiĭ pr. 53, Moscow, 117924 Russia

e-mail: korobkin@sci.lebedev.ru

Received July 6, 2004

Abstract—The dynamics of fast (a current rise time of $\leq 10^{11}$ A/s) laser-induced vacuum discharges with moderate amplitudes of the current (≤10 kA) and voltage (≤20 kV), as well as medium storage energy (20 J), is studied. It is shown experimentally that the initial conditions specified by the energy and duration of laser radiation are a decisive factor governing the discharge dynamics. Two types of beam–plasma instabilities separated in space and time are discovered, and their occurrence conditions are analyzed. The first type of instability, observed early in the discharge, is associated with pinch structures at the front of the cathode jet expanding into a vacuum. The second type arises either at the peak or at the trailing edge of the current pulse and is accompanied by generation of hard (with an energy of ≥100 keV) bremsstrahlung from the anode region. The increase of the hard component energy over the current source potential is attributed to breaking due to plasma erosion.

INTRODUCTION

In [1], experimental studies concerning fabrication of small-size quasi-point high-contrast (in terms of the characteristic lines of the Ti anode) X-ray sources were reported. The sources of interest are based on a vacuum diode with a plasma cathode that is formed by nanosecond laser pulses and are intended for the microscopy of moving objects with high refractive-index and density gradients. A most important property of such a source is that its operation can be strictly synchronized with a process being studied in the object and related instrumentation. The feasibility of operation at any desired voltage and the virtual constancy of the anode potential at the initial stage of the discharge, which is due to a small total charge (in comparison with the charge of the capacitive storage) transferred by an electron beam emitted from the laser plasma make it possible to meet the condition of maximal contrast (an increase of the characteristic radiation intensity over the bremsstrahlung intensity) $U = (3–4)U_0$, where U_0 is the excitation threshold of characteristic radiation.

The need for cutting the duration of a pulse from the X-ray source by increasing the laser radiation power density at the cathode (according to [1]), as well as for decreasing the laser pulse energy in order to improve the cathode service time, implies a picosecond time of plasma formation. However, tentative analysis has shown that, if the electron emitter is formed by a 30-ns laser pulse of energy ≥100 mJ, the contrast of the Ti K lines ($\geq 10^2$) weakens substantially both when the cathode plasma is generated by a ≥5-mJ laser pulse and when a laser pulse shrinks to several picoseconds. It has been found that the spectral composition of the radiation (studied by the filtering method) under the above operating conditions of the source contains a hard component with an energy above the bremsstrahlung energy corresponding to the current source potential. At an accelerating potential difference of 20 kV, X-ray quanta emitted from the anode of the source had an energy of 25 keV. These effects suggest that additional accelerating mechanisms function in the discharge. Furthermore, recent experimental and theoretical investigations into low-inductive [2, 3], laser-induced [4, 5], and vacuum discharges have revealed a variety of physical phenomena (generation of multiply charged ion beams by cathode jet plasmas, occurrence of nonstationary emissive centers at the moving boundary of the cathode torch, current aperiodic focusing and defocusing, breaking due to plasma-induced erosion, etc.) that can be attributed to various types of plasma instability. In this work, we experimentally study the effect of initial conditions on instability development and attendant processes, including generation of hard X-ray radiation in fast laser-induced discharges. Also, we carry out comparative analysis of the X-ray source in which the plasma cathode is formed by picosecond and nanosecond laser pulses. Laser control of current passage in the discharge could allow parameter stabilization of this source, cut the pulse duration, and advance on the way to designing a small-size X-ray source with an X-ray quantum energy exceeding the current source potential.

1. EXPERIMENTAL

The laboratory setup used in the experiments consists of a mode-locked neodymium glass laser (wavelength $\lambda = 1.06$ μm, output $J \leq 1$ J, light pulse duration

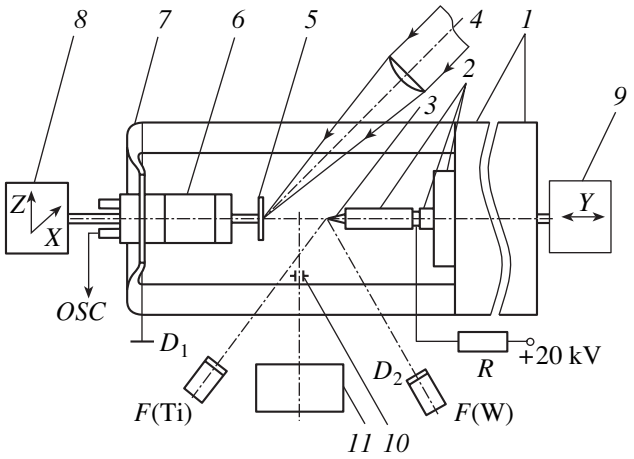

Fig. 1. Experimental scheme. (*1*) 0.1-μF capacitor, (*2*) insulating spacers, (*3*) conical titanium anode, (*4*) laser beam (λ = 1.06 μm), (*5*) massive titanium target (cathode), (*6*) coaxial current shunt (17 mΩ), (*7*) flexible conductor, (*8*, *9*) positioners, (*10*) aperture of camera-obscura, and (*11*) system visualizing spatial distribution of X rays from discharge gap. D_1, *p–i–n* diode with Ti filter; D_2, *p–i–n* diode with W filter; and *R*, 100-MΩ charging resistor.

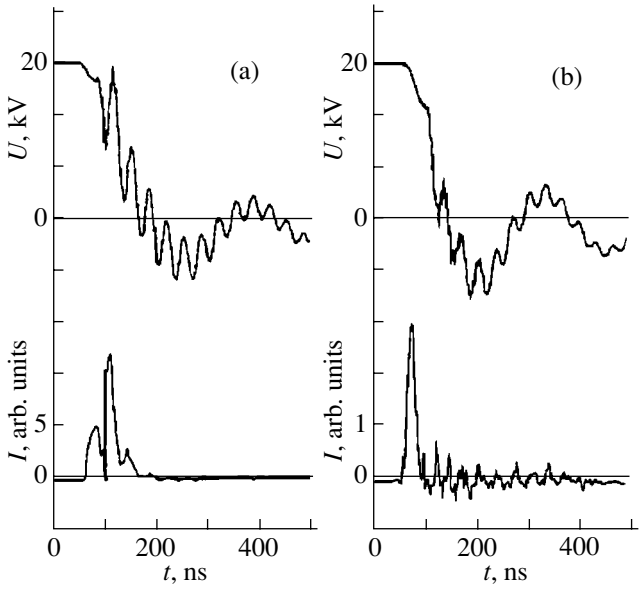

Fig. 2. Waveforms of voltage *U* across the 4.7-μF capacitor and intensity *I* of the X-ray radiation from the anode with quantum energies of ≥2 kV. The electrode spacing is 4 mm; the discharge current, 3 kA. The laser pulse duration is 27 ps; the laser pulse energy is (a) 2 and (b) 100 mJ. The first of three current pulses in panel (a) corresponds to the X-ray radiation arising when the electrons emitted by the laser plasma strike the anode. The subsequent pulses arise when the anode is subjected to the electron beams generated in discharge instabilities.

τ = 27 ps, and power density *P* on the target $P \le 10^{14}$ W/cm^2) and a *Q*-switched neodymium glass laser ($J \le 0.5$ J, τ = 30 ns, and $P \le 10^{11}$ W/cm^2), a vacuum diode, and a diagnostic station. The diode includes a dc voltage source ($U \le +20$ kV) and an interaction chamber (evacuated to a pressure of 5×10^{-3} Torr), in which a grounded plane-parallel titanium target (cathode), a titanium conical anode with a tip diameter of 250 μm, and a capacitive storage are placed. The electrode gap can be varied from 1 to 30 mm. A vacuum discharge is initiated by laser radiation focused into a spot of diameter 200 μm on the target. The inductance of the diode circuit, which is measured in the short-circuited mode, depends on the electrode geometry and design of the capacitor. With a K15-10a ceramic capacitor of capacitance 4.7 nF used in the circuit, the inductance equals 0.2 μH or more depending on the configuration of flexible electrode terminals. In the case of a K75-48M 0.1-μF-capacitor and the near-coaxial electrode geometry, the inductance equals 0.1 μH. The scheme of the experiment with the low-inductance discharge loop is presented in Fig. 1.

The current in the diode circuit was measured with a 17-mΩ coaxial shunt; the voltage across the storage capacitor, by a frequency-independent resistive voltage divider. The output X-ray radiation and its time characteristics in the energy range 0.4–50 keV were measured with Quantrad 100 PIN-250 silicon *p–i–n* diodes. The signals were recorded using a Lecroy 9350A oscilloscope with a passband of 500 MHz. The spatial distribution of the X-ray radiation from the discharge gap was visualized by means of a camera-obscura and a microchannel-plate recorder. Measurements of the anode current with a Faraday cup were not carried out because of the intricate geometry of the diode. However, we recorded the time waveform of the X-ray radiation from the anode, i.e., traced the beamlike current passage early in the discharge and at time instants instability arises.

2. RESULTS AND DISCUSSION

In the experiments, we analyzed the waveforms of the current, voltage, and X-ray radiation of the vacuum diode for different energies of discharge-initiating laser pulses. The geometry and electrical circuit of the diodes were similar to those described in [1], while the duration of a plasma-generating laser pulse was shorter, 27 ps.

Figure 2 shows typical waveforms of the voltage across the 4.7-nF capacitor and of the X-ray radiation from the diode's anode for accelerating voltage *U* = 20 kV, electrode spacing *d* = 4 mm, a circuit inductance of 0.2 μH, and a discharge current of no more than 3 kA. The *p–i–n* diode detected X-ray quanta of energy $E \ge 2$ keV. At the initial stage of the spark discharge, the voltage decays slowly and the current variation follows the Child's law. The increase in the current is associated with a shrinkage of the electrode gap and an increase in the emitting area of the laser plasma. At this stage of the discharge, the beamlike regime of current passage is observed, which is accompanied by X-ray emission from the anode. In our situation, with the electrode gap

and laser energy optimized, the maximal beam current did not exceed 100 A. The typical voltage drop is 15% of the applied value, which cannot noticeably affect the contrast of characteristic lines.

At the next stage of the discharge, the rate of voltage drop grows because of ion accumulation in the gap and the formation of the region (hump of potential [6, 7]) where U exceeds the cathode–anode voltage. This region serves as a potential well for electrons. In this region, effective ionization of the residual gas and electrode material vapor takes place, causing the plasma to expand rapidly and the current to grow.

When the plasma was generated by a laser pulse with $J < 100$ mJ (and, particularly, with J ranging from 1 to 10 mJ), the waveforms (Fig. 2a) showed X-ray bursts at the anode and voltage jumps across the capacitor at the second phase of the discharge, which are indicative of instabilities. The X-ray burst intensity at the second stage might considerably exceed the intensity of an X-ray pulse that is generated by the anode subjected to the electron beam emitted from the laser plasma. However, the current waveforms did not exhibit any irregularity (except for small-amplitude oscillations) at the time instants the instabilities were observed. The decrease in the contrast of the characteristic lines is explained, in this case, by a rapid fall of the anode potential and the formation of electron beams in a wide energy range at the second phase of the discharge. Current passage became stable when the laser energy was increased, and the anode did not emit X-rays at the second stage of the discharge at $J \geq 100$ mJ (Fig. 2b). It should be noted that each set of parameters U and d corresponds to a fixed laser energy above which current passage became stable.

When studying various operating conditions of the vacuum diode, we found that two time-separated types of instability are possible. The first arises at the spark stage of the discharge; the second, at the peak or trailing edge of the current pulse. At an accelerating voltage of 20 kV, type-II instability occurred randomly: their regular occurrence was observed at not too high voltages (about 7 kV), electrode gaps of 2–4 mm, and a laser pulse energy of 2 mJ. The increase in the inductance to 0.8 μH resulted in a decline of the current (by 30%) and a rise in the voltage across the capacitor above voltage U initially applied to the diode. This indicates that matching between the initial inductance of the discharge loop and plasma load influences current passage in the discharge even for gaps as short as those used in the experiments. At low accelerating voltages and currents, type-I instability was absent.

As was noted above, discharge instabilities also arise when the cathode plasma is generated by a nanosecond laser pulse. In connection with this, we studied current passage at different light beam power densities at the cathode. For fixed d (4 mm) and U (20 kV), the plasma emitter of electrons was created by a picosecond laser pulse with energy $J = 100$ mJ and power density at the focal spot $P = 10^{13}$ W/cm^2 and also by a pulse with the same energy and $P = 1.6 \times 10^{10}$ W/cm^2. Discharge instabilities were not observed in both cases and did not arise with increasing energy of the plasma-generating pulse. This indicates that it is the energy deposit from the laser radiation (the initial volume of the plasma in the gap) that specifies the stability of current passage. At the early stage of the discharge, the X-ray pulse duration depends on the laser radiation plasma density at the cathode. In the former case considered above, it equaled 18 ns; in the latter, 27 ns. Thus, an increase in the laser plasma expansion rate causes the X-ray pulse duration to decrease. At a nanosecond laser pulse energy of ≤50 mJ, type-I instabilities arose, while being not so pronounced as in the case of the picosecond pulse. In general, an increase in the duration of a laser pulse forming the plasma emitter has a stabilizing effect on current passage.

Thus, our results show that optimization of the initial conditions specified by the laser radiation parameters leads to stabilization of current passage in the discharge and makes it possible to cut the duration of a pulse from the X-ray source. At the same time, it is impossible to unambiguously answer the question as to which type of instability causes generation of a high-energy electron beam and the hard component of the X-ray radiation. A low sensitivity of photographic materials to X-ray radiation of energy ≥10 keV, along with a low spectral sensitivity of *p–i–n* diodes at energies of ≥20 keV, did not allow us to visualize the gap in hard X rays and, thereby, completely resolve the time waveform of the radiation. Therefore, we raised the energy and current of the discharge by increasing the capacitance of the storage capacitor (to 0.1 μF), modifying the electrode configuration, and decreasing the inductance of the discharge loop (to 0.1 μH). As a result, at $U = 20$ kV and $d = 4$ mm, the discharge current was raised to ~10 kA.

Under such conditions, the waveforms of the current, voltage, and X-ray radiation did not differ radically from those obtained under the conditions discussed previously. As in the former case, plasma instabilities (generation of a train of X-ray pulses at the anode) were observed when the discharge was initiated by a laser pulse with $\tau = 27$ ps and energies of 1–10 mJ. However, as the discharge current grew, the yield of X-ray radiation increased at least by one order of magnitude and, therefore, the radiation was easier to detect.

To determine the spectral range and the directivity diagram of the X-ray radiation from the anode, we used two *p–i–n* diodes arranged at different angles to the discharge axis. The diode with a 15-μm-thick Ti filter (transparent for X-ray quanta with energy $E \geq 2$ keV, i.e., for the bremsstrahlung and characteristic radiation of Ti) faced the anode, and the diode with a 50-μm-thick tungsten filter (transparent for quanta of energy $E \geq 30$ keV, i.e., for the bremsstrahlung of Ti) was placed at a right angle to the discharge axis or behind

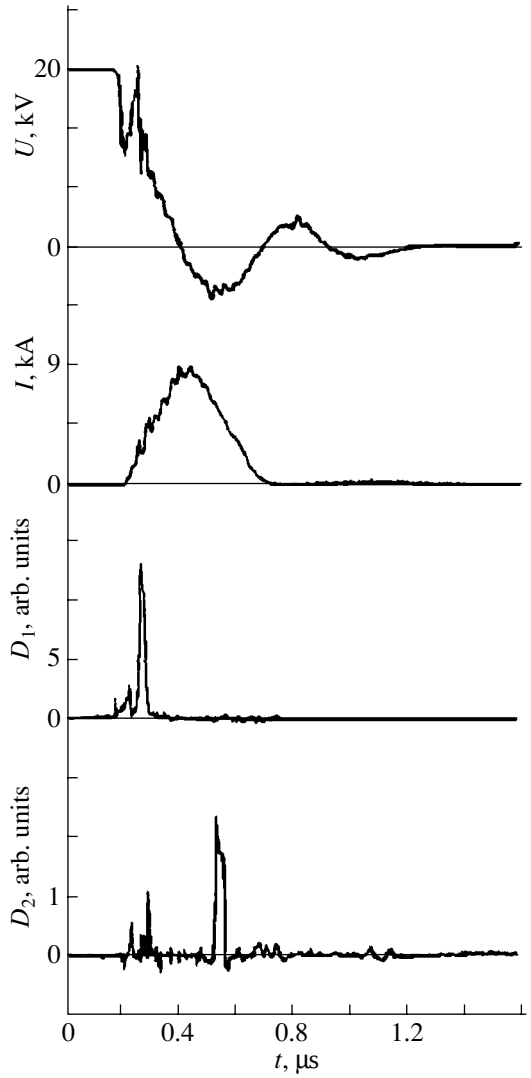

Fig. 3. Waveforms of voltage U across the 0.1-μF capacitor; discharge current I; and X-ray radiation intensity from the anode: D_1, the signal from the p–i–n diode with the Ti filter transmitting quanta with $E \geq 2$ keV; D_2, the signal from the p–i–n diode with the W filter transmitting quanta with $E \geq 30$ keV. The electrode spacing is 4 mm; the laser pulse duration and energy are, respectively, 27 ps and 2 mJ.

the anode. In the experiments, the tungsten-filter diode detected X-ray quanta of energy ≥30 keV. The intensity of hard X rays increased as the angle of this diode was varied from 90° to 130° and tended to zero in the direction to the diode that faced the anode. This suggests that the directivity diagrams of the bremsstrahlung and characteristic radiation differ. The time waveform of the X-ray radiation showed that the hard component is due to electron beams generated by instabilities of both types. However, major contributors are the beams associated with type-II instability, which arises either at the peak or at the trailing edge of current pulse. The beams associated with type-I instability are of a lower energy; therefore, generation of X-ray quanta with an energy

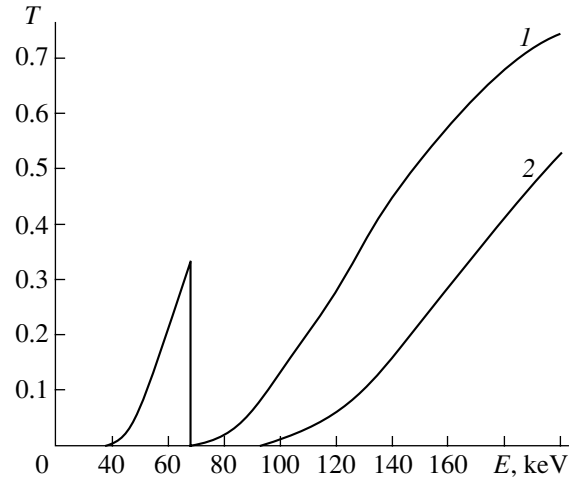

Fig. 4. Transmission T of (*1*) Ta(300 μm) and (*2*) Ta(300 μm) + Cu(11 mm) structure.

higher than the current source potential is of statistical character. As a whole, the time waveform of the anode radiation with energies above 2 keV represented two time-separated trains of X-ray pulses, of which the second one regularly had the hard component of energy $E \geq 30$ keV (Fig. 3).

Along with the time measurements, we visualized the integral spatial distribution of the X-ray radiation from the discharge gap with a camera obscura. Because of the presence of the hard component, the aperture of the camera obscura (100 μm in diameter) was made in a 300-μm-thick tantalum plate (transmission T of the tantalum plate is shown in Fig. 4). A 0.3-μm-thick Formvar (polyvinyl formal resin) film transmitting X-ray quanta of energy ≥50 eV served as a filter. Imaging was accomplished using a microchannel-plate system whose sensitivity at energies above 10 keV is much over the spectral sensitivity of X-ray photographic materials. The images were sensed from the screen (fiber-optic plate) with a CCD camera. Obscuragrams taken of the gap at $U \leq 10$ kV and $J = 2$ mJ showed the presence of an extra soft X ray source, which is on the discharge axis nearer to the cathode. As the voltage (and, hence, the current) rose from 1 to 10 kV, so did the X-ray intensity and new sources appeared (Fig. 5). In our experiments, their maximal number was four. As a rule, the number of the sources coincided with the number of X-ray pulses emitted from the anode of the p–i–n diode. These pulses are due to type-I instabilities. Based on the aforesaid, we may argue that there is a distinct correlation between the sources of soft X rays and type-I instabilities. Accordingly, instabilities of this type can be related to waveguide-type current passage because of pinch-induced waists at the front of a cathode jet expanding into a vacuum [3]. Replacing the Formvar filter by 4- and 6-μm-thick polyethylene films (transmitting the radiation of energies ≥110 and ≥140 eV, respectively), we managed to establish that

the maximal energy of X-ray quanta emitted from the waists of the cathode jet does not exceed 150 eV at U = 10 kV and J = 2 mJ. An increase in the laser pulse energy to 10 mJ lowers the plasma temperature in the waists, reduces the anode radiation intensity, and extends the delay time between current passage and emission of an X-ray pulse (pulses) from the anode. At J = 500 mJ, the additional source in the discharge gap disappear. This is another evidence that pinching is behind type-I instability. Discharge initiation by high-power laser radiation provides conditions when the dynamic pressure at the front of the cathode jet exceeds the magnetic field pressure. As the plasma expands into the electrode gap and the current grows, the situation reverses and the current channel contracts.

The images also show the presence of an X-ray source in the anode region of the gap that includes the hard component. The radiation came out from the plasma cloud around the conical anode (Fig. 5). Sometimes, the spatial distribution of this radiation was nonuniform, which indicates filamentation of the near-anode plasma. Hard radiation with $E \le 30$ keV arose at relatively low voltages, 1–5 kV. With an increase in the voltage, the energy of the radiation sharply grows, and, at $U > 10$ kV, the recording system was incapable of imaging the discharge gap, since X-ray quanta transmitted through the base of the camera-obscura. At U = 20 kV, quanta with $E \ge 100$ keV were separated out by sequentially attenuating the radiation using a set of copper plates with a total thickness of 11 mm and a 300-μm-thick tantalum plate (the transmission of the entire structure is shown in Fig. 4). In this case, it is not improbable that the microchannel plate detects secondary fluorescent X rays in the tantalum characteristic lines. However, secondary radiation detection in our geometry might take place only if the hard radiation transmitted through the entire set of attenuators.

Today, the commonly accepted concepts of anomalous acceleration of particles in a vacuum discharge are the formation of a deep nonstationary potential well at the front of a cathode torch (which is associated with the ecton mechanism of cathode spot functioning [8]) and breaking due to plasma-induced erosion in plasma-focus systems [9]. In our case, as follows from the experimental data, the most plausible process responsible for generation of hard X-ray quanta with an energy exceeding the current source potential by at least one order of magnitude is plasma erosion breaking near the anode. The electron beams generated at the first and second stages of the spark discharge cause intense plasma formation at the anode surface. Also, the heat flux, if any, from the heated pinch (filament), along with the Joule heat being released at the contact surface, results in explosive evaporation of the anode material. The evaporation breaks the discharge loop, inducing an additional emf that accelerates the electron flux. In the transition vapor layer near the metal, the electrons are decelerated, giving rise to hard X-ray radiation. Experimental studies on the yield of hard X rays

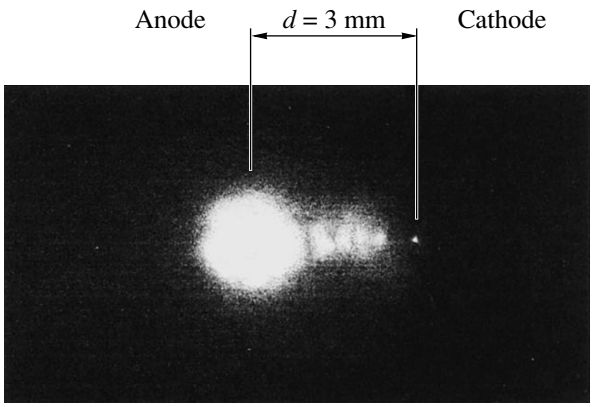

Fig. 5. Spatial distribution of the X-ray radiation from the discharge gap with quantum energies of ≥50 keV. The voltage across the capacitor is 10 kV; the laser pulse duration and energy are, respectively, 27 ps and 2 mJ.

depending on the anode geometry and material count in favor of such a model. The intensity and energy of the radiation increased when the titanium anode was replaced by the higher Z and higher vaporization temperature tungsten anode and decreased when the plane anode was substituted for the needle-like anode. In terms of this method, it is not surprising that the increase in the discharge current from 3 to 10 kA, which was accomplished by varying the discharge loop parameters, with the voltage across the storage capacitor remaining unchanged (20 kV), led to an increase in the X-ray radiation energy from 25 to 100 keV or higher. However, since the discharge gap was imaged in the integral regime, the model of breaking due to plasma erosion in plasma microfocus formation needs further verification.

CONCLUSIONS

Thus, we established that the initial conditions (the laser plasma volume in the discharge gap and the duration of a discharge-initiating pulse) are a crucial factor governing stable current passage in the gap. Under our conditions, a decrease in the laser pulse energy and duration causes instability, two types of which (beam–plasma instabilities) were regularly observed in the experiments. A minor increase in the discharge current under the stable current passage regime causes a significant rise in the energy of the hard X rays. We believe that this rise is the result of intense breaking due to plasma erosion. Results on studying the process dynamics (time- and space-resolved analysis of the anode plasma structure) and absolute measurements of the hard radiation yield will be reported in further publications.

In addition, we demonstrated that laser control of current passage in a vacuum discharge, specifically, in an X-ray radiation source, is feasible. Creation of a plasma emitter of electrons by a picosecond laser pulse

with a power density at the cathode of $\geq 10^{13}$ W/cm^2 and energy $J \geq 100$ mJ, combined with electrode gap optimization, allowed us to stabilize current passage and cut the X-ray pulse duration. At $J = 370$ mJ and $d = 10$ mm, the X-ray pulse was contracted to 10 ns, with the number of quanta in Ti K lines kept at a level of 10^{11} quanta/pulse [1] and the maximal contrast of the characteristic radiation relative to the bremsstrahlung retained.

ACKNOWLEDGMENTS

This work was supported by the Russian Foundation for Basic Research (grant nos. 01-02-17589, 02-02-16966, and 03-02-16366) and the All-Russia program "Integration" (grant no. I-0651).

REFERENCES

1. A. A. Erokhin, A. S. Kishinets, Yu. V. Korobkin, *et al.*, Zh. Éksp. Teor. Fiz. **119**, 1151 (2001) [JETP **92**, 998 (2001)].
2. M. F. Artamonov, V. I. Krasov, and V. L. Papernyĭ, Zh. Éksp. Teor. Fiz. **120**, 1404 (2001) [JETP **93**, 1216 (2001)].
3. I. A. Krinberg and V. L. Paperny, J. Phys. D **35**, 549 (2002).
4. N. Vogel and V. A. Skvortsov, IEEE Trans. Plasma Sci. **25**, 553 (1997).
5. N. Fogel', Pis'ma Zh. Éksp. Teor. Fiz. **61**, 622 (1998) [JETP Lett. **61**, 642 (1998)].
6. N. N. Koval', Yu. D. Korolev, V. B. Ponomarev, *et al.*, Fiz. Plazmy **15**, 747 (1989) [Sov. J. Plasma Phys. **15**, 432 (1989)].
7. A. V. Bolotov, A. V. Kozyrev, A. V. Kolesnikov, *et al.*, Zh. Tekh. Fiz. **61** (1), 40 (1991) [Sov. Phys. Tech. Phys. **36**, 23 (1991)].
8. S. A. Barengol'ts, G. A. Mesyats, and E. A. Perel'shteĭn, Zh. Éksp. Teor. Fiz. **118**, 1358 (2000) [JETP **91**, 1176 (2000)].
9. N. V. Filippov, Fiz. Plazmy **9**, 25 (1983) [Sov. J. Plasma Phys. **9**, 14 (1983)].

Translated by V. Isaakyan

Technical Physics, Vol. 50, No. 9, 2005, pp. 1145–1149. Translated from Zhurnal Tekhnicheskoĭ Fiziki, Vol. 75, No. 9, 2005, pp. 40–43.

GAS DISCHARGES, PLASMA

Influence of the Axial Magnetic Field on the Current Instability and on the Collective Acceleration of Ions in Plasma Diodes

A. A. Plyutto

Sukhumi Physicotechnical Institute, Sukhumi, 384914 Abkhazia, Georgia

e-mail: sfti@km.ru

Received October 26, 2004

Abstract—It is shown that, while suppressing transverse electron motion, the axial magnetic field with an induction of up to 6.8×10^{-2} T in the gap of a plasma diode has no significant effect on the current instability and on the acceleration of ions at electron beam currents of ≤40 A. The increase in both the critical current and the period of current oscillations is related to an increase in the plasma density after applying the magnetic field. The maximum energy of the accelerated magnesium ions decreases by ≈25% at an induction of 1.7×10^{-2} T and does not depend on the magnetic field in the range $(1.7–6.8) \times 10^{-2}$ T. © *2005 Pleiades Publishing, Inc.*

INTRODUCTION

To clarify the physical picture of ion acceleration in electron beams and to formulate a relevant theoretical model, as well as to understand mechanisms behind current instability, it is important to examine the role of transverse electron motion by applying an axial magnetic field. Previous studies of the influence of such a field on the acceleration of ions by a relativistic electron beam gave ambiguous results. When accelerating ions in a gas, a magnetic field of 2.5×10^{-2} T either suppressed acceleration at all [1] or decreased the ion energy by two to three times and the number of ions by two orders of magnitude [2]. In diode systems [3, 4], the magnetic field did not change the maximum ion energy, but at a magnetic field of 3×10^{-1} T, the number of the accelerated ions decreased substantially [4]. With a pulsed puffing of deuterium [5], the field with an induction of 4×10^{-1} and 8×10^{-1} T decreased the number of the accelerated ions by one order of magnitude but had no effect on the maximum ion energy within the experimental error. In this context, it is of interest to further investigate the influence of the axial magnetic field on the current instability and the acceleration of ions in a plasma diode under conditions such that the magnetic self-field of the electron beam is much less than the external axial magnetic field.

EXPERIMENTAL SETUP AND MEASUREMENT TECHNIQUE

A schematic of the experimental setup is shown in Fig. 1a. The plasma in chamber *1* was produced by cathode spots of an arc discharge with a current of 100–120 A. The discharge was ignited between magnesium cathode *2* and annular anode *3*. The plasma flowing with a velocity of 10^4 m/s through emission orifice *4* entered the acceleration gap of diode *l*, to which an accelerating voltage of 2–8 kV was applied after breakdown of discharger *K*. After this, an unstable mode of the current flow and electron-beam formation was established. The acceleration of ions began at the instant when the current of relaxation oscillations reached its critical (maximum) value. The pulsed current was maintained by capacitor $C = 0.5$ μF. The diode current was measured using resistor $R_3 = 4\ \Omega$, the signal from which was applied to an oscilloscope, and the

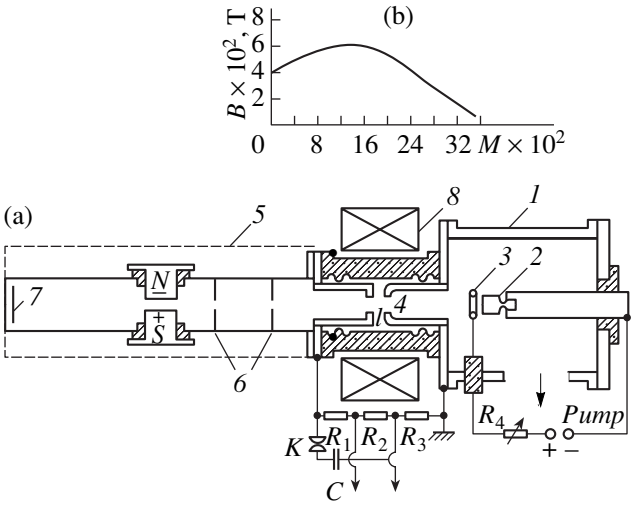

Fig. 1. Experimental setup and the electric circuit diagram.

1063-7842/05/5009-1145$26.00 © 2005 Pleiades Publishing, Inc.

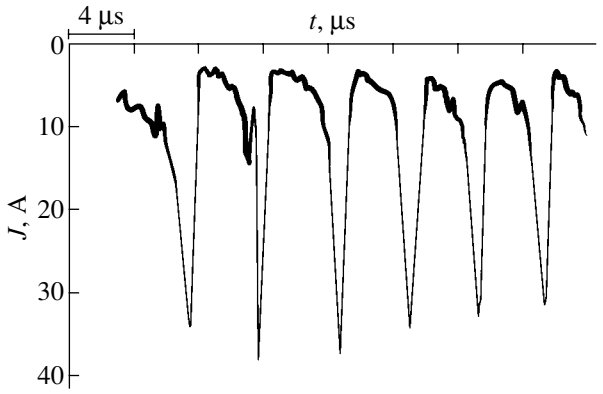

Fig. 2. Waveform of the electron current in the acceleration gap at $B = 7 \times 10^{-2}$ T.

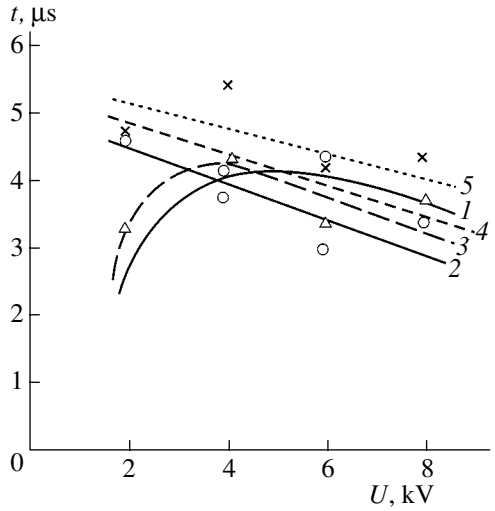

Fig. 3. Period of relaxation oscillations T_0 vs. initial acceleration voltage U for different values of the magnetic field in the acceleration gap: B = (*1*) 0, (*2*) 1.7×10^{-2}, (*3*) 3.4×10^{-2}, (*4*) 5.1×10^{-2}, and (*5*) 6.8×10^{-2} T.

diode voltage was measured using resistors $R_2 + R_3$, comprising one of the arms of the $R_1/(R_2 + R_3) = 1300\ \Omega/25\ \Omega$ voltage divider. The composition and energy distribution of the accelerated ions were analyzed by the parabola method using mass spectroscope *5* and by recording on photoplate *7*. The exposure was varied from 10^3 to 10^4 current pulses. A analysis was performed for a narrow axial ion beam cut by 1-mm-diameter diaphragms *6*.

Diode acceleration gap l was at the center of 830-turn solenoid *8* (0.2 m in diameter and 0.16 m in length), which produced the axial magnetic field. The profile of the magnetic field along the system axis for a solenoid current of 20 A is shown in Fig. 1b. An asymmetry of the field profile is caused by the influence of steel vacuum chamber *1*. Other elements of the setup that were placed in the magnetic field were made of nonmagnetic materials. The solenoid was aligned and fixed rigidly with respect to the system axis. A mutual displacement or misalignment of the axes of the solenoid and the analyzer led to a sharp decrease (up to complete suppression) in the current of the accelerated ions that entered the mass analyzer through diaphragms *6*.

EXPERIMENTAL RESULTS

In the unstable discharge mode, the applied axial magnetic field did not qualitatively change the character of the current. Both with and without a magnetic field, the current underwent relaxing oscillations (Fig. 2). At an initial acceleration voltage of $U \geq 4$ kV, the oscillation period somewhat increased with magnetic induction and decreased with U (Fig. 3). At U = 2 kV, the oscillation period increased nearly twofold for magnetic fields of 1.7×10^{-2}, 5.2×10^{-2}, and 6.8×10^{-2} T, whereas for 3.4×10^{-2} T, it increased insignificantly. This is related to the existence of two oscillation modes (with longer and shorter periods), which are seemingly determined by different arcing conditions.

An important characteristic of the unstable discharge mode and acceleration process is the ripple ratio $F = (J_c - J_m)/\bar{J}$ [6, 7], where J_m and $\bar{J}$ are the minimum and average values of the current, respectively, and J_c is the critical current. The magnetic field had no effect on F at magnetic fields of up to 5.2×10^{-2} T (Fig. 4), and a small increase in F was observed at 6.8×10^{-2} T.

The critical current increases with the magnetic field faster than linearly (Fig. 4, curves *1–3*). The reason for this is an increase in the plasma density. The plasma source is in a mirror magnetic field (Fig. 1b). As the plasma flows from the cathode, it is compressed by the magnetic field and the plasma density increases, reaching its maximum value in the acceleration gap. The plasma density in the gap increases with the magnetic field and solenoid current by the same law as the critical current does (Fig. 4, curve *4*). The density of the plasma ions (in m^{-3}) was determined from the relation $n = 1.5 \times 10^{18} J_i$, where J_i is the ion current (in A) extracted from plasma when the voltage polarity across the acceleration gap is reversed.

In some cases, applying a magnetic field resulted in a low-frequency (~10 kHz) modulation of the relaxation oscillations (200–300 kHz). Such a modulation is related to a regular motion of the cathode spots in a magnetic field from the front to the side surface of the cathode. As a result, the plasma density, the electron current in the acceleration gap, and the frequency of the relaxation oscillations change.

The axial magnetic field does not drastically affect the composition and energy of the ions accelerated axially in the electron beam [6]. Depending on the arcing conditions and the onset of instabilities, two types of mass spectrograms were observed: with nearly the

same number of Mg^{+1} and Mg^{+2} ions or with the prevalence of Mg^{+1} ions. In the first type of mass spectrograms, the composition of the accelerated ions was approximately the same as that in the plasma and the ion mass spectrum was insignificantly affected by the magnetic field. In the second type of mass spectrograms, applying a magnetic field led to an increase in the content of Mg^{+2} ions and a decrease in the number of low-energy ions (Fig. 5).

The maximum ion energy somewhat decreased as the magnetic field was increased to 1.7×10^{-2} T and then did not depend on the magnetic induction (Fig. 6). Since the critical current increased with induction (Fig. 4), the maximum ion energy did not depend on the electron beam current in the range from 6–8 to 30–35 A. The character of the dependence of the maximum ion energy on the initial acceleration voltage did not change when the magnetic field was applied (Fig. 7). In the presence of a magnetic field, the density of the axial ion flux decreased and the direction of ion motion was determined by the position of the solenoid axis.

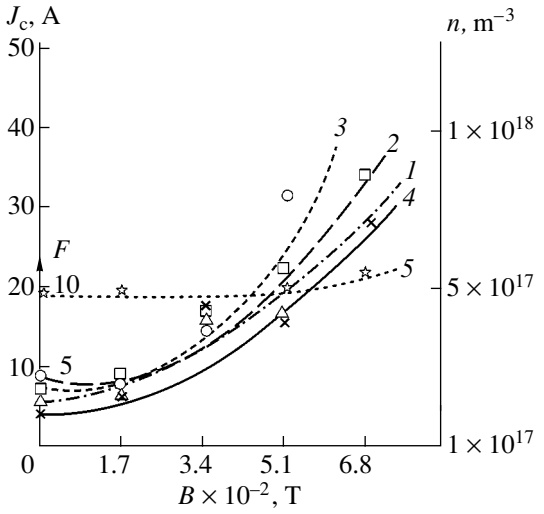

Fig. 4. Critical current J_c (at U = (*1*) 2, (*2*) 4, and (*3*) 6 kV), (*4*) plasma density n in the acceleration gap, and (*5*) ripple ratio F as functions of the magnetic induction B.

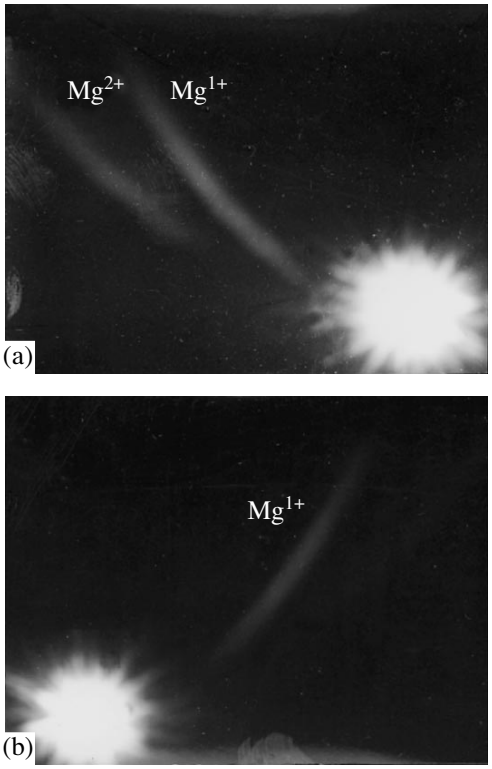

Fig. 5. Mass spectrograms of the accelerated ions at B = (a) 0 and (b) 6.8×10^{-2} T.

DISCUSSION

The axial magnetic field B performs several functions in the diode gap and in the region where the ions are accelerated: it magnetizes the plasma electrons, prevents the pinching of the diode current by the magnetic self-field $B_\perp$, and suppresses the transverse motion of the beam electrons. The electrons are magnetized when the condition $r_\lambda = 12/B \ll r$ (where r_λ is the Larmor radius and r is the radius of the emission orifice) is satisfied, which implies $B \geq 5 \times 10^{-3}$–10^{-2} T. Pinching is prevented when $B > 2 \times 10^{-1} J_m/r$; i.e., for $J_c = 35$ A and $r = 0.008$ m, we have $B > 9 \times 10^{-4}$ T. The transverse motion of the electron beam in the region where the ions are accelerated is suppressed at $B \geq 5 \times 10^{-3}$–2×10^{-2} T, and that in the drift space is suppressed at $B \geq (2–3) \times 10^{-2}$ T.

Our experiments demonstrate that the axial magnetic field insignificantly affects the current instability. Since the axial magnetic field suppresses transverse electron motion, we can suppose that this motion does not play a governing role under our experimental conditions and the current instability can thus be considered in a one-dimensional approximation. Therefore, the main results from one-dimensional computer simulations of unstable discharge modes in thermionic converters [8, 9] also apply to vacuum arc diodes.

When the current is minimum, the plasma boundary emitting electrons is in the middle of the diode and the external voltage is mainly applied between this boundary and the anode. The space charge sheath of the electron beam screens the plasma from the external field. As the boundary propagates toward the anode with the plasma ion velocity (~10^4 m/s), the sheath becomes thinner and the diode current increases. When the current density approaches its critical (maximum) value, the electron flow velocity becomes higher than the electron thermal velocity, the screening sheath breaks, and the external field penetrates into the plasma. This leads to the formation of a new emitting boundary in the emission orifice and a new space charge sheath, across

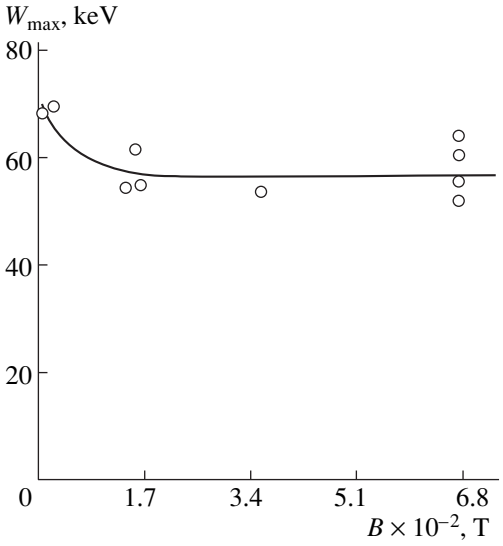

Fig. 6. Maximum energy of the accelerated ions W_{max} vs. magnetic induction B for U = 8 kV.

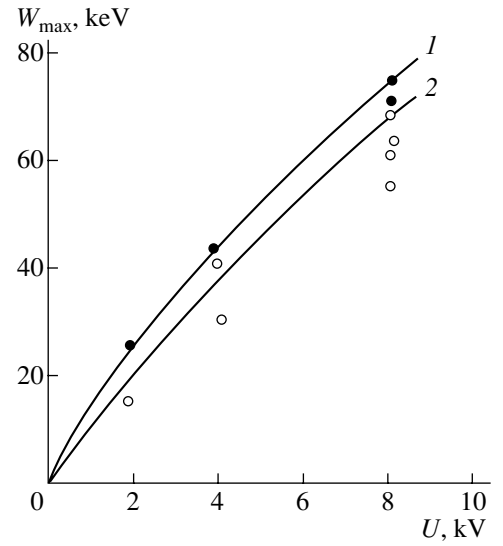

Fig. 7. Maximum energy of the accelerated ions W_{max} vs. initial acceleration voltage U for B = (*1*) 0 and (*2*) 6.8 × 10^{-2} T.

which a significant fraction of the external voltage falls. The plasma then breaks, and a positively charged transitional plasma is produced on the anode side. This is confirmed by probe measurements. The new plasma boundary propagates toward the anode with the plasma ion velocity. The electron beam formed in the break region passes through the transitional plasma and turbulizes it. As a result, the electron beam is spread over energy and the ions are accelerated to energies that are 20–40 times higher than the external potential. The transitional plasma is destroyed by both the external field and the electron beam, which transfers a fraction of its momentum and energy to the accelerated ions. The length of the voltage fall region (which includes the space charge sheath and the turbulized plasma) increases, whereas the electron current decreases. When the current is minimum, the transitional plasma almost disappears and a new cycle of relaxation oscillations begins. The period of relaxation oscillations T_0 is equal to the time during which the plasma flowing from the source fills the region occupied by the transitional plasma. The length of this region is the sum of diode gap length l, the length of the region lying beyond emission orifice *4* (Fig. 1) (it increases with orifice diameter d), and the length of the region inside the accelerating electrode (it extends with decreasing voltage U across the diode). This explains the observed dependence of T_0 on U and d [7]. The high-frequency oscillations predicted by computer simulations and observed experimentally are excited when the current reaches its maximum. These oscillations can change the plasma and diode potentials and can lead to the energy spread of the electron beam. Since the critical current is proportional to the plasma density in the source (Fig. 4), the thermal electron velocity does not change during a discharge. The critical current is two to three times higher than the saturation current of the plasma emitter.

The acceleration of heavy magnesium ions is not suppressed by the axial magnetic field; this, however, does not mean that the acceleration is one-dimensional in character. Strong turbulence can neutralize the action of the magnetic field. The acceleration region is highly inhomogeneous [10, 11]: there are current filaments [12], in which the ions are accelerated, and compression regions [10, 11, 13], from which the accelerated ions are emitted. The axial magnetic field probably prevents the plasma compression and the formation of numerous accelerating structures, thereby decreasing the number and energy of the accelerated ions.

REFERENCES

1. B. Ecker, S. Putnam, and D. Drickey, IEEE Trans. Nucl. Sci. **20**, 301 (1973).
2. D. O. Strow and R. B. Miller, IEEE Trans. Nucl. Sci. **24**, 645 (1977).
3. W. W. Destler, L. E. Floyd, J. T. Cremer, *et al.*, in *Proceedings of the 4th International Conference on High Power Electron and Ion Beam (Research and Technology), Palaiseau, 1981*, Vol. 2, pp. 659–666.
4. A. V. Burdakov, V. S. Koidan, A. I. Rogozin, *et al.*, Zh. Éksp. Teor. Fiz. **80**, 1391 (1981) [Sov. Phys. JETP **53**, 712 (1981)].
5. L. E. Floyd and W. W. Destler, J. Appl. Phys. **57**, 1592 (1985).

6. V. N. Ryzhkov, A. A. Plyutto, P. E. Belensov, *et al.*, Zh. Tekh. Fiz. **52**, 2074 (1972) [Sov. Phys. Tech. Phys. **27**, 1273 (1972)].
7. P. E. Belensov, A. T. Kapin, A. A. Plyutto, *et al.*, Zh. Tekh. Fiz. **34**, 2120 (1964) [Sov. Phys. Tech. Phys. **9**, 1633 (1964)].
8. P. Burger, J. Appl. Phys. **36**, 1938 (1965).
9. W. H. Gutler and P. Burger, J. Appl. Phys. **37**, 2867 (1966).
10. A. A. Plyutto and A. T. Kapin, Zh. Tekh. Fiz. **45**, 2533 (1975) [Sov. Phys. Tech. Phys. **20**, 1578 (1975)].
11. A. A. Plyutto, K. V. Suladze, S. M. Temchin, *et al.*, At. Energ. **27**, 418 (1969).
12. J. D. Luce, H. L. Sahlin, and T. R. Crites, IEEE Trans. Nucl. Sci. **20**, 336 (1973).
13. G. P. Mkheidze, A. A. Plyutto, and E. D. Korop, Zh. Tekh. Fiz. **41**, 952 (1971) [Sov. Phys. Tech. Phys. **16**, 749 (1971)].

Translated by V. Bugarya

Technical Physics, Vol. 50, No. 9, 2005, pp. 1150–1157. Translated from Zhurnal Tekhnicheskoĭ Fiziki, Vol. 75, No. 9, 2005, pp. 44–51.

GAS DISCHARGES, PLASMA

Statistical Model of the Lightning Leader Attraction to Ground Objects

M. M. Rezinkina, V. V. Knyazyev, and V. I. Kravchenko

Molniya Research and Engineering Institute, National Technical University, Kharkov Polytechnical Institute, Kharkov, 61013 Ukraine

Received January 12, 2005

Abstract—A statistical model of the lightning channel attraction to ground objects is proposed based on the analysis of the available experimental data on the breakdown of long air gaps and the propagation of the lightning leader channel. The model allows one to estimate the probability of lightning interception by a lightning rod and of lightning damage of the protected object. Examples of calculating the probabilities of lightning strike to the lightning rod and neighboring areas are presented. © *2005 Pleiades Publishing, Inc.*

INTRODUCTION

At present, lightning-rod protection zones around objects with a height of up to 150 m are specified by regulations [1]. However, the existing methods for determining these zones do not allow one to account for the entire complex of phenomena influencing the process of lightning protection. Lightning damage of such objects as missile launch complexes and oil storage tanks can lead to significant material losses and technogenic catastrophes. This necessitates the development of models allowing one to more exactly estimate the probability of lightning damage. Such models are also necessary for estimating the efficiency of new methods of lightning protection.

Because of the difficulties encountered in investigating natural lightning, much effort has been devoted to mathematical and physical modeling of the processes accompanying the development of lightning. In some studies (see, e.g., [2–4]), the distribution of the electrostatic field near a lightning rod and other objects under thunderstorm conditions were calculated. Such calculations are usually performed under the following assumptions: the critical corona field is E_c = 30 kV/cm and the critical fields that are necessary for the development of the positive and negative leaders are E_{cr}^{+} = 5 kV/cm and E_{cr}^{-} = 10 kV/cm, respectively. In [5], a 3D stochastic fractal model of lightning propagation was proposed. However, this model did not take into account fluctuations of such important parameters as the leader propagation velocity, the leader head potential, the external electric field strength, etc. The authors also did not consider the process of lightning strike to a ground object. In [6], the so-called electrogeometric lightning model was used. This model assumes the existence of a functional dependence between the maximum lightning current and the length r to which the lightning channel stretches during each next stage of its propagation. The spatial orientation of the lightning stages is assumed to be determined by a statistical distribution, the parameters of which depend on the distance to the ground. It is also assumed that the entire discharge channel is formed when some object or the ground is located at a distance less than r from the already formed incomplete discharge channel. A disadvantage of such an approach is that the influence of the electric field distribution on the propagation velocity and direction of the lightning leader is ignored. In [7], a 2D fractal model was developed that described the propagation of a stepped leader stroke toward the ground and the development of an upward leader from the ground. The practical application of this model is, however, limited by its qualitative character. In [8], a fractal theory was used to describe the development of a high-voltage discharge directed toward the ionosphere. In [9], results were presented from the fractal modeling of lightning strikes to ground objects, lightning rods, and the ground for different lightning polarities, different angles at which lightning approaches the ground, different ground topologies, and different ratios between the height and width of a building. The existence of local regions with an increased electric field (e.g., building's frontons) was also taken into account. The probability of breakdown was assumed to depend on the electric field strength as $p \sim E^{\eta}$. However, the method for choosing the η value, which significantly affects the development of the lightning channel, was not described.

Another stochastic fractal model of streamer and leader propagation in long discharge gaps was proposed in [10]. The model assumes that the streamers emerge stochastically and their propagation velocity depends on the electric field strength. The average propagation time of the streamers was calculated, and only those streamers whose propagation time was no less than this average time were assumed to continue

1063-7842/05/5009-1150$26.00 © 2005 Pleiades Publishing, Inc.

growing. The leader was assumed to propagate in the most probable propagation direction, with the propagation probability depending on the electric field strength. Disadvantages of this model are that it is two-dimensional and that the boundary conditions were formulated quite unclear (the dimensions of the computation region also were not indicated). According to the data of É.M. Bazelyan and Yu.P. Raizer, whose works are cited by the authors of this model, the streamer (leader) velocity depends on the potential difference between the head of the streamer (leader) and the point toward which it propagates (see, e.g., [11]). Meanwhile, in the model, the leader velocity was assumed to be constant and equal to 10^4 m/s, while the applied voltage, which was assumed to be equal to the leader channel voltage, was varied from 480 to 790 kV. There was also no clear reasoning behind the method for choosing the time step in modeling streamer development and for calculating the probability of leader propagation. Thus, the exponent in the dependence of the breakdown probability on the electric field strength was not indicated. It is also unclear how the leader propagation time (which is significantly longer than the streamer propagation time) is accounted for. The physical processes discussed in [10], as well as the experimental data provided by the authors, bear only an indirect relation to the development of the lightning leader channel because they operate with gap lengths that are three orders of magnitude shorter and with voltages that two to three orders of magnitude lower than those associated with lightning.

Therefore, in order to solve the problem of lightning protection, it seems expedient to elaborate a stochastic mathematical model describing the development of the lightning leader channel in the final stage of its propagation to the ground. The model should also take into account the dependence of the leader propagation velocity on the electric field strength, the 3D distribution of the electric field around the lightning rod and protected objects, a reduction in the streamer resistance in the final-jump phase, and the grounding resistance of the protected objects.

At present, a large amount of experimental data has been accumulated on the electrophysical characteristics of long sparks and lightnings, as well as on the protected zones of singe lightning rods. This data were used as a basis for the development of our model.

1. EXPERIMENTAL DATA USED IN DEVELOPING THE MODEL

According to [11], the attraction of lightning to a ground object is caused by the influence of the latter on the distribution of the cloud electric field, which directs the leader, on average, downward, toward the ground. The mechanism behind the action of such weak external fields ($E_0 \sim 100$ V/cm) on the propagation of the lightning leader, whose field strength is no less than E_{cr}^{+} = 5 kV/cm for positive and E_{cr}^{-} = 10 kV/cm for negative leaders, is explained in [11] as follows: the leader velocity is determined by the difference between the leader head potential U_h and the external field potential U_0 in the head location. The high potential drop

$$\Delta U = |U_h - U_0| \sim 10\text{–}100 \text{ MV}$$

over a relatively short streamer zone creates the field $E_L \approx$ 5–10 kV/cm $\gg E_0$, which is sufficient for the development of a streamer and then a leader. The authors of [11] believe that the external field either accelerates or decelerates the leader. The leader velocity is a certain function of the absolute value of the voltage difference at the leader head, $v_L = f(\Delta U)$, where U_0 in the expression for ΔU is a function of the radius vector $\mathbf{r}$ of the head. In [11], the following empirical relation between the leader velocity v_L and the voltage at the leader head was presented:

$$v_L \approx a U_h^{1/2}. \quad (1)$$

Since $U_0 \ll U_h$, it can be assumed that $\Delta U \approx U_h$ and, therefore, $v_L \sim |\Delta U|^{\gamma}$, where $\gamma = 1/2$. As a result, in [11], the following equation for leader acceleration was obtained:

$$\begin{aligned} \frac{dv_L}{dt} &= \pm\frac{dv_L}{d\Delta U}\left(-\frac{dU_h}{dt} + \frac{dU_0}{d\mathbf{r}}\cdot\frac{d\mathbf{r}}{dt}\right) \\ &= \pm\gamma\frac{v_L}{\Delta U}\left(-\frac{dU_h}{dt} - \mathbf{E}_0\cdot\mathbf{v}_L\right), \end{aligned} \quad (2)$$

where the positive and negative signs refer to a negative and a positive leader, respectively.

The second term in Eq. (2) leads to the acceleration of a negative leader if it propagates in the direction opposite to the field vector. The higher the external field strength and the smaller the angle between the field vector and the leader propagation velocity, the higher the acceleration.

When the charged channel of a downward leader is shorted instantaneously to the ground, the discharge current through the grounded end of the channel should also reach its peak value instantaneously. In this case, the peak current depends only on the wave impedance of the channel and is independent of its active resistance. In reality, the current in the main stoke increases over a few microseconds and, sometimes, over a few tens of microseconds. In [11], such a relatively slow growth of the lightning current was attributed to the properties of the commutator, whose role in this case is played by the streamer zone of the downward leader. According to this approach, the current growth rate and the current rise time near the ground are determined by the processes in the vanishing streamer zone of the former leader, rather than in its channel. The authors of [11] believe that indirect evidence for this is that, for a positive lightning, whose streamer zone is longer than that of a negative lightning at the same voltage, the cur-

rent rise time is several times longer. This opinion is maintained by V.A. Rakov, who pointed out that the processes in the final-jump phase, during which the lightning current front is formed, are determined by the impedance of the plasma switch at the point of lightning strike [12]. Therefore, the leader's streamer zone, which serves as a commutator, has a finite resistance and contracts over a finite time. The slope of the current front is determined by the decay rate of the resistance of this intermediate element between the leader channel and the ground. The duration of the pulse itself is determined by the length of the channel through which the wave of the main stroke propagates.

According to [11], in the final-jump phase, which begins when the streamer zone reaches the electrode of opposite polarity (the ground or a grounded object in the case of lightning), the streamer discharges through the electrode surface. The streamer velocity increases rapidly as the streamer zone contracts. This sharp increase in the current, which lasts over a few microseconds, precedes the current pulse of the main stoke. The latter begins when the leader channel reaches the electrode.

The development of breakdown of a long (up to 29 m) rod–plane gap to which a positive voltage was applied was studied in [13]. It was pointed out that the leader consists of a narrow plasma channel and a fan-shaped streamer zone (ionization zone), which occupies a certain volume ahead of the channel and feeds it. The channel transports the electrode potential and, accordingly, the region of the strong electric field into the gap, thus ensuring the leader development. The propagation velocity of the streamer head is higher than that of the leader head by one order of magnitude. The authors of [13] distinguished two main stages of a long-gap breakdown. The first stage lasts from the formation of a corona to the instant a which the outer boundary of the leader's streamer zone contacts the opposite electrode. In the second (final-jump) stage, the streamer zone reaches the opposite electrode and its length decreases, while the length of the leader channel grows. The number density of the streamers in the streamer zone, the velocities of the streamers and leaders (v_{st} and v_L), and the discharge current i_p grow as the streamer zone contracts (by approximately one order of magnitude as compared to its initial length), while the streamer resistance decreases.

The streamer resistance per unit length is on the order of 10^{12} Ω/m [14]. This means that, as the streamer crosses the gap (this stage lasts over 10–20 μs), the head of the streamer looses a galvanic contact with the point of its origin. The leader resistance per unit length RP_L is about 10 Ω/m [11]. Presumably, the discharge channel resistance per unit length in the final-jump phase, RP_F, is equal to a certain intermediate value between the streamer and leader resistances per unit length. The value of RP_F can be estimated from the following considerations: According to the experimental results of [13], the development of a discharge in the final-jump phase depends significantly on the external resistance R_0, which is included in the discharge circuit between the high-voltage source and the discharge gap. Thus, under the experimental conditions of [13], the external resistance R_0 was relatively low ($R_0 < 10^3$ Ω), while the streamer and leader velocities and the current were $v_{st} = 5 \times 10^7$ m/s, $v_L = 10^6$ m/s, and $i_p = 10^3$ A, respectively, and the duration of the final-jump phase was shorter than 10 μs. At a sufficiently high external resistance ($R_0 > 10^5$ Ω), the final-jump phase can be prolonged to a few thousand microseconds, while the streamer and leader velocities and the discharge current can be reduced to $v_{st} = 10^5$ m/s, $v_L = 10^3$ m/s, and $i_p =$ 1 A, respectively. Therefore, when the discharge circuit in the final-jump phase becomes disconnected, the resistance of the streamer zone and the external resistance, which are connected in series, play the role of a voltage divider. Apparently, at $R_0 < 10^3$ Ω, the voltage is mainly applied to the discharge gap, while at $R_0 > 10^5$ Ω, most of the voltage is applied to R_0, which leads to the slowing down of the discharge processes in the final-jump phase. Taking into account that the length of the discharge gap in [13] was a few meters, we can use the following estimate for the average streamer resistance per unit length in the final-jump phase: $RP_F^{av} \sim 10^4$ Ω/m.

2. MAIN IDEAS AND ASSUMPTIONS USED IN DEVELOPING A MATHEMATICAL MODEL FOR DESCRIBING THE ATTRACTION OF THE LIGHTNING LEADER TO A GROUND OBJECT

Since the majority of lightning leaders transport a negative charge toward the ground (see, e.g., [15, 16]), we will further concentrate on negative lightning, although the model described below can be applied to positive lightnings as well. According to [17], the length of the streamer zone during breakdown of a long air gap is approximately equal to the height from which the leader begins to be attracted to the ground electrode. This equally applies to both positive and negative leaders. The same principle can also be applied to ultra-long sparks—lightning. According to the available experimental data, the streamer head looses a galvanic contact with the leader due to the high resistance of the relatively cold plasma in the streamer channels, and the ensemble of streamers produces a streamer zone in which the electric field distribution is nearly uniform because the field is equalized by the excessive charge of the numerous streamer heads [13]. We will assume that the so-called last stroke, i.e., the last stage of the lightning leader propagation toward the ground and to the objects located on it, begins when the streamer zone reaches them. In essence, the last stroke is the propagation of the leader channel through the streamer zone in

the final-jump phase. We will also assume that it is from this instant that the lightning leader begins to be attracted to a ground object that will subsequently be struck by lightning. By the length of the streamer zone, we mean the distance from the leader head at which the streamers stop propagating [11, 18]. During the development of a negative leader, the lowest electric field strength in the streamer zone is approximately equal to $E_L^- = 10$ kV/cm; hence, the height of the attraction zone, which is equal to the initial length of the streamer zone in the final-jump phase, is

$$L_{st0} \sim U_m/E_L^-. \quad (3)$$

For a lightning voltage of $U_m = 10$–100 MV, the height of the attraction zone is 10–100 m, which agrees with the commonly accepted values of this height (see, e.g., [19]).

Through the ground areas and grounded objects to which the streamer zone is connected after the beginning of the final-jump phase, the current

$$i_F = U_m/(RP_F L_{st} + R_R + R_G) \quad (4)$$

begins to flow. Here, i_F is the discharge current in the final-jump phase, RP_F is the streamer channels' resistance per unit length in the final-jump phase, R_R is the resistance of the ground part of the lightning rod, R_G is the resistance of the ground area over which the current spreads, and L_{st} is the length of the streamer zone.

It was pointed out in [13] that, in the final-jump phase of the leader development in long air gaps, the leader channels are highly branched. Moreover, several parallel branches with their own heads can develop simultaneously. We will assume that, in the final stage of the lightning propagation toward the ground, several leader channels develop concurrently and the return stroke occurs through the channel that first reaches a zero-potential node. Taking into account that the diameters of the leader channels are many orders of magnitude smaller than their length and the distance between them, we will ignore the mutual influence of the leaders through their electric fields.

Since the process of the leader propagation through the ionized streamer zone is stochastic in character, we will consider all the possible directions of the leader propagation. To determine the probability of lightning strike to a given object, we will consider how a leader approaches it from different distances in the axial and azimuthal directions and at different angles with respect to the vertical axis. The leader can have different initial velocities in the range $v_{L0} = 10^5$–10^6 m/s (see, e.g., [11]). Since the values of L_{st} and v_L are determined by the electric potential of the leader head U_m (see Eqs. (1), (3)), they are mutually dependent. Therefore, specifying the potential U_m, we thereby define the values of L_{st} and v_{L0}. Let us divide the problem into two parts—the field and the chain ones—and solve them at each time step. The initial time in our simulations is the beginning of the final-jump phase, i.e. the instant at which the streamer zone comes into contact with a grounded node.

Let us consider a scenario of the leader development in one of the possible directions, e.g., along a straight line directed toward the lightning rod or a protected object with the spatial coordinates (x_P, y_P, z_P). We denote the initial coordinates of the leader head by (x_L, y_L, z_L). The initial distance between the leader and the given object is

$$R_{PL0} = \sqrt{(x_P - x_L)^2 + (y_P - y_L)^2 + (z_P - z_L)^2}.$$

Dividing R_{PL0} into N_L parts, we obtain the spatial step by which the lightning channel propagates in numerical simulations: $\Delta d_L = R_{PL0}/N_L$. If the leader velocity remains constant, then the time step is also constant,

$$\Delta t_i = \text{const} = R_{PL0}/v_L.$$

Assuming that the leader propagation is described by Eq. (2) (i.e., considering accelerated propagation), we find that the ith time step is equal to

$$\Delta t_i = [\sqrt{(4v_L^2(i-1) + 8a_i R_{PL0})} - 2v_L(i-1)]/2a_i,$$

where $v_L(i-1)$ is the leader velocity at the $(i-1)$th and a_i is the leader acceleration at the ith step.

We can then calculate the distribution of the electric field at the nth time step $t_n = \sum_{i=1}^{n} \Delta t_i$, taking into account a specific configuration of the leader channel at this time step. After this, using Eq. (2) and the newly found potentials and electric field strengths around the leader head, we can calculate the leader acceleration $a(n)$ at the nth time step. From this acceleration, we find the new propagation velocity of the leader $v(n)$ and the new length of the contracted streamer zone $L_{st}(n) = L_{st0} - n\Delta d_L$, because the leader had propagated toward the object by Δd_L.

Then, we calculate the circuit. We assume that, in the final-jump phase, the leader head is connected galvanically to the grounded node through the resistance $R_F = RP_F L_{st}$ of the corresponding streamer from the streamer zone. In determining the discharge current, it is necessary to take into account a decrease in R_F, because the streamer resistance RP_F per unit length is inversely proportional to the current flowing through it and L_{st} decreases as the leader propagates.

According to [20], the dependence of the spark resistance on the current and time that was proposed by Rompe and Weitzel was obtained under the assumption that the internal energy of the discharge is completely spent on ionization, molecular excitation, and electron gas heating and that there are no losses for heat conduc-

tion, radiation, and channel expansion:

$$RP(i, t) = 1/\sqrt{2a_{RV}/p\int_0^t i^2 dt}, \quad (5)$$

where a_{RV} is a coefficient, equal to 0.8–1.0 atm cm^2/sV for oxygen and nitrogen [20], and p is the pressure.

For a spark current on the order of a few kiloamperes or more [20], the expansion of the discharge channel starts to influence the channel conductivity. In this case, the dependence $RP(i, t)$ can be described analytically according to the Braginskiĭ model [21], further developed in [22],

$$RP(i, t) = 1/\left[k_b\int_0^t i^{2/3} dt\right], \quad (6)$$

where $k_b = (4\pi\sigma^2/\rho_0\xi)^{1/3}$, ρ_0 is the density of the gas in which the discharge occurs, σ is the specific conductivity of the discharge channel (equal to 3×10^2 S/cm for air), and ξ is a coefficient ($\xi = 4.5$) [20].

In deriving Eq. (6), it was assumed that the channel conductivity reaches a certain value and then remains constant, whereas the channel resistance is determined solely by its expansion. In [23], the following formula, which generalizes Eqs. (5) and (6) for the spark resistance per unit length, was derived:

$$RP(i, t) = 1/\left\{k_n\left[\int_0^t i^\gamma dt\right]^\delta\right\}, \quad (7)$$

where k_n, γ, δ, and C_1 are parameters, equal to

$$k_n = \sqrt{2a/p}, \quad \gamma = 2, \quad \delta = 0.5, \quad (8)$$

for the Rompe–Weitzel model and

$$k_n = k_b, \quad \gamma = 2/3, \quad \delta = 1 \quad (9)$$

for the Braginskiĭ model.

Therefore, in calculating the streamer resistance in the final-jump phase by formula (7), we used coefficients (8) for currents of $i_F < 10^3$ A and coefficients (9) for $i_F > 10^3$ A.

It was assumed that the lightning leader channel came into contact with the node if the latter was touched by the leader channel or if the resistance of the attached streamer per unit length decreased to

$$RP_F = k_F RP_L, \quad (10)$$

where $RP_L = 10$ Ω/m is the leader channel resistance per unit length and k_F is a coefficient varying in the range 1–10. It was assumed in our simulations that $k_F = 10$.

Condition (10) can be regarded as a criterion for the transformation of a streamer channel into a leader one, because it is the low conductivity of the streamer channel that ensures the absence of galvanic coupling between the streamer and the leader.

In order to describe the lightning attraction to a grounded object, we will use the minimum time–maximum probability principle. This principle and its application to the problem of lightning protection are well known (see, e.g., [24]). According to this principle, the probability of lightning strike to a certain node is inversely proportional to the time during which the leader propagates to this node.

The above algorithm was used to calculate the time t_{ik} that was necessary for a leader channel to reach the ith node in the kth version of the leader propagation scenario, which was determined by the value of the initial radial distance L_R from the lightning rod (or a ground object) to the leader channel, by the deviation angle α of the leader from the vertical axis, and by the leader channel voltage U_m, which defined the values of L_{st} and v_{L0}. The area S into which lightning was expected to strike was divided into N regions, each with an area of S/N. It was assumed that the probability density of lightning strike within the S/N area was uniform and was determined by the probability of lightning strike to its central node. The values of t_{ik} were calculated for all N ground nodes to which lightning could strike, and the minimum time $t_k = \{t_{ik}\}_{\min}$ was determined. It was also assumed that lightning could strike only those M nodes for which the ratio of the leader propagation time to t_k exceeded unity by no more than $\delta = 0.1$. The δ value was determined by the scatter in the average values of breakdown voltages of a few-meter-long air gaps with a strongly nonuniform field (see, e.g., [11]). For the rest $N - M$ nodes, the strike probability was assumed to be negligibly small. Hence, it was assumed that

$$p_{ik} > 0, \quad \text{if} \quad 1/t_{ik} \geq (1 - k_p)1/t_k, \quad (11)$$

$$p_{ik} = 0, \quad \text{if} \quad 1/t_{ik} < (1 - k_p)1/t_k, \quad (12)$$

where $k_p = \delta = 0.1$ is a coefficient.

The probability of lightning strike to the ith region with an area of S/N was then determined as

$$p_{ik} = (1/t_{ik})/\sum_{j=1}^{M}(1/t_{jk}). \quad (13)$$

We performed detailed calculations for K different initial positions of the leader channel relative to a given object. The probability of lightning strike to the ith node was defined using Eq. (13) as

$$p_i = \sum_{k=1}^{K} p_{ik}/K. \quad (14)$$

Therefore, performing calculations by the above algorithm and using Eq. (14), we could find the probability of lightning strike to the object under consideration.

3. EXAMPLES OF NUMERICAL SIMULATIONS OF THE LIGHTNING LEADER ATTRACTION

An important parameter of lightning protection is the potential U_m that the lightning leader carries to the ground. The current of the main stroke I_m, which causes the strongest damages, is proportional to U_m. According to [11], U_m depends on I_m as

$$U_m \approx Z_m I_m.$$

Based on the data from [11], we find that the Z_m value lies within the range $Z_m \approx 800$–$1200\ \Omega$.

Measurements of the lightning current provide experimental data on the probability distribution of lightning strikes for a given discharge current. According to [25], the current of negative lightning exceeds 7 kA with a probability of 0.95 and 2 kA with a probability of 0.995 (this value was obtained using an approximation). We will use these values when verifying the results of calculations of the radii of the zones protected by single lightning rods with different interception probabilities. According to [1], the radius of the zone protected by a lightning rod of height h is $R_M \approx 1.1h$ for an intercept probability of $p = 0.995$ and $R_M = 1.5h$ for $p = 0.95$. Let us use the above algorithm of calculating the probability of lightning strike to different ground areas around a lightning rod to determine R_M for $p = 0.995$ and 0.95. We consider the most unfavorable situation, in which the downward leader does not deviates from the vertical axis ($\alpha = 0°$) at the maximum distance from the lightning rod, $L_R = R_M$ (where L_R is the initial radial distance between the lightning rod and the leader channel). A square grid with a mesh size of $\Delta = 5$ cm, which was chosen to be equal to the average cross section of the lightning rod, was overlaid on the ground around the lightning rod. The calculations of the times during which the leader propagates to all the nodes of this grid at $R_M = 1.5h$ showed that, at $U_m \geq 8$ MV (which corresponded to $I_m \geq 6$–10 kA), the probability of lightning strike to the lightning rod was equal to unity, because the time required for the leader to reach any other node exceeded t_k by a factor of more than 1.1. For $R_M = 1.6h$ and $U_m \geq 8$ MV, the probability of lightning strike to the rod was less than unity. Similar calculations performed for $R_M = 1.1h$ and $U_m \geq 2.5$ MV ($I_m \geq 2$–3 kA) gave $p_M = 1$, while for $R_M = 1.2h$, we obtained $p_M < 1$. Therefore, we can conclude that our model allows one to correctly calculate the radii of the zones protected by a single lightning rod as functions of the lightning interception probability.

Figure 1 illustrates the results of numerical calculations performed using a computer code based on the above model. In calculations, the height of the lightning rod was assumed to be $h = 10$ m and the initial radial distance from the lightning rod to the lightning leader was $L_R = 15$ m. The figure shows the distributions of the

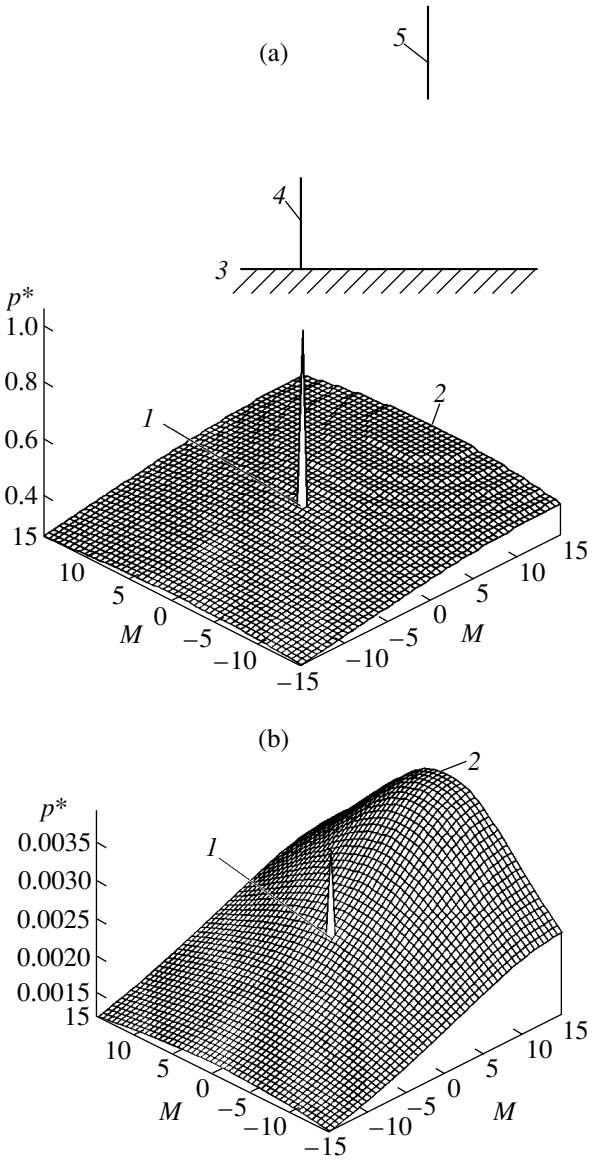

Fig. 1. Probability distribution of lightning strikes to a rod and the surrounding ground area for lightning potentials of U_m = (a) 50 and (b) 3 MV: (*1*) location of the lightning rod on the ground, (*2*) point above which the process of lightning leader attraction begins, (*3*) ground, (*4*) lightning rod, and (*5*) lightning leader.

lightning strike probability around a lightning rod,

$$p_i^* = (1/t_i)/\sum_{j=1}^{M}(1/t_j), \qquad (15)$$

where t_i is the time during which the leader propagates to the ith node and M is the number of nodes for which $1/t_i \geq (1 - k_p)1/\{t_i\}_{\min}$.

These probabilities were calculated for all the possible nodes to which lightning could be attached, including those for which the condition $1/t_i \geq (1 - k_p)1/\{t_i\}_{\min}$ was not satisfied. The sum of the reciprocals of the

leader propagation times for those M nodes for which $1/t_i \geq (1 - k_p)1/\{t_i\}_{\min}$ was chosen as a basic value in the denominator of formula (14). Therefore, relative probability (15) differs from absolute probabilities (11) and (12) in that no probabilities in it are zeroed out. This is done in order to visualize the results obtained and to simplify their comparison and interpretation.

Figure 1a corresponds to the case where the potential of the lightning leader is $U_m = 50$ MV, while Fig. 1b corresponds to the case with $U_m = 3$ MV. Numerals *1* and *2* in the figure denote the location of the lightning rod on the ground and the point above which the process of lightning leader attraction begins, respectively. It can be seen that, at $U_m = 50$ MV, the relative probability of lightning strike to the rod is more than five times larger than the probability of lightning strike to the protected ground area. The difference in the probabilities of lightning strike to the rod (p_m^*) and to the protected ground area (p_z^*) decreases as the lightning potential is decreased to $U_m = 10$ MV and lower (see Fig. 1b). It is assumed that the probability of lightning strike to the rod in the first case (see Fig. 1a) is equal to unity, because the time during which the lightning leader propagates to any node located on the ground exceeds the time during which it propagates to the rod by more than 10%. In the second case (Fig. 1b), the time during which the leader propagates to the rod is somewhat longer (by 6%) than the minimum time required for the leader to propagate to the ground; this means that lightning will not strike the rod. The probability of the occurrence of lightning with a voltage of $U_m = 3$ MV (which corresponds to $I_m \approx 2.5$–3.75 kA) is 0.95 [25]. The 0.995 probability corresponds to the smaller radius of the zone protected by the lightning rod: $R_M \approx 1.1h$. Therefore, the absence of lightning strikes to the rod for $R_M = 1.5h$ and $U_m = 3$ MV agrees with the experimental data cited in the regulations [1].

It can be seen from the results of calculations (see Fig. 1) that it is rather difficult to intercept a low-voltage lightning. A comparison of Fig. 1a and Fig. 1b shows that the probability of lightning interception by a lightning rod decreases with a decrease in the lightning potential.

The assumption that the attraction of the lightning leader to a ground object begins after the lightning streamer zone reaches this object allows us to explain the large attraction radii (20–100 m) of negative lightnings. Our calculations show that, at such distances from the ground object to the high-voltage leader channel, the electromagnetic interaction between them is negligibly weak. That the leader is remotely controlled by the ground object can naturally be explained if we assume that, after the streamer channel contacts the object, the leading channel (whose resistance changes nonlinearly as the leader approaches the object and the discharge current increases) begins to develop between them. This assumption, in our opinion, is the only explanation of the fact that the downward and upward leaders meet one another, because their electromagnetic interaction is negligibly weak due to the small radius of the zone occupied by the electromagnetic fields of these thin discharge channels.

CONCLUSIONS

(i) The adequacy of calculating the radius of the zone protected from negative lightning by a single lightning rod is confirmed by the agreement between the results obtained using the model proposed in this paper and the normalized results obtained for lightning rods with heights of less than 150 m at two values of the lightning interception probability.

(ii) The model proposed can be used to perform comparative calculations for different types of lightning rods (e.g., active ones), as well as to determine the probability of lightning strikes to ground objects of various geometric configurations, including those with heights larger than 150 m.

(iii) The model allows one to explain difficulties associated with the interception of positive lightning, whose attraction begins at heights significantly lower than those for negative lightning.

(iv) The model can be used to determine the distances between several neighboring lightning rods that protect a grounded object with a given (including very high) degree of reliability.

REFERENCES

1. *Technical Manual for Lightning Protection of Buildings, No. 34.21.122-87* (Énergoatomizdat, Moscow, 1989) [in Russian].
2. M. Akyuz and V. Cooray, J. Electrost. **51–52**, 319 (2003).
3. F. D'Alessando and J. R. Gumley, in *Proceedings of the 24th International Conference on Lightning Protection, Birmingham, 1998*, pp. 457–462.
4. M. M. Rezinkina, in *Proceedings of the 24th International Conference on Lightning Protection, Birmingham, 1998*, pp. 924–928.
5. E. Mansell, D. MacGorman, C. Ziegler, and J. Straka, J. Geophys. Res. **107** (9).
6. C. Portela, in *Proceedings of the IEEE International Symposium on Electromagnetic Compatibility (EMC), Denver, 1998*, Vol. 2, pp. 1018–1023.
7. A. A. Dul'zon, V. V. Lopatin, M. D. Noskov, *et al.*, Zh. Tekh. Fiz. **69** (4), 48 (1999) [Tech. Phys. **44**, 394 (1999)].
8. N. Petrov and G. Petrova, Zh. Tekh. Fiz. **69** (4), 134 (1999) [Tech. Phys. **44**, 472 (1999)].
9. N. I. Petrov, G. N. Petrova, and F. D'Alessandro, IEEE Trans. Dielectr. Electr. Insul. **10**, 641 (2003).
10. D. P. Agoris, V. P. Gharalambakov, E. Pyrgioty, and S. Grzybowski, in *Proceedings of the 26th International Conference on Lighting Protection, Cracow, 2002*, pp. 270–274.

11. E. M. Bazelyan and Yu. P. Raizer, *Lightning Physics and Lightning Protection* (Institute of Physics, Bristol, 2000; Fizmatlit, Moscow, 2001).
12. V. A. Rakov, IEEE Trans. Electromagn. Compat. **43**, 654 (2001).
13. B. N. Gorin and A. V. Shkilev, Elektrichestvo, No. 2, 29 (1974).
14. E. M. Bazelyan and I. M. Razhanskiĭ, *Spark Discharge in Air* (Nauka, Novosibirsk, 1988) [in Russian].
15. D. V. Razevig, *Atmosphere-Induced Voltage Surges in Electric Power Lines* (Gosénergoizdat, Moscow, 1959) [in Russian].
16. M. A. Uman, *Lightning* (McGraw-Hill, New York, 1968; Mir, Moscow, 1972).
17. E. M. Bazelyan, B. N. Gorin, and V. I. Levitov, *Physical and Engineering Grounds of Lightning Protection* (Gidrometeoizdat, Leningrad, 1978) [in Russian].
18. E. M. Bazelyan and Yu. P. Raizer, Usp. Fiz. Nauk **170**, 753 (2000) [Phys. Usp. **43**, 701 (2000)].
19. M. Uman and V. Rakov, Bull. Am. Meteorol. Soc. **83**, 1809 (2002).
20. G. A. Mesyats, *Generation of High-Power Nanosecond Pulses* (Sov. Radio, Moscow, 1974) [in Russian].
21. S. I. Braginskiĭ, Zh. Éksp. Teor. Fiz. **34**, 1548 (1958) [Sov. Phys. JETP **7**, 1068 (1958)].
22. S. I. Andreev and B. I. Orlov, Zh. Tekh. Fiz. **35**, 1411 (1965) [Sov. Phys. Tech. Phys. **10**, 1097 (1965)].
23. V. V. Kremnev and G. A. Mesyats, *Multiplication and Transformation of Pulses in High-Current Electronics* (Nauka, Novosibirsk, 1987) [in Russian].
24. R. Briet, Intern. J. EMC^{TM}, ITEM^{TM}, 91 (1997).
25. International Standard CEI/IEC 1312-1, *Protection against Lightning Electromagnetic Impulse* (IEC, Geneve, 1995).

Translated by B. Chernyavskiĭ

Technical Physics, Vol. 50, No. 9, 2005, pp. 1158–1161. Translated from Zhurnal Tekhnicheskoĭ Fiziki, Vol. 75, No. 9, 2005, pp. 52–55.

GAS DISCHARGES, PLASMA

Microstructure of the Current Channels in a Nanosecond Spark Discharge in Atmospheric-Pressure Air in Uniform and Highly Nonuniform Electric Fields

A. V. Perminov and A. A. Tren'kin

All-Russia Research Institute of Experimental Physics, Russian Federal Nuclear Center, Sarov, Nizhni Novgorod Oblast, 607190 Russia

e-mail: karelin@ntc.vniief.ru

Received February 2, 2005

Abstract—The microstructure of a nanosecond spark discharge in atmospheric-pressure air in uniform and highly nonuniform electric fields is investigated. It is found that an 0.1- to 0.4-mm spark channel consists of a large number (from 100 to 1000) of 5- to 10-μm-diameter microchannels distributed nearly uniformly over the channel cross section. The current amplitude in the spark is 1.5–3 kA, and the current density in a microchannel is 10^7 A/cm^2. It is shown that the formation of the microstructure cannot be attributed to ionization–heating instability. The instability of the ionization wave front is suggested as a mechanism for the microstructure formation. © *2005 Pleiades Publishing, Inc.*

INTRODUCTION

The problem of the geometric parameters of current channels (the radii r of streamers and sparks) is being widely discussed in the literature because the channel cross-sectional area determines the current density; the electron temperature; and, therefore, the influence of the discharge on the gas. These parameters are rather difficult to measure using optical and electron-optical methods, which is related to the relatively low integral resolution of the recording apparatus of high-voltage devices [1]. It should also be noted that the inner structure of the current channel can be unresolvable against the background of the glowing external shell.

It is commonly accepted that the minimum possible value of r is limited by the radial ionization expansion of the channel, which agrees with the results of optical measurements ($r \geq 0.1$ cm) in high-voltage discharges in air [1]. However, it was shown in [2–4], where a high-voltage diffuse aperiodic nanosecond discharge ignited in air between a plane and a parallel wire was investigated by the autograph method, that the current channels had a rather complicated transverse structure. It was found that the current channels consisted of 1- to 10-μm-diameter microchannels distributed nearly uniformly over the channel cross section. At an average channel diameter of 3 mm and a current of 10 A, the number of microchannels reached 1000. Groups of microchannels with $r \leq 10$ μm were also found in a barrier discharge [5].

In the present study, the microstructure of the current channel of a nanosecond spark discharge in atmospheric-pressure air in uniform and highly nonuniform electric fields was investigated by the autographs method. It was found that, at a spark current of 1.5–3 kA, the spark channel with a diameter of 0.1–0.4 mm consisted of a large number of 5- to 10-μm-diameter microchannels.

EXPERIMENTAL SETUP

The experimental setup (see Fig. 1) consisted of a power supply (*PS*), discharge gap (*DG*), and diagnostic equipment. A 14-cascade Arkad'ev–Marx generator with air dischargers, a storage capacitance of 400 pF, and an internal resistance of 20 Ω [6] was used as a high-voltage pulse generator (HVPG). With a load resistance of $R = 270$ Ω, the current rise time was 20 ns and the voltage pulse amplitude was 200 kV. The HVPG could provide voltage pulses of both positive and negative polarity in the discharge gap. One of the electrodes was powered, while the second one was grounded through shunt *SH*.

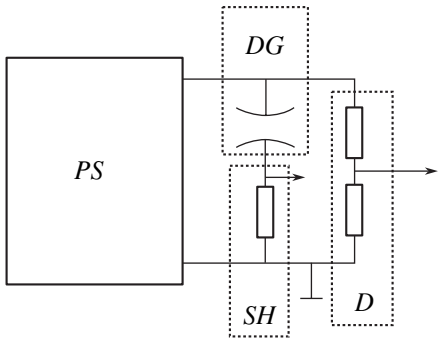

Fig. 1. Schematic of the experimental setup.

1063-7842/05/5009-1158$26.00 © 2005 Pleiades Publishing, Inc.

A spark in a uniform electric field was produced by applying negative voltage pulses, whereas that in a highly nonuniform electric field was produced by applying both negative and positive voltage pulses. Gaps with a uniform electric field were formed by two identical Chang-profile electrodes with a plane-surface diameter of 15 mm, maximum diameter of 40 mm, and height of 20 mm. Gaps with lengths of $d = 3$ and 5 mm were used. To reliably record the current channel imprints, the electrodes were made of bismuth, which has a relatively low sublimation energy.

To study the spark channel structure in a highly nonuniform electric field, a point–plane gap with a length of $d = 3.5$ cm was used. The diameter of the plane copper electrode was 9.5 cm. The point electrode with a length of 7 cm, diameter of 7 mm, vertex angle of 20°, and tip curvature radius of 0.2 mm was made of aluminum alloy. A 10-μm aluminum foil was used to record the channel microstructure. The foil was set on a dielectric ring, which was installed in the middle of the discharge gap, in parallel to the plane electrode.

The voltage U across the discharge gap was measured using screened resistive divider D and the current I was measured using low-inductive coaxial shunt SH. The voltage and current signals were recorded by a digital oscilloscope with a bandwidth of 500 MHz.

In each shot, we photographed the spark and its imprints on the electrode surfaces. A side view of the spark was taken by a digital camera installed at a distance of 0.5 m from the gap. The imprints of the current channels on the electrodes were photographed by a microscope with a 15-fold magnification and 5-μm resolution.

EXPERIMENTAL RESULTS

Typical voltage and current waveforms of a spark discharge produced in a uniform 3-mm gap and the corresponding photographs of the spark and its imprint are presented in Figs. 2–4. The amplitude of the discharge voltage was 25 kV, the current rise time (including prepulse) was 15 ns, and the current amplitude was 3 kA. The prepulse at the front of the voltage pulse is associated with the specific features of HVPG operation and is presumably related to the nonsimultaneous action of the dischargers.

The diameter of the discharge imprint on the grounded electrode is $\Delta \approx 0.4$ mm. It can be seen that the spark possesses an internal microstructure in the form of an ensemble of 5- to 10-μm diameter microchannels distributed nearly uniformly over the channel cross section. In the central part of the imprint, the metal is melted and the individual microchannels merge into craters with diameters of 20–30 μm. The total number of microchannels is $N = 600$–900. A similar picture was also observed on the powered electrode.

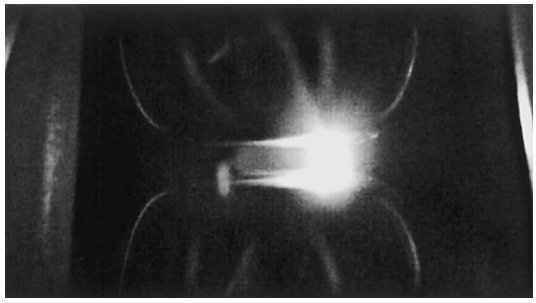

Fig. 2. Photograph of the discharge in a uniform electric field.

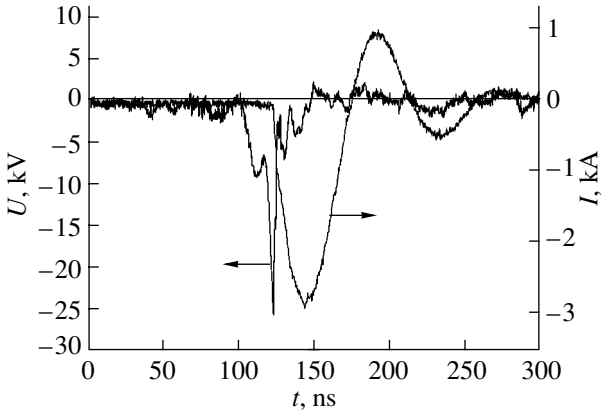

Fig. 3. Waveforms of the discharge voltage and current in the case of a uniform electric field.

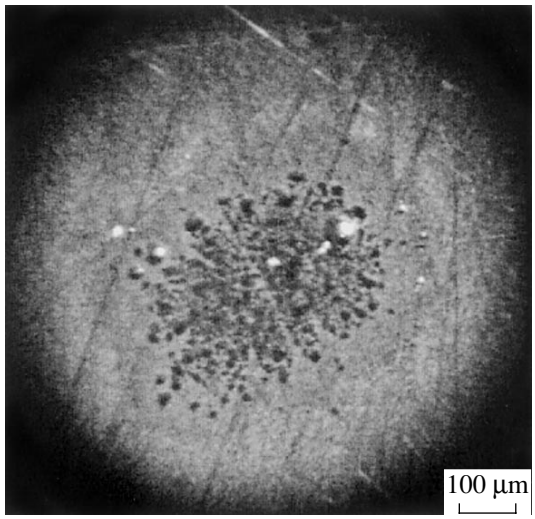

Fig. 4. Imprint of a spark on the grounded electrode in the case of a uniform electric field.

For $d = 5$ mm, we also observed microstructured spark imprints with a diameter of $\Delta \approx 0.4$ mm on both electrodes. However, because of the stronger melting of the electrode surface, the picture was fuzzier and the microchannels in the central part of the imprints merged into 20- to 100-μm-diameter craters. Neverthe-

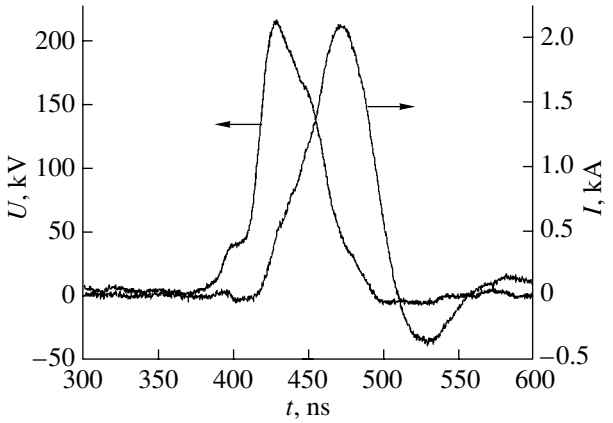

Fig. 5. Waveforms of the discharge voltage and current in the case of a highly nonuniform electric field.

less, individual microchannels with diameters of Δ_{mic} = 5–10 μm could still be distinguished at the periphery. The estimated discharge energy for d = 3 and 5 mm was 0.16 and 0.18 J, respectively. This indicates that the stronger electrode melting in the second case is apparently a result of the larger energy deposition.

Assuming that the microstructure exists at the instant of the maximum current I and that the current is uniformity distributed between microchannels, we obtain the following estimate for the average current density $\langle j_{mic} \rangle$ in microchannels:

$$\langle j_{mic} \rangle = \frac{4I}{\pi N (\Delta_{mic})^2} = 10^7 \text{ A/cm}^2,$$

which significantly exceeds the previously observed values [7]. The above $\langle j_{mic} \rangle$ value is apparently the lower estimate because the minimum microchannel diameter Δ_{mic} observed in our experiments was determined by the microscope resolution and the average value of Δ_{mic} can be even smaller.

Typical voltage and current waveforms of a spark discharge produced in a highly nonuniform field are shown in Fig. 5. Both for the positive and negative polarity, the spark developed from the point electrode to the central part of the foil and then from the foil edge to the grounded electrode.

Visually, there was only one spark channel; however, on the foil side facing the point electrode, imprints of two to five closely spaced 0.1- to 0.3-mm-diameter channels were observed. Within these channels, there were imprints of nearly uniformly distributed microchannels with an average diameter of 5 μm. The average density of microchannels was 7.8×10^3 mm^{-2}. Through holes were sometimes observed in the foil instead of the channel imprints. No influence of the electrode polarity on the electrical and spatial characteristics of a discharge was detected.

DISCUSSION

It is well known that the microstructure of arc and high-current diffuse discharges is related to the nonuniformity of heat release in the current channel. The microstructure forms at $t \geq 100$ ns after applying the discharge voltage. For example, when investigating high-current diffuse discharges in argon [8], the formation of numerous filaments with diameters of ~100 μm was observed at $t \geq 100$ ns in an initially uniform discharge. It was shown that the formation of the microstructure was related to the onset of ionization–heating instability.

Since the discharge duration in our experiments is very short (≤100 ns), the formation of the observed microstructure cannot be attributed to the contraction of the plasma channel due to the onset of ionization–heating instability. Let us estimate the time t_i required for the onset of instability under our experimental conditions. According to [9], we have

$$t_i = \frac{\gamma(\gamma - 1)p}{jE},$$

where γ is the adiabatic exponent, $p = 10^5$ Pa is the pressure, j is the current density, and E is the electric field strength.

Assuming γ = 1.22 as a lower estimate, we obtain $t_i \approx 10^{-5}$ s, which is much longer than the entire duration of the gas discharge.

It is more logical to assume that, in this case, the microstructure forms as a result of the instability of the ionization wave front [4, 10, 11] during either the bridging of the gap or the propagation of the return wave. The length of the avalanche–streamer transition under our experimental conditions is $z_{cr} < d$; i.e., breakdown is of the streamer type. Let us find a lower estimate for the time t_c during which the gap is bridged, assuming that the length of a uniform gap is d = 5 mm and the breakdown occurs due to the propagation of strong streamer ionization waves (in this case, the propagation velocity of the ionization wave is maximal and reaches $v \sim 10^9$ cm/s). As a result, we obtain $t_c \sim d/v = 5 \times 10^{-10}$ s. The time during which the instability of the ionization wave front develops is $t_i \sim \lambda/\mu E$ [10], where λ is the characteristic spatial scale of perturbations, μ is the electron mobility, and E is the average electric field in the gap by the instant of breakdown. Substituting $\lambda = 10^{-3}$ cm into this expression, we obtain $t_i \sim 10^{-11}$ s. Note that the field E causing instability near the channel head is much higher than the average field in the gap; therefore, the above value of t_i should be considered an upper estimate. Thus, we have $t_i \ll t_c$, which means that the instability of the ionization wave front can lead to the formation of a microstructure. The fact that the microchannel diameters are close to each other in our case too suggests the unique mechanism of microstructure formation.

Micron-diameter current channels can exist only if the gap is bridged very rapidly, so that the microchannels heads have no time to overlap, and, on the other hand, if the radial ionization expansion of the microchannels is absent. The latter can be explained as follows: The radial field between microchannels (both within a group of microchannels and outside it) is a superposition of the fields of a large number of nearly identically charged microchannels. In this case, the field strength at the boundary of the channel is determined by its diameter, whereas inside the channel, the field is weakened [12].

CONCLUSIONS

The microstructure of a nanosecond spark discharge in uniform and highly nonuniform electric fields has been investigated. It is shown that the formation of the microstructure cannot be attributed to ionization–heating instability. The instability of the ionization wave front is suggested as a mechanism for the microstructure formation. Micron-diameter channels can exist only if the gap is bridged very rapidly, so that the microchannels heads have no time to overlap, and, on the other hand, if the radial ionization expansion of the microchannels is absent because of the superposition of the fields of a large number of microchannels. The presence of a microstructure in spark, high-voltage diffuse, and barrier discharges allows us to suggest that the complicated structure of the current channel is a common feature of high-voltage nanosecond discharges. We believe that the results obtained will stimulate further investigations (both fundamental and applied) of this phenomenon.

ACKNOWLEDGMENTS

We thank V.I. Karelin for his help in formulating the problem and preparing the paper.

REFERENCES

1. E. M. Bazelyan and Yu. P. Raizer, *Spark Discharge* (Mosk. Fiz. Tekh. Inst., Moscow, 1997; CRC, Boca Raton, 1998).
2. V. G. Samoĭlovich, V. I. Gibalov, and K. V. Kozlov, *Physical Chemistry of the Barrier Discharge* (Mosk. Gos. Univ., Moscow, 1989) [in Russian].
3. S. N. Buranov, V. V. Gorokhov, V. I. Karelin, *et al.*, Kvantovaya Élektron. (Moscow) **18**, 891 (1991).
4. S. N. Buranov, V. V. Gorokhov, V. I. Karelin, *et al.*, in *Collection of Scientific Works*, Ed. by V. D. Selemir and A. E. Dubinov (RFYaTs-VNIIÉF, Sarov, 1998), pp. 39–67.
5. S. N. Buranov, V. V. Gorokhov, V. I. Karelin, *et al.*, in *Proceedings of the 12th IEEE International Pulsed Power Conference, Monterey, 1999*, pp. 1421–1424.
6. S. V. Voevodin, V. V. Gorokhov, and V. I. Karelin, Prib. Tekh. Éksp., No. 3, 67 (2000).
7. Yu. D. Korolev and G. A. Mesyats, *Field-Emission and Explosive Processes in the Gas Discharge* (Nauka, Novosibirsk, 1982) [in Russian].
8. Yu. I. Bychkov, F. I. Suslov, K. A. Tinchurin, and A. G. Yastremskiĭ, Fiz. Plazmy **17**, 196 (1991) [Sov. J. Plasma Phys. **17**, 114 (1991)].
9. *Encyclopedia of Low-Temperature Plasma*, Ed. by V. E. Fortov (Nauka, Moscow, 2000), Vol. 1, p. 148 [in Russian].
10. E. D. Lozanskiĭ and O. B. Firsov, *Theory of Spark* (Atomizdat, Moscow, 1975) [in Russian].
11. O. A. Sinkevich, Teplofiz. Vys. Temp. **41**, 695 (2003).
12. V. I. Karelin and A. A. Tren'kin, in *Proceedings of the 2nd Scientific and Technical Conference "Youth in Science"* (RFYATS–VNIIÉF, Sarov, 2003), pp. 608–611.

Translated by B. Chernyavskiĭ

Technical Physics, Vol. 50, No. 9, 2005, pp. 1162–1165. Translated from Zhurnal Tekhnicheskoĭ Fiziki, Vol. 75, No. 9, 2005, pp. 56–59.

SOLIDS

Temperature–Concentration Effect in Insulator–Conductor Systems

V. A. Sotskov

Berbekov Kabardino-Balkar State University, ul. Chernyshevskogo 173, Nalchik, 360004 Russia
e-mail: sozkov_va@rambler.ru

Received December 15, 2004

Abstract—A study of the bulk resistivity and permittivity of several insulator–conductor macrosystems versus the conducting component concentration and temperature has revealed an anomalous concentration range. A qualitative model accounting for these dependences on the basis of the percolation and fractal theories is proposed. © *2005 Pleiades Publishing, Inc.*

INTRODUCTION

At the present time, investigation into the electrophysical properties of composite materials is becoming more and more important [1–4] in materials science. Development of advanced materials with unique properties and their related devices has become possible owing to the breakthrough in the physics of disordered systems. It has been demonstrated in many studies [1–9] that insulator –conductor composites may offer intriguing properties near the percolation threshold. The search for materials with such properties and their application in practice is a challenging problem in materials science. A considerable variation in the conductivity, temperature resistance coefficient, and other properties, which is observed near the percolation transition, makes it possible to produce materials with different properties with the same technology [1] by slightly varying one of the components. For example, a wide variety of commercial self-recovery fuses for electrical setups has been designed based on polymer–conductor composites [4]. However, little is known about the dependence of the electrophysical parameters of a macrosystem on the conducting component concentration in model systems that are appropriate for analysis of processes in electronics [1, 5]. In addition, some features of real physical systems (for instance, the contact resistance between particles in a conductor, etc.) considerably distinguish them from ideal mathematical models. Therefore, a detailed look at real processes is required [5–8].

The aim of this study is to experimentally investigate the bulk resistivity and permittivity versus the conducting component volume concentration and temperature in insulator–conductor macrosystems.

EXPERIMENTAL

As model systems to study the conductivity of macroscopically disordered systems, we used a paraffin–conductor system. As was shown in [5], the most appropriate materials for investigating macrosystems are low-melting insulators paraffin and ceresin, which have a high resistivity, are easy to mold and chemically inactive relative to the majority of metals and semiconductors [9–11], etc. Moreover, their linear and volumetric expansion coefficients differ significantly from those of conductors [12], which makes it possible to appreciably change the volume of the matrix at a relatively small temperature variation. P1 solid oil paraffin was used as an insulating matrix. The resistivity of the paraffin was found to be $\rho \approx 1 \times 10^{10.5}\ \Omega$ m [5]. When choosing conducting components, we were guided by the following considerations.

(1) The conductors must form a series of substances with different resistivities. In systems with different resistivities, conducting chains (fractals) form in different way, which provides additional information on their structure and interaction.

(2) Some of the conductors must be uniform in properties and be free of oxide overlayers. Other conductors, on the contrary, must have a complex structure and be covered by oxides of different resistivity in order that the particle–particle contact resistance in the system under consideration be varied [8].

(3) The conductors must have both a negative (as in paraffin [5, 12]) and a positive temperature resistance coefficient (TRC).

Using a filler with varied properties, one can draw a conclusion (by comparing the electrophysical properties of the composites) about the structure of the conducting chains in it. In view of the above requirements, graphite, iron, and aluminum particles were employed as conducting inclusions. The materials chosen were the following: thermographite (S-1 dry colloidal graphite with a main particle size of 4×10^{-6} m), pure-grade iron (a main particle size of 6×10^{-6} m), and pure-grade aluminum (a main particle size of 10×10^{-6} m after

screening). From the standpoint of minimizing the contact resistance, graphite as a conducting component has a number of advantages over metals [5]. Since carbon oxides are gases, one can ignore the formation of oxide films on the particles no matter what the production technology of graphite. Resistivities ρ of surface oxide layers were taken to be equal to 1×10^5 Ω m for iron particles and $1 \times 10^{9.5}$ Ω m for aluminum particles [8]. For carbon, iron, and aluminum, TRC α was taken to be equal to $\alpha = -2 \times 10^{-4}$ K^{-1}, $+4.2 \times 10^{-3}$ K^{-1}, and $+6.51 \times 10^{-3}$ K^{-1} [12], respectively. Thus, three composites (paraffin–graphite, paraffin–iron, and paraffin–aluminum) were analyzed. These composites are listed in order of increasing particle–particle contact resistance in the conductor [8]. Prior to preparation of the composites, the iron-containing samples were demagnetized by the standard methods. The mixer and other facilities in contact with the composites were made of nonmagnetic materials. Preparation of the samples was described in detail elsewhere [5–8]. The sample to be studied represented a capacitor with plates made of electrolytic copper. The capacitor was filled with a mixture of paraffin and conducting particles in a certain concentration. The samples were prepared so as, on the one hand, to prevent intense evaporation of the paraffin (which is inevitable at long-term mixing and a high temperature of the melt) and, on the other hand, to provide the reproducibility of the electrophysical parameters for most of the samples with the same concentration. The samples with the same concentration of the conducting component exhibited a spread (3–5%) in the electrical parameters, such as resistivity, capacitance, and figure of merit. No less than five samples with a given concentration of the conducting component in the composite were prepared. The concentration of the conducting component was changed in 5 wt% intervals and then was converted to volume percent. Heating of the samples in a thermostat with an average rate of 1.7×10^{-3} K/s was accompanied by measurement of the electrophysical parameters.

The dc resistivity of the samples was measured by the standard two-probe technique. The capacitance and figure of merit were measured at a frequency of 1 kHz using the standard bridge. We took the dependences $C = f(T)$ and $Q = f(T)$, where C and Q are the capacitance and figure of merit of the capacitors with different conductor concentrations. On the basis of these data, the temperature dependence of imaginary part ε" of the permittivity (i.e., $\log\varepsilon'' = f(T)$, where $\varepsilon = \varepsilon' + j\varepsilon''$ [9]) were calculated. The TRC was determined as follows:

$$\alpha = \frac{1}{\rho}\frac{\partial\rho}{\partial T}\ \text{K}^{-1}\ [9].$$

RESULTS

The results of our investigation are presented in Figs. 1–3. Figure 1 shows the dependence $\log\rho = f(T)$ for the paraffin–iron system. The dependences $\log\rho = f(T)$ and $\log\varepsilon' = f(T)$ for the paraffin–graphite and paraffin–iron systems are similar in many ways, although they have certain features of their own, which will be discussed below. As an example, let us analyze the results obtained for the paraffin–iron composite. As is seen from Fig. 1 (curve *1*), the resistivity of pure paraffin drops with increasing temperature. In materials with a molecular lattice (including paraffin [9, 12]), the conductivity is small and is governed largely by impurities [9]. The decrease in the resistivity with increasing temperature can be explained by the presence of ionized impurities. The curves $\log\rho = f(T)$ do not have kinks up to the melting point. This fact indicates that the conductivity in the temperature range considered does not turn into the intrinsic conductivity. Up to conducting components concentrations of approximately $x < 0.314$, the behavior of the curves for the paraffin–iron composite changes insignificantly. However, in the range $0.314 < x < 0.603$, the run of the curves $\log\rho = f(T)$ (Fig. 1, curves *3* and *4* for the paraffin–iron system) changes sharply. The sign of the TRC (i.e., the slopes of the curves) becomes opposite. The same behavior, but for $0.066 < x < 0.29$, is observed in the paraffin–graph-

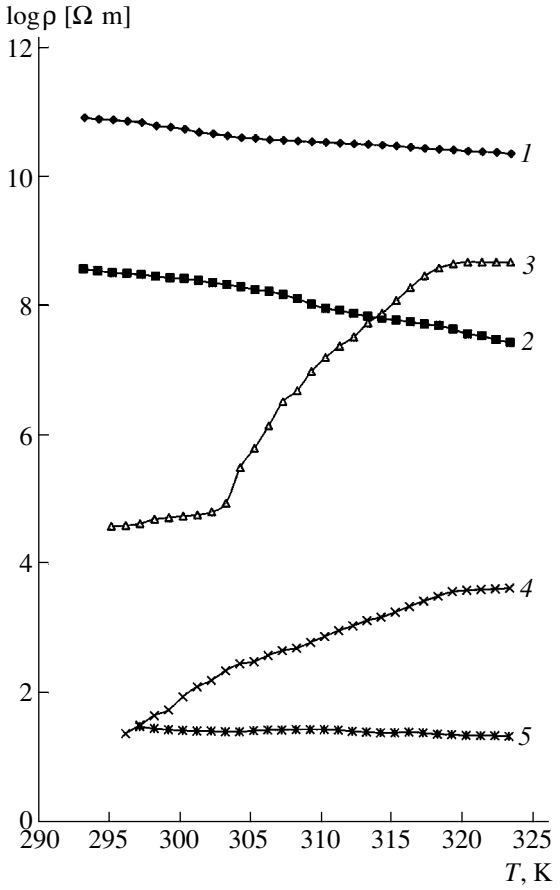

Fig. 1. Temperature dependence of the logarithm of the bulk resistivity: (*1*) Paraffin and paraffin–iron composites with an iron content of (*2*) 21, (*3*) 31, (*4*) 60, and (*5*) 79 vol%.

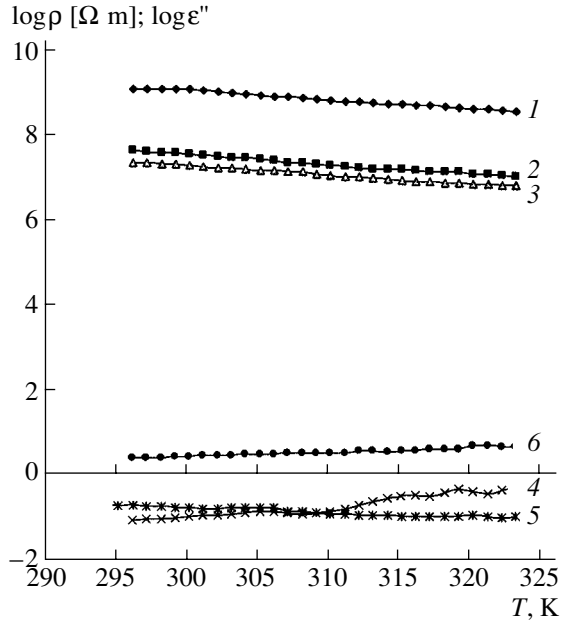

Fig. 2. Temperature dependence of the logarithm of the bulk resistivity for the paraffin–aluminum composite with an aluminum content of (*1*) 36, (*2*) 25, and (*3*) 92 vol%. (*4–6*) Temperature dependence of the logarithm of the imaginary part of the permittivity for the same concentrations.

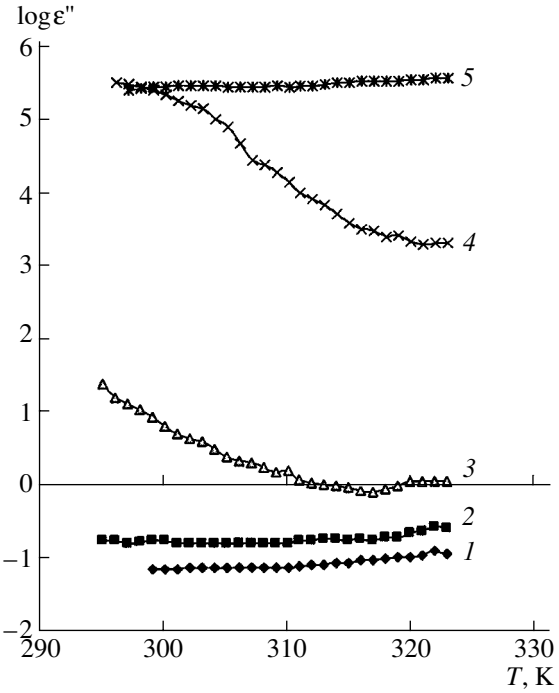

Fig. 3. Temperature dependence of the logarithm of the imaginary part of the permittivity. (*1*) Paraffin and paraffin–iron composites with an iron content of (*2*) 21, (*3*) 31, (*4*) 60, and (*5*) 79 vol%.

ite system. Here, at conductor concentrations $x > 0.29$, the TRC becomes negative again. For the paraffin–iron composite, the resistivity and TRC of the composite tend toward those of iron with increasing conductor concentration. It should be noted that, in anomalous regions, the TRC may be very high both at certain temperatures and throughout the temperature range. For example, at $T \approx 313$ K, $\alpha = +2.1$ K^{-1} ($x \approx 0.108$) in the paraffin–graphite system and $\alpha = +1.4$ K^{-1} ($x \approx 0.31$) for the paraffin–iron system. For the former system, the same was observed earlier in [8], which validates the results obtained in this work. The TRC of the paraffin–graphite system is greater than that for the paraffin–iron one, all other things being equal. The curves $\log\rho = f(T)$ for the paraffin–aluminum system (Fig. 2, curves *1–3*) behave in a radically different way: these are straight lines decreasing monotonically with an increase in both temperature and concentration. The TRC of the paraffin–aluminum system is negative and differs little from that of paraffin. As is known [9], parameter ε" characterizes losses in the measuring cell (capacitor). These losses may include relaxation and conductivity losses. As is seen from curve *1* in Fig. 3, the relaxation losses in pure paraffin are comparatively low. The losses (i.e., ε") increase largely with an increase in the conductor concentration. For example, the behavior of curves *2–5* in Fig. 3 can be explained by increasing losses due to the conductivity of the composite. In the anomalous range, the dependence $\log\varepsilon" = f(T)$ is represented by descending curves *3* and *4*. Thus, for conducting component concentrations in the range $0.066 < x < 0.29$, the losses in the paraffin–graphite and paraffin–iron systems decrease with increasing temperature. For the paraffin–aluminum composite (Fig. 2, curves *4–6*), the temperature dependence $\log\varepsilon" = f(T)$ is insignificant; for this system, the concentration dependence is much more essential.

DISCUSSION

The appearance of the anomalous concentration ranges cannot be explained by the properties of the individual components involved: paraffin or conductor (graphite, iron, and aluminum). Their presence is also independent of the sign of the TRC of the conductor: these ranges are observed both in graphite (having a negative TRC) and in iron (positive TRC). Moreover, in aluminum with a positive TRC, these ranges are absent at all. Moreover, the above values of the TRC ($\alpha = +2.1$ K^{-1} at $x \approx 0.108$ in the paraffin–graphite system and $\alpha = +1.4$ K^{-1} at $x \approx 0.31$ for the paraffin–iron system at $T \approx 313$ K) found experimentally differ much from the value of the TRC for graphite and iron. Since paraffin is a saturated hydrocarbon and the sample temperature in the process of preparation did not exceed 55°C, no intermediates can appear in the systems under investigation [5, 10, 11]. The only regularity that can be traced in the data obtained is a correlation between the

existence of the anomalous range (and its associated value of the TRC) and the particle–particle contact resistance in the conductor. In [8], it was shown that the contact resistance in the composites studied increases in the order paraffin–graphite, paraffin–iron, and paraffin–aluminum. One can assume that the effect observed may be associated with the specific structure and specific properties of composite's conducting fractal chains in the anomalous range. Since the contact resistance between particles in graphite is the lowest, this anomalous effect in the paraffin–graphite system is the highest. The highest contact resistance is between aluminum particles; accordingly, the effect is totally absent. The difference between the concentrations at which the anomalous ranges exist in the paraffin–graphite and paraffin–iron systems can also be explained by different contact resistances between particles in the conductor. Iron particles are covered by an oxide layer. Therefore, a higher concentration of these particles is required if a structure similar in conductivity to the graphite structure is to form [8, 13]. It was assumed [13] that, in the paraffin–graphite system, TRC sign reversal with increasing temperature is caused by the formation of non-self-similar fractals. The emergence of larger fractals ($d > 55$ μm) with a more developed surface may change the electrophysical properties of the paraffin–graphite system (in particular, the sign and behavior of the TRC). One can suppose that the structure of conducting chains in the anomalous range is such that an increase in the temperature of the composite breaks the fractal continuity (relative shear). Such processes disturb the general fractal structure: the number of "red" edges and, accordingly, the resistivity grow. The measurements of the resistivity and of the imaginary part of the permittivity are consistent with each other, because losses in a composite are due to electric conduction and quantity ε" drops with increasing temperature and resistance. Outside the anomalous concentration ranges mentioned above, the structure of conducting chains is such that, at low concentrations, relative shear or disconnection of the chains affects the conductivity of the composite insignificantly, since the number of long conducting chains is still small. Once the upper limit of the anomalous concentration range is exceeded, disconnection or relative shear of one chains close other ones, since the number of fractals is already large and the average number of red and blue edges changes insignificantly.

CONCLUSIONS

(1) The bulk conductivity and permittivity in the paraffin–graphite, paraffin–iron, and paraffin–aluminum macrosystems were experimentally investigated as a function of the volume concentration of a conducting component and temperature.

(2) For the paraffin–graphite and paraffin–iron composites, the anomalous conductor concentration ranges, $0.066 < x < 0.29$ and $0.314 < x < 0.603$, respectively, were found. Within these ranges, the TRC of the composites either varies or takes anomalously high values, which are untypical of the constituents. In the paraffin–aluminum composite, such ranges are absent.

(3) A qualitative model explaining the observations in terms of the percolation and fractal theories is suggested.

REFERENCES

1. E. V. Kharitonov, *Insulating Materials with Inhomogeneous Structure* (Radio i Svyaz', Moscow, 1983) [in Russian].
2. A. V. Turik, A. I. Chernobabov, G. S. Radchenko, and S. A. Turik, Fiz. Tverd. Tela (St. Petersburg) **46**, 2139 (2004) [Phys. Solid State **46**, 2213 (2004)].
3. A. B. Khanikaev, A. B. Granovskiĭ, and J. P. Clerc, Fiz. Tverd. Tela (St. Petersburg) **44**, 1537 (2002) [Phys. Solid State **44**, 1611 (2002)].
4. *Modern Electronics: Advanced Devices*, Issue 4: *Polyswitch Self-Restoring Safety Fuses* (Dodeka, Moscow, 1998), pp. 25–57 [in Russian].
5. V. A. Sotskov and S. V. Karpenko, Zh. Tekh. Fiz. **73** (1), 107 (2003) [Tech. Phys. **48**, 100 (2003)].
6. V. A. Sotskov, Pis'ma Zh. Tekh. Fiz. **30** (11), 38 (2004) [Tech. Phys. Lett. **30**, 461 (2004)].
7. V. A. Sotskov, Pis'ma Zh. Tekh. Fiz. **30** (12), 1 (2004) [Tech. Phys. Lett. **30**, 487 (2004)].
8. V. A. Sotskov, Zh. Tekh. Fiz. **74** (11), 107 (2004) [Tech. Phys. **49**, 1501 (2004)].
9. V. V. Pasynkov, *Electronic Materials* (Vysshaya Shkola, Moscow, 1980), pp. 155–160 [in Russian].
10. A. M. Petrov, Kh. V. Bal'yan, and A. T. Troshchenko, *Organic Chemistry* (Vysshaya Shkola, Moscow, 1963) [in Russian].
11. *Chemical Encyclopedic Dictionary* (Sov. Éntsiklopediya, Moscow, 1983) [in Russian].
12. *Tables of Physical Quantities*, Ed. by I. K. Kikoin (Atomizdat, Moscow, 1976) [in Russian].
13. V. A. Sotskov, Poverkhnost, No. 2, 79 (2004).

Translated by Yu. Vishnyakov

Technical Physics, Vol. 50, No. 9, 2005, pp. 1166–1169. Translated from Zhurnal Tekhnicheskoĭ Fiziki, Vol. 75, No. 9, 2005, pp. 60–63.

SOLIDS

Skin Effect in Metals: Passage to the Infinite Conductivity Limit

A. I. Spitsyn

Kharkov National University of Radio Electronics, Kharkov, 433053 Ukraine

Received October 26, 2004

Abstract—The infinite conductivity limit in the classical skin effect in metals is considered. The analysis is carried out with and without taking into account the influence of free electron relaxation, as well as local relationships between the electric field and current density, in the free electron model. Both ultimately nonlocal and real limits are considered for the indefinitely increasing free path. © *2005 Pleiades Publishing, Inc.*

In this paper, we consider limiting processes as applied to the skin effect in metals when the metal conductivity tends to infinity. The metal is assumed to be isotropic, linear, and homogenous. Consider first the simple case of the classical skin effect, which is observed at room temperature in normal (nonsuperconducting) metals. Let an electromagnetic radiation with frequency ω be incident on flat surface S of the metal occupying the half-space. We shall further assume that the typical range of electromagnetic field variation over the surface far exceeds the depth of field penetration into the metal, and so the field at a given point can be considered as uniform and depending on only the coordinate normal to the metal surface.

The Cartesian coordinate system is taken such that its origin is at the metal boundary, the z axis is directed along normal **n** inward to the metal, and the y and x axes lie in the metal plane. Without loss of generality, we assume that the field is linearly polarized and the x and y axes are aligned with electric field vector **E** and magnetic field vector **H**, respectively. In the case at hand (room temperature), current density **j** and electric field **E** are locally related as $\mathbf{j} = \sigma\mathbf{E}$ (Ohm's law), where σ is the metal conductivity, at any point of the metal. From the Maxwell equations and Ohm's law, the solution to the problem of the skin effect has the form

$$E = E_x = ZH(0)e^{-z/\delta_{com}}, \quad H = H_y = H(0)e^{-z/\delta_{com}},$$
$$Z = i\omega\mu_0\delta_{com} = \sqrt{\frac{i\omega\mu_0}{\sigma}}, \quad \delta_{com} = \sqrt{\frac{1}{i\omega\mu_0\sigma}}. \qquad (1)$$

Here, $Z = E(0)/H(0) = R + iX$ is the surface impedance of the metal; δ_{com} is the complex penetration depth in the classical skin effect [1]; and R and X are the surface resistance and reactance, respectively.

If one considers the classical skin effect and lets the conductivity tend to infinity ($\sigma \longrightarrow \infty$), relationships (1) yield in the limit the ideal boundary condition $E_{\tan}|_s = 0$ and surface impedance Z vanishes. In this limit, the electromagnetic field does not penetrate into the metal but the behavior of tangential components $H_{\tan}$ and $E_{\tan}$ is different if we put $H(0) = \text{const}$. The z dependences of the magnitudes of E and $H \sim \exp(-z/\delta_{cl})$, where $\delta_{cl} = \sqrt{2/\omega\mu_0\sigma}$ is the classical penetration depth, are shown in Figs. 1a and 1b for three values of conductivity $\sigma_3 > \sigma_2 > \sigma_1$. As the conductivity increases, the magnetic field, remaining constant in magnitude at the boundary (if we assume that the magnetic field of the wave incident on the metal is constant, the magnetic field on the surface will change only slightly and tend to a certain constant limit), is forced out of the conductor and concentrates in a narrow surface layer. Unlike the magnetic field, the electric field decreases with increasing σ and vanishes at the metal surface in the limit $\sigma \longrightarrow \infty$.

In the limiting process considered, the relaxation of conductivity electrons is disregarded. According to the free electron model [1], the dc conductivity is given by $\sigma = ne^2\tau/m$, where $\tau = l/V_F$; n is the volume electron density; e, m, and l are the electron charge, mass, and free path, respectively; τ is the relaxation time; and V_F is the electron velocity at the Fermi surface. For the electromagnetic field harmonically varying with time, inclusion of relaxation leads to relationships (1) where σ is changed to $\sigma/(1 + i\omega\tau)$, with the condition $\sigma \longrightarrow \infty$ being reduced to the condition $l \longrightarrow \infty$. With this in mind, we obtain from (1)

$$\delta_{com}^2 = \frac{1 + i\omega\tau}{i\omega\mu_0\sigma} = \frac{m}{\mu_0 ne^2} - \frac{i}{\omega\mu_0\sigma}. \qquad (2)$$

It then follows that, at $l \longrightarrow \infty$, the complex penetration depth tends to real value $\delta_0 = \sqrt{m/\mu_0 nl^2}$, where δ_0 is the plasma penetration depth. In this case, the electromagnetic field penetrates into metal to a finite depth and the limiting process results in superconductivity with **j** and **E** locally related as $\mathbf{j} = \mathbf{E}/i\omega\mu_0\delta_0^2$. In this

nondissipative limit, the surface impedance at the metal boundary is equal to purely imaginary value $Z = i\omega\mu_0\delta_0$.

Above, the relationship between the current density and electric field was assumed to be local; i.e., the current density at any metal point is determined by the electric field at this point. Since the current density at a point inside the metal depends on the electric field within a domain about the free path in size, Ohm's law will apply if the free path is small compared with skin depth δ_{sk}, over which the field changes appreciably. As l increases, the depth of penetration into the metal decreases; consequently, l may become equal to, or even much larger than, δ_{sk} (by the skin depth, we will mean the quantity $\delta_{sk} = \mathrm{Re}\,\delta_{com}$ [1]). Then, the local relationship $\mathbf{j} = \sigma\mathbf{E}$ is invalid and, when considering the limiting process, should be changed to the general relationship, which is fulfilled for metals at low temperatures [2]. In the free electron model, the z dependence of the electric field can be expressed as [1, 3]

$$E(z) = \frac{2i\omega\mu_0 H(0)}{\pi}\int_0^\infty \frac{\cos kz\,dk}{k^2 + i\omega\mu_0\tilde{\Omega}(k)}, \qquad (3)$$

where

$$\tilde{\Omega}(k) = \frac{2\pi c_E\xi}{(k\xi)^3}[(1 + (k\xi)^2)\arctan(k\xi) - k\xi],$$
$$\xi = \frac{l}{1 + i\omega\tau}, \quad c_E = \frac{3}{4\pi i\omega\mu_0\delta_{com.l}^2\xi}. \qquad (4)$$

Here, $\delta_{com.l} = ((1 + i\omega\tau)/i\omega\mu_0\sigma)^{1/2}$ is the complex penetration depth under the assumption that the local relationship $\mathbf{j} = \sigma\mathbf{E}/(1 + i\omega\tau)$ is fulfilled in the metal. Later on, we consider the microwave range (i.e., the maximum frequency is limited by several hundreds of gigahertz), which is of most interest. Then, for high l, quantity $|\xi|$ will approach the value V_F/ω, which is much higher than skin depth δ_{sk}. In this case, the results in the limit $|\xi| \longrightarrow \infty$ approach those obtained in the real physical limit $l \longrightarrow \infty$. (Note that, in the formal limit $\xi = l/(1 + i\omega\tau) \longrightarrow \infty$, quantities l and $a = \omega\tau$ should be considered as independent and quantity l should be regarded as infinitely high, at least of higher order than parameter $a = \omega\tau$.) In [2], the limiting process $|\xi| \longrightarrow \infty$ was studied at $a = 0$ and $\xi = l$. This limit has been called the anomalous limit.

Let us find a relationship for surface impedance Z_∞ in the anomalous limit. An expression for surface impedance $Z = E(0)/H(0)$ is found from (3) at $z = 0$,

$$Z = \frac{2i\omega\mu_0}{\pi}\int_0^\infty \frac{dk}{k^2 + i\omega\mu_0\tilde{\Omega}(k)}. \qquad (5)$$

Passing to the limit $\xi \longrightarrow \infty$, $\mathrm{Re}\,\xi > 0$, in the integrand in (5) and taking into account that $\delta_{com.l}^2\xi$ is a constant value independent of free path l and $i\omega\mu_0\tilde{\Omega}(k)$ tends to $3\pi/4\delta_{com.l}^2\xi k$, as follows from (4), we recast Eq. (5) as

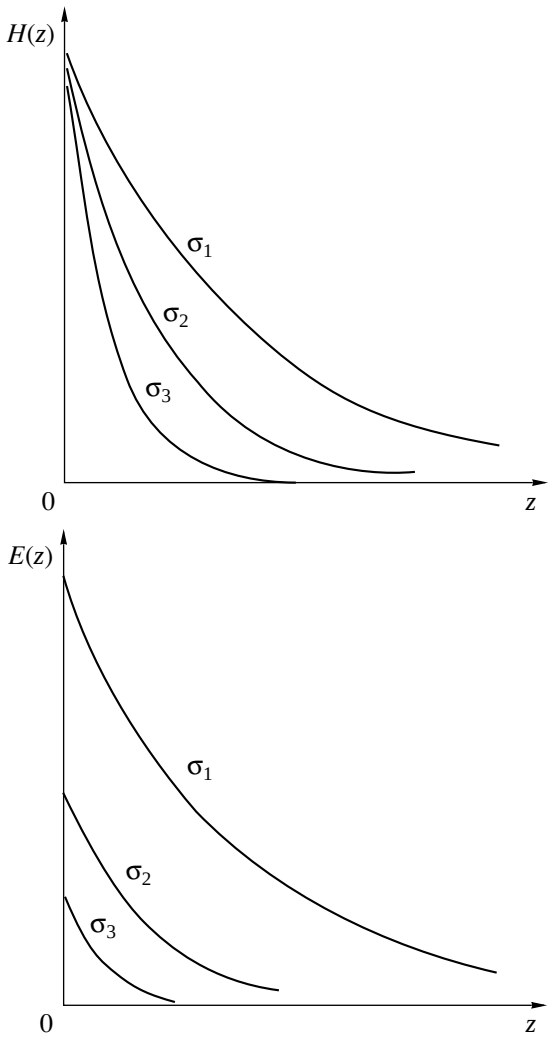

Fig. 1.

$$Z_\infty = \frac{2i\omega\mu_0}{\pi}\int_0^\infty \frac{k\,dk}{k^3 + i\beta}, \quad \beta = \frac{3\pi}{2\delta_{cl}^2 l}. \qquad (6)$$

The integral in expression (6) is reduced to the tabulated one by changing the variable to k^3 [4, integral no. 5 in p. 298]; hence, the surface impedance in the anomalous limit is given by

$$Z_\infty = \frac{2\omega\mu_0}{3\sqrt{3}}\beta^{-1/3}(1 + i\sqrt{3}). \qquad (7)$$

The anomalous limit $\xi \longrightarrow \infty$ is physically unjustified, because quantity a also tends to infinity at $l \longrightarrow \infty$ ($\sigma \longrightarrow \infty$) and ξ tends to a high but finite value, $\xi_\infty = -iV_F/\omega$, in the frequency range considered. In this limit,

surface impedance Z can be conveniently approximated as follows. In the expansion of $\tilde{\Omega}(k)$ at large ξ, we leave the term $i\omega\mu_0\tilde{\Omega}(k) = i\beta(1/k - 4/k^2\pi\xi)$. After integration in Eq. (5), the surface impedance can be represented in the form

$$Z = Z_\infty + Z_1 = Z_\infty\left(1 + \frac{2\sqrt{3}}{\pi}\frac{\delta_\infty}{\xi_\infty}\right), \quad (8)$$

where $\delta_\infty = Z_\infty/i\omega\mu_0$ is the complex penetration depth in the anomalous limit. Note that the inaccuracy in representation of $\tilde{\Omega}(k)$ at $|\xi k| < 1$ is described by terms of a higher order of smallness.

Thus, in the limit of infinitely long free path l, the value of the surface impedance in the anomalous limit is augmented by a small correction of order $|\delta_\infty/\xi_\infty| \ll 1$ in the frequency range considered.

Note that the same case of large l was analyzed in [5] when surface reactance $X = \mathrm{Im}Z$ was considered in the microwave range. The value of $X_1 = \mathrm{Im}Z_1$, which depends on the magnetic field energy and the kinetic energy of charge carriers, is responsible for an addition to the field inductance in the anomalous limit $L_\infty = X_\infty/\omega$ and for a small kinetic inductance.

The previous consideration was concerned with the microwave range, where the results are close to those in the anomalous limit. However, at high frequencies, $\omega\tau$ may be equal to, or even far exceed, unity. Although the free path may be infinitely large in this case, the value of $|\xi|$ will increase only slightly. Quantity ξ_∞ will take a finite value, and the results will be other than those in the anomalous limit. For high $\omega\tau$ at room temperature, the results in the limit $l \longrightarrow \infty$ will approach those for the local case $|\xi| \ll \delta_{sk}$ (see (2)).

Let us consider losses in the anomalous limit using the technique used in [1] for current density calculation. We introduce the local spherical coordinate system at arbitrary point z inside the metal. Proceeding similarly to [1], for component j_1 of the current density that is due to electrons moving through this point in the solid angle between directions Θ_0 and $\pi - \Theta_0$ ($\Theta_0 < \pi/2$), we can write $j_1 = \int_{-\infty}^{+\infty}\Omega_1(z - z')E(z')dz'$ with the kernel

$$\Omega_1(z - z') = \pi c_E\int_{1/\cos\Theta_0}^{\infty}\left(\frac{1}{u} - \frac{1}{u^3}\right)\exp(-|z - z'|u/\xi)du, \quad (9)$$

which coincides with the volume kernel at $\Theta_0 = 0$.

Then, using Eq. (3), one derives a relationship for part j_1 of the current density and passes to the limit $\xi \longrightarrow \infty$, as was demonstrated above in the derivation of Z_∞. For any angle Θ_0, the limiting process yields for j_1 the same relationship as for the total current density ($\Theta_0 = 0$).Thus, in the anomalous limit, the electrons moving parallel to the flat surface of the metal contribute to the current density and losses at any point inside the metal. This is in accordance with the Pippard concept of inefficiency [1].

Now let us consider the local loss distribution in the anomalous limit. From Eq. (3) and a relationship for the current density that results from Eq. (3) by introducing factor $\tilde{\Omega}(k)$ under the integral sign and passing to the limit $\xi \longrightarrow \infty$ (as was done in the derivation of surface impedance Z_∞), we arrive at the following distributions of the electric field and current density in the anomalous limit:

$$E(z) = \frac{2i\omega\mu_0 H(0)}{\pi}\int_0^\infty\frac{k\cos kz}{k^3 + i\beta}dk,$$
$$j(z) = \frac{2i\beta H(0)}{\pi}\int_0^\infty\frac{\cos kz}{k^3 + i\beta}dk. \quad (10)$$

The final relationships for E and j in terms of special functions can be found by the technique used in [6] for the anomalous limit in superconductors. Let a relationship between j and E for the fields harmonically varying at point z be written in the form $j(z) = \sigma(z)E(z)$, where $\sigma(z) = \sigma_R(z) + i\sigma_x(z)$ is the local complex conductivity. Then, the volume density of the active power (transferred to electrons or, on the contrary, to the electromagnetic field) is

$$\frac{1}{2}\mathrm{Re}(j^*E) = \frac{1}{2}\sigma_R(z)|E|^2.$$

The dependence of dimensionless quantity $\tilde{\sigma}_R = \omega\mu_0\beta^{-2/3}\mathrm{Re}\sigma(\tilde{z})$ on dimensionless coordinate $\tilde{z} = z\beta^{1/3}$ calculated by (10) is shown in Fig. 2. The curve $\sigma_R(z)$ is seen to be nonmonotone. When moving, electrons interact with the electric field, transferring the energy from one regions of the metal to others [1]. Because of electron–metal ion collisions, the electron momenta diminish, causing energy dissipation (this holds true in the limit $\xi \longrightarrow \infty$ too). These factors have an influence on the current density and electromagnetic field patterns inside the metal.

The dependence $\sigma_R(z)$ implies that regions exist inside the metal where $\sigma_R < 0$. This is because, in the self-consistent field, there are regions in the metal where the period-averaged energy is transferred to the field (the electromagnetic field is "generated" at points with $\sigma_R < 0$). Through the boundaries of such a region, the mean electromagnetic energy flux is radiated to other regions of the metal. The total power transferred to the current, $\int_0^\infty\sigma_R|E|^2dz/2$, is equal to the total loss power, $R_\infty|H(0)|^2/2$ ($R_\infty = \mathrm{Re}Z_\infty$), inside metal, which is converted to heat.

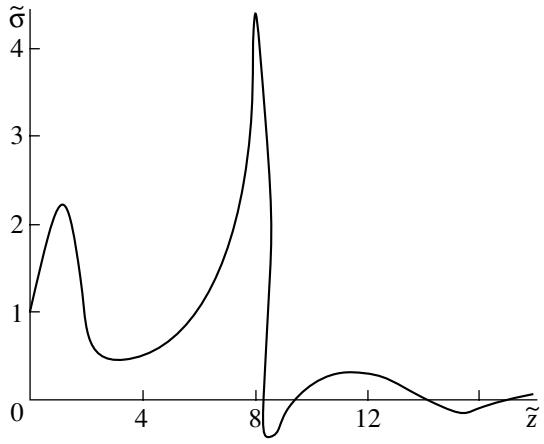

Fig. 2.

In conclusion, we will turn to the field distribution at high but finite values of ξ, $|\xi| \gg \delta_{sk}$. In the anomalous limit $\xi \longrightarrow \infty$, differentiating $E(z)$ given by (10) by parts yields a main asymptote at $z \gg \delta_{sk}$,

$$E(z) = -\frac{81\sqrt{3}}{32\pi}\frac{E(0)}{(z/\delta_\infty)^2}. \qquad (11)$$

At $|\xi| \gg \delta_{sk}$, the field structure differs little from that in anomalous limit as long as $z \le |\xi|$ and meets Eq. (11) far away from the surface. At $z \gg |\xi|$, Eq. (10) fails in describing the electromagnetic field. Between these two ranges, there lies an intermediate (transition) range. The main asymptote at $z \gg l$ for the case $a = \omega\tau = 0$ was found in [2]. We will find a main asymptote in the general case for $\omega\tau \neq 0$ and finite ξ.

Let us take the limits of integration in relationship (3) for $E(z)$ from $-\infty$ to $+\infty$ and substitute $\exp(ikz)/2$ for $\cos kz$. Next, we take the segment of the real axis between $-R_0$ and $+R_0$, enclose it by a circle of radius R_0 in the upper half-plane, and make a cut at the logarithmic branch point along the ray from i/ξ to $\infty i/\xi$. The relationship for $E(z)$ can now be found with the residue theorem through residues at the poles and integrals along the banks of the cut. Under the anomalous conditions, the integrals along the banks of cut make a major contribution at large z. Changing the variable to $\xi k/i$ and making transformations similar to those made in [2], we come to an expression for $E(z)$ at $z \gg |\xi|$,

$$E(z) = -AE(0)\left(1 - \frac{2}{3}\frac{\delta_{com.l}^2}{\xi^2}\right)\frac{\delta_\infty}{\delta_{com}}\frac{e^{-z/\xi}}{(z/\delta_\infty)^2}, \qquad (12)$$

$$A = \frac{81\sqrt{3}\pi}{64}.$$

In the limit $|\xi| \gg |\delta_{com.l}|$, the complex penetration depth is $\delta_{com} \approx \delta_\infty$. In this case, we have $E(z) = -AE(0)\exp(-z/\xi)/(z/\delta_\infty)^2$. In the limit $l \longrightarrow \infty$, $\xi \longrightarrow \xi_\infty$.

REFERENCES

1. F. F. Mende and A. I. Spitsyn, *Surface Impedance of Superconductors* (Naukova Dumka, Kiev, 1985) [in Russian].
2. G. E. H. Reuter and E. H. Sondheimer, Proc. R. Soc. London, Ser. A **195**, 336 (1948).
3. A. I. Spitsyn, Zh. Tekh. Fiz. **72** (4), 128 (2002) [Tech. Phys. **47**, 499 (2002)].
4. A. P. Prudnikov, Yu. A. Brychkov, and O. I. Marichev, *Integrals and Series*, Vol. 1: *Elementary Functions* (Nauka, Moscow, 1981; Gordon and Breach, New York, 1986).
5. A. I. Spitsyn, Radiotekh. Élektron. (Moscow) **38**, 2152 (1993).
6. A. I. Spitsyn, Zh. Tekh. Fiz. **64** (4), 68 (1994) [Tech. Phys. **39**, 385 (1994)].

Translated by M. Astrov

Technical Physics, Vol. 50, No. 9, 2005, pp. 1170–1177. Translated from Zhurnal Tekhnicheskoĭ Fiziki, Vol. 75, No. 9, 2005, pp. 64–70.

SOLIDS

Concentration Dependences of the Properties of Multicomponent PZT-Based Piezoelectric Ceramics in the Morphotropic Transition Range

O. A. Demchenko*, L. A. Resnitchenko*, O. N. Rasumovskaya*, A. V. Turik, L. A. Shilkina*, and S. I. Dudkina***

** Research Institute of Physics, Rostov State University, pr. Stachki 194, Rostov-on-Don, 344090 Russia*
e-mail: olesia_demch@mail.ru

*** Department of Physics, Rostov State University, pr. Stachki 194, Rostov-on-Don, 344090 Russia*

Received February 2, 2005

Abstract—The following three ternary PZT-based systems are studied in detail: $0.98Pb(Ti_xZr_{1-x})O_3$–$0.02Pb(Nb_{1/2}Bi_{1/2})O_3$, $0.98(Pb_{0.9727}Sr_{0.0273})(Ti_xZr_{1-x})O_3$–$0.02Pb(Nb_{1/2}Bi_{1/2})O_3$ + 1 wt% PbO, and $0.98(Pb_{0.9727}Sr_{0.0273})(Ti_xZr_{1-x})O_3$–$0.02Pb(Nb_{1/2}Bi_{1/2})O_3$ + 2 wt % $PbGeO_3$, where $0.45 \le x \le 0.49$ and the concentration step is $\Delta x = 0.025$. A number of concepts are formulated regarding the phase diagrams of PZT-type systems near the morphotropic transition. A scheme for real tetragonal–rhombohedral transformation is given. The maxima of the electrophysical characteristics of the solid solutions from the morphotropic range are shown to be caused mainly by an appearing intermediate phase. Analysis of the insulating, piezoelectric, and mechanical properties of the samples demonstrates that there is a group of solid solutions that are promising materials for high-temperature piezoelectric devices operating in the medium-frequency band. © *2005 Pleiades Publishing, Inc.*

INTRODUCTION

Most applications of piezoelectric ceramics, the radio and telecommunication industry, nondestructive control and diagnostics, hydroacoustics, the automotive industry, shipbuilding, the aircraft industry, and medical and household appliances are based on traditional compositions including PZT. There is a constant stimulus to search for more efficient materials for specific applications, which is caused by new piezotechnical problems appearing in each of the industries. The most attractive approach to solving these problems seems to be the design of multicomponent compounds (modified by various additions) of the type $Pb(Ti_xZr_{1-x})O_3 + \sum_n (PbB'_{1-\alpha}B''_\alpha O_3)_n$ (n = 1–4), whose compositions correspond to the morphotropic transition range (MTR). This range is characterized by the thermodynamic instability of coexisting phases and, hence, extremal dielectric and electromechanical properties of the related solid solutions (SSs).

Recent publications (e.g., see review [1] and references therein) indicate that the MTR morphology is more complex than was accepted earlier and make it necessary to comprehensively study the behavior of the structural and electrophysical characteristics of the related SSs inside this range. To do this and to use the data obtained for designing practically important piezoelectric materials, we continue the investigation [2] of ternary $0.98Pb(Ti_xZr_{1-x})O_3$–$0.02(PbB'_{1-\alpha}B''_\alpha)O_3$ systems, which have not yet been studied. As third components, the authors of [2] used $BaW_{1/3}Bi_{2/3}O_3$ (ferroelectric with a Curie temperature of 450°C) and "$SrW_{1/3}Bi_{2/3}O_3$" (hypothetical compound). In this work, we also introduce the complex oxide $PbNb_{1/2}Bi_{1/2}O_3$, which has no an intrinsic crystalline form, into the PZT system and perform stoichiometric and hyperstoichiometric modification of SSs by Sr and Ge (the latter is introduced in the form of $PbGeO_3$). The choice of these third components and modifiers is caused by the possibility of reaching high Curie temperatures T_C, which are typical of bismuth compounds, and high piezoelectric parameters, which are provided by "soft ferroelectric" Ba and Sr cations, in the systems and by the possibility of improving the workability of the objects via the formation of low-melting Ge-containing eutectics.

EXPERIMENTAL

The compositions of the SSs to be studied are the following:

$$0.98Pb(Ti_xZr_{1-x})O_3 - 0.02Pb(Nb_{1/2}Bi_{1/2})O_3,$$

$$0.98(Pb_{0.9727}Sr_{0.0273})(Ti_xZr_{1-x})O_3$$

$$- 0.02Pb(Nb_{1/2}Bi_{1/2})O_3 + 1\ \text{wt\%}\ PbO,$$

$$0.98(Pb_{0.9727}Sr_{0.0273})(Ti_xZr_{1-x})O_3$$

$$- 0.02Pb(Nb_{1/2}Bi_{1/2})O_3 + 2\ \text{wt\%}\ PbGeO_3$$

1063-7842/05/5009-1170$26.00

$$(0.45 \le x \le 0.49).$$

The concentration step was $\Delta x = 0.025$. Since the contents of third components in these SSs are low, the phase diagrams of these systems should be close to the phase diagram of the base PZT system. Therefore, the concentration step chosen should ensure the formation of SSs in the MTR.

The SSs were prepared by a standard ceramic technology: solid-state two-stage synthesis at temperatures $T_1 = T_2 = 800$°C for isothermal holding times $\tau_1 = \tau_2 =$ 4 h followed by baking at temperatures $T_{bake} = 1180$ or 1200°C for 3 h.

The sample densities were determined by hydrostatic weighing in octane. X-ray diffraction studies were carried out on a DRON-3 diffractometer (FeK_α radiation, Mn filter) using the Bragg–Brentano scheme. X-ray diffraction patterns were recorded using the θ–2θ method in the step-by-step scanning mode at a scanning 2θ step of 0.01° and a counting time of 10 s at each point and in the continuous mode of recording diffraction patterns on a chart strip at counter speeds of 0.5 and 0.25 deg/min. The lattice parameters and percentage of phases were estimated by the formulas

$$\mu_T = 100 - (\mu_{PSC} + \mu_{Rh}),$$

$$\mu_{PSC} = (I_{200}^{PSC} \times 100)/(I_{200}^{T} + I_{002}^{T} + I_{200}^{Rh} + I_{200}^{PSC}),$$

$$\mu_{Rh} = (I_{200}^{Rh} \times 100)/(I_{200}^{T} + I_{002}^{T} + I_{200}^{Rh} + I_{200}^{PSC}),$$

where μ_T, μ_{PSC}, and μ_{Rh} are the contents of the tetragonal (T), pseudocubic (PSC), and rhombohedral (Rh) phases, respectively, and I_{200} and I_{002} are the maximum intensities of these phases. The parameter of T cell uniform deformation δ_T was determined by the formula $\delta_T = 2/3(c/a - 1)$, where a and c are the T cell parameters.

We studied disk samples 10 mm in diameter and 1 mm thick. Electrodes were applied via baking a silver-containing paste at 800°C for 0.5 h. The samples were polarized in a polyethylene–siloxane liquid as follows: they were placed in a chamber at room temperature, and the temperature was smoothly increased to 140°C in 15–20 min; this growth was accompanied by an increase in the electric field from 0 to 2.5–3.0 kV/mm. After holding at this temperature for 20–25 min, the samples were cooled to 60–40°C in the field within 20 min.

For studying the electrophysical properties of the SSs under study, we measured their dielectric, piezoelectric, and mechanical properties at room temperature according to [3]. Using the techniques described in [3], we measured the permittivities of the poled ($\varepsilon_{33}^T/\varepsilon_0$) and nonpolarized ($\varepsilon/\varepsilon_0$) samples, the dielectric losses $\tan\delta$ in a weak field, the electromechanical coupling coefficient K_p of an in-plane vibration mode, the piezoelectric modulus d_{31}, and the mechanical Q_M. The parameters were calculated by the formulas given in [3] with a program developed by Demchenko (the Delphi 5 programming environment). We also studied the temperature dependences of the parameters $\varepsilon/\varepsilon_0$ and $\tan\delta$ in a temperature range of 20–500°C at a frequency of 1 kHz.

RESULTS AND DISCUSSION

The measured density of the samples is 96–98% of the theoretical density; therefore, they are considered to be dense. In combination with the absence of impurity phases in the samples (which was supported by X-ray diffraction), this fact indicates a high reliability of our structural and electrophysical measurements. This reliability is also confirmed by the repeatability of the effects detected (12–15 samples of each composition were studied). In the systems under analysis, phase states are similar; therefore, as an illustrating example, we chose the $0.98Pb(Ti_xZr_{1-x})O_3$–$0.02Pb(Nb_{1/2}Bi_{1/2})O_3$ system.

An analysis of the X-ray diffraction patterns of the SSs of this system shows that, at $x \approx 0.485$, they have two diffuse maxima in the angular range $55° < 2\theta < 59°$ between the 002 and 200 lines of the T phase. The maximum located closer to the 002 line of the T phase corresponds to the 200 line of PSC-phase clusters with a parameter $a \approx 4.1$ Å. The other maximum corresponds to the 200 line of Rh-phase clusters with a parameter $a \approx 4.07$ Å. It is impossible to determine the symmetry of the PSC phase in more detail under our experimental conditions. As is seen from Fig. 1, the X-ray diffraction lines are strongly diffused and overlapped, which is caused by complex phase compositions of the SSs and similar lattice parameters of the coexisting phases. The coherent domains of the newly formed phases are small, which also broadens the lines.

In [4, 5], we showed that B-cation displacements in Ti-containing complex oxides are modulated as a result of periodically repeated shifts in their crystallographic planes. This modulation results in diffuse maxima, which distort and broaden the line profiles, at the diffraction line wings. It should also be noted that, apart from Ti and Zr ions, oxygen octahedra in the SSs under study are occupied by Bi ions, which have a higher scattering power. As a result, the diffuse maxima increase and the diffraction line profiles become distorted to a higher degree. As x decreases, the maxima of the PSC and Rh phases increase, the line intensities of the T phase decrease, and the line widths increase. At $x = 0.45$–0.46 (depending on the conditions of SS preparation), the PSC and T phases disappear and the samples become purely rhombohedral.

Figure 2a shows the x dependences of the structural characteristics of the samples fabricated at the optimum temperature ($T_{bake} = 1200$°C). These characteristics are seen to behave nonmonotonically inside the MTR. For example, one can see two constant (or weakly varying)

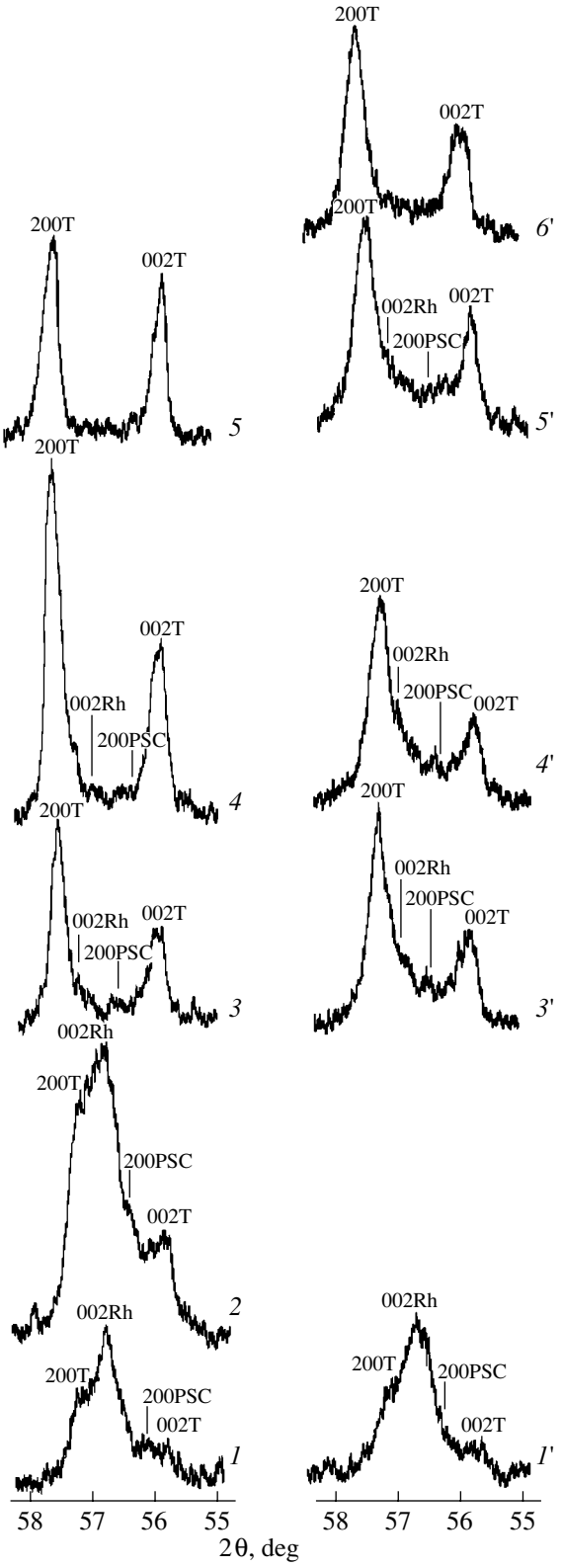

Fig. 1. Fragments of the X-ray diffraction patterns of the $0.98Pb(Ti_xZr_{1-x})O_3$–$0.02Pb(Nb_{1/2}Bi_{1/2})O_3$ SSs fabricated at T_{bake} = (a) 1200 and (b) 1180°C. x = (*1*, *1*') 0.45, (*2*) 0.455, (*3*, *3*') 0.47, (*4*, *4*') 0.475, (*5*, *5*') 0.48, and (*6*') 0.485.

lattice-parameter segments at the periphery of MTR ($0.455 \le x \le 0.465$, $0.47 \le x \le 0.48$) that are adjacent or closely spaced to the boundaries of transition into single-phase (Rh or T) states and at the center of MTP ($0.465 < x < 0.47$), where the lattice parameters change sharply. The parameters $\mu_{Rh}(x)$ and $\mu_T(x)$, which characterize the Rh- and T-phase contents, respectively, behave similarly. On the contrary, the PSC-phase content is constant at the center of MTP and changes sharply near the morphotropic boundaries, forming maxima in the constant lattice-parameter segments. The approximation of the right descending branch of $\mu_{PSC}(x)$ to $\mu_{PSC} = 0$ allows us to restrict the PSC-phase region from the side of $PbTiO_3$ to the concentration $x \approx 0.492$. Thus, the MTR width Δx is equal to 0.041 ($0.451 < x < 0.492$) (for T_{bake} = 1200°C).

Figure 2b shows the concentration dependences of the structural characteristics of the samples having the same compositions but prepared at a lower T_{bake} (1180°C). It is seen that these dependences substantially resemble those given above. The main differences are a shift in the MTR toward $PbTiO_3$, the broadening of the MTR by a factor of almost 1.5 ($\Delta x \approx 0.058$, $0.462 < x < 0.520$; the second morphotropic boundary was detected as in the first case), a shift in the first constant structural-parameter segment toward the single-phase Rh area, a sharp change in $\mu_{PSC}(x)$, $\mu_{Rh}(x)$, and $\mu_T(x)$ inside the MTR, and the absence of a pronounced maximum in $\mu_{PSC}(x)$ at the Rh boundary.

As follows from the results given above, the morphotropic transition from the T into Rh phase in these SS systems with decreasing $PbTiO_3$ content occurs as follows. First, SSs containing the T phase and the intermediate PSC phase are formed. As x decreases, the PSC phase transforms gradually into the Rh phase, the SSs contain three phases (T + PSC + Rh), and the contents of the two latter phases increase. After reaching a certain concentration, the amount of the PSC phase decreases and that of the Rh phase increases. This sequence of phase transitions in the concentration range under study seems to be natural if we take into account the following factors. Above T_C, the structures of both systems become cubic (C). The T cell ($a = b < c$, $\alpha = \beta = \gamma = 90°$) can smoothly transform into a cubic cell when the a and b parameters increase and the c parameter decreases. The Rh cell ($a = b = c$, $\alpha = \beta = \gamma \neq 90°$) can smoothly transform into a cubic cell when the angle α increases to 90°. The T cell cannot smoothly transform into the Rh cell. This transformation can occur either through the C phase, when the linear cell parameters are gradually equalized and, then, the angle α decreases, or through a phase with lower symmetry (e.g., monoclinic symmetry), whose cell has unequal linear parameters and undergoes angular distortion. This means that at least three phases should simultaneously coexist in the MTR, namely, an SS with a high Ti content and the T distortion of the perovskite cell; an SS with a high Zr content and the Rh distortion of the

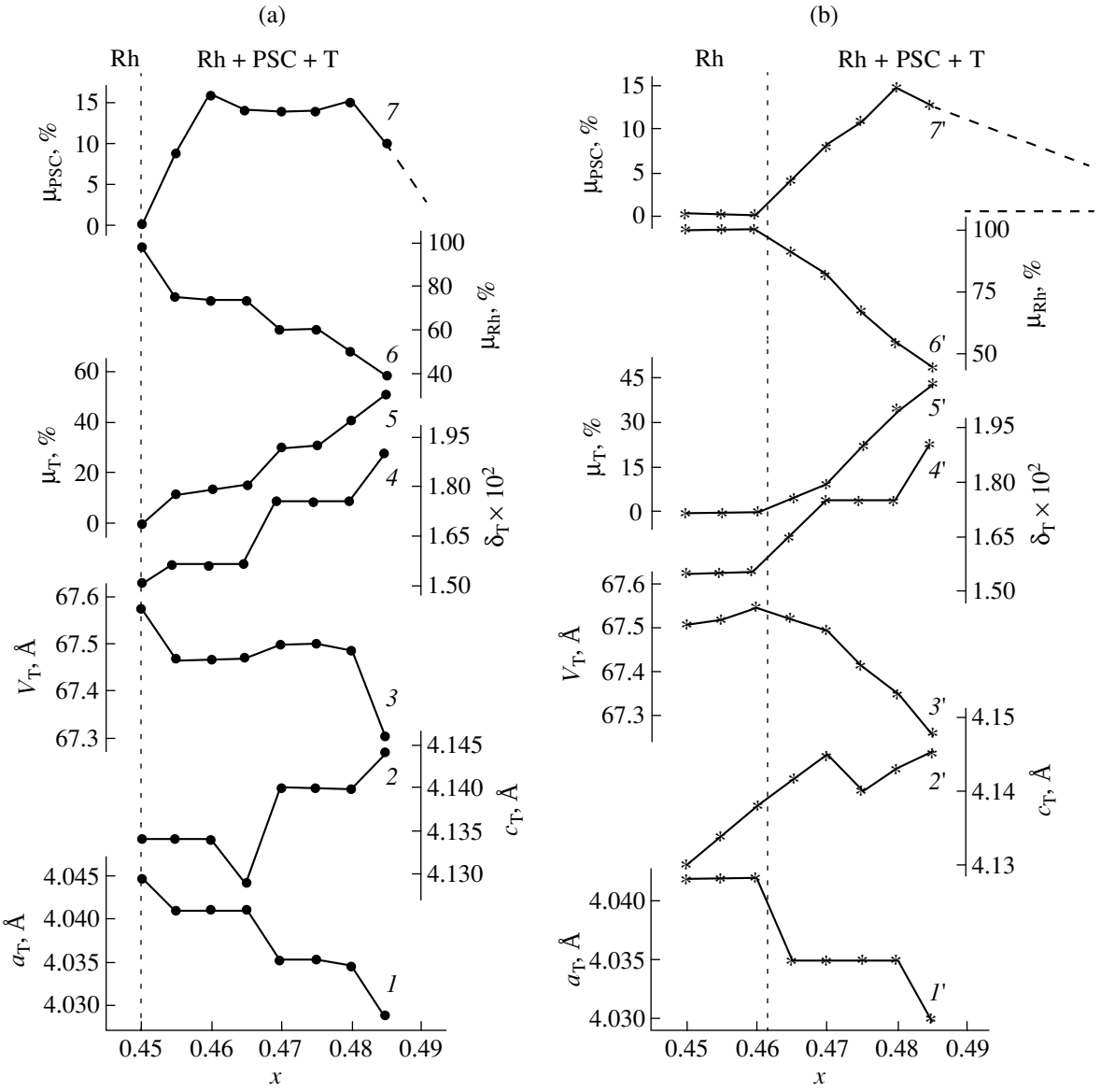

Fig. 2. Concentration dependences of the structural characteristics of the $0.98Pb(Ti_xZr_{1-x})O_3$–$0.02Pb(Nb_{1/2}Bi_{1/2})O_3$ SSs fabricated at T_{bake} = (a) 1200 and (b) 1180°C. (*1*, *1*') a_T, (*2*, *2*') c_T, (*3*, *3*') volume V_T, (*4*, *4*') T cell uniform deformation parameter δ_T, (*5*, *5*') T phase content μ_T, (*6*, *6*') Rh phase content μ_{Rh}, and (*7*, *7*') PSC phase content μ_{PSC}.

cell; and an intermediate SS (intermediate phase, IP [14, 15]) that has a monoclinic distortion of the perovskite cell, as was shown in [6–16] for the PZT system and other similar systems. It is obvious that, depending on the SS preparation conditions, both the formation rate of the PSC and Rh phases and the MTR width can change.

Note that an additional PSC phase in PZT-based SSs lying in the T–Rh transition range was first detected in [17] well before the appearance of works dealing with the IP in the MTR. The authors of [17] studied a PKR-7M material [18] designed at the Research Institute of Physics, Rostov State University, on the basis of one of the five-component $Pb(Ti,Zr)O_3 + \sum_{n=3}(PbB'_{1-\alpha}B''_{\alpha}O_3)_n$ systems. This MTR in [17] was classified as a transition region containing an additional phase. The content of the additional phase in the samples at room temperature was about 50%. An analysis of the diffraction line widths showed that this phase had small coherent domains (smaller than 400 Å) (in our case, their size is ~300 Å). In [16], this additional phase was treated as a phase with metastable polarization characteristic of relaxer ferroelectrics.

Inside the MTR, the electrophysical characteristics of the SSs fabricated at T_{bake} = 1200°C (Fig. 3a) behave similarly to the structural characteristics: they behave

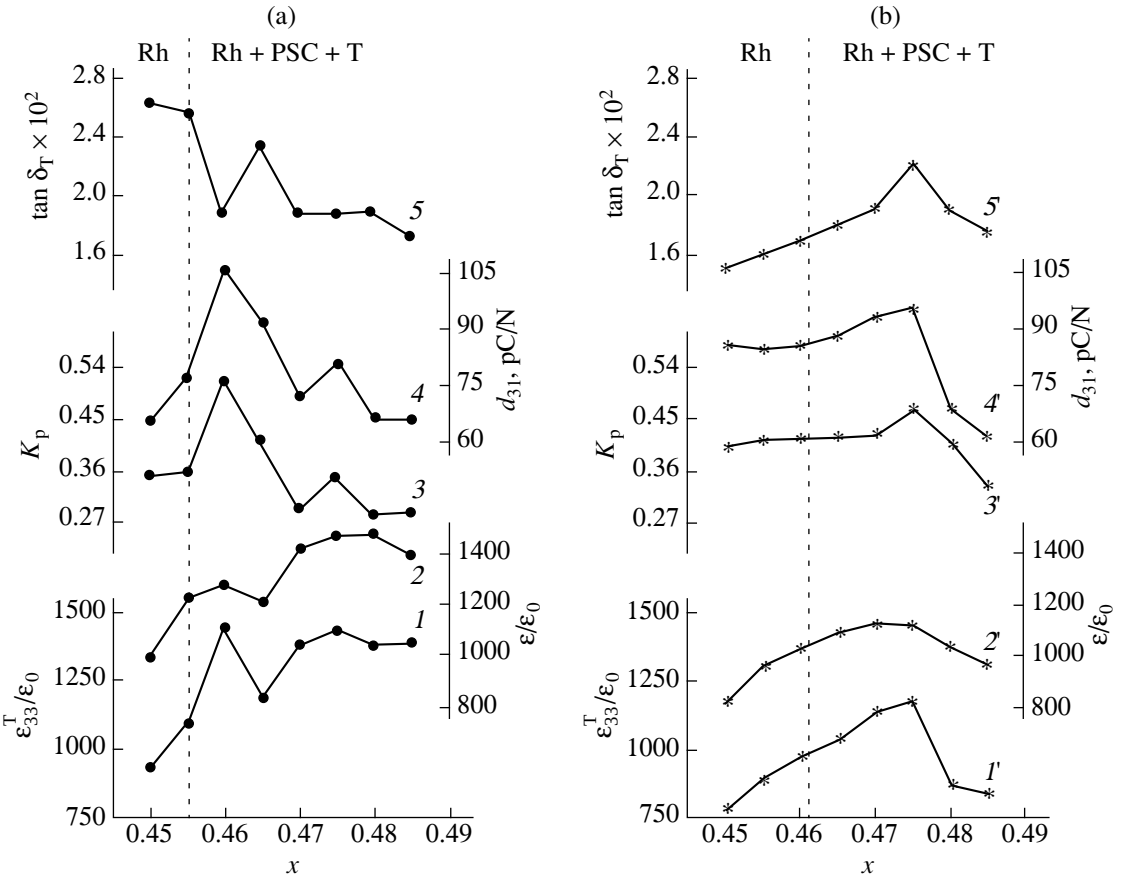

Fig. 3. Concentration dependences of the electrophysical characteristics of the $0.98Pb(Ti_xZr_{1-x})O_3$–$0.02Pb(Nb_{1/2}Bi_{1/2})O_3$ SSs fabricated at T_{bake} = (a) 1200 and (b) 1180°C. (*1*, *1*') $\varepsilon_{33}^T/\varepsilon_0$, (*2*, *2*') $\varepsilon/\varepsilon_0$, (*3*, *3*') K_p, (*4*, *4*') d_{31}, and (*5*, *5*') $\tan\delta$.

nonmonotonically, forming maxima near both morphotropic boundaries. In the SSs baked at lower T_{bake} temperatures (Fig. 3b), all characteristics do not form maxima at the Rh boundary, and they form maxima only near the transition into the T phase. This behavior can result from insufficient quality of the samples (low density, heterogeneity). In both cases, the dielectric and piezoelectric characteristics are maximum at the maximum content of the PSC phase. This is related to the easy motion of interphase boundaries and domain walls (easy rotation of a polarization vector) in the three-phase MTR [1, 8, 13, 19], which results in an increase in the response of the system to external electrical and mechanical actions. Thus, the role of the IP in the formation of the macroscopic properties of the SSs under study is seen to be important. The examination of the temperature dependence of $\varepsilon/\varepsilon_0$ in the paraelectric phase reveals anomalies in the x dependence of the Curie constant C_W, which is a fundamental characteristic; similar anomalies were detected in [20]. These anomalies are caused by a shape-memory effect, which consists in the fact that paraelectric cubic ceramic retains the residual mechanical stresses that are accumulated during the formation of a multicomponent structure.

The facts and considerations given above and an analysis of the reported data allow us to formulate a number of concepts regarding the phase diagrams of PZT-type systems near the MTR.

(1) Based on the form of the phase diagrams of the PZT system and related multicomponent systems (having similar phase boundaries), we classify them as Roozeboom SS diagrams of the first type with peritectoid decomposition in the solid state [21].

(2) These diagrams reflect the processes of the formation of a continuous series of the SSs of the high-temperature modifications of system components (which are cubic for $PbTiO_3$ and $PbZrO_3$) and the peritectoid decomposition of the SSs of the low-temperature modifications. This decomposition is characterized by (i) gradual dissolution of one of the phases (e.g., the T phase) and the precipitation of another phase (Rh), (ii) limited solubility of the low-temperature modifications (T and Rh), (iii) the formation of a concentration range (MTR) where two SSs with limiting concentrations are in equilibrium, and (iv) constant SS parameters (physical properties) inside the MTR.

(3) The range of coexistance of phases is relatively narrow, and the boundary components of the systems under study form wide isomorphic areas with each

Table 1. Tetragonal--rhombohedral transformation in PZT-type systems when going from ideal to real objects

<table>
<tr><td colspan="2" rowspan="3">(a) SS(T) ⟶</td><td colspan="5">SS(T) + SS(Rh) ⟶</td><td colspan="2" rowspan="3">SS(Rh)</td></tr>
<tr><td colspan="5">SS decomposition in MTR</td></tr>
<tr><td colspan="5">MTR</td></tr>
<tr><td colspan="2" rowspan="3">(b) SS(T) ⟶</td><td>SS(T + Rh) ⟶</td><td colspan="2">SS(T + Rh) + SS(Rh + T) ⟶
Segment with constant parameters
SS decomposition</td><td>SS(Rh + T) ⟶</td><td colspan="2" rowspan="3">SS(Rh)</td></tr>
<tr><td colspan="4">MTR</td></tr>
<tr><td colspan="2" rowspan="3">(c) SS(T) ⟶</td><td>SS(T + IP) ⟶</td><td colspan="2">SS(IP) ⟶</td><td>SS(IP + Rh) ⟶</td></tr>
<tr><td colspan="4">MTR</td></tr>
<tr><td rowspan="2">(d) SS(T) ⟶
Single-phase area</td><td rowspan="2">$SS(T)_{IP}$ ⟶
Heterophase area with IP clusters</td><td>$SS(T + IP)_{Rh}$ ⟶
Two-phase area with Rh clusters</td><td>$SS(T + IP)_{Rh}$
$+ SS(IP + T)_{Rh}$ ⟶
Segment with constant parameters</td><td>SS(T + IP
+ Rh) ⟶</td><td>$SS(Rh + IP)_{T}$
$+ SS(IP + Rh)_{T}$ ⟶
Segment with constant parameters</td><td>$SS(Rh + IP)_{T}$ ⟶
Two-phase area with T clusters</td><td>$SS(Rh)_{IP}$ ⟶
Heterophase area with IP clusters</td><td>SS(Rh)
Single-phase area</td></tr>
<tr><td colspan="5">Heterophase range (MTR)</td></tr>
</table>

Table 2. Electrophysical characteristics of the SSs in the systems $0.98(Pb_{0.9727}Sr_{0.0273})(Ti_xZr_{1-x})O_3$–$0.02Pb(Nb_{1/2}Bi_{1/2})O_3$ + 1 wt % PbO and $0.98(Pb_{0.9727}Sr_{0.0273})(Ti_xZr_{1-x})O_3$–$0.02Pb(Nb_{1/2}Bi_{1/2})O_3$ + 2 wt % PbGeO

SS composition	x	$\varepsilon_{33}^T/\varepsilon_0$	$\tan\delta \times 10^2$	K_p	$\lvert d_{31}\rvert$, pC/N	Q_M
$0.98(Pb_{0.9727}Sr_{0.0273})(Ti_xZr_{1-x})O_3$–$0.02Pb(Nb_{1/2}Bi_{1/2})O_3$ + 1 wt% PbO	0.465	1630	1.47	0.34	90.2	190
	0.46	1614	1.54	0.34	90.8	171
	0.455	1362	1.96	0.36	88.3	178
	0.45	1184	2.09	0.41	92.1	180
$0.98(Pb_{0.9727}Sr_{0.0273})(Ti_xZr_{1-x})O_3$–$0.02Pb(Nb_{1/2}Bi_{1/2})O_3$ + 2 wt% PbGeO	0.465	1666	1.75	0.51	136	111
	0.46	1507	1.94	0.47	122	120
	0.455	1508	2.14	0.58	145	121
	0.45	1420	2.32	0.56	134	122

other [22]. Therefore, the dissolution of the low-temperature modifications can be considered as the formation of an SS with a discontinuity in the phase diagram at certain component concentrations.

(4) Such a phase diagram is caused by substantial differences in the shapes of the crystal lattice cells of the boundary components more than by the difference in their symmetries [23]. These differences do not permit a gradual transition from one structure into another; as a result, the SS decomposes.

(5) The form of the phase diagrams of such systems (perfect single crystals) can be described in terms of the classic thermodynamics of solutions, which can consist of two phases [24].

(6) In real ferroelectric crystals (polycrystals, ceramics), the properties of SSs cannot be thermodynamically described because of their complex hierarchical structure (domains, grains) and the high sensitivity of these properties, especially in the range of coexisting phases, to the characteristics of the components, fabrication conditions, and external actions. These factors can cause deviations from stoichiometry, SS composition fluctuations, the formation of point and extended defects, and an increase in the phase concentration range.

(7) The history of samples causes differences (which were detected in different experiments) in the MTR length; in the "filling" of the MTR by phases of different symmetries and compositions, including cluster structures [25] and the IP; and in the behavior of structural and electrophysical parameters inside the MTR.

(8) For real objects, the T–Rh transformation can be represented in the form of schemes (a)–(d) in Table 1, which become more complex as the results of more comprehensive studies of PZT-type systems are accumulated and interpreted.

The lower (most probable) scheme differs from the ideal scheme by low rates of diffusion processes occurring during solid-phase synthesis, which hinders the reaching of equilibrium states. Note that the formation of two segments with constant SS parameters detected in this work is related to the appearance of the IP and, as a consequence, to the SS formation by this scheme.

(9) The dielectric, piezoelectric, and electromechanical characteristics of the SSs most often change smoothly (just as does the structure) in single-phase areas far from the MTR, nonmonotonically (just as the structure) in heterogeneous areas (where new-phase clusters appear) in the vicinity of the MTR, and in an extremal manner near morphotropic boundaries (when the IP content is maximum in the segments of constant structural parameters).

(10) SSs from the MTR have a high defect concentration, which is caused by their heterophase compositions. This fact is indicated by, e.g., the minimum values of the baking temperature, the electrical resistivity (for *p*-type conduction), the activation energies of reactions, and the energy gap and the maximum deviation of the electrophysical parameters from the average value [26].

(11) SSs from the MTR are thermodynamically stable. For example, as compared to the single-phase SSs, they exhibit the maximum change in their fundamental characteristic (T_C) when they are subjected to external actions, such as technological processes [26].

(12) As the number of components increases, the form of the phase diagrams becomes more complex, and the decomposition of SSs can also depend on the differences in the diffusion activities of different cations. We believe that, due to this reason, the IP was first discovered in the most complex system of the well-known multicomponent systems, which included eight cation types [17].

An analysis of Fig. 3 and Table 2, which lists the electrophysical characteristics of the SSs of two other systems to be studied, shows that there is a group of SSs (with $x = 0.455$–0.465) that are promising for practical application. Rather high values of T_C (350–360°C), K_p (0.50–0.58), and d_{31} (100 pC/N) at low values of $\tan\delta$ (<0.02) and Q_M (<200) make it possible to use the SSs having such parameters in high-temperature broadband

transducers. As compared to all well-known high-temperature materials [18] having low values of $\varepsilon_{33}^{T}/\varepsilon_0$ (~50–500) and, hence, used in high-frequency devices, we fabricated SSs having much higher values of $\varepsilon_{33}^{T}/\varepsilon_0$ (1300–1500) in this work and in [2]. These high values make such SSs promising for high-temperature piezoelectric devices operating in the medium-frequency band.

ACKNOWLEDGMENTS

This work was supported by the Russian Foundation for Basic Research, project no. 02-02-17781.

REFERENCES

1. B. Nohada, Curr. Opin. Solid State Mater. Sci. **6**, 27 (2002).
2. O. A. Demchenko, L. A. Reznichenko, L. A. Shilkina, *et al.*, Pis'ma Zh. Tekh. Fiz. **30** (3), 62 (2004) [Tech. Phys. Lett. **30**, 113 (2004)].
3. *State Standard 110444-87: Piezoelectric Ceramic Materials*, 1988.
4. L. A. Reznichenko, L. A. Shilkina, S. V. Titov, and O. N. Razumovskaya, in *Proceedings of the International Symposium "Ordering in Minerals and Alloys" (OMA-2000), Rostov-on-Don, 2000*, pp. 127–138.
5. L. A. Reznichenko, L. A. Shilkina, S. V. Titov, *et al.*, Kristallografiya **48**, 421 (2003) [Crystallogr. Rep. **48**, 377 (2003)].
6. B. Noheda, D. E. Cox, G. Shirane, *et al.*, Appl. Phys. Lett. **74**, 2059 (1999).
7. B. Noheda, J. A. Gonzalo, R. Guo, *et al.*, Phys. Rev. B **61**, 8687 (2000).
8. R. Guo, L. E. Cross, S.-E. Park, *et al.*, Phys. Rev. Lett. **84**, 5423 (2000).
9. B. Noheda, D. E. Cox, G. Shirane, *et al.*, Phys. Rev. Lett. **86**, 3891 (2001).
10. G. Xu, H. Luo, *et al.*, Phys. Rev. B **64**, 020102 (2001).
11. Z.-G. Ye, B. Noheda, M. Dong, *et al.*, Phys. Rev. B **64**, 184114 (2001).
12. D. E. Cox, B. Noheda, G. Shirane, *et al.*, Appl. Phys. Lett. **79**, 400 (2001).
13. B. Noheda, D. E. Cox, G. Shirane, *et al.*, Phys. Rev. B **63**, 014103 (2001).
14. V. Yu. Topolov and A. V. Turik, Fiz. Tverd. Tela (St. Petersburg) **43**, 1525 (2001) [Phys. Solid State **43**, 1585 (2001)].
15. V. Yu. Topolov and A. V. Turik, Fiz. Tverd. Tela (St. Petersburg) **44**, 1295 (2002) [Phys. Solid State **44**, 1355 (2002)].
16. D. La-Orauttapond, B. Noheda, Z.-G. Ye, *et al.*, Phys. Rev. B **65**, 144101 (2002).
17. Ya. B. Bogosova, G. M. Konstantinov, and M. F. Kupriyanov, Izv. Akad. Nauk, Ser. Fiz. **57** (6), 89 (1993).
18. A. Ya. Dantsiger, O. N. Razumovskaya, L. A. Reznichenko, L. D. Gridnev, R. U. Devlikanova, S. I. Dudkina, S. V. Gavrilyachenko, N. V. Dergunova, and A. N. Klevtsov, *Efficient Piezoelectric Ceramic Materials: A Handbook* (AO "Kniga," Rostov-on-Don, 1994) [in Russian].
19. W. Dmowski, T. Egami, L. Farber, *et al.*, AIP Conf. Proc. **582**, 33 (2001).
20. A. V. Turik, M. F. Kupriyanov, E. N. Sidorenko, and S. M. Zaĭtsev, Zh. Tekh. Fiz. **50**, 2146 (1980) [Sov. Phys. Tech. Phys. **25**, 1251 (1980)].
21. V. Ya. Anosov, M. I. Ozerova, and Yu. Ya. Fialkov, *Grounds of Physicochemical Analysis* (Nauka, Moscow, 1976) [in Russian].
22. V. P. Sakhnenko, N. V. Dergunova, and L. A. Reznichenko, *Energy Crystal Chemistry of Solid Solutions of Compounds with Oxygen-Occupied Octahedra and Simulation of Piezoelectric Ceramic Materials* (Rostov. Ped. Univ., Rostov-on-Don, 1999) [in Russian].
23. G. B. Bokiĭ, *Crystal Chemistry* (Nauka, Moscow, 1971) [in Russian].
24. L. D. Landau and E. M. Lifshitz, *Course of Theoretical Physics*, Vol. 5: *Statistical Physics* (Nauka, Moscow, 1976; Pergamon, Oxford, 1980).
25. S. V. Titov, L. A. Shilkina, L. A. Reznichenko, *et al.*, Pis'ma Zh. Tekh. Fiz. **26** (18), 9 (2000) [Tech. Phys. Lett. **26**, 810 (2000)].
26. E. M. Kuznetsova, L. A. Reznichenko, and I. P. Raevskiĭ, in *Proceedings of the International Symposium "Ordering in Minerals and Alloys" (OMA-2000), Rostov-on-Don, 2000*, pp. 59–67.

Translated by K. Shakhlevich

Technical Physics, Vol. 50, No. 9, 2005, pp. 1178–1181. Translated from Zhurnal Tekhnicheskoĭ Fiziki, Vol. 75, No. 9, 2005, pp. 71–75.

SOLID-STATE ELECTRONICS

Thermal Expansion and Thermal Conductivity of Single-Crystal $Cu_xAg_{1-x}InS_2$ Solid Solutions Grown by the Moving Solvent Method

I. V. Bodnar and L. V. Yasyukevich

Belarussian State University of Information Science and Radio Engineering, ul. Brovki 17, Minsk, 220072 Belarus

e-mail: chemzav@gw.bsuir.unibel.by

Received October 13, 2004

Abstract—Single crystals of $Cu_xAg_{1-x}InS_2$ solid solutions are grown by the moving solvent method. The compositions and structures of the single crystals are determined. The thermal expansion coefficients of these crystals are determined with a dilatometer. The thermal expansion coefficients are found to vary linearly with concentration *x*. The thermal conductivity of the crystals is measured by the absolute method, and the concentration dependence of the thermal conductivity is constructed. This dependence is shown to have a minimum near the equimolar composition. © *2005 Pleiades Publishing, Inc.*

INTRODUCTION

$CuInS_2$ and $AgInS_2$ belong to I–III–VI_2 ternary semiconductor compounds, most of which crystallize into the chalcopyrite structure. These compounds have a high absorption coefficient ($\alpha \geq 10^4$ cm^{-1}) and show direct interband transitions, which makes them promising for light-emitting diodes generating linearly polarized radiation, optical filters, and high-efficiency photoelectric converters [1–5]. Solid solutions based on these compounds are also of practical interest, since their physical parameters can be smoothly varied. Earlier [6, 7], we studied the physicochemical properties of such materials.

In this work, we pioneer the study of the thermal expansion and thermal conductivity of single-crystal $CuInS_2$ and $AgInS_2$ ternary compounds, as well as of $Cu_xAg_{1-x}InS_2$ solid solutions, grown by the moving solvent method.

EXPERIMENTAL

$CuInS_2$ and $AgInS_2$ compounds and $Cu_xAg_{1-x}InS_2$ solid solutions were presynthesized by the horizontal two-temperature method from pure elements (copper, silver, V4 indium, and extra-pure grade sulfur additionally purified by multiple sublimation) [7].

The ingots synthesized were used to grow single crystals. To this end, they were powdered and loaded into graphitized quartz ampoules with an inner diameter of 10–12 mm. Metallic indium (1.5–2.0 g), which was used as a solvent, was placed at the bottom of the ampoules. Upon evacuation, the ampoule was placed in a vertical resistance furnace with three independent heating zones. The temperature of the upper zone was maintained at 1150–1200 K; that of the annealing zone, at 1020–1050 K. The ampoule with the melt was held in the furnace for 24 h and then was lowered through the solidification front to the bottom zone with a velocity of 0.18–0.26 mm/h at a temperature gradient of ≈30 K/cm. After homogenizing annealing, the furnace temperature was decreased to 500 K at a rate of ≈5 K/h and the furnace was turned off. The single crystals grown by this method had a diameter of 10–12 mm and a length of up to 50 mm. Their homogeneity was proved by electron probe X-ray microanalysis and X-ray diffraction.

The compositions of the compounds and solid solutions were determined by electron microprobe analysis with a JEOL electron probe X-ray microanalyzer. The results are listed in the table. The calculated values are seen to agree well with the experimental data.

The equilibrium state of the compounds and the homogeneity of the solid solutions were checked by X-ray diffraction. X-ray diffraction patterns were recorded with a DRON-3M diffractometer (CuK_α radiation) using a nickel filter. The samples for X-ray diffraction analysis were prepared by grinding the crystals with subsequent pressing the powders into a special holder. To relieve grinding-induced mechanical stresses, the powders were annealed at 650 K for 3 h.

RESULTS AND DISCUSSION

Our studies show that both the $CuInS_2$ and $AgInS_2$ ternary compounds and their related solid solutions crystallize into the chalcopyrite structure and that the crystals grown are homogeneous (as indicated by the fact that high-angle lines in the X-ray diffraction pat-

Data of electron probe X-ray analysis for the $CuInS_2$ and $AgInS_2$ ternary compounds and $Cu_xAg_{1-x}InS_2$ solid solutions

x	Cu, wt %		Ag, wt %		In, wt %		S, wt %	
	calculation	experiment	calculation	experiment	calculation	experiment	calculation	experiment
0.0	–	–	37.61	37.84	40.03	39.67	22.36	22.06
0.2	4.57	4.48	31.05	31.20	41.31	41.50	23.07	22.82
0.4	9.45	9.50	24.05	23.93	42.67	42.79	23.83	23.78
0.6	14.65	14.57	16.58	16.49	44.12	44.22	24.65	24.72
0.8	20.22	20.30	8.58	8.46	45.68	45.77	25.52	25.47
1.0	26.20	26.15	–	–	47.35	47.80	26.45	26.05

terns are resolved). The lattice parameters calculated by the least squares method are the following: $a = 5.523 \pm 0.002$ Å and $c = 11.125 \pm 0.005$ Å for $CuInS_2$ and $a = 5.879 \pm 0.002$ Å and $c = 11.204 \pm 0.005$ Å for $AgInS_2$. These values are consistent with the data obtained by other methods [8, 9]. These parameters vary linearly with copper concentration x (in accordance with Vegard's law), obeying the relationships

$$a = 5.523 + 0.356x,$$

$$c = 11.125 + 0.079x.$$

We measured the thermal expansion of the $CuInS_2$ and $AgInS_2$ ternary compounds and their solid solu-

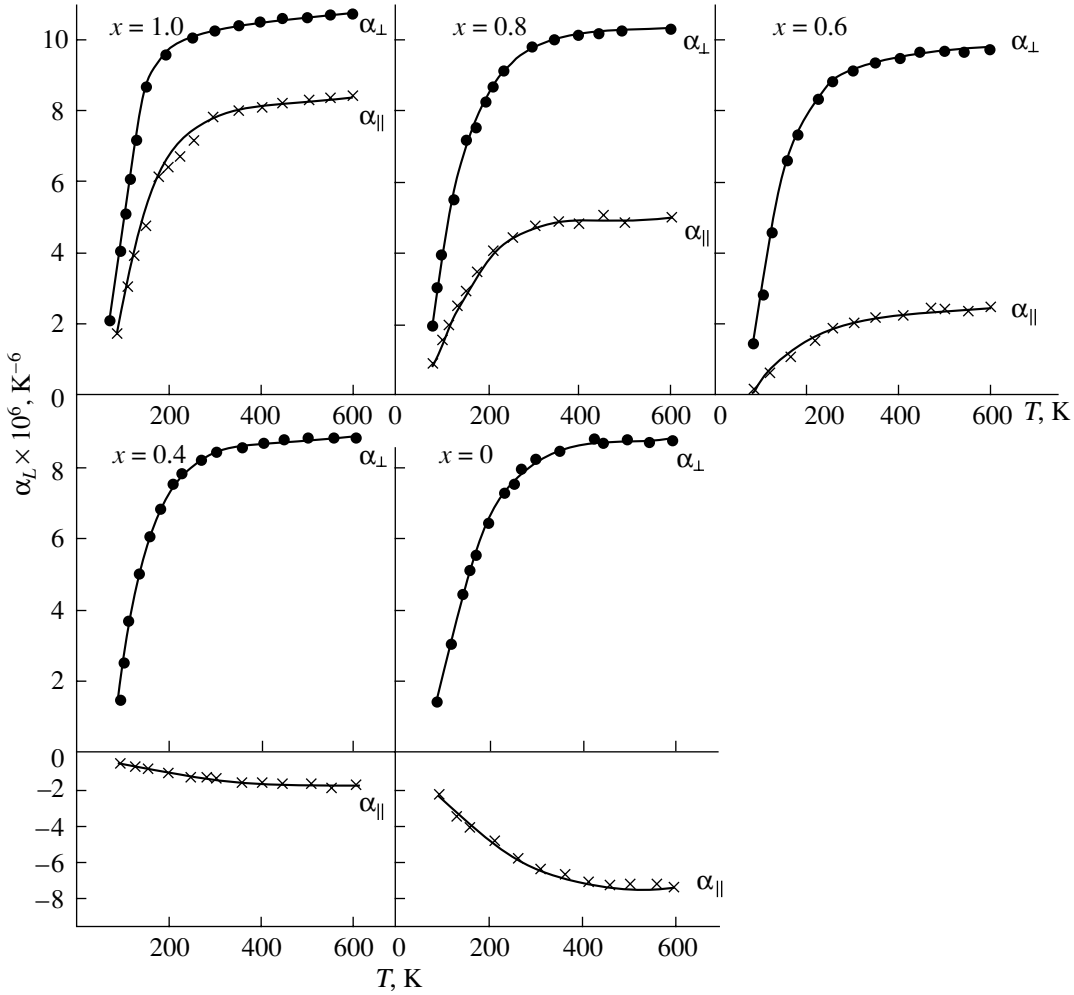

Fig. 1. Temperature dependences of thermal expansion coefficients α_L for the $CuInS_2$ and $AgInS_2$ compounds and $Cu_xAg_{1-x}InS_2$ solid solutions.

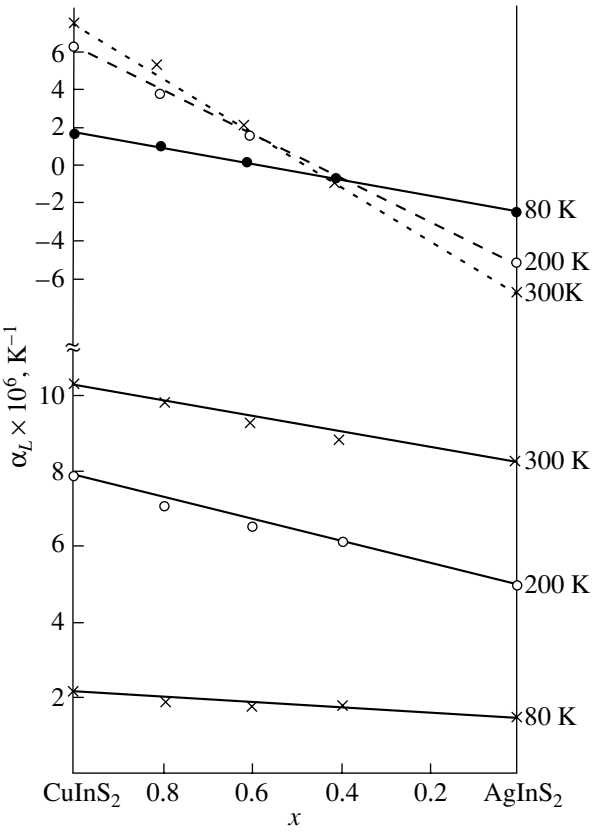

Fig. 2. Concentration dependences of the thermal expansion coefficient for the $Cu_xAg_{1-x}InS_2$ solid solutions.

tions, using a quartz dilatometer, in which the thermal expansion of solids is measured with respect to that of quartz [10]. Before measurements, the device was evacuated and filled with an inert gas to prevent the decomposition and oxidation of the sample. The temperature was measured by a Chromel–Alumel thermocouple with an accuracy of 5%. The samples were heated with a low rate, ≈5 K/min, to ensure reliable results. The temperature dependences of elongation $\Delta l/l_0$ of the materials were taken from single-crystal platelets measuring $10 \times 4 \times 3$ mm and oriented parallel ($\alpha_\parallel$) and perpendicular ($\alpha_\perp$) to their principal axes.

The thermal expansion coefficient (TEC) was calculated by the formula

$$\alpha = \frac{l}{l_0}\frac{dl}{dT}, \qquad (1)$$

where l_0 is the sample initial length and dl/dT is the change in the sample length upon heating by 1 K.

Figure 1 shows the temperature dependences of thermal expansion coefficients α_L for the $CuInS_2$ and $AgInS_2$ compounds and $Cu_xAg_{1-x}InS_2$ solid solutions. It follows from Fig. 1 that the thermal expansion of both the compounds and solid solutions is anisotropic: $\alpha_\parallel \ll \alpha_\perp$. In the $CuInS_2$ compound and solid solutions with $x > 0.5$, both thermal expansion coefficients are positive, while in $AgInS_2$ and the solid solutions with $x < 0.5$, $\alpha_\perp$ is positive and $\alpha_\parallel$ is negative. Also, the absolute values of both thermal expansion coefficients increase linearly with temperature in the range 80–300 K. Above 300 K, the rate of their increase slows down and the coefficients depend on temperature only weakly. Such a temperature dependence of the thermal expansion coefficients is also characteristic of other I–III–VI_2 compounds and their related solid solutions [11–13].

The concentration dependences of linear thermal expansion coefficients $\alpha_\perp$ and $\alpha_\parallel$ for various temperatures are shown in Fig. 2. It is seen that these coefficients increase linearly with x. The discrepancy between our results and the data in [14] is likely to be due to different techniques used to measure the thermal expansion parameters. For example, in [14], the thermal expansion was measured by the X-ray diffraction method. However, it was noted [10] that the X-ray diffraction and dilatometric methods of TEC determination give physically different results. The former method gives the TEC of a crystal structure, while the dilatometric method gives the TEC of a material. This argument can explain the difference in the concentration behavior of $\alpha_\parallel$ and $\alpha_\perp$.

Thermal conductivity χ of the compounds and solid solutions were measured by the absolute stationary method [15] in a temperature range of 300–550 K using the samples with the same dimensions as above. The measurement accuracy was ≈6%. In this method, the amount of heat having passed through a sample is determined from the power of a furnace heater, $W = IV$, and the thermal conductivity is calculated by the formula

$$\chi = Wl/S\Delta T, \qquad (2)$$

where l is the distance between the thermocouples, S is the cross-sectional area of the sample, and ΔT is the temperature gradient.

Figure 3 shows the temperature dependences of the thermal conductivities of the $CuInS_2$ and $AgInS_2$ compounds and $Cu_xAg_{1-x}InS_2$ solid solutions. The thermal conductivity measured is due basically to the lattice component, since its electronic component calculated by the Wiedemann–Franz relationship does not exceed 1% of the value measured.

For the $CuInS_2$ and $AgInS_2$ compounds, the thermal conductivity in the temperature range 300–400 K is described by the dependence of type T^{-1}, which is characteristic of three-phonon scattering. This result agrees with the Peierls theory, according to which χ is inversely proportional to temperature at temperatures above the Debye temperature. In this case, we are dealing with phonon–phonon scattering, when three phonons exchange energy between each other (three-phonon processes). As a result, one phonon disappears

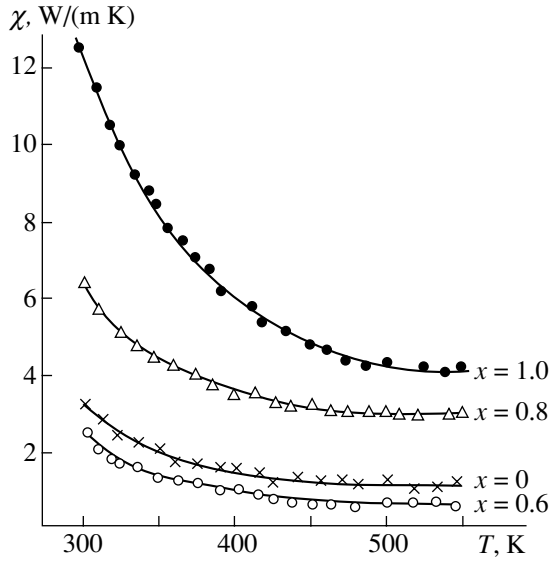

Fig. 3. Temperature dependences of the thermal conductivity for the $CuInS_2$ and $AgInS_2$ compounds and $Cu_xAg_{1-x}InS_2$ solid solutions.

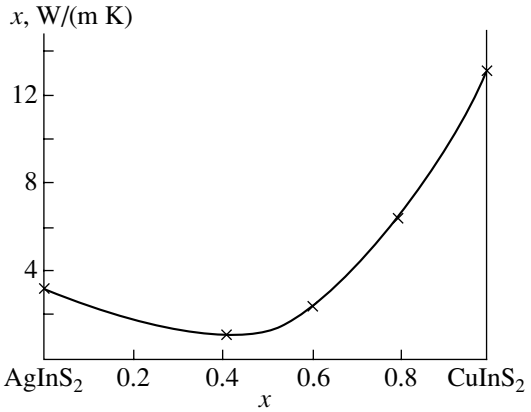

Fig. 4. Concentration dependence of the thermal conductivity for the $Cu_xAg_{1-x}InS_2$ solid solutions.

and two new phonons appear or two phonons disappear and one new phonon arises. At higher temperatures, χ varies as T^{-n} $(0 < n < 1)$, which means that scattering by impurities and lattice defects dominates. In the $Cu_xAg_{1-x}InS_2$ solid solutions, the power-type dependence $\chi \sim T^{-n}$ is observed throughout the temperature range studied; hence, the basic scattering mechanism is scattering by lattice defects. Accordingly, the temperature dependence of χ is weak.

Figure 4 shows the concentration dependence of the thermal conductivity for the $Cu_xAg_{1-x}InS_2$ solid solutions. This curve has a minimum near the equimolar composition. The considerable decrease in χ of the solid solutions compared with that of the initial compounds is due to breaking of the lattice periodicity in the solid solutions because of the random distribution of atoms over equivalent sites. In solids, dissimilar atoms, though occupying regular lattice positions (sites), are disordered. Because of this, the atomic weights and force constants vary randomly from site to site, causing phonon scattering. Therefore, solid solutions can be viewed as intermediates between the crystalline state (the crystal lattice persists) and the amorphous state (the disordered arrangement of atoms). For solid solutions, the degree of disorder is maximal at the equimolar composition; accordingly, their thermal conductivity near this composition is minimal.

CONCLUSIONS

Using the moving solvent method, we grew single-crystal $Cu_xAg_{1-x}InS_2$ solid solutions, determined their compositions and crystal structure, and measured their thermal expansion coefficients and thermal conductivities. For the solid solutions with $x > 0.5$, both thermal expansion coefficients ($\alpha_\parallel$ and $\alpha_\perp$) are found to be positive, whereas for $AgInS_2$ and the solid solutions with $x < 0.5$, $\alpha_\perp$ is positive and $\alpha_\parallel$ is negative. The TEC varies linearly with concentration x, and the thermal conductivity has a minimum at the near-equimolar composition.

REFERENCES

1. N. A. Goryunova, *Compound Diamond-Like Semiconductors* (Sov. Radio, Moscow, 1968) [in Russian].
2. Yu. V. Rud' and Z. A. Parimbekov, Zh. Tekh. Fiz. **54**, 2253 (1984) [Sov. Phys. Tech. Phys. **29**, 1320 (1984)].
3. Yu. V. Rud' and Z. A. Parimbekov, Fiz. Tekh. Poluprovodn. (Leningrad) **17**, 281 (1983) [Sov. Phys. Semicond. **17**, 178 (1983)].
4. K. W. Mitchell, Annu. Rev. Mater. Sci. **12**, 401 (1982).
5. *Current Topics in Photovoltaics*, Ed. by T. Coutts and J. Meakin (Academic, London, 1985; Mir, Moscow, 1988).
6. I. V. Bodnar, B. V. Korzun, and L. V. Yashukevich, J. Mater. Sci. **33**, 183 (1998).
7. I. V. Bodnar, Neorg. Mater. **34**, 16 (1998).
8. G. S. C. Abrahams and J. L. Bernstein, J. Chem. Phys. **59**, 5415 (1973).
9. I. V. Bodnar, N. S. Orlova, and I. N. Tsyrel'chuk, Neorg. Mater. **31**, 899 (1995).
10. S. I. Novikova, *Thermal Expansion of Solids: A Handbook* (Nauka, Moscow, 1974) [in Russian].
11. I. V. Bodnar, Fiz. Tekh. Poluprovodn. (St. Petersburg) **37**, 1285 (2003) [Semiconductors **37**, 1247 (2003)].
12. I. V. Bodnar, Izv. Akad. Nauk SSSR, Ser. Neorg. Mater. **17**, 583 (1981).
13. I. V. Bodnar and B. V. Korzun, Mater. Res. Bull. **18**, 519 (1983).
14. N. S. Orlova and I. V. Bodnar, Neorg. Mater. **37**, 1084 (2001).
15. A. S. Okhotin, A. S. Pushkarskiĭ, and V. V. Gorbachev, *Thermal Physical Properties of Semiconductors* (Atomizdat, Moscow, 1972) [in Russian].

Translated by K. Shakhlevich

Technical Physics, Vol. 50, No. 9, 2005, pp. 1182–1185. Translated from Zhurnal Tekhnicheskoĭ Fiziki, Vol. 75, No. 9, 2005, pp. 76–79.

**OPTICS,
QUANTUM ELECTRONICS**

Aberration-Free Lateral Shear Holographic Interferometry

A. M. Lyalikov

Kupala State University, Grodno, 230023 Belarus

e-mail: lyalikov@inbox.ru

Received September 10, 2003; in final form, December 27, 2004

Abstract—Lateral shear interferometry is considered as a possible means for optical correction of wave fronts reconstructed from singly and doubly exposed holograms. Optical aberrations are eliminated in a moiré pattern by superposing two lateral shear interferograms using waves diffracted by original holograms. It is shown that the singly exposed hologram allows compensation for only optical inhomogeneities due to the substrate, while the doubly exposed hologram also excludes aberrations due to the recording system. The experimental results supporting the efficiency of the method as applied to imperfect substrates of holograms are presented. © *2005 Pleiades Publishing, Inc.*

INTRODUCTION

Wave fronts reconstructed from a hologram can be studied by a variety of optical methods [1, 2]. Using the same hologram of an object studied, one can obtain two-beam interferograms, shear interferograms with arbitrary parameters of fringes, and various shadow patterns. This considerably extends the body of information on the object. While the correction of aberrations due to a recording system (optical aberrations) and compensation for substrate inhomogeneities pose no difficulties for two-beam interferometry [1], they present a serious challenge for shear interferometry and shadow techniques. The reason is that the formation of a shear interferogram, as well as of a shadow pattern, usually involves only one wave reconstructed from the hologram. To date, a number of methods have been suggested for partial [3–5] and complete [6, 7] compensation for aberrations of either type in shadow patterns. However, complete compensation for optical distortions in shear interferograms requires that at least a pair of holograms and an interfacing optical system be used [6, 8], which considerably complicates the experiment.

Shear interferometry, its both conventional and holographic techniques, enjoys today wide application in various fields of science and engineering [9–13].

In this study, we propose methods of correcting substrate distortions and optical aberrations in lateral shear interferograms formed by wave fronts reconstructed from holograms. These methods considerably extend the potential of lateral shear holographic interferometry as applied to holograms on imperfect substrates and loosen requirements for the aberration characteristics of optical systems.

Let us assume that a wave front having passed through a phase object is holographically recorded. Let us consider how shear interferograms free of optical distortions can be obtained using singly and doubly exposed holograms.

EXPERIMENTAL

Figure 1 shows the optical scheme used to obtain aberration-free lateral shear interferograms using both singly and doubly exposed holograms. Hologram *1* is illuminated by a collimated He–Ne laser beam. Diaphragm *3* placed in the second focal plane of objective *2* separates out the reconstructed wave. Objective *4* collimates the reconstructed wave and directs it to four-mirror lateral shear interferometer *5*. The design of the interferometer allows for variation both of the fringe spatial frequency and of the lateral shear of the interferograms recorded in plane *6*. The record plane was optically interfaced with hologram *1* by objectives *2* and *4*.

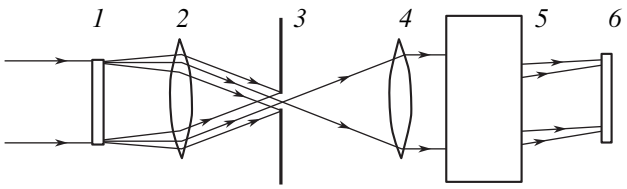

Fig. 1. Optical scheme for obtaining aberration-free lateral shear interferograms.

1063-7842/05/5009-1182$26.00

SINGLY EXPOSED HOLOGRAM

The amplitude transmission of a singly exposed hologram recorded under linear conditions [2] for the fringes perpendicular to the x axis has the form

$$\tau_1 \sim 1 + \cos[2\pi\xi_n x + \varepsilon + \varphi]. \quad (1)$$

Here, ξ_n is the spatial frequency of the holographic pattern ($\xi_n = 1/T$, where T is the spatial period of the holographic pattern), ε is the phase distortion due to optical aberrations, and φ is the phase shift induced by the object.

Assume that singly exposed hologram (1) is illuminated by a collimated beam so that the wave reconstructed normally to the hologram in the first diffraction order is expressed as

$$A_1 = a_1 \exp[i(\chi + \varepsilon + \varphi)], \quad (2)$$

where χ is the phase distortion inserted by optical inhomogeneities of the hologram substrate.

It is seen from Eq. (2) that the wave front includes not only the valid signal described by function φ but also distortion ($\chi + \varepsilon$) associated with substrate inhomogeneities and optical aberrations. Wave (2), separated out by diaphragm (*3*) (Fig. 1), enters lateral shear interferometer *5*. In our method of correction, the interferogram to be recorded in plane *6* must be adjusted to the spatial frequency of the resulting fringes. This can be achieved by specifying not only a shift between the interfering beams but also the angle defining the spatial frequency of the fringes. In this case, the intensity distribution in a shear interferogram appears as

$$I_1 \sim 1 + \cos[2\pi\xi_1 x + \Delta\chi + \Delta\varepsilon + \Delta\varphi], \quad (3)$$

where ξ_1 is the spatial frequency of the fringes, $\Delta\chi = \chi - \chi'$, $\Delta\varepsilon = \varepsilon - \varepsilon'$, and $\Delta\varphi = \varphi - \varphi'$. The primed functions describe changes in the wave front of one wave shifted with respect to the other in recording a lateral shear interferogram. The signal detected is distorted by substrate inhomogeneities $\Delta\chi$ and optical aberrations $\Delta\varepsilon$.

In the case of a singly exposed hologram, only substrate-related distortions can be eliminated. To do this, along with interferogram (3), one should record, in the same interferometer, another shear interferogram with the same shift and also adjusted to the resulting fringe pattern; however, in the latter case, the interferogram is obtained using the wave transmitted through hologram (1) in the forward direction (i.e., the diffracted wave of the zero order). The wave front of such a wave is deformed by only substrate inhomogeneities, and its complex amplitude is

$$A_0 = a_0 \exp(i\chi), \quad (4)$$

where a_0 is the real amplitude of the wave transmitted in the forward direction.

In this case, the intensity distribution in a shear interferogram is given by

$$I_0 \sim 1 + \cos[2\pi\xi_1 x + \Delta\chi]. \quad (5)$$

Distortions introduced by inhomogeneities in the substrate of hologram (1) can be eliminated by successively recording two lateral shear interferograms (3) and (5) either on one mutual substrate or on two different substrates. In the latter case, the chemically treated substrates are aligned exactly.

Although the moiré pattern is obtained, in the former case, by adding and, in the latter, by multiplying the amplitude transmissions of the high-frequency structures of the interferogram, it is the same in both cases [14, 15]. To increase the visibility of the moiré pattern, filtering of the spatial frequencies can be applied. Usually, the diaphragm placed in the second focal plane of the objective cuts out the first diffraction order from the light transmitted through superposed shear interferograms. It can be demonstrated [14, 15] that, in both cases considered above, the moiré patters is described by the expression

$$I_{10} \sim 1 + \cos[\Delta\varepsilon + \Delta\varphi]. \quad (6)$$

Moiré pattern (6) is free of the distortions associated with the substrate of hologram (1). However, optical aberrations cannot be eliminated by using a singly exposed hologram.

DOUBLY EXPOSED HOLOGRAM

In order to compensate for the distortions related to optical aberrations when holograms are recorded on a mutual substrate, the hologram should be exposed twice: with and without the object. At the second exposure, carrier frequency ξ_m must be so much different from the frequency at the first exposure, ξ_n, that beam separation by diaphragm *3* during the subsequent reconstruction of the wave fronts (Fig. 1) will be reliable. The amplitude transmission of a doubly exposed hologram under the linear recording conditions has the form

$$\tau_2 \sim 2 + \cos[2\pi\xi_n x + \varepsilon + \varphi] + \cos[2\pi\xi_m x + \varepsilon]. \quad (7)$$

Here, unlike the case of the singly exposed hologram, both substrate-related distortions and optical aberrations can be compensated for. Now, the wave diffracted by the second holographic structure of doubly exposed hologram (7) in the first order is used for recording the second shear interferogram. The complex amplitude of this wave is

$$A_2 = a_2 \exp[i(\chi + \varepsilon)], \quad (8)$$

where a_2 is the real amplitude.

Fig. 2. Lateral shear interferogram visualizing optical inhomogeneities in the substrates of the initial doubly exposed hologram (adjustment to an infinitely wide fringe).

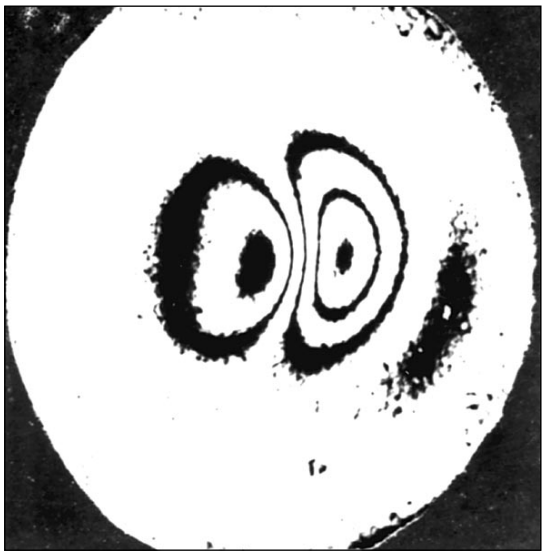

Fig. 3. Moiré pattern of the lateral shear interferogram for the polymethylmethacrylate sample with substrate inhomogeneities and optical aberrations eliminated.

In this case, the intensity distribution in the lateral shear interferogram is

$$I_2 \sim 1 + \cos[2\pi\xi_1 x + \Delta\chi + \Delta\varepsilon]. \quad (9)$$

The procedure of optical correction here is the same as that for the singly exposed hologram; i.e., the resulting shear interferograms can be recorded either on two separate substrates with subsequent alignment or on a mutual doubly exposed substrate. However, in contrast to (6), the moiré pattern is described by the slightly different expression

$$I_{12} \sim 1 + \cos[\Delta\varphi], \quad (10)$$

which contains neither substrate inhomogeneities nor optical aberrations.

With doubly exposed holograms, one can obtain shear interferograms of an object with complete compensation for both optical aberrations and inhomogeneities of the holographic substrate. However, this version of lateral shear holographic interferometry, which requires double exposure and a change in the carrier frequency, is generally more laborious than that using single-exposure recording. Therefore, it is preferable if the amount of optical aberrations is comparable to the valid signal.

EXPERIMENTAL RESULTS

The optical correction technique proposed was verified in studying melting zones of heat-treated planar polymethylmethacrylate samples. A doubly exposed (before and after the treatment) hologram was recorded with a Mach–Zehnder interferometer on an FG-690 holographic film. The diameter of the field of observation was 26 mm. The wave aberrations of the recording system were ~0.3λ. When recording the doubly exposed hologram, the carrier frequency was varied by rotating the reference beam between the exposures.

Following the above procedure, a lateral shear interferogram was recorded on a mutual substrate with the use of the wave fronts reconstructed from the doubly exposed hologram. The lateral shear of interfering wave fronts in a four-mirror shear interferometer was set equal to 3.0 mm. Figure 2 shows the shear interferogram adjusted to an infinitely wide fringe (the lateral shear is 3.0 mm), which visualizes optical inhomogeneities in the substrate of the initial doubly exposed hologram. The low quality of the film is evident. Figure 3 is the moiré pattern obtained by illuminating the doubly exposed hologram, where both the distortions due to the substrate and optical distortions are eliminated. To improve the visibility of the fringe pattern, spatial frequency filtering (separation of the first diffraction order) was applied. The moiré pattern shown in Fig. 3 visualizes the behavior of function $\Delta\varphi$ with substrate inhomogeneities and optical aberrations eliminated.

CONCLUSIONS

The aberration-free version of lateral shear holographic interferometry may provide a high measurement accuracy in studying phase objects using holograms on low-grade substrates and inexpensive optics.

REFERENCES

1. *Holographie Optique: Developpements–Applications*, J. Vienot, Ch. Smigielski, and H. Royer (Dunod, Paris, 1971; Mir, Moscow, 1973) (translated from French).
2. A. K. Beketova, A. F. Belozerov, A. N. Berezkin, *et al.*, *Holographic Interferometry of Phase Objects* (Nauka, Leningrad, 1979) [in Russian].
3. J. W. Goodman, *Introduction to Fourier Optics* (McGraw-Hill, New York, 1968; Mir, Moscow, 1970).
4. N. M. Spornik, Opt. Mekh. Prom-st, No. 1, 74 (1976).
5. I. S. Zeĭlikovich and A. M. Lyalikov, Opt. Spektrosk. **68**, 197 (1990) [Opt. Spectrosc. **68**, 112 (1990)].
6. N. M. Spornik, A. F. Belozerov, and A. I. Byval'tsev, USSR Inventor's Certificate No. 39654, Byull. Izobret., No. 36 (1973).
7. A. M. Lyalikov, Opt. Spektrosk. **75**, 161 (1993) [Opt. Spectrosc. **75**, 96 (1993)].
8. A. F. Tuev, Opt. Zh., No. 4, 75 (1993).
9. P. V. Ivanov, A. V. Koryabin, and V. I. Shmal'gauzen, Kvantovaya Élektron. (Moscow) **27**, 78 (1999).
10. J. Schwider, Optik (Germany) **108** (4), 181 (1998).
11. V. I. Sokolov, Kvantovaya Élektron. (Moscow) **31**, 891 (2001).
12. V. G. Gusev, Opt. Zh., No. 4, 3 (1992).
13. V. G. Gusev, Opt. Zh., No. 11, 48 (1997).
14. *Holographic Nondestructive Testing*, Ed. by R. K. Erf (Academic, New York, 1974; Mashinostroenie, Moscow, 1979).
15. C. M. Vest, *Holographic Interferometry* (Wiley, New York, 1979; Mir, Moscow, 1982).

Translated by A. Sidorova

Technical Physics, Vol. 50, No. 9, 2005, pp. 1186–1190. Translated from Zhurnal Tekhnicheskoĭ Fiziki, Vol. 75, No. 9, 2005, pp. 80–84.

OPTICS, QUANTUM ELECTRONICS

Lasing from an Electron-Beam-Excited Nonchain HF Laser

N. G. Ivanov and V. F. Losev

Institute of High-Current Electronics, Siberian Division, Russian Academy of Sciences, Akademicheskiĭ pr. 4, Tomsk, 634055 Russia

e-mail: losev@ogl.hcei.tsc.ru

Received October 20, 2004

Abstract—The lasing parameters of a nonchain chemical HF laser (an active volume of 20 l) excited by a fast electron beam are studied at different energies delivered to the gas. It is shown that the laser operates efficiently when the energy deposited is below 30 J/l. Above specific excitation energies of 60–70 J/l, both the lasing efficiency and the laser output decrease. © *2005 Pleiades Publishing, Inc.*

INTRODUCTION

Nonchain chemical HF/DF lasers are highly efficient coherent sources radiating in the near-IR range (λ = 2.6–5.0 μm). Owing to the many-lined spectrum of laser radiation, which covers the absorption spectra of many human-activity-related environmental pollutants, such lasers are indispensable radiation sources for environmental protection and monitoring systems.

Chemical nonchain lasers are usually pumped by an electric discharge or a fast electron beam. The latter approach is the most promising for exciting high-energy (>100 J) lasers. The standard working mixture for HF lasers consists of SF_6 and H_2 gases [1, 2]. The former is an electronegative gas with a large cross section of plasma electron attachment to molecules. In [3, 4], an anomalous propagation of an electron beam through mixtures containing electronegative gases was discovered. The main anomaly was that electrons penetrated into an electronegative gas to a depth considerably smaller than their extrapolated range; in other words, the beam was "blocked." The anomalous behavior of the electron beam energy deposited into SF_6 was demonstrated in [5]. It was found that the excitation area was smaller than predicted when the SF_6 pressure exceeded 5.5×10^4 Pa. Based on the calculation, it was supposed that such anomalous behavior of the energy may be due to a large amount of the space charge, which forms in the plasma because of its low conductivity. As a result, the electron beam behaves as if it were confined by the space charge field, since a major fraction of the electron beam energy is spent on work against this field.

If such an uncommon situation occurs in the working mixture of a chemical laser, its performance may be adversely affected. An F_2–O_2–H_2–SF_6 chain chemical laser excited by a microsecond electron beam with a maximum electron energy in the diode of 450 keV was studied in [6]. The conditions under which the confinement of an electron beam had an influence on lasing were determined. It was shown that the lasing energy was no longer a linear function of specific excitation energy E at $E > 50$ J/l. The shrinkage of the lasing range in the H_2–SF_6 mixture was observed when the mixture density exceeded 3.5 g/l.

A different situation was observed in [7, 8], where the excitation of the H_2–SF_6 mixture by a radially convergent electron beam resulted in a high lasing efficiency (≈10%) and the role of the space charge was considered to be insignificant [8].

Since the data concerning the presence of the space charge and its influence on the HF laser performance are contradictory, it is of interest to investigate this type of laser in more detail. In this work, we study the energy and time parameters of a nonchain HF laser versus the pumping electron beam energy density in order to see whether there is an anomaly in the lasing parameters and search for optimal conditions of excitation.

EXPERIMENTAL

The experimental setup was similar to that used previously for excitation of a XeCl laser [9]. It includes a laser chamber, two vacuum diodes placed on opposite sides of the chamber, and six Arkadyev–Marx generators. The diodes with explosive-emission graphite cathodes were fed by three parallel-connected generators containing ten stages each (the capacity per stage is 0.1 μF). The charging voltage of the generators was 80 kV. The diodes generated 800-ns-wide 40-kA current pulses with an electron energy of 450 keV. The pulsed electron beams of cross-sectional area 13 × 150 μm generated by the diodes were injected into the laser chamber through 50-μm-thick titanium foil or a Lavsan film[1] covering a metallic grid, which served as the anode of the diodes. The oppositely placed foils in the laser chamber were 12 cm apart. The chamber was a cylinder of capacity 60 l. A cavity was formed by the

[1] Russian equivalent of Dacron.

1063-7842/05/5009-1186$26.00 © 2005 Pleiades Publishing, Inc.

TlBr windows of the laser chamber, which were 20 cm in diameter and had a transmission of 75% in the 2.5–3.0 μm range, and a plane external aluminum mirror. An $H_2 + SF_6$ gas mixture at a pressure between 0.3 and 1.0 atm served as the lasing medium.

The pump energy (power) density used to excite the laser was varied. This was done in three ways. First, the energy delivered to the gas substantially depended on the absorbent material. For example, substitution of the Lavsan film for titanium foil raised the energy deposit by about half as much again. Second, one or two diodes were used for excitation. In this case, the pump energy increased roughly twofold. Finally, the pump energy density rose twofold when the pressure of the gas mixture was varied from 0.3 to 1.0 atm.

The laser energy density distribution over the beam's cross section was measured with an IKT-1N calorimeter; the laser output, with a set of coupled TPI2-7 calorimeters with a total surface area of 24 × 24 cm. The waveform of laser shots was recorded by an S8-14 oscilloscope using an FSG-22 photoresistor. The electron beam energy deposited into the gas was estimated both theoretically and experimentally by the method of pressure jump in the SF_6 gas. A 6MD-Kh1B mechanotron served as a pressure sensor, and its signal was applied to the oscilloscope. The energy deposit was calculated by the Monte Carlo method under the assumption that the space charge field in the plasma does not influence the electron beam. The lasing parameters were determined at the first shot in a fresh gas mixture, since at the second shot the output dropped by a factor of 1.5–2.

EXPERIMENTAL RESULTS

Figure 1 shows the electron beam energy deposited into the gas as a function of the SF_6 pressure for one-side and two-side pumping. As the pressure grows from 0.30 to 0.95 atm, the energy increases approximately twofold and then tends toward saturation. The substitution of the Lavsan film for the titanium foil causes the pump energy to increase by 1.6 times.

First, we optimized the component ratio SF_6/H_2 in the mixture as a function of the gas pressure and the pump energy density. Figure 2 presents the lasing energy density per square centimeter versus the composition of the mixture for one-side excitation. It is seen that, as the component ratio varies in the range $SF_6 : H_2 = (20–100) : 1$, the energy density remains virtually the same both near the foil, where the pump energy density is high, and far away from it (lower energy density). This is true both for 0.5 and 1 atm. It follows that the same component ratio can be used in a wide range of our experimental conditions. Therefore, all the results presented below were obtained for the ratio $SF_6 : H_2 = 50 : 1$.

In the first series of experiments, the electron beam was injected into the laser chamber through the titanium foil. We compared the parameters of laser radiation for one- and two-side excitations. Since the diode parameters were close to each other, switching of the second diode raised the pump energy nearly twofold. The laser output versus the gas pressure in these two cases is depicted in Fig. 3a. For comparison, this figure also shows the pressure dependence of the output (curve *4*) calculated as a sum of the outputs obtained when the beams pump the laser independently. In the pressure range from 0.3 to 0.7 atm, the behavior of the laser output in the two-beam pump mode (curve *3*) is

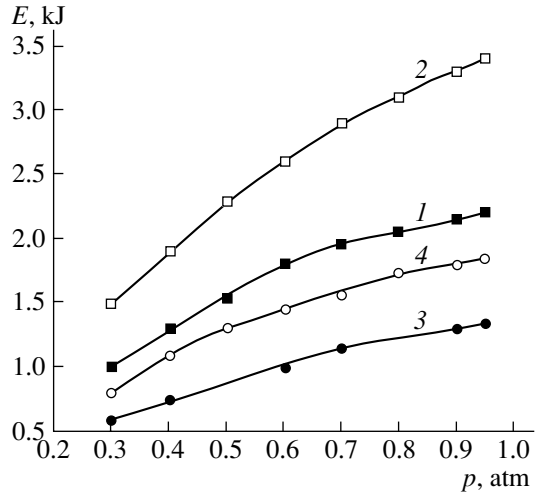

Fig. 1. Pressure dependence of the electron beam energy deposited into the SF_6 gas through (*1*, *3*) titanium foil and (*2*, *4*) Lavsan film in the (*1*, *2*) two-side and (*3*, *4*) one-side pump modes.

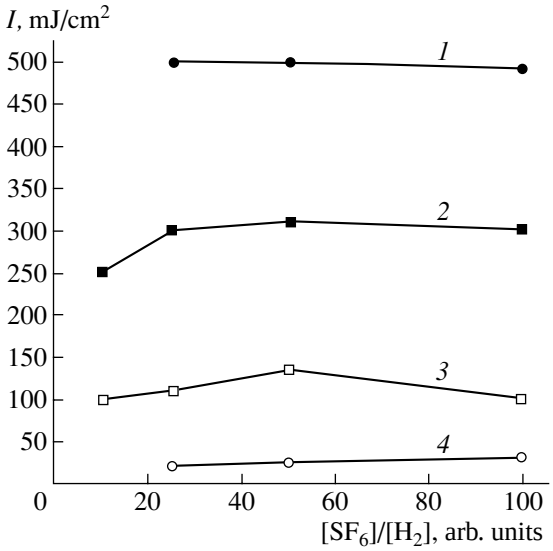

Fig. 2. Laser output density vs. the concentration ratio SF_6/H_2 under one-beam excitation through the titanium foil at a gas pressure of (*2*, *3*) 0.5 and (*1*, *4*) 1 atm. Measurements were made (*1*, *2*) 2 and (*3*, *4*) 10 cm away from the foil.

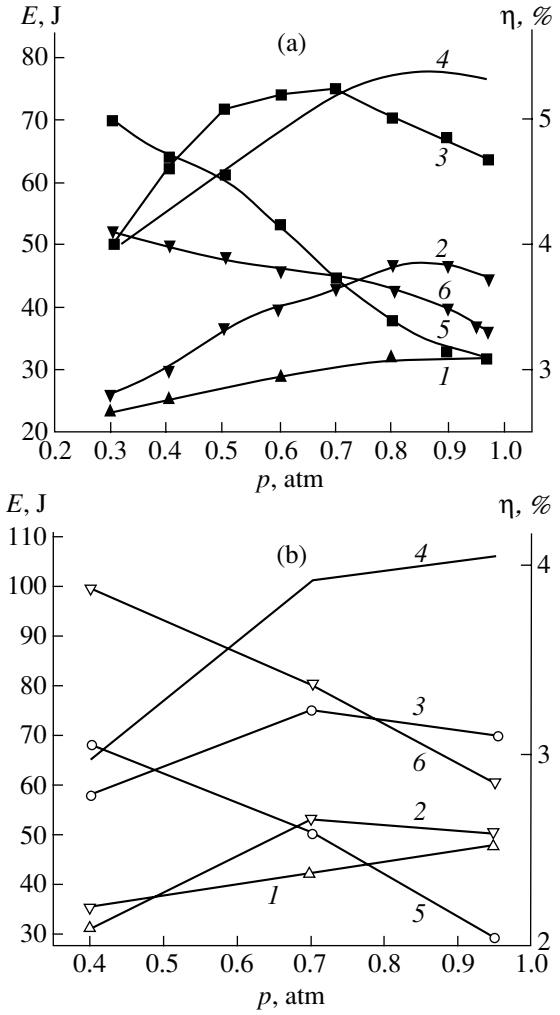

Fig. 3. (*1*–*4*) Laser output and (*5*, *6*) lasing efficiency vs. the pressure of the gas mixture excited through the (a) titanium and (b) Lavsan foils from (*1*) one side, (*2*, *6*) the other side, and (*3*, *5*) both sides simultaneously. (*4*) The sum of curves *1* and *2*.

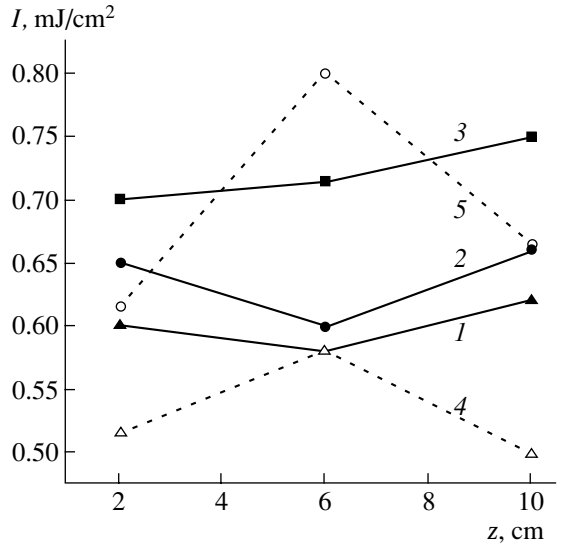

Fig. 4. (*1*–*3*) Laser output density distribution in the two-beam pump mode and (*4*, *5*) the calculated sum of the partial energies for a gas pressure of (*1*, *4*) 0.5, (*2*) 0.9, and (*3*, *5*) 0.7 atm.

seen to be normal. Anomaly appears when the pressure exceeds 0.7 atm (i.e., the energy decreases with pressure). First, the lasing energy (laser output) decreases with the energy deposit up to 1 atm and, second, the lasing energy decreases when the energy of either beam (in the case of independent pumping) rises (curves *1* and *2*).

Of certain interest is the output density distribution over the laser beam section for various pressures. The record of the output radiation on thermosensitive paper (autograph) indicates that the energy distribution is nearly uniform over the 12×12-cm section at 0.5 atm, though several local spots of higher and lower densities are also observed. Raising the pressure to 1 atm lowers the energy density in the central part of the beam (Fig. 4).

The laser output density was measured in both the one- and two-beam pump modes. Figure 4 plots the energy density distribution between the titanium foils for three values of the gas pressure in the two-beam mode. It is evident that the distribution is fairly uniform for all the pressures. The maximal energy density, as well as the total energy, is maximal at 0.7 atm. At pressures of about 0.9 atm, the energy density drops both in the central part of the chamber and near the foils. Thus, the behavior of the laser output density, as well as of the total laser output, at pressures above 0.7 atm can be regarded as anomalous in terms of this paper.

At the second stage of the experiment, when a Lavsan film was used as an energy adsorbent and, correspondingly, the pump level was increased by a factor of 1.6, the amount of the total energy remained almost the same (Fig. 3b). In this case, the estimated sum of two partial energies under separate operation of the diodes exceeds the energy in the two-beam mode throughout the pressure range (from 0.40 to 0.95 atm). In other words, the range of anomaly (an excess of the calculated lasing energy over the experimental value) expands and shifts towards lower pressures.

The lasing efficiency (the output-to-deposited energy ratio) invariably grows as the pumping level decreases (Fig. 3). This was observed both when the gas pressure declined and when the Lavsan film was changed to the titanium foil. The efficiency was maximum (5%) in the two-beam pump mode with the titanium foil at a gas pressure of 0.3 atm. Remarkably, for pressures above 0.7 atm, the lasing efficiency in the one-beam mode with the titanium foil was higher than in the two-beam mode.

Figure 5 demonstrates the time waveforms of two successive laser shots for the same gas mixture in the

presence of the titanium foil. The waveform of the second shot is seen to differ considerably.

DISCUSSION

Thus, the most remarkable feature emerging from the set of our experimental data is a decrease or a disproportionate increase in the laser output with pump energy, as vividly follows from Figs. 1 and 3. The former shows that (i) a rise in the gas pressure to 1 atm increases the energy deposit under all experimental conditions, (ii) the energy deposit increases approximately twofold in the case of two-side beam injection, and (iii) the pump energy increases by a factor of 1.6 when a Lavsan film is substituted for titanium foil. Normally, the output must grow in proportion to the energy deposit in all the three cases. Let us turn, however, to Fig. 3. As the pressure exceeds 0.7 atm, the output (curves *3*) declines for both the titanium foil and the Lavsan film in the two-beam mode. With the Lavsan film substituted for the titanium foil, the maximal output increases only slightly, from 45 to 50 J (curves *2*), in the one-beam mode and remains the same, 75 J, in the two-beam mode (curves *3*). In other words, neither substitution of a Lavsan film for titanium foil nor a change to two-beam pumping result in an expected increase in the laser output.

The feature discussed above is most probably related to a large amount of the space charge forming in the plasma [5, 6]. Indeed, if an electron beam imparts charge q to the gas, the resulting plasma is bound to carry the same charge q by virtue of the continuity equation, which states that the charge is the same at any point of a medium. The beam electrons will move in an electric field that arises in the plasma bearing space charge q. In normal gases, where the concentration of plasma electrons is high, the plasma conductivity is fairly high and the electric field of the space charge is low. For example, the electric field in an electron-beam-excited KrF laser was estimated as 0.8–1.0 kV/cm [10] (at the center of a laser chamber 20 cm in diameter, the potential does not exceed 10 kV). This field slows down fast electrons moving in the active volume. However, since electron energies in excimer lasers range typically from 300 to 500 keV, the electron energy spent on work against this field is insignificant. Note that the fraction of an electronegative gas in the gas mixture is about 0.1% for a KrF laser (F_2) and 98% for an HF laser (SF_6). Because of such a high SF_6 concentration in the SF_6–H_2 mixture, the attachment rate of plasma electrons in an HF laser is by three orders of magnitude higher than that in an excimer laser. It follows that the plasma conductivity is substantially lower and the electric field is appreciably higher than in excimer lasers. Note that conduction in the plasma of HF lasers may be both ionic and electronic. Slowing down of fast electrons by the space charge means that part of the kinetic energy of the beam is converted to the potential energy of the electric field. The kinetic energy cannot disappear at all: it is spent on motion of heavy ions and electrons whose energy is insufficient for excitation and ionization of the mixture components and eventually is merely converted into heat.

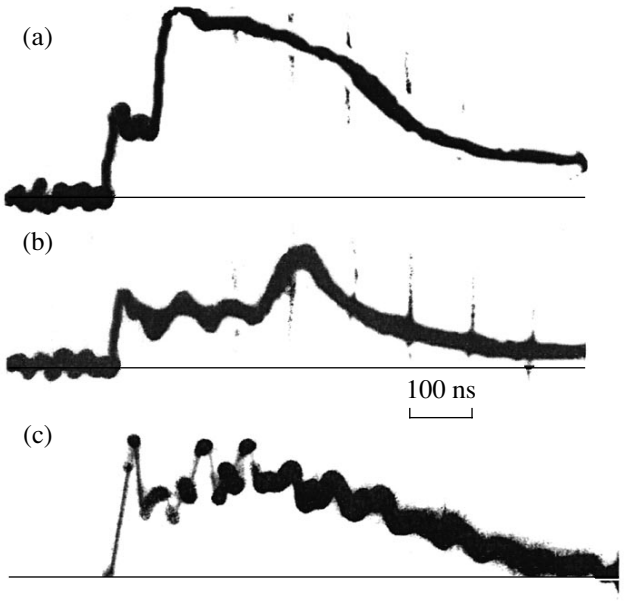

Fig. 5. Time waveforms of (a, b) the first laser shot in the central part of the beam and (c) the second shot at the beam periphery. The gas pressure 0.7 atm, two-beam pumping through the titanium foil.

It seems that the influence of the space charge in our experimental conditions is so strong that it noticeably decreases the laser energy. This effect is highlighted when the pressure in laser mixture exceeds 0.7 and 0.3 atm in the cases with the titanium foil and Lavsan film, respectively (Fig. 3). At these pressures, the lasing energy observed in the experiments with two-beam pumping becomes lower than the calculated sum of the partial energies of the beams. In both cases, the average energy deposit into the gas is roughly the same, 60–70 J/l. This energy level can be therefore considered as critical in our experimental conditions: from this point on, the space charge in the plasma has an appreciable effect on the lasing efficiency and laser output. Accordingly, one can estimate a critical level of the space charge associated with the electron beam; in our case, it equals $(3.0–3.5) \times 10^{-4}$ C/l.

The maximal lasing efficiency, 5%, is attained in the experiments with the titanium foil in the two-beam pumping mode at a pressure of 0.3 atm (Fig. 3a). In one-beam pumping mode at the same pressure, the efficiency reduces to 4% because of nonuniform excitation. For pressures above 0.7 atm, the efficiency in the one-beam mode is higher than in the two-beam mode. It is likely that the effect of the space charge is enhanced in the latter case. The use of the Lavsan film increases the pump power but diminishes the efficiency to 3%. In all the cases, the lasing efficiency lowers with

rising pressure. It seems likely that the effect of the space charge in the case of the titanium foil takes place at pressures from 0.3 to 0.4 atm too but is much weaker than at higher pressures.

The time waveform of HF laser shots also deserves attention. As a rule, they looked as though consisting of two time-separated components (Fig. 5). Upon the second switching of the laser with the same mixture, the delay time between the components was longer. Why the shots have such a form remains unclear; it is not improbable that there appears an additional mechanism of HF molecule formation with the participation of molecular fluorine [7, 8].

CONCLUSION

The investigation into the energy parameters of the HF laser as functions of the energy density delivered by the electron beam (pump power) shows that a rise in the pump level above 60–70 J/l leads to a decrease or a disproportionate increase in the laser output. When the pump level exceeds 30 J/l, the lasing efficiency drops irrespective of experimental conditions. To raise the efficiency, it seems advantageous to reduce the electron beam current density (i.e., to lower the density of energy deposit) and still leave the electron energy the same. This conjecture is supported by earlier results [5, 6, 8], which indicate that, at low densities of the electron beam, the laser normally operates with a high efficiency [8], while at elevated current densities, the electron beam in the gas and the lasing parameters behave in an unusual manner [5, 6].

REFERENCES

1. M. Gastaud, J. Bouesc, and M. Autric, Proc. SPIE **3092**, 585 (1996).
2. E. N. Abdullin, A. M. Efremov, B. M. Koval'chuk, *et al.*, Pis'ma Zh. Tekh. Fiz. **23** (5), 58 (1997) [Tech. Phys. Lett. **23**, 193 (1997)].
3. E. V. Grabovskiĭ, V. P. Denisenko, V. K. Zhivotov, *et al.*, Zh. Tekh. Fiz. **49**, 2224 (1979) [Sov. Phys. Tech. Phys. **24**, 1226 (1979)].
4. I. I. Ramirez and K. R. Prestwich, J. Appl. Phys. **50**, 4988 (1979).
5. V. P. Bashurin, S. D. Velikanov, A. Ya. Dovgiĭ, *et al.*, Dokl. Akad. Nauk SSSR **287**, 614 (1986) [Sov. Phys. Dokl. **31**, 256 (1986)].
6. S. D. Velikanov, M. V. Sinitsin, V. D. Urlin, *et al.*, Kvantovaya Élektron. (Moscow) **23**, 25 (1996).
7. V. M. Orlovskiĭ, A. G. Ponomarenko, E. F. Sosnin, *et al.*, Zh. Tekh. Fiz. **69** (1), 76 (1999) [Tech. Phys. **44**, 69 (1999)].
8. M. E. Erofeev, V. M. Orlovskiĭ, V. S. Skakun, *et al.*, Kvantovaya Élektron. (Moscow) **30**, 486 (2000).
9. Yu. I. Bychkov, N. G. Ivanov, V. F. Losev, *et al.*, Kvantovaya Élektron. (Moscow) **17**, 300 (1990).
10. Ken-Ichi Ueda, Laser Part. Beams **7**, 375 (1989).

Translated by A. Sidorova

Technical Physics, Vol. 50, No. 9, 2005, pp. 1191–1194. Translated from Zhurnal Tekhnicheskoĭ Fiziki, Vol. 75, No. 9, 2005, pp. 85–88.

ACOUSTICS, ACOUSTOELECTRONICS

On Acoustic Stimulation of Atmospheric Precipitation

G. A. Galechyan

Institute of Applied Physics, National Academy of Sciences of Armenia, Yerevan, Armenia

e-mail: galechian@web.am

Received November 2, 2004

Abstract—Stimulation of atmospheric precipitation by acoustic waves is considered. The interaction of acoustic waves with fog particles and the acoustic coagulation phenomenon are analyzed. It is proposed that the effect of amplification of sound in a weakly ionized gas be used to prevent sound decay away from the source in a foggy environment. © *2005 Pleiades Publishing, Inc.*

Artificial stimulation of precipitation remains a challenging problem of environmental technology. Pioneering experiments in this field were carried out as early as at the beginning of the 20th century [1]. This problem constitutes a part of the more general problem of atmospheric control, including such issues as fog dispersion; hail prevention; removal of atmospheric freon, which attacks the ozone layer of the Earth; and others.

Stimulation of precipitation is considered a very promising technique for drought prevention. Artificial rainfall was first accomplished in the Netherlands in 1931 by aircraft-aided infusion of fine-grained solid carbonic acid into supercooled clouds. The intensity of those rains was low because of a small vertical extent of the clouds subjected to the reagent, and so this attempt was not appreciated that time.

Efforts to stimulate rainfall by dispersing active reagents in clouds proceeded after World War II in many countries and were accompanied by relevant computations and thorough analysis of the results. Later, more advanced (electrical, acoustic, and laser) methods were employed to cause artificial rainfall [1].

In this study, we consider rainfall stimulation by acoustic waves. A basic disadvantage of this method is decay of sound waves propagating in the atmosphere. It appears, however, that this drawback can be overcome by using the effect of sound amplification in weakly ionized gases.

Let us synopsize the publications concerned with acoustic stimulation of precipitation [2–8]. In [2], evaporation of drops in relation with temperature pulsations due to the periodic compression and expansion of the air under the action of acoustic waves was studied. It was shown that drops of a certain critical radius may evaporate under these conditions because of a temperature rise. Large drops, whose temperature remains constant, may merge together when subjected to a strong acoustic field. In [3, 4], the coagulation process was described using a stochastic approach and numerical simulation. To this end, the drop size microdistribution in uniform fog was calculated. It was found that, 5 s after exposure of a cloud with a water vapor content of 2 g/m^3 to sound waves with a frequency of 300 Hz and intensity of 140 dB, a maximum in the drop size distribution shifts towards larger values. Within 15 min of sound application, another (degenerate) peak appears near 500 μm, which corresponds to precipitation.

Interaction between sound waves and suspended particles was touched upon in [5, 6]. It is established that such systems feature unstable equilibrium, which leads to coagulation of drops. In this case, coagulation is due to a collective field produced by the hydrodynamic interaction of particles rather than by pairwise attraction between particles as was noted in [3, 4].

In [8], experiments with artificial fog in a 500-m^3 chamber were described. Sound waves were generated by an audio-frequency generator with an output power of up to 20 kW [9]. The waves were emitted through a horn radiator. The field with a frequency in the range from 170 to 200 Hz turned out to be the most efficient. Low-intensity (below 1.7×10^{-3} W/cm^2) sound accelerated fog dispersion by 20–30 times and drastically changed the fog microstructure. Full-scale experiments in the frequency range from 100 to 300 Hz with a sound intensity at the end of the horn ranging from 0.12 to 0.21 W/cm^2, which corresponds to 150 dB [10], were also performed. At a distance of 30–40 m from the source, appreciable changes in cloud drops were observed: the higher the water content in the fog, the more profound and faster the changes. Also, the sound field with the parameters mentioned above caused changes in the fog microstructure. The experiments indicated that the effect of sound waves on the fog grows with acoustic power. Review [8] outlines the results on chemical stimulation of precipitation near the Sevan lake, which is at an altitude of 1900 m. The Sevan lake (a total surface area of about 1200 km^2), surrounded by the Gegamskiĭ and Vardenisskiĭ ridges, represents a unique test area for acoustic-wave stimulation of precipitation.

1063-7842/05/5009-1191$26.00

The basic difficulty associated with acoustic stimulation of precipitation is the damping of sound waves with distance from the source. In the idealized case of isotropic propagation, when neither scattering nor absorption of the sound is taken into account, the acoustic intensity decreases proportionally to the squared distance to the source. Actually, however, both scattering and absorption take place under natural conditions (this is especially true for fog, where these processes are more intense than in the air); accordingly, the damping is even a stronger function of distance. It is this situation that was observed in the experiments under natural conditions [7].

A possible way of preventing acoustic wave damping in fog is to take advantage of the phenomenon of sound amplification in weakly ionized molecular gases. This effect is explained by the nonradiative *V–T* relaxation of gas molecules from their vibrational excited states. During relaxation, the energy is transferred to the wave, thereby increasing its intensity. In [11–14], a linear theory of sound wave propagation in a molecular gas was developed that disregards mutual interaction between the wave and an amplifying medium. A theory elaborated upon in [15, 16] includes this effect.

Amplification of acoustic waves from an external source that travel along a positive column of a glow in a molecular gas was studied in [17, 18]. The experiments were carried out in pure nitrogen and a nitrogen–oxygen mixture at gas pressure $P = 78$ mm Hg in a discharge tube with an inner diameter of 9.8 cm. A sound wave of frequency 170 Hz was introduced into the discharge by an electrodynamic radiator fixed at one of the tube ends. A microphone was placed at the opposite end behind the electrode.

The amplification coefficient for a sound wave of intensity $J = 72$ dB in the nitrogen discharge (a discharge current of 120 mA) was found to be $K_i = 5.6$ m^{-1}. In the discharge initiated in an $N_2 + 10\%O_2$ mixture, the amplification coefficient increased to $K_i = 8$ m^{-1}. This is because the constant of oxygen-induced vibrational relaxation of nitrogen is two orders of magnitude higher than in the case of nitrogen–nitrogen relaxation. It should be noted that the rate of the vibrational relaxation of nitrogen due to water molecules is three orders of magnitude higher than that due to nitrogen. This means that the amplification factor of a sound wave can be considerably increased by adding a small amount of water vapor to a weakly ionized nitrogen plasma. It is therefore interesting to investigate amplification of sound in weakly ionized gases at elevated pressures up to the atmospheric value.

Another challenge associated with sound stimulation of precipitation is provision of weakly ionized air as a medium with vibrationally excited molecules in the way of a sound wave. In the fog, such an ionization can be produced by using microwave radiation, laser beams, or electric fields. Below, we will briefly discuss ionization of the atmosphere by microwaves without considering a number of attendant effects, such as a change in the electric potential of a cloud and growth of drops, which may enhance coagulation, and others.

Monograph [19] deals with theoretical and experimental investigation into the formation of artificially ionized areas in the air by means of high-frequency electric fields. The feasibility of creating such areas at altitudes between 30 and 40 km to establish reliable communication is analyzed. It is supposed that a microwave discharge be initiated by two or more crossed beams of radio waves. The results of model laboratory experiments with microwave discharges are described.

Generation of a microwave discharge in the troposphere aimed at eliminating the freon contamination, which attacks the terrestrial ozone layer, from the air basin is considered in [20, 21].

An electrodeless discharge in the air is initiated by a high-frequency electric field. The electrons moving in this field and colliding with neutral air molecules gain an energy sufficient for ionization. When a certain critical ionization frequency is exceeded, the gas breaks down, causing an exponential increase in the electron and ion concentration with time: $n_e \sim \exp(\gamma_i t)$, where γ_i is the ionization frequency, which rapidly rises with high-frequency field amplitude.

A discharge initiated in high-pressure (to 500 mm Hg) gases by a train of microwave pulses is discussed in [19, 21, 22]. Specifically, the initiation of a microwave discharge in air by pulses with wavelength $\lambda_f \approx 2$ cm, duration $\tau_f = 10$–30 μs, and repetition rate $f \approx 2$ Hz is considered. A special feature of this discharge is spatial inhomogeneity: the electron concentration is high in the central part, where $n_e \cong 10^{16}$–10^{17} cm^{-3} and the electron temperature is $T_e \cong 5$ eV, and low at the periphery ($n_e \cong 10^{12}$ cm^{-3}, $T_e = 0.5$–0.7 eV). The electron concentration rapidly drops within 10 μs after the pulse and then tends toward a quasi-steady-state value with a slow decay of the plasma.

Let us estimate the *V–T* relaxation time in a microwave discharge at an air pressure of 700 mm Hg. Late in the decay, the gas temperature in the plasma lowers substantially; let it be 300 K. In pure nitrogen, the *V–T* relaxation constant is $k_{VT} \cong 10^{-16}$ cm^3/s [23]; in the case of plasma quenching by molecular oxygen, $k_{VT} \cong 2.3 \times 10^{-16}$ cm^3/s [24]; and for quenching by water with a temperature ranging from 300 to 963 K, $k_{VT} \cong 10^{-13}$ cm^3/s [25]. The time of vibrational *V–T* relaxation in the fog (an $N_2 + O_2 + H_2O$ mixture) can be found by the formula [24]

$$\frac{1}{\tau_{VT}} = \frac{1}{\tau_{VT1}}\frac{P_1}{P} + \frac{1}{\tau_{VT2}}\frac{P_2}{P} + \frac{1}{\tau_{VT3}}\frac{P_3}{P},$$

where P_1, P_2, and P_3 are the partial pressures of nitrogen, oxygen, and water vapor, respectively, in the atmospheric air and τ_{VT1}, τ_{VT2}, and τ_{VT3} are the times of nitro-

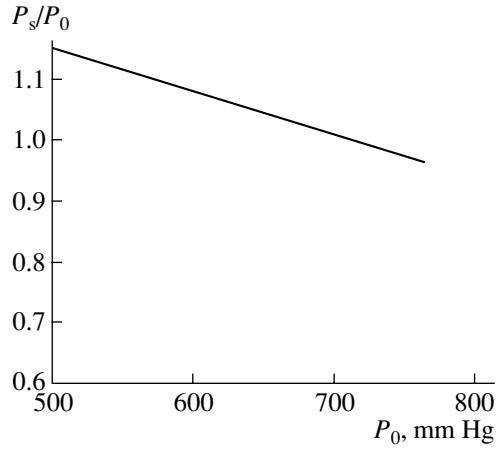

Relative sound pressure vs. the atmospheric pressure for air temperature $T = 0°C$.

gen quenching by nitrogen, oxygen, and water, respectively.

Assume that the water vapor content in the air equals 2 g/m^3, which corresponds to a partial pressure of about 1 mm Hg under the conditions considered. Calculation by the above formula yields $\tau_{VT} \cong 0.5 \times 10^{-3}$ s for the relaxation time of vibrationally excited nitrogen in the plasma of humid air. Taking into account that a sound wave acting on the fog should have frequency f between 100 and 300 Hz, we obtain $\tau_{VT} < \tau_s$. That is, in the fog, the relaxation frequency of vibrationally excited levels is appreciably higher than the sound frequency and so the acoustic wave will be amplified.

The results given in [21, 22, 26] suggest that a microwave discharge under field conditions is feasible. It is known that the microwave discharge plasma decays slowly. Therefore, generating microwave discharge pulses with a repetition rate of several hundreds of hertz for several seconds, one can create a plasma object that, being exposed to a sound wave, amplifies it, causing precipitation at large distances. For long-range probing, it seems reasonable to apply synchronous scanning by radio and sound waves.

Consider the altitude dependence of the relative sound pressure using the formula $P_s = \sqrt{2J\rho V_s}$ [27], where J is the sound wave intensity, ρ is the gas density, and V_s is the sound velocity.

The figure shows relative sound pressure P_s/P_0 versus the atmospheric pressure (altitude). Here, P_0 is the sound pressure at an atmosphere pressure of 760 mm Hg (the measurements were taken near the lakes Sevan and Issyk-Kul, which are at an altitude of 1900 and 1600 m, respectively, which correspond to atmospheric pressures of about 600 and 620 mm Hg). As follows from the figure, the relative sound pressure grows with a decrease in the atmospheric pressure for intensity J = 150 dB and air temperature $t = 0°C$. Therefore, high-altitude regions are preferable as test areas for experiments on precipitation stimulation.

In conclusion, note the following. As is seen from the plot, the efficiency of precipitation stimulation grows with altitude at a constant sound intensity. Furthermore, the stimulation will be more efficient if an acoustic generator with a radiator is aboard an airborne vehicle. In this case, acoustic waves propagating through a cloud oppositely to the direction of flight will leave a trace in the form of coagulated drops. A suitable vehicle could be a helicopter because of its ability to vary the flying height and move through a cloud with a high moisture concentration to provide intense coagulation. With parameters of an acoustic generator chosen optimally, the shuttle of a helicopter through clouds would stimulate precipitation.

This method can be used for dissipation of clouds prone to hail formation over terrains that frequently suffer from damage done by hail.

ACKNOWLEDGMENTS

The author is grateful to É. A. Arutyunyan for valuable discussion.

REFERENCES

1. L. G. Kachurin, *Physical Principles of Action on Atmospheric Processes* (Gidrometeoizdat, Leningrad, 1990) [in Russian].
2. E. L. Aleksandrov and Yu. S. Sedunov, Tr. Inst. Prikl. Geofiz. (Leningrad) **1**, 39 (1965).
3. M. P. Foster and J. C. Paflam, J. Weather Modif. **17**, 38 (1985).
4. M. P. Foster and J. C. Paflam, J. Geophys. Res. **93**, 747 (1988).
5. B. E. Nemtsov and V. Ya. Eidman, Akust. Zh. **35**, 882 (1989) [Sov. Phys. Acoust. **35**, 513 (1989)].
6. B. E. Nemtsov, Dokl. Akad. Nauk SSSR **314**, 355 (1990) [Sov. Phys. Dokl. **35**, 820 (1990)].
7. V. V. Vyal'tsev, A. Z. Makharashvili, and V. G. Khorguani, Tr. Inst. Prikl. Geofiz. (Leningrad) **1**, 47 (1965).
8. E. A. Arutyunyan and R. A. Kazaryan, Vestn. Mezhdunar. Akad. Nauk Ékologii i Bezopasnosti Zhiznedeyatel'nosti, No. 7, 79 (1999).
9. V. V. Vyal'tsev and V. G. Khorguani, Akust. Zh. **6** (1961) [Sov. Phys. Acoust. **6** (1961)].
10. L. A. Sena, *Physical Quantities: Units of Measure and Dimensions* (Nauka, Moscow, 1988) [translated from English].
11. E. Ya. Kogan and V. P. Mal'tsev, Zh. Tekh. Fiz. **47**, 653 (1977) [Sov. Phys. Tech. Phys. **22**, 391 (1977)].
12. H.-J. Bauer and H. E. Bass, Phys. Fluids **16**, 988 (1973).
13. E. Ya. Kogan and N. E. Molevich, Izv. Vyssh. Uchebn. Zaved. Fiz., No. 7, 53 (1986).
14. A. I. Osipov and A. V. Uvarov, Inzh.-Fiz. Zh. **55**, 149 (1988).
15. E. Ya. Kogan and N. E. Molevich, Zh. Tekh. Fiz. **56**, 941 (1986) [Sov. Phys. Tech. Phys. **31**, 573 (1986)].

16. A. V. Eletskiĭ and E. V. Stepanov, Khim. Fiz. **8**, 1247 (1989).
17. G. A. Galechyan and A. R. Mkrtchyan, Akust. Zh. **48**, 314 (2002) [Acoust. Phys. **48**, 268 (2002)].
18. G. A. Galechyan and A. R. Mkrtchyan, Pis'ma Zh. Tekh. Fiz. **27** (14), 68 (2002) [Tech. Phys. Lett. **27**, 605 (2002)].
19. N. D. Borisov, A. V. Gurevich, and G. M. Milikh, *Artificially Ionized Region in the Atmosphere* (Izd. Akad. Nauk SSSR, Moscow, 1986) [in Russian].
20. A. V. Gurevich, A. G. Litvak, *et al.*, Usp. Fiz. Nauk **170**, 1118 (2000).
21. G. M. Batanov, S. I. Gritsinin, I. A. Kossyi, *et al.*, Tr. Fiz. Inst. Akad. Nauk SSSR **160**, 174 (1985).
22. S. I. Gritsinin, I. A. Kossyi, V. P. Silakov, and N. M. Tarasova, in *Proceedings of the 18th International Conference on Phenomena in Ionized Gases (ICPIG'18), Swansea, 1987*, p. 232.
23. S. Lukasik and J. Young, J. Chem. Phys. **27**, 1149 (1957).
24. V. N. Kondrat'ev, *Chemical Kinetics of Gas Reactions* (Akad. Nauk SSSR, Moscow, 1958; Pergamon, Oxford, 1964).
25. M. Whitson and R. McNeal, J. Chem. Phys. **66**, 2696 (1977).
26. G. A. Askar'yan, G. M. Batanov, A. E. Barkhudarov, *et al.*, Fiz. Plazmy **18**, 1198 (1992) [Sov. J. Plasma Phys. **18**, 625 (1992)].
27. L. Bergmann, *Ultrasonics* (Bell, London, 1938; Inostrannaya Literatura, Moscow, 1956).

Translated by A. Sidorova

Technical Physics, Vol. 50, No. 9, 2005, pp. 1195–1200. Translated from Zhurnal Tekhnicheskoĭ Fiziki, Vol. 75, No. 9, 2005, pp. 89–94.

RADIOPHYSICS

Integrated Ferroelectric Millimeter-Wave Phase Shifters with a Periodic Structure

O. Yu. Buslov, V. N. Keis, A. B. Kozyrev, I. V. Kotel'nikov, and P. V. Kulik

St. Petersburg State Electrotechnical University, ul. Prof. Popova 5, St. Petersburg, 197376 Russia

e-mail: mcl@eltech.ru

Received November 23, 2004

Abstract—Integrated phase shifters with a periodic structure that includes $BaSrTiO_3$ ferroelectric varactors parallel- and series-connected to the transmission line are investigated theoretically and experimentally. The phase shifters are designed for the frequency range 26–32 GHz. The dispersion characteristics and insertion losses in the transmission line of the phase shifters are analyzed with regard to the dependence of the capacitance and loss tangent of the varactors on control voltage and temperature. It is shown that parasitic amplitude modulation in the phase shifters can be suppressed if the connection scheme of the varactors takes into account the voltage dependence of the their loss tangent. In the phase shifters with series-connected varactors, the temperature dependence of the phase shift is much weaker than in those with parallel-connected varactors. © *2005 Pleiades Publishing, Inc.*

INTRODUCTION

The phase shifter (PS) is a basic component of phase-scanned arrays used in radars and communications (including satellite communications) systems. Phase shifters based on ferrites and semiconductor diodes are now the most popular [1]. Simultaneously, research is under way on developing PSs with microelectromechanical [2] and piezoelectric [3] systems, as well as ferroelectric PSs [4, 5]. Ferroelectric PSs seem to be very promising, since they offer a high speed of phase shift control, wide dynamic range, and good radiation hardness. In addition, they are cheap and easy to fabricate. At the same time, ferroelectrics have a number of disadvantages from the standpoint of their use in microwave PSs, such as a high temperature coefficient of the permittivity and, under certain conditions, a significant voltage dependence of the loss tangent. The first disadvantage imposes stringent requirements for thermal stabilization of the ferroelectric devices. The second causes the parasitic amplitude modulation of a valid signal when its phase is voltage-controlled. Note that the dielectric losses as a function of voltage may both increase and decrease at different frequencies, depending on the composition of and the defect density in ferroelectric films [6, 7]. Temperature stabilization schemes for film ferroelectric PSs were described in [5], but they were not validated by electrodynamic analysis.

In this work, we demonstrate the possibility of suppressing the negative effects mentioned above by analyzing transmission lines regularly terminated by series- or parallel-connected ferroelectric varactors. The analysis of the structures is made in wide ranges of frequencies (1–60 GHz), temperatures (78–320 K), and control fields (0–40 V/μm) [6–9]. The experiments were carried out on integrated PSs built around slot and microstrip lines. The interconnection of these lines on a $BaSrTiO_3$ ferroelectric film provided periodic switching of the varactors. It is shown that the experimental data corroborate analytical results.

1. PHASE SHIFT AND INSERTION LOSSES IN THE PHASE SHIFTERS

Coplanar, slot, and slot–waveguide lines are the most appropriate for PSs with parallel-connected ferroelectric varactors, while a microstrip line is best suited for PSs with series-connected varactors. Figure 1 shows parts of the periodic structures and equivalent circuits of a PS cell based on slot and microstrip lines. The relationship between the wave propagation constant ($\gamma = \beta + j\alpha$) and parameters of the cell components is as follows [7]:

$$\cosh\gamma l = \cosh(\beta + j\alpha)l = 1 + YZ, \qquad (1)$$

where

$$Y = j\left(Y_0\tan\frac{\beta_0 l}{2} + \omega C\right) + \omega C\tan\delta,$$

$$Z = jZ_0\sin\beta_0 l + 2\alpha_0 Z_0 l$$

for the circuit with parallel-connected varactors and

$$Y = jY_0\sin\beta_0 l,$$
$$Z = j\left(Z_0\tan\frac{\beta_0 l}{2} - \frac{1}{\omega C}\right) + \frac{\tan\delta}{\omega C} + \alpha_0 Z_0 l \qquad (2)$$

for the circuit with series-connected varactors.

1063-7842/05/5009-1195$26.00 © 2005 Pleiades Publishing, Inc.

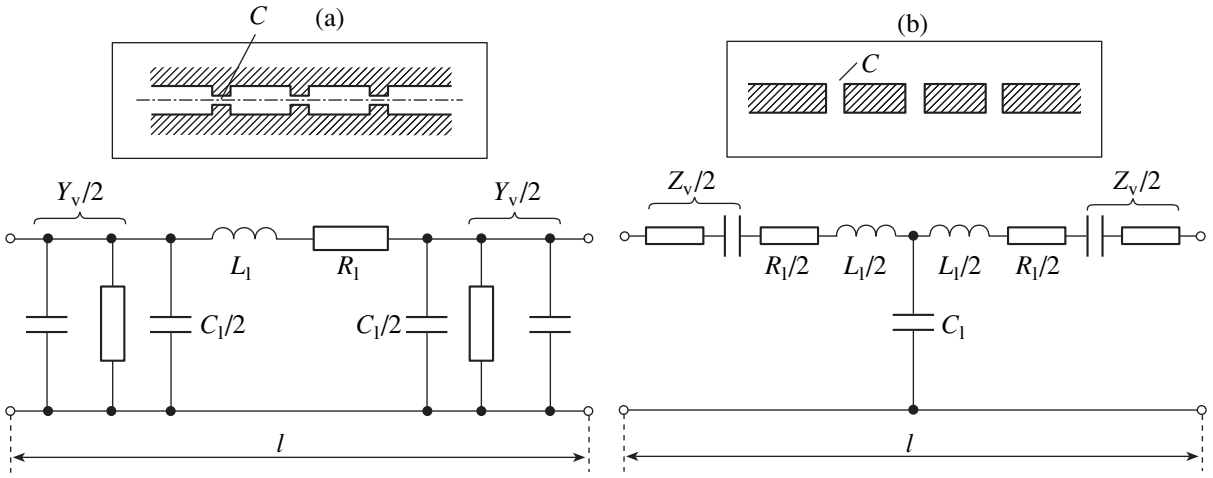

Fig. 1. (a) Slot and (b) microstrip transmission lines regularly terminated by varactors. R_l, L_l, and C_l are the related parameters per unit length of the unterminated line and $Y_v = j\omega C + \omega C\tan\delta$ and $Z_v = -j/\omega C + \tan\delta/\omega C$ are the conductance and resistance of the varactor in the circuit with parallel- and series-connected varactors.

In the above expressions, $Z_0 = 1/Y_0$, β_0, and α_0 are the characteristic impedance, propagation constant, and damping constant of the unterminated transmission line, respectively; l is the length of the cell; and C and $\tan\delta$ are the capacitance and loss tangent of the ferroelectric varactors inserted into the line.

Substituting the cell parameters into (1) and separating the real and imaginary parts, one can obtain the dispersion relations and relationships for the insertion losses per cell and characteristic impedance of the line,

$$\cos\beta_p l = \cos\beta_0 l - Z_0\omega C(U,T)\sin\beta_0 l, \quad (3)$$

$$L_p(\text{dB}) = 8.68\left[Z_0\omega C(U,T)\tan\delta(U,T)\sin\beta_0 l + 2\alpha_0 l\left(\tan\frac{\beta_0 l}{2} + Z_0\omega C(U,T)\right)\right]\cos\beta_p l, \quad (4)$$

$$Z_{cp} = [(Y_0\operatorname{cosec}\beta_0 l)^2 - (\omega C - Y_0\operatorname{cosec}\beta_0 l)^2]^{-0.5} \quad (5)$$

for the PSs with parallel-connected varactors and

$$\cos\beta_s l = \cos\beta_0 l + \frac{Y_0}{\omega C(U,T)}\sin\beta_0 l, \quad (6)$$

$$L_s(\text{dB}) = 8.68\left(\frac{Y_0}{\omega C(U,T)}\tan\delta(U,T)\sin\beta_0 l + \alpha_0 l\sin\beta_0 l\right)\operatorname{cosec}\beta_s l, \quad (7)$$

$$Z_{cs} = \left[(Z_0\operatorname{cosec}\beta_0 l)^2 - \left(\frac{1}{\omega C} + Z_0\cot\beta_0 l\right)^2\right]^{0.5} \quad (8)$$

for the PSs with series-connected varactors.

For further analysis of the lines regularly terminated by ferroelectric varactors, it is necessary to know the microwave properties of the ferroelectric components and their response to a control voltage. Typical temperature dependences of the capacitance, $C(T)$, and frequency dependences of the insertion losses, $\tan\delta(f)$, at different control voltages for varactors made of highly oriented near-single-crystalline $BaSrTiO_3$ films obtained by magnetron sputtering [8, 9] are depicted in Fig. 2. It is noteworthy that capacitance $C(T)$ remains almost constant in a wide temperature range when a maximal control voltage is applied. Note also that the monotonically descending dependence $C(U)$ is characteristic of ferroelectric films irrespective of their composition and degree of imperfection. However, the run of the voltage dependence of the microwave dielectric losses varies in accordance with the composition of the film, defect density in it, and measurement frequency. For example, for highly imperfect $BaSrTiO_3$ films obtained by the ceramic technology [6], the frequency dependences of $\tan\delta$ taken at different bias voltages exhibit a crossover (Fig. 2c), unlike the dependences for the near-single-crystalline films. Thus, when designing microwave shifters, one should take into account the voltage dependence of the microwave losses in the ferroelectric film in order to suppress amplitude modulation, which inevitably arises in a device with variable insertion losses $L(\tan\delta(U))$.

Using Fig. 2a, we will analyze the phase variation in the structures with series- and parallel-connected varactors when the temperature varies in the range T_{min}–T_{max} and the control voltage varies in the range 0–U_{max}. Figure 3 plots the phase shift per cell versus its electrical length at different ratios $Z_0/X_c = Z_0\omega C$, where Z_0 is the wave impedance of the unterminated line and X_c is the characteristic reactance of a ferroelectric varactor.

From these dependences, as well as from the curves $C(T, U)$, the following conclusions can be drawn. At maximal temperature T_{max} and maximal control voltage U_{max} applied to the PS with parallel-connected varactors, the phase shift per cell is $\Delta\varphi(T_{max})$ (for example, in going from point *1* to point *2*; Figs. 2a and 3). The number of cells is $n = 360\ \text{deg}/\Delta\varphi(T_{max})$. At minimal operating temperature T_{min} and $U = 0$, the capacitance of the varactor grows (point *3*). At T_{min} and U_{max}, the phase shift per cell is $\Delta\varphi(T_{min})$ (transition from point *3* to point *2*). The additional phase shift due to a temperature change is obviously equal to $\Delta\varphi(T) = \varphi(T_{min}) - \varphi(T_{max})$. Similarly, considering the curves in Figs. 2a and 3 for the PSs with series-connected varactors, we note that $\Delta\varphi_p(T) > \Delta\varphi_s(T)$; that is, the range of temperature-related phase variation (transition from point *1* to point *3* and vice versa) in the case of series-connected varactors is always wider than for varactors connected in parallel. Remarkably, this inequality holds at any Z_0/X_c and any electric length $\beta_0 l$ of the cell provided that $n\Delta\varphi(T_{max}) = 360°$. Thus, one may infer that the PSs with series-connected varactors are preferable as to the effect of temperature on the phase characteristics.

Consider the possibility of suppressing parasitic amplitude modulation in these structures with regard to different dependences $\tan\delta(U)$ for varactors based on various films (Figs. 2b and 2c). From expressions (4) and (7) for the insertion losses, it follows that ferroelectric varactors are major contributors to the PS losses. It is noteworthy that the losses of parallel-connected varactors are proportional to the capacitance multiplied by the loss tangent, $L_p \sim C(U)\tan\delta(U)$, while for series-connected varactors, the losses vary as the ratio of the above quantities, $L_s \sim \tan\delta(U)/C(U)$. It is clear that, for varactors with the descending curve $\tan\delta(U)$ (higher-than-crossover frequencies in Figs. 2b and 2c), parasitic amplitude modulation in the PS can be effectively suppressed when the varactors are connected in series. In the opposite case of the ascending curve $\tan\delta(U)$ (lower-than-crossover frequencies in Fig. 2c), the undesired effect can be effectively suppressed by connecting varactors in parallel.

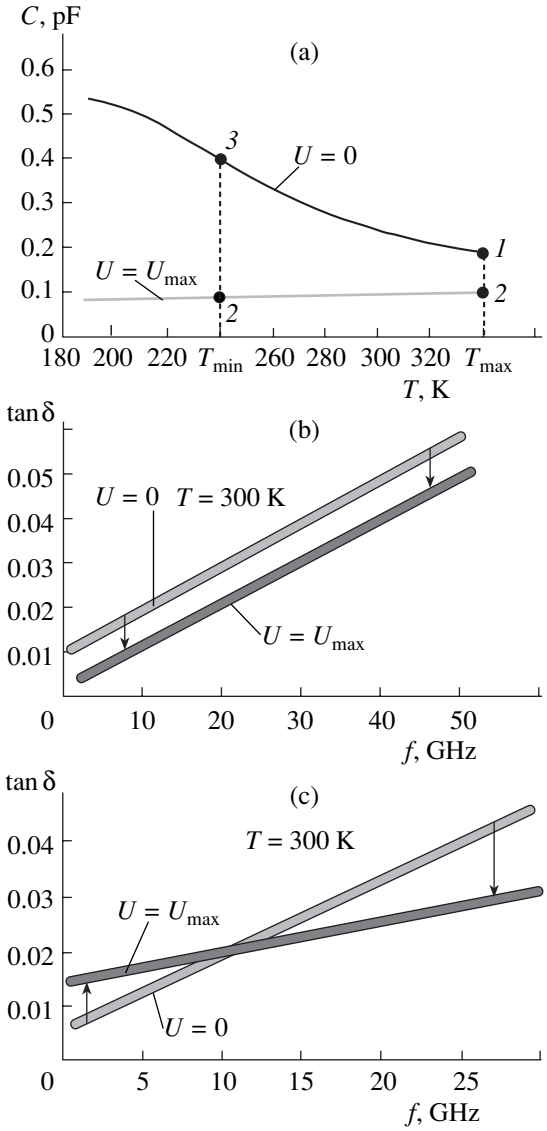

Fig. 2. Temperature dependences of the (a) capacitance (the film thickness is ≈1 μm; the metallic electrode spacing and length are ≈5 μm and 0.4 mm, respectively) and the frequency dependences of the loss tangent for varactors made of (b) highly oriented and (c) ceramic films at different control voltages.

2. PHASE SHIFTER DESIGN AND EXPERIMENTAL RESULTS

In this work, we experimented with integrated PSs based on slot and microstrip transmission lines with series- and parallel-connected varactors. The devices represent a multilayer structure (substrate, $BaSrTiO_3$ film, and metallization). The metallization on the ferroelectric film provides periodic switching of the varactors. The $Ba_{0.3}Sr_{0.7}TiO_3$ film ≈1 μm thick was applied on a 0.5-mm-thick Polikor substrate by high-frequency magnetron sputtering. Metallic electrodes 0.4 mm long and ≈5 μm apart were made by copper evaporation with subsequent gold plating. The controllability of the varactors (which is defined as a relative change in the capacity due to application of a control voltage) is equal to

$$k = \frac{C(U = 0)}{C(U_{max} = 300\ \text{V})} \cong 2.0.$$

The ferroelectric film had a descending dependence $\tan\delta(U)$ similar to that shown in Fig. 2b. The integrated PS based on the periodic structure with varactors connected to the slot line in parallel has $n = 11$ cells and is schematically depicted in Fig. 4a. The PS is soldered

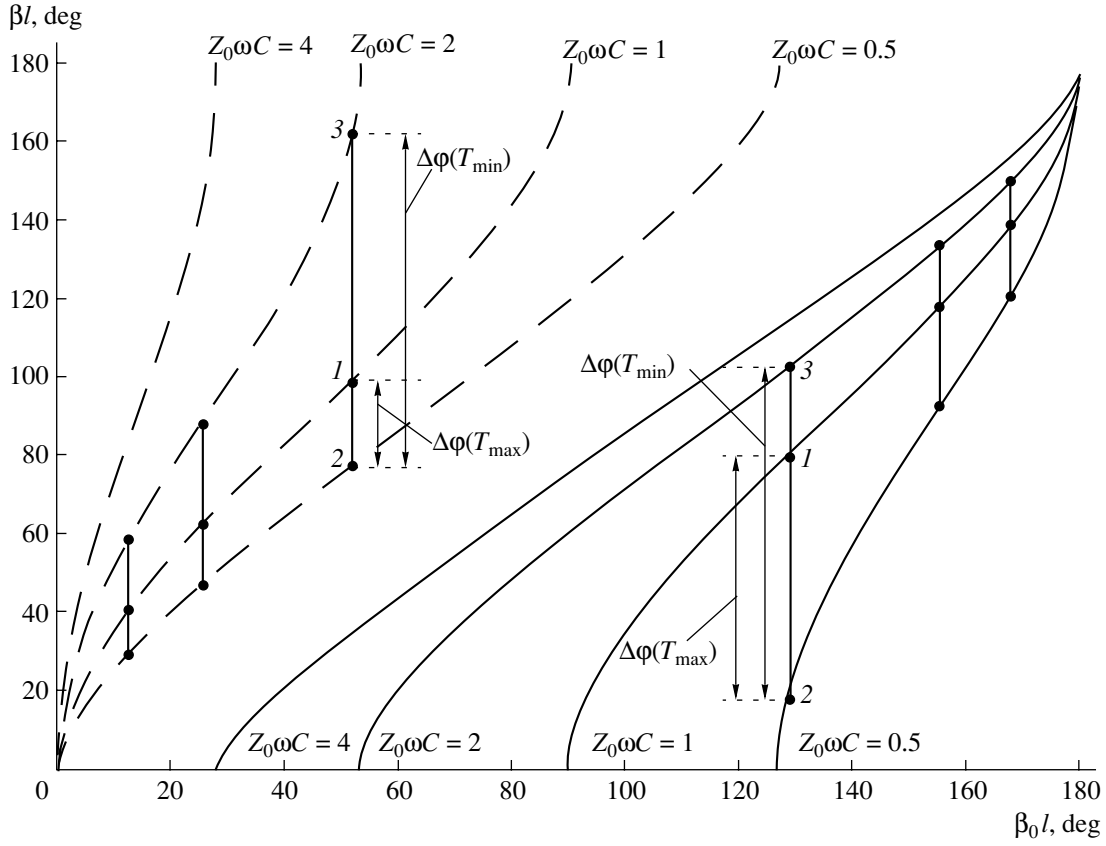

Fig. 3. Dispersion relations for the phase shifters with parallel- (dashed lines) and series-connected (continuous lines) ferroelectric varactors at different ratios Z_0/X_c.

in the slot line made of the Rogers RT/Duroid 6002 material [10] and mounted on the *E* plane of a waveguide. The ferroelectric phase shifter is matched to the waveguide by means of exponential-line transformers. To apply a control voltage to the ferroelectric component, one of the electrodes on the transmission line is insulated from the body of the waveguide with a 20-μm-thick mica plate.

The PS with series-connected ferroelectric varactors is shown in Fig. 4b. It is based on a regular microstrip line with a ferroelectric film and also consists of 11 cells. The structure is matched to the microstrip line with two step quarter-wavelength transformers. In both types of PSs, the decoupling of the microwave and control circuits was accomplished with a low-pass filter and equaled –20 dB and the reflection coefficient exceeded –15 dB in the frequency range 26–32 GHz.

Figure 5 demonstrates the analytical and experimental frequency dependences of the transfer coefficient and phase shift of the devices with series- and parallel-connected ferroelectric varactors. These dependences strengthen the earlier conclusion that the amplitude modulation of the transfer coefficient in the PSs with series-connected varactors can be suppressed in the case of the descending curve $\tan\delta(U)$. Additional temperature-related phase shifts at the zero control voltage

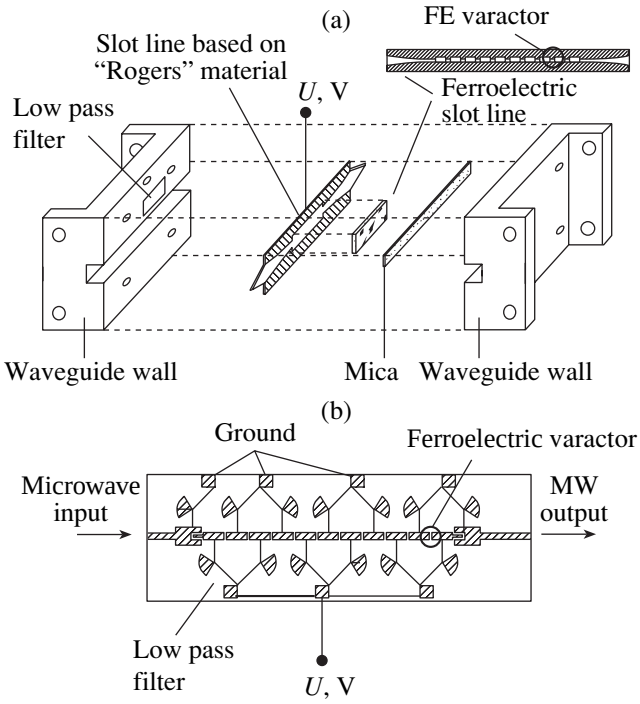

Fig. 4. Schematic of the phase shifters with (a) parallel connection of the varactors to the slot line and (b) series connection of the varactors to the microstrip line.

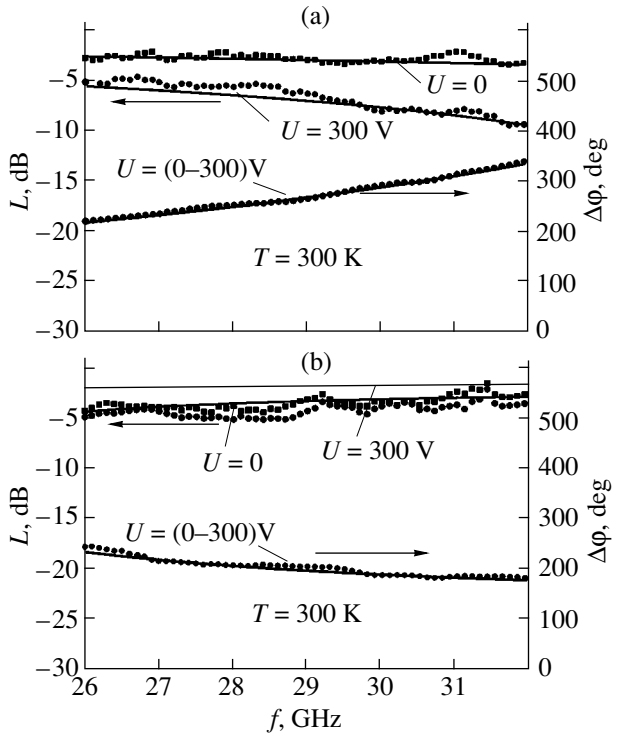

Fig. 5. Analytical and experimental frequency dependences of the insertion losses and phase shift at various control voltages for (a) parallel- and (b) series-connected varactors.

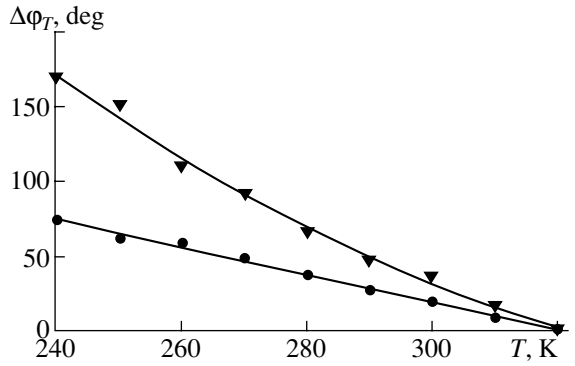

Fig. 6. Parasitic (temperature-related) phase shift for (▼) parallel- and (●) series-connected varactors.

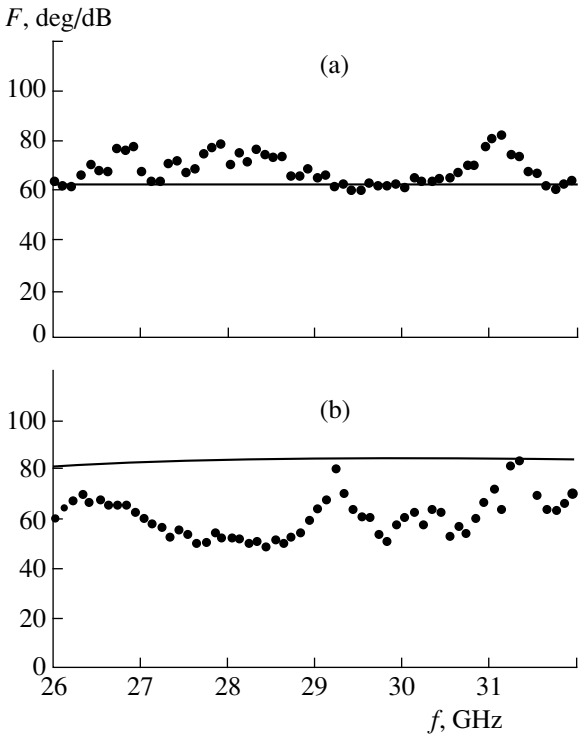

Fig. 7. Analytical (continuous lines) and experimental (data points) frequency dependences of the figure of merit of the phase shifter for (a) parallel- and (b) series-connected varactors.

in the two structures considered are shown in Fig. 6. The earlier conclusion that series connection of the varactors raises the temperature stability of the phase shift in the PS is supported again. Note, however, that the temperature stability of the structure, while considerably improved by properly choosing the circuit design, is still insufficient: the temperature coefficient of phase (TCP) at series connection of varactors, $K_\varphi[\Delta\varphi_T/\Delta T] \cong 1$ deg/K (Fig. 6), remains too high for a number of applications. When the varactors are connected in parallel, the TCP equals 2 deg/K. The TCP can be raised further (up to $K_\varphi \longrightarrow \infty$) by applying a temperature-dependent control voltage to the ferroelectric varactors [11].

Based on the experimental data, we estimated the figure of merit of ferroelectric PSs,

$$F = \frac{\Delta\varphi}{\sqrt{L(U=0)L(U=U_{\max})}}[\text{deg/dB}]. \qquad (9)$$

The data for F represented in Fig. 7 demonstrate good agreement between the analytical and experimental data. The figure of merit in the frequency range considered is rather high, $F \approx 60$ deg/dB. Note that the experimental figure of merit for the structure with series-connected ferroelectric varactors is somewhat lower than the analytical value. This is because the control circuits influence the characteristics of the ferroelectric capacitors, impairing the controllability of the ferroelectric varactors.

CONCLUSIONS

Based on the microwave properties of ferroelectrics and theoretical analysis of periodic structures with series- and parallel-connected ferroelectric varactors, it is demonstrated that parasitic amplitude modulation in the PSs can be suppressed and their temperature stability and other parameters can be improved by properly choosing the circuit design. Our theoretical statements

are validated in experiments with two types of integrated phase shifter intended for the frequency range 26–32 GHz. Specifically, the figure of merit of the device reaches 60 deg/dB.

REFERENCES

1. J. Uher and W. Hoefer, IEEE Trans. Microwave Theory Tech. **39**, 643 (1991).
2. A. Borgioli, Y. Liw, A. S. Narga, and R. A. York, IEEE Microwave Guid. Wave Lett. **10**, 7 (2000).
3. Y. Poplavko, Y. Prokopenko, V. Kazmirenko, and B. Kim, in *Proceedings of the 12th International Conference "Microwave and Telecommunication Technology" (CriMiCo'02), Sevastopol, 2002*, pp. 376–378.
4. E. G. Erker, A. S. Nagra, Yu. Liu, *et al.*, IEEE Microwave Guid. Wave Lett. **10**, 10 (2000).
5. O. G. Vendik, *Ferroelectrics in Microwave Technology* (Sov. Radio, Moscow, 1979) [in Russian].
6. A. Kozyrev, V. Keis, V. Osadchy, *et al.*, Integr. Ferroelectr. **34**, 189 (2001).
7. A. Kozyrev, V. Keis, O. Buslov, *et al.*, Integr. Ferroelectr. **34**, 271 (2001).
8. S. V. Razumov and A. V. Tumarkin, Pis'ma Zh. Tekh. Fiz. **26** (16), 17 (2000) [Tech. Phys. Lett. **26**, 705 (2000)].
9. S. V. Razumov, A. V. Tumarkin, M. M. Gaidukov, *et al.*, Appl. Phys. Lett. **81**, 1675 (2002).
10. http://www.rogerscorporation.com/mwu/translations/prod.htm
11. A. Prudan, A. Kozyrev, A. Zemtsov, *et al.*, Integr. Ferroelectr. **58**, 1337 (2003).

Translated by V. Isaakyan

Technical Physics, Vol. 50, No. 9, 2005, pp. 1201–1206. Translated from Zhurnal Tekhnicheskoĭ Fiziki, Vol. 75, No. 9, 2005, pp. 95–100.

ELECTRON AND ION BEAMS, ACCELERATORS

Enhanced Effectivity of Autoresonant Acceleration of Electrons by Gaussian Laser Radiation

V. P. Milant'ev and S. P. Stepina

People's Friendship University of Russia, Moscow, 117198 Russia

e-mail: vmilantiev@sci.pfu.edu.ru

Received September 28, 2004

Abstract—The autoresonant mechanism of acceleration of relativistic electrons by combined Gaussian laser radiation, which consists of radiation of the lowest and first modes, is considered. It is shown that acceleration by combined radiation is more effective than acceleration by Gaussian beams of the lowest or the first mode. © *2005 Pleiades Publishing, Inc.*

INTRODUCTION

The cyclotron autoresonance mechanism discovered in 1962 by Kolomenskiĭ, Lebedev, and Davydovskiĭ [1, 2] forms the basis of one of the promising vacuum methods for accelerating charged particles [3–8]. The interest in the autoresonant acceleration method has increased substantially after the development of high-power laser radiation sources. According to calculations, the rate of acceleration in an autoresonant laser accelerator may be comparable to the rate of acceleration attained in plasma acceleration methods (on the order of GeV/m) [6–8]. Under definite conditions, an autoresonant accelerator may serve as a source of a femtosecond planar electron beam [7].

Theoretical analysis of the autoresonant acceleration mechanism is usually carried out by approximating accelerating laser radiation by a Gaussian beam of the lowest mode; in this case, the condition that the electric field of radiation in free space must satisfy the equation $\mathrm{div}\mathbf{E} = 0$ is not always observed. In general, laser radiation in the quasi-optical approximation is a superposition of Gauss-Hermite beams of various modes [9]. Analysis of autoresonant acceleration of electrons by a Gaussian laser beam of the first mode revealed that the rate of acceleration by the first-mode beam may be higher than by the lowest-mode beam under definite conditions [10]. This means that the choice of accelerating laser radiation of the lowest mode is not optimal. In this connection, we consider here the mechanism of autoresonant acceleration of electrons by combined laser radiation formed by the beams of the lowest and first modes. It will be shown that on the segment corresponding to acceleration, the motion of electrons can be treated as autoresonant to a high degree of accuracy and than the effectivity of acceleration by a combined laser beam can be higher that in the case of an individual laser beam of the lowest mode or the first-mode beam. The segment of autoresonant acceleration is noticeably reduced in this case.

GAUSSIAN LASER RADIATION FIELD

In the quasi-optical approximation, the Gaussian monochromatic radiation is described by a parabolic equation. In the case of axisymmetric beams propagating along the z axis, this equation has the general solution in the form of a linear superposition of modes [9]

$$A(r, z) = \exp\{-\zeta\}\sum_{m=0}^{\infty}\frac{A_m(0)}{(1+iD)^{m+1}}L_m[\zeta]. \qquad (1)$$

Here, $\zeta \equiv r^2/a^2(1 + iD)$, where $r = \sqrt{x^2 + y^2}$ is the distance from the beam axis (z axis), a is the waist of the beam, $D = 2z/ka^2 \equiv z/z_R$ is the dimensionless diffraction length, $k = 2\pi/\lambda = \omega/c$ is the wave number, ω is the wave frequency, c is the velocity of light in vacuum, $z_R = ka^2/2$ is the Rayleigh length, and $L_m(\zeta)$ are the mth order Chebyshev–Laguerre polynomials. Number m cannot be too large to remain in the range of applicability of the parabolic equation. To analyze the motion of charged particles, we must know the individual components of the accelerating radiation field. We assume that expression (1) specifies the vector potential of the electromagnetic field, while the scalar potential is determined from the Lorentz gauge condition

$$\varphi = \frac{1}{ik}\mathrm{div}\mathbf{A}.$$

The electric and magnetic field components of the Gaussian beam can be determined using the familiar formulas

$$\mathbf{B} = \mathrm{curl}\mathbf{A}, \quad \mathbf{E} = -\frac{1}{c}\frac{\partial\mathbf{A}}{\partial t} - \nabla\varphi. \qquad (2)$$

Formula (1) implies that the lowest modes have the largest amplitudes near the symmetry axis of the Gaussian beam ($|\zeta| \ll 1$) since $|A_{m+1}(0)| \le |A_m(0)|/(m + 1)$.

1063-7842/05/5009-1201$26.00

Let us consider laser radiation in the form of a superposition of two Gaussian beams, one being the beam of the lowest mode and the other the first-mode beam. Such a combined beam can be described by the formula

$$A(r,z,t) = \left[\frac{A_0(0)}{1+iD} + \frac{A_1(0)}{(1+iD)^2}(1-\zeta)\right] \times \exp\{-\zeta\}\exp\{i(kz-\omega t)\}. \quad (3)$$

We assume for simplicity that the vector potential has only one component A_x. We also represent the initial complex values of vector potential in the form

$$A_{0,1}(0) = A_{0,1}\exp\{i\alpha_{0,1}\},$$

where $A_{0,1}$ and $\alpha_{0,1}$ are the real amplitude and phase, respectively.

In this case, using formulas (2), we obtain the general expressions for the electric and magnetic field components, which have a rather intricate form:

$$E_x = E\exp\{i\Theta\}\left[1 + \frac{A_1}{A_0}\frac{B_1}{1+D^2}\exp\{i(\Psi_2-\Psi_1+\alpha)\} + \frac{4X^2}{k^2a^2(1+D^2)}\exp\{i(\Psi_3-\Psi_1)\} - \frac{2}{k^2a^2(1+D^2)}\exp\{i(\Psi_4-\Psi_1)\} + \frac{A_1}{A_0}\frac{4X^2B_3}{k^2a^2(1+D^2)}\exp\{i(\Psi_5-\Psi_1+\alpha)\} - \frac{A_1}{A_0}\frac{2B_2}{k^2a^2\sqrt{(1+D^2)^3}}\exp\{i(\Psi_6-\Psi_1+\alpha)\}\right] + \text{c.c.},$$

$$E_y = \frac{4EXY}{k^2a^2(1+D^2)}\exp\{i\Theta\}\left[\exp\{i(\Psi_3-\Psi_1)\} + \frac{A_1}{A_0}\frac{B_3}{(1+D^2)}\exp\{i(\Psi_5-\Psi_1+\alpha)\}\right] + \text{c.c.},$$

$$E_z = \frac{2EX}{ka\sqrt{1+D^2}}\exp\{i\Theta\}[\exp\{i(\Psi_7-\Psi_1)\} + \frac{A_1}{A_0}\frac{2B_2}{(1+D^2)}\exp\{i(\Psi_6-\Psi_1+\alpha)\} + \frac{2B_2}{k^2a^2(1+D^2)}\exp\{i(\Psi_6-\Psi_1)\} - \frac{A_1}{A_0}\frac{R^4}{k^2a^2(1+D^2)^2}\exp\{i(\Psi_9-\Psi_1+\alpha)\} - \frac{12A_1}{A_0}\frac{B_1}{k^2a^2\sqrt{(1+D^2)^3}}\exp\{i(\Psi_8-\Psi_1+\alpha)\}] + \text{c.c.}, \quad (4)$$

$$B_x = 0,$$

$$B_y = E\exp\{i\Theta\}\left[1 - \frac{2B_1}{k^2a^2(1+D^2)}\exp\{i(\Psi_2-\Psi_1)\} + \frac{A_1}{A_0}\frac{B_1}{\sqrt{1+D^2}}\exp\{i(\Psi_2-\Psi_1+\alpha)\} + \frac{A_1}{A_0}\frac{B_4}{k^2a^2(1+D^2)}\exp\{i(\Psi_{10}-\Psi_1+\alpha)\} - \frac{2R^4}{k^2a^2\sqrt{(1+D^2)^3}}\exp\{i(\Psi_{11}-\Psi_1+\alpha)\}\right] + \text{c.c.},$$

$$B_z = \frac{2EY}{ka\sqrt{1+D^2}}\exp\{i\Theta\}[\exp\{i(\Psi_7-\Psi_1)\} + \frac{A_1}{A_0}\frac{B_2}{(1+D^2)}\exp\{i(\Psi_6-\Psi_1+\alpha)\}] + \text{c.c.}$$

In these formulas, the following notation is introduced:

$$E = \frac{kA_0}{\sqrt{1+D^2}}\exp\left\{-\frac{R^2}{1+D^2}\right\}$$

is the Gaussian beam amplitude; $\Theta = \Theta_0 + \Psi_1 + \alpha_0$ is the Gaussian beam phase, where $\Theta_0 = kz - \omega t + R^2/(1+D^2)$;

$$\Psi_1 = \arctan\frac{1}{D};$$

$$\Psi_2 = \arctan\frac{(1-D^4)-R^2(1-3D^2)}{2D(1+D^2)-R^2D(3-D^2)};$$

$$\Psi_3 = \arctan\frac{1-3D^2}{D(3-D^2)}; \quad \Psi_4 = \arctan\frac{1-D^2}{2D};$$

$$\Psi_5 = \arctan\frac{3(D^4-6D^2+1)(1+D^2)-R^2(5D^4-10D^2+1)}{12D(1-D^4)-R^2D(D^4-10D^2+5)};$$

$$\Psi_6 = \arctan\frac{2R^2D(2-D^2)-2D(3-D^2)(1+D^2)}{2(1-3D^2)-R^2(D^4-6D^2+1)};$$

$$\Psi_7 = \arctan\frac{2D}{D^2-1};$$

$$\Psi_8 = \arctan\frac{4D(D^4-1)+DR^2(D^4-10D^2+5)}{(D^4-6D^2+1)(1+D^2)-R^2(5D^4-10D^2+1)},$$

$$\Psi_9 = \arctan\frac{2D(3D^4-10D^2+3)}{D^6-15D^4+15D^2-1};$$

$$\Psi_{10} = \frac{(3D^2-1)(1+D^2)+2R^2(D^4-6D^2+1)}{D(D^2-3)(1+D^2)+8R^2D(1-D^2)};$$

$$\Psi_{11} = \arctan\frac{5D^4-10D^2+1}{D(D^4-10D^2+5)};$$

$$B_1 = \sqrt{(R-1)^2+D^2};\quad B_2 = \sqrt{(R-2)^2+4D^2};$$

$$B_3 = \sqrt{(R-3)^2+9D^2};$$

$$B_4 = \sqrt{(2R-1)^2+D^2};$$

$\alpha = \alpha_1 - \alpha_0$ is the phase shift; $R = r/a$; $X = x/a$; and $Y = y/a$.

In the quasi-optical approximation, parameter $1/ka$ is small. Consequently, not all terms in formulas (4) are of the same order of magnitude. It can be seen that the radiation considered here is an electromagnetic wave with linear polarization, which is slightly distorted by small corrections.

EQUATIONS OF MOTION OF ELECTRONS IN THE FIELD OF COMBINED GAUSSIAN RADIATION

Let us consider relativistic motion of an electron in the field of laser radiation (4) propagating along a uniform magnetic field $\mathbf{B}_0 = (0, 0, B_0)$. To separate cyclotron rotation of the electron, we introduce the standard substitution

$$\mathbf{p} = p_\parallel \mathbf{e}_z + p_\perp(\mathbf{e}_x\cos\Theta_c + \mathbf{e}_y\sin\Theta_c). \qquad (5)$$

Here, $p_\parallel$ and $p_\perp$ are the longitudinal and transverse momentum components relative to the magnetic field direction and Θ_c is the phase of cyclotron rotation (gyrophase). The equations of motion of the electron in this field have a rather complex form. These equations contain the gyrophase, the phase of the wave, and their combinations. Such a system of equations is called a two-periodic (or two-frequency) system. In the case of a strong magnetic field, gyrophase Θ_c is treated as a fast variable. The wave phase Θ_0 is also considered to be a fast independent variable. In this case, the system of equations of motion can be simplified by averaging over fast phases [3]. The equation for the phase of the wave "seen" by the particle must be included in the system of general equations of motion of particles. In cyclotron resonance, the difference between the cyclotron frequency and the wave frequency (with Doppler shift) is very small (equal to zero at exact resonance). The difference between the corresponding fast phases in this case becomes a "slow" or "semi-fast" variable. Such a slow variable for electrons is the resonance combination of phases $\Psi_{res} = \Theta_0 + \Theta_c + \Psi_1$. Since terms of the order of $1/ka$ are small in the quasi-optical approximation, such terms can be omitted in the equations of motion for dynamic variables $p_\parallel$ and $p_\perp$. However, such small terms are significant in the equation for the resonance phase since the difference between the wave frequency and gyrofrequency is small in resonance. Under such assumptions, after averaging over fast phases (the phase of the wave and gyrophase), and over their nonresonant combinations, we can obtain a simplified system of equations of motion of an electron in the combined Gaussian beam under investigation:

$$\frac{dP_\parallel}{d\tau} = -\frac{\varepsilon P_\perp}{\gamma}\cos\Psi_{res} - \frac{A_1}{A_0}\frac{\varepsilon P_\perp B_1}{\gamma\sqrt{1+D^2}}\cos(\Psi_{res}+\Psi_{21}+\alpha),$$

$$\frac{dP_\perp}{d\tau} = \varepsilon\left(\frac{P_\parallel}{\gamma}-1\right)\cos\Psi_{res}$$

$$-\frac{A_1}{A_0}\frac{\varepsilon B_1}{1+D^2}\left(1-\frac{1}{\sqrt{1+D^2}}\right)\cos(\Psi_{res}+\Psi_{21}+\alpha),$$

$$\frac{d\gamma}{d\tau} = -\frac{\varepsilon P_\perp}{\gamma}\cos\Psi_{res}$$

$$-\frac{A_1}{A_0}\frac{\varepsilon P_\perp B_1}{\gamma\sqrt{1+D^2}}\cos(\Psi_{res}+\Psi_{21}+\alpha),$$

$$\frac{d\Theta_c}{d\tau} = \frac{\Omega}{\gamma} - \frac{\varepsilon}{P_\perp}\left(\frac{P_\parallel}{\gamma}-1\right) - \sin\Psi_{res}$$

$$-\frac{A_1}{A_0}\frac{\varepsilon B_1}{P_\perp\sqrt{1+D^2}}\left(\frac{P_\parallel}{\gamma}-1\right)\sin(\Psi_{res}+\Psi_{21}+\alpha)$$

$$-\frac{2\varepsilon\Phi_1\sqrt{1+D^2}}{P_\perp}\sin(\Psi_{res}+3\Psi_1)$$

$$+\frac{2\varepsilon B_1\Phi_1}{P_\perp}\sin(\Psi_{res}+\Psi_{21})$$

$$+\frac{2\varepsilon R^2 P_\parallel\Phi_1}{\gamma P_\perp\sqrt{1+D^2}}\sin(\Psi_{res}+9\Psi_1+\alpha)$$

$$-\frac{A_1}{A_0}\frac{\varepsilon P_\parallel B_4\Phi_1}{\gamma P_\perp}\sin(\Psi_{res}+\Psi_{51}+\alpha)$$

$$+\frac{4\varepsilon X\Phi_1}{P_\perp}(X\sin(\Psi_{res}+5\Psi_1) - Y\cos(\Psi_{res}+5\Psi_1)) \qquad (6)$$

$$-\frac{A_1}{A_0}\frac{2\varepsilon B_2\Phi_1}{\gamma P_\perp\sqrt{1+D^2}}\sin(\Psi_{res}+\Psi_{41}+\alpha)+\frac{A_1}{A_0}\frac{4\varepsilon X B_3\Phi_1}{\gamma P_\perp(1+D^2)}$$

$$\times[X\sin(\Psi_{res}+\Psi_{31}+\alpha)-Y\cos(\Psi_{res}+\Psi_{31}+\alpha)],$$

$$\frac{d\Theta_0}{d\tau}=\frac{P_\parallel}{\gamma}-1+\frac{2D\Phi_2}{1+D^2}+\frac{P_\parallel}{\gamma}\Delta,$$

$$\frac{d\Psi_1}{d\tau}=-\frac{2P_\parallel\Phi_1}{\gamma},$$

$$\frac{d\Psi_2}{d\tau}=\frac{2D\Phi_2}{B_1^2}-\frac{2P_\parallel\Phi_1}{\gamma B_1^2}[3R^2-R(D^2-5)+2(D^2+1)],$$

$$\frac{d\Psi_3}{d\tau}=\frac{6D\Phi_2}{B_3^2}-\frac{2P_\parallel\Phi_1}{\gamma B_3^2}[5R^2-3R(D^2-9)+36(D^2+1)],$$

$$\frac{d\Psi_4}{d\tau}=\frac{4D\Phi_2}{B_2^2}-\frac{8P_\parallel\Phi_1}{\gamma B_2^2}[R^2-R(D^2+2)+3(D^2+1)],$$

$$\frac{d\Psi_5}{d\tau}=\frac{4D\Phi_2}{B_4^2}-\frac{2P_\parallel\Phi_1}{\gamma B_4^2}[16R^2-2R(D^2+1)+3(D^2+1)],$$

$$\frac{dR}{d\tau}=2\Phi_2,\quad \frac{dD}{d\tau}=\frac{2P_\parallel}{k^2a^2\gamma},$$

$$\frac{dX}{d\tau}=\frac{P_\perp}{ka\gamma}\cos\Theta_c,\quad \frac{dY}{d\tau}=\frac{P_\perp}{ka\gamma}\sin\Theta_c.$$

In this system of equations, we introduced the following dimensionless quantities and parameters: momentum components $P_\parallel = p_\parallel/m_0c$, $P_\perp = p_\perp/m_0c$, where m_0 is the electron mass; dimensionless time $\tau = \omega t$; parameter

$$\varepsilon=\mu\exp\left\{-\frac{R^2}{1+D^2}\right\}/\sqrt{1+D^2},$$

where $\mu = ekA_0/m_0c\omega$ is the dimensionless amplitude of the wave; $\gamma = \sqrt{1+P_\parallel^2+P_\perp^2}$ is the relativistic factor; and parameter $\Omega = \omega_{c0}/\omega$, where $\omega_{c0} = eB_0/m_0c$ is the classical cyclotron frequency. We also introduced the notation $\Phi_1 = 1/k^2a^2(1+D^2)$,

$$\Phi_2=\frac{P_\perp}{\gamma ka}[X\cos\Theta_c+Y\sin\Theta_c],$$

$$\Psi_{ij}=\Psi_i-\Psi_j.$$

The wave phase Θ_0 is treated as an independent variable along with the gyrophase [3, 8, 10]. Consequently, system (6) also contains the equation for the wave phase, where quantity $\Delta = 2R^2(1-D^2)/k^2a^2(1+D^2)^2$ determines the mean frequency shift of the Gaussian radiation.

As in the case of a plane wave, system (6) leads to the integral [3]

$$\gamma - P_\parallel = \text{const} \equiv G.$$

If constant G is equal to Ω, relation

$$\gamma - P_\parallel = \Omega \tag{7}$$

is the condition of the cyclotron resonance of the electron with the wave, which is preserved in the case of a vacuum plane wave during the entire period of motion of the particle. This is precisely autoresonance [3]. The resonant frequency combination (7) corresponds to the combination of phases $\Theta_0 + \Theta_c$. The presence of relation (7) in system (6) is due to the fact that the abovementioned small terms were omitted. If we take into account the frequency shift in Gaussian radiation, the condition of cyclotron resonance of the particle with the wave, in accordance with Eqs. (6), will be not relation (7), but

$$\gamma - P_\parallel(\Delta+1) = \Omega. \tag{8}$$

In contrast to the case of a plane wave (with a waist $a \longrightarrow \infty$), cyclotron resonance condition (8) is not an integral of motion of system (6). This means that the condition of cyclotron resonance of a particle with a wave in a Gaussian beam is not conserved in general during the motion of the particle; consequently, the autoresonant mode is ruled out. However, numerical solution of system (6) shows that the departure from resonance in a combined Gaussian beam over a small distance is actually small, so that the motion of the particle over this distance can be approximately treated as autoresonant (Fig. 1).

NUMERICAL SOLUTION

System of equations (6) is too complicated and was solved numerically for this reason. Numerical solution was carried out using the Runge–Kutta technique for a CO_2 laser with radiation intensity $I = 1.8\times10^{15}$ W/cm^2 and wavelength $\lambda = 10.6$ μm under the cyclotron resonance condition (8) at the instant of injection. The width of the Gaussian beam was assumed to be $a = 0.16$ cm. For such parameters of the Gaussian beam, the Rayleigh length is $z_R = 75.8$ cm. The magnetic field $B_0 = 100$ kG. It should be noted that parameter Ω is very small for the laser radiation in question. This means that, if cyclotron resonance condition (8) is satisfied at the initial instant, the dimensionless longitudinal momentum of the particle being accelerated differs from the relativistic factor $P_{\parallel 0} \approx \gamma_0$ only slightly. In other words, the particles being accelerated must be ultrarelativistic. For this reason, the electron injection energy was assumed to be $E = 25.9$ MeV ($\gamma_0 = 50.8$) in our calculations.

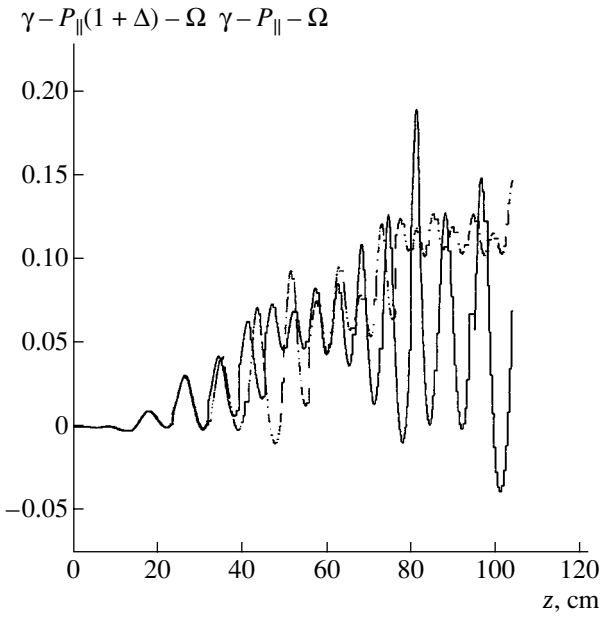

Fig. 1. Variation of the resonance frequency shift in the direction of propagation of combined radiation. The solid and dashed curves correspond to condition (8) and (7), respectively.

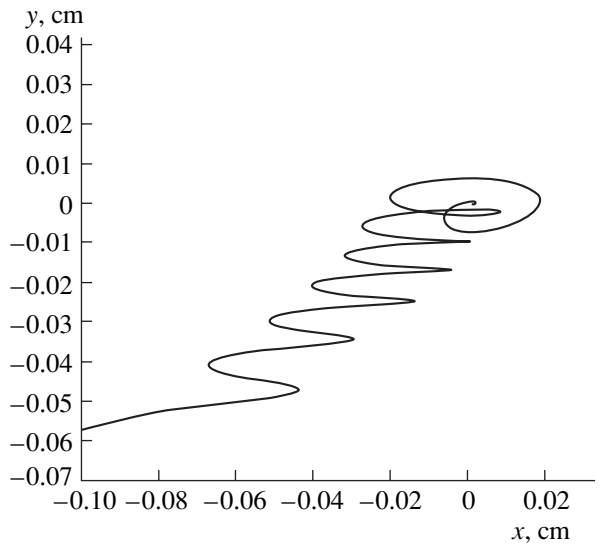

Fig. 3. Trajectory of an electron being accelerated and traversing a distance $z \approx 55$ cm in a plane perpendicular to the direction of propagation of combined Gaussian radiation.

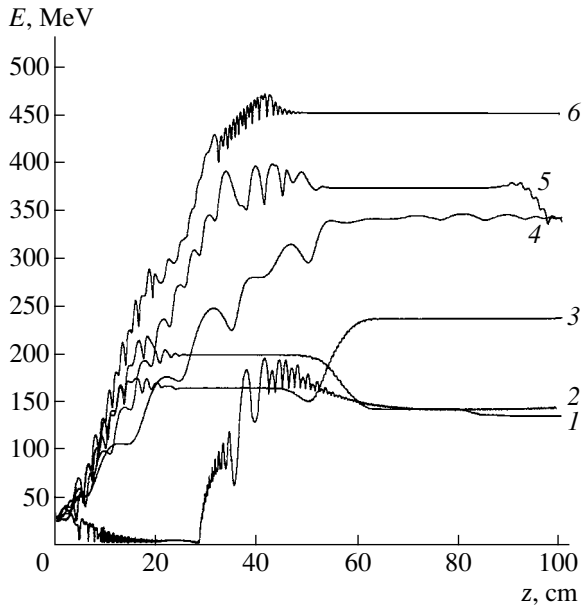

Fig. 2. Accumulation of energy by a particle in the field of a combined Gaussian beam for various ratios of the amplitudes of the first and lowest modes and for various relations between the phases: $A_1/A_0 = 1$, $\Theta_i = \Psi_i = 0$, $\alpha = \pi/2$ (*1*); $A_1/A_0 = 1$, $\Theta_i = \Psi_i = 0$, $\alpha = 0$ (*2*); $A_1/A_0 = 0.5$, $\Theta_i = \Psi_i = \pi/2$, $\alpha = \pi/2$ (*3*); $A_1/A_0 = 0.1$, $\Theta_i = \Psi_i = 0$, $\alpha = \pi/2$ (*4*); $A_1/A_0 = 0.01$, $\Theta_i = \Psi_i = 0$, $\alpha = \pi/2$ (*5*); $A_1/A_0 = 0.01$, $\Theta_i = \Psi_i = 0$, $\alpha = 0$ (*6*).

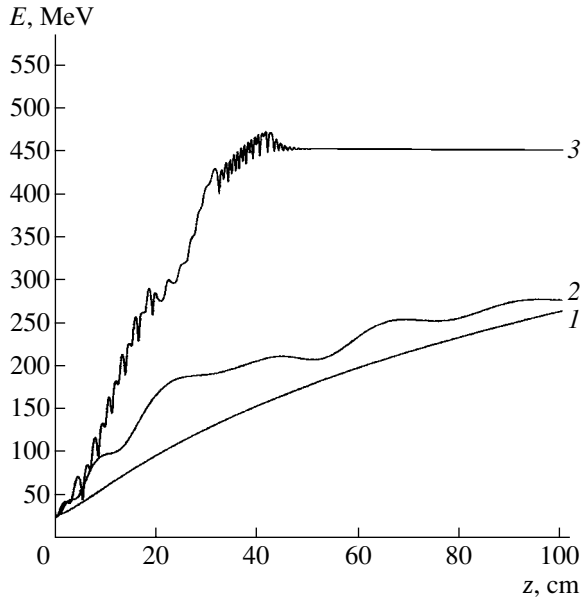

Fig. 4. Effectivity of autoresonant acceleration of electrons by Gaussian laser radiation: acceleration in the field of a Gaussian beam of the lowest mode (*1*), Gaussian beam of the first mode (*2*), and combined Gaussian beam (*3*).

We assume that the cyclotron resonance condition (8) holds exactly at the instant of injection; we consider particles starting on the symmetry axis ($x = y = 0$) of the Gaussian beam at $z = 0$. The solution of system (6) noticeably depends on the ratio of the amplitudes of the lowest- and first-mode beams, as well as on their initial phases. By way of example, Fig. 2 shows the dependence of the particle energy on the distance in the direction of propagation of Gaussian radiation for various ratios of the amplitudes corresponding to the first and zeroth modes and for various relations between the phases. It can be seen that, in a certain range of param-

eters, electrons accumulate a substantial energy over a small distance on the order of half the Rayleigh length; a tendency to saturation is observed in this case. In this respect, the autoresonant mechanism of acceleration by combined radiation basically differs from the mechanism of acceleration by radiation of the lowest mode [8] or by a Gaussian beam of the first mode [10]. The sharp decrease in the segment corresponding to acceleration in the case of combined Gaussian radiation is due to the fact that detuning from resonance occurs at an earlier stage as compared to the cases of the lowest or the first mode. This is demonstrated in Fig. 1 as well as in Fig. 3 showing the evolution of the electron trajectory in the transverse plane from the instant of its injection (at $x = y = z = 0$) to the time corresponding to $z \approx 55$ cm. It can be seen that the motion is complex by nature and the particle acquiring acceleration is rapidly displaced in the transverse direction.

Analysis of the results represented in Fig. 2 and analogous figures shows that the energy of particles interacting with combined Gaussian radiation and injected under exact cyclotron resonance conditions varies in an intricate chaotic way. Most particles injected at various phase relations acquire a substantial energy prior to detuning from resonance, while a small fraction of particles with unfavorable phases fall out of the acceleration mode. The particles acquire the maximal energy when radiation of the first mode "spoils" the field of the first mode only slightly. The interval of autoresonant acceleration of electrons by combined Gaussian radiation (about half the Rayleigh length) is smaller than in the case of Gaussian radiation of the lowest or the first mode. However, it can be seen from Fig. 4 that the rate of acceleration and the maximal energy accumulated by particles in the field of combined Gaussian radiation are much higher than in the case of radiation at the lowest or first mode. Thus, the role of radiation at the first mode of comparatively low intensity is reduced, on the one hand, to a rather rapid detuning from the cyclotron resonance of a particle with a wave and, on the other hand, to a more rapid accumulation of energy by particles.

CONCLUSIONS

The results of our calculations show that the mechanism of autoresonant acceleration of electrons by Gaussian laser radiation of the lowest mode cannot be regarded as optimal. More effective is autoresonant acceleration by combined Gaussian radiation formed by a Gaussian beam of the lowest mode and a first-mode beam with a relatively low intensity. In this case, a compact accelerator (with a length of approximately half the Rayleigh length) and a high acceleration rate can be designed. The effectivity of acceleration can be enhanced using appropriate profiling of the driving magnetic field. Probably, a cascade autoresonant accelerator will be optimal.

ACKNOWLEDGMENTS

This study was carried out under the program "Universities of Russia: Fundamental Research."

REFERENCES

1. A. A. Kolomenskiĭ and A. N. Lebedev, Dokl. Akad. Nauk SSSR **145**, 1259 (1962) [Sov. Phys. Dokl. **7**, 745 (1962)]; Zh. Éksp. Teor. Fiz. **44**, 259 (1963).
2. V. Ya. Davydovskiĭ, Zh. Éksp. Teor. Fiz. **43**, 886 (1962) [Sov. Phys. JETP **16**, 886 (1962)].
3. V. P. Milant'ev, Usp. Fiz. Nauk **167**, 3 (1997) [Phys. Usp. **40**, 1 (1997)].
4. C. Wang and Y. L. Hirshfield, Phys. Rev. E **51**, 2456 (1995).
5. Y. I. Salamin, F. H. M. Faisal, and C. H. Keitel, Phys. Rev. A **62**, 053809 (2000).
6. Y. L. Hirshfield and C. Wang, Phys. Rev. E **61**, 7252 (2000).
7. T. C. Marshall, C. Wang, and Y. L. Hirshfield, Phys. Rev. ST Accel. Beams **4**, 121 301 (2001).
8. V. P. Milant'ev and Ya. Shaar, Zh. Tekh. Fiz. **70** (8), 100 (2000) [Tech. Phys. **45**, 1054 (2000)].
9. M. B. Vinogradova, O. V. Rudenko, and A. P. Sukhorukov, *The Theory of Waves* (Nauka, Moscow, 1990) [in Russian].
10. V. P. Milant'ev and S. P. Stepina, Vopr. At. Nauki Tekh., No. 4, 40 (2003).

Translated by N. Wadhwa

Technical Physics, Vol. 50, No. 9, 2005, pp. 1207–1211. Translated from Zhurnal Tekhnicheskoĭ Fiziki, Vol. 75, No. 9, 2005, pp. 101–105.

ELECTRON AND ION BEAMS, ACCELERATORS

Generation of Multiply Charged Refractory Metals in an Electron-Cyclotron Resonant Discharge in a Direct Magnetic Trap

A. V. Vodopyanov*, S. V. Golubev*, D. A. Mansfeld*, A. G. Nikolaev, E. M. Oks**, S. V. Razin*, K. P. Savkin**, and G. Yu. Yushkov****

**Institute of Applied Physics, Russian Academy of Sciences, Nizhni Novgorod, 603950 Russia*
e-mail: avod@appl.sci.nnov.ru
***Institute of High-Current Electronics, Siberian Division, Russian Academy of Sciences, Tomsk, 634055 Russia*
Received December 15, 2004

Abstract—The possibility of additional ionization of refractory metal ions in the vacuum arc plasma injected to a magnetic trap due to additional heating of electrons by microwave radiation under the conditions of electron-cyclotron resonance is demonstrated. High-power short-wave radiation of gyrotrons used in experiment makes it possible to work with a higher (on the order of 10^{13} cm^{-3}) density of the plasma and to ensure the confinement parameter at a level of 3×10^8 cm^{-3} s at an electron temperature sufficient for multiple ionization. © *2005 Pleiades Publishing, Inc.*

INTRODUCTION

A number of problems in further development of nuclear and atomic physics (such as the synthesis of new chemical elements) require the production of high-current beams of multiply charged ions of heavy elements in view of high nuclear thresholds of nuclear reactions and low cross sections of such reactions. Since the energy of accelerated ions increases with their charge and the yield of nuclear reactions is proportional to the current in a beam of such ions, the problem of synthesis of new elements is directly connected with the development of high-current sources of multiply charged ions of heavy elements. The use of electron-cyclotron resonance (ECR) discharge in a magnetic trap of ion sources ensures generation of ion beams of gases with a strong current and a high average chargeability. For example, a Xe^{20+} beam with a current of 0.6 mA was demonstrated in [1].

ECR sources of multiply charged ions can ensure generation of ionic gas beams; however, all elements in the Periodic System heavier than xenon are in the solid state of aggregation under normal conditions. Nevertheless, multiply charged ions of heavier elements [1] which are in the solid state under normal conditions, but possess relatively low melting and boiling temperatures were obtained in a number of ECR sources. To introduce neutral atoms into an ECR source, various crucibles are used, in which the working substance is heated and evaporated. The ECR breakdown in this situation occurs in metal vapors almost in the same way as in gases. A considerable disadvantage of such a scheme is the difficulty of operation with refractory elements (with a melting point above 1500°C).

To obtain multiply charged ions of refractory metals, it is necessary to ensure local evaporation of the material, which can be done by means of a high-power laser pulse [2] or by using a vacuum arc discharge with a cathode spot [3]. The application of a vacuum arc discharge appears more expedient in the given case in view of its simplicity and effectiveness. Plasma sources based on a vacuum arc can ensure generation of metal ion beams with a current up to several amperes both in the pulsed and CW operation mode [3]. The ionic composition of the plasma is determined by the material of the cathode, which can be made of any conducting (including refractory) material. The average charge of ions in the plasma of such a source is 1.5–2 for a wide range of cathode materials [3]. Using special methods such as application of a magnetic field to the near-cathode region, additional current pulses of the arc discharge, or injection of an electron beam into the plasma of the vacuum arc, it is possible to increase the average charge of ions; however, the average chargeability of ions increases in this case only by a factor of two [4, 5].

It appears as logical to use a vacuum-arc plasma generator for injecting the plasma of refractory metals into an ECR source to further increase the degree of ionization of metallic ions in a magnetic trap upon electron heating at the electron-cyclotron resonance with the pumping wave.

Attempts at injection of the vacuum arc plasma into an ECR-based discharge system have been made earlier [6, 7]; however, a noticeable effect of additional stripping of vacuum arc plasma ions was not obtained. In our opinion, this is due to the fact that the confinement parameter $N_e\tau_i$ (N_e is the electron density and τ_i is the

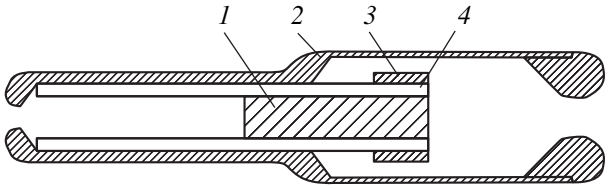

Fig. 1. Schematic of a vacuum-arc plasma generator: cathode (*1*), hollow anode (*2*), igniting electrode (*3*), and ceramic insulator (*4*).

lifetime of ions in the trap), which determines the possibility of formation of multiply charged ions, did not attain the value required for multiple ionization. Indeed, plasma was heated in these studies by microwave generators operating in the centimeter range of wavelengths, which are traditionally used for ECR sources of multiply charged ions. Accordingly, the electron density N_e in these experiments did not exceed 10^{12} cm^{-3} [8, 9].

In the case of injection of a vacuum arc plasma into a magnetic trap, the lifetime of ions in it is found to be relatively short. As a matter of fact, deceleration of a plasma jet or trapping of ions from a vacuum arc discharge into a magnetic trap is a complicated problem; apparently, the value of τ_i is determined by the trap size and the velocity of plasma flow from a vacuum-arc discharge. Since the velocity of the ion flow is approximately equal to 10^6 cm/s [3], the confinement parameter $N_e\tau_i$ did not exceed 10^8 cm^{-3} s for a 100-cm trap in the experiments described in [6, 7]; this value of the confinement parameter is obviously insufficient for the formation of multiply charged ions [10]. This fact is apparently responsible for the absence of a noticeable increase in the chargeability of ions in the experiments described in [8, 9]. At the same time, the lifetime of ions in the magnetic trap in traditional ECR sources in experiments with gases attains several milliseconds, while the value of the confinement parameter exceeds 10^9 cm^{-3} s.

This study is devoted to analysis of generation of multiply charged ions of refractory metal in a plasma with substantially higher density, which is achieved by using a more powerful gyrotron (up to 100 kW) as well as a shorter-wave radiation (f = 37.5 GHz). It should be noted that, in accordance with estimates obtained using the method developed in [11], the intensity of microwave radiation must be at a level of tens of kW/cm^2 for maintaining the electron temperature in the discharge at a level optimal for the formation of multiply charged ions. Such intensity can easily be attained using modern gyrotrons [12].

1. EXPERIMENTAL SETUP

The experiments were performed on the ECR experimental test bench at the Institute of Applied Physics, Russian Academy of Sciences. A special miniature plasma generator was constructed at the Institute of High-Current Electronics, Siberian Division, Russian Academy of Sciences, for studying additional ionization of multiply charged ions of metals of a vacuum-arc discharge in a magnetic trap with electron heating under the ECR conditions. The design of this generator is shown schematically in Fig. 1. A vacuum-arc discharge initiated by an auxiliary discharge over the surface of a dielectric generates a plasma of the material of cathode *1*, which fills hollow anode *2*. The cathode is made of platinum. As the dielectric, we used a thin ceramic tube *4* mounted between cathode *1* and anode *3* of the auxiliary discharge. For an electrode gap of the auxiliary discharge of ~1 mm, it is sufficient to apply a voltage pulse of 7 kV with a duration of 10–30 μs between the cathode and the igniting electrode for exciting cathode spots and initiating a vacuum arc.

The block diagram of the setup is shown in Fig. 2. Plasma generator *1* was mounted on the axis of the system in the vicinity of one of the magnetic mirrors of the trap formed by two coils *2*. The power source of the plasma generator ensured a current pulse of an arc discharge with a duration ~100 μs; the current could be varied from 80 A to 3 kA. The power source was placed

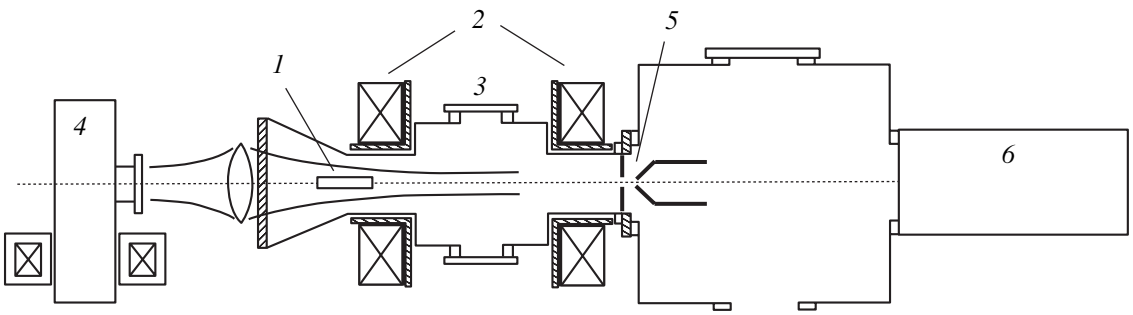

Fig. 2. Block diagram of the experimental setup: plasma generator (*1*); 27-cm-long magnetic trap with a mirror ratio of 5, the field at the mirrors is up to 3 T (*2*); discharge vacuum chamber on a high-voltage platform (*3*); gyrotron (*4*); two-electrode extractor with an aperture of 1 mm and an extraction voltage up to 10 kV (*5*); and magnetostatic ion beam analyzer with an ion charge/mass parameter of 15–20 (*6*).

on a high-voltage platform since an ion-accelerating voltage up to 10 kV was applied to the anode of the plasma generator connected to the discharge chamber. Discharge vacuum chamber *3* placed in the magnetic trap had a Teflon window through which radiation from gyrotron *4* was introduced to the discharge region (radiation frequency 37.5 GHz, power up to 100 kW, and pulse duration 1.5 ms). Microwave radiation interacting with electrons of the plasma under the ECR conditions noticeably increased their energy, which in turn led to additional ionization of ions by electron impacts. Two-electrode extractor *5* mounted at a distance of 14 cm behind the second magnetic mirror of the trap was intended for accelerating ions. The ionic beam formed in this way was fed to magnetostatic analyzer *6*, where the ionic chargeability spectrum was measured.

2. ESTIMATION OF THE PARAMETER OF PLASMA CONFINEMENT IN THE MAGNETIC TRAP

The velocity of ions in the vacuum-arc discharge plasma is one of the main parameters determining the effectiveness of generation of multiply charged ions in the system studied here. For a fixed size of the magnetic trap, this velocity determines the time of interaction of hot electrons with metal ions and, accordingly, the degree of ionization of these ions. Another important parameter characterizing the operation of the system is the density of the plasma getting to the magnetic trap from the plasma generator. Preliminary experiments were performed to determine these parameters.

It is well known that the presence of a magnetic field in the cathode region of a vacuum-arc discharge increases the discharge voltage and, accordingly, the velocity of ions emitted by cathode spots [13]. The time of interaction between hot electrons and the vacuum-arc discharge plasma was estimated from analysis of extraction current oscillograms for various values of the magnetic field of the trap (Fig. 3). It was found that the velocities of ions increase with the magnetic field in the region of the vacuum-arc discharge. The magnetic-field dependence of the velocity of ions obtained from such oscillograms is shown in Fig. 4. As in [13], we also detected a substantial increase in the voltage of the vacuum arc upon an increase in the magnetic field (Fig. 5), which also served as an indirect evidence of the increase in the velocity of ions in the plasma jet emitted by the cathode spots during the vacuum-arc discharge. Our measurements show that the effect of the magnetic field on the vacuum arc voltage and on the velocity of ions in the plasma jet has a tendency to saturation in magnetic field exceeding 1.5 T; consequently, we can assume in our estimates that the average velocity of platinum ions is $V_{Pt} \approx 1.5 \times 10^6$ cm/s. Thus, the time of interaction of platinum ions with hot electrons in the trap is $\tau_i = L_{trap}/V_{Pt} \approx 18$ μs, where $L_{trap} = 27$ cm is the length of the trap.

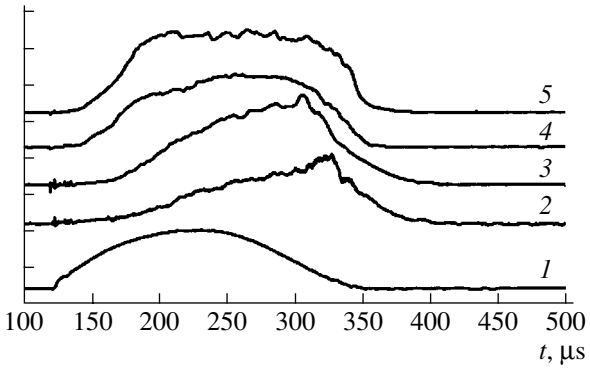

Fig. 3. Oscillograms: vacuum-arc discharge current (*1*), ion extraction currents for magnetic fields of 0, 1.5, 1.8, and 2.6 T in the magnetic trap mirror, respectively (*2*–*5*). The peak current in the arc is 150 A.

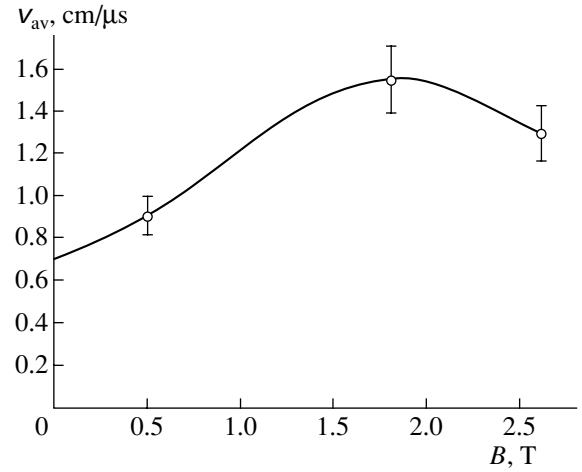

Fig. 4. Average flow velocity of the vacuum-arc discharge plasma as a function of the magnetic field at the trap mirrors. The arc current is 150 A.

The plasma density in the vacuum arc discharge in the magnetic trap can be estimated from the absolute value of the current of ions extracted from the plasma. For example, for a vacuum-arc current of 115 A, a current of $I_{extr} = 2.5$ mA passes through a hole of diameter $d_{extr} = 1$ mm (i.e., through an area of $S_{extr} = 7.8 \times 10^{-3}$ cm^2) in the plasma electrode of the extractor. Consequently, the plasma density is $N_e \approx I_{extr}/(V_{Pt} e S_{extr}) \approx 1.3 \times 10^{12}$ sm^{-3}, where e is the electron charge. If we assume that plasma propagates from the plasma generator to the extractor only along magnetic field lines, the plasma density in the region of the magnetic mirrors of the trap will be $N_e \approx 3.7 \times 10^{12}$ cm^{-3}.

At the same time, the plasma density may vary over wide limits due to a change in the vacuum arc current. If we assume that a density of 1.7×10^{13} cm^{-3}, which is the critical density for a microwave radiation frequency of 37.5 GHz, is optimal for ECR heating, the confine-

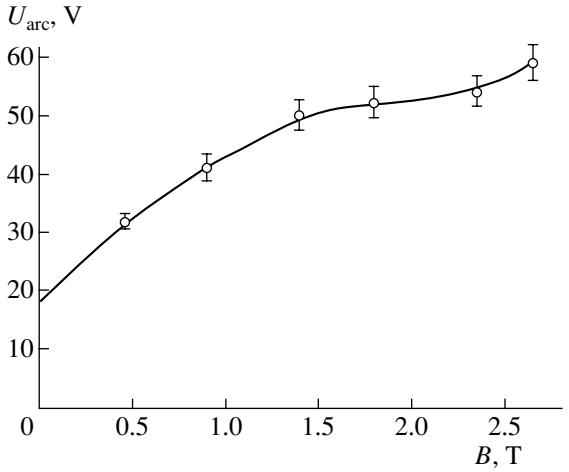

Fig. 5. Arc voltage as a function of the magnetic field at the magnetic trap mirrors. The arc current is 150 A.

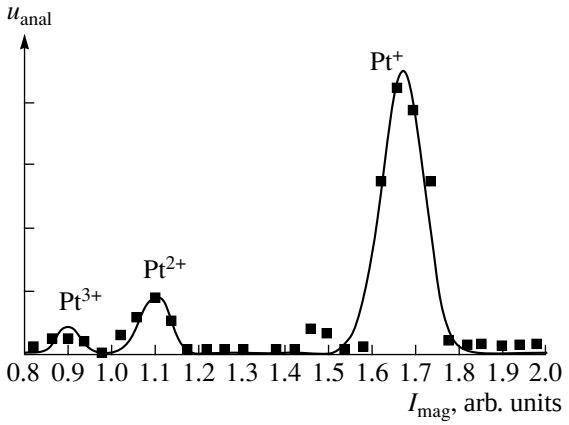

Fig. 6. Charge state distribution of platinum ions in vacuum-arc discharge plasma in the magnetic field of the trap. The arc current is 140 A, and the magnetic field at the mirror traps is 1.3 T.

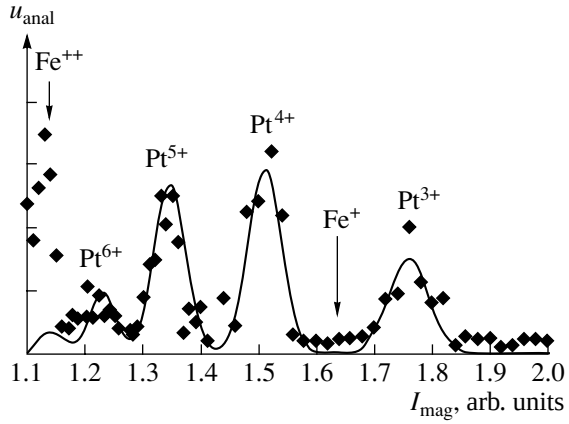

Fig. 7. Charge spectrum of platinum for optimal parameters: vacuum arc current 80 A, magnetic field at the trap mirrors 2.6 T, and introduced microwave power 63 kW.

ment parameter is $N_e\tau_i \approx 3 \times 10^8$ cm^{-3} s. Such a confinement parameter for ions suggests substantial additional ionization of metal ions provided that the electron temperature is sufficient for this process.

3. GENERATION OF MULTIPLY CHARGED METAL IONS IN A MAGNETIC TRAP WITH ECR HEATING

We carried out experiments on additional ionization of refractory metal ions in a vacuum arc discharge plasma in a magnetic trap with ECR electron heating by radiation from a gyrotron with a platinum cathode. The melting point of platinum is 1600°C. For recording the chargeability distribution of ions, an extractor was mounted and an ion-beam analyzer was used in the system. The typical voltage applied to the discharge chamber was +3.5 kV. With such an accelerating voltage, the resolving power $(q/m)/\Delta(q/m)$ of the analyzer, where q and m are the ion charge and mass, respectively, is sufficiently high and amounts to 15. At the same time, the ions of heavy elements under investigation, beginning from a charge of +3, remain in the working range of the electromagnet rotating the beam (the maximal current of the electromagnet is determined by the potentialities of a stabilized dc source).

In our experiments, the following parameters were varied: the vacuum-arc discharge current, the magnetic field in the trap, and the microwave radiation power. Figure 6 shows the chargeability distribution of platinum ions in the absence of microwave pumping. In this case, the average charge is 1.2. To obtain the maximal average charge of platinum ions in experiments with ECR heating, we had to reduce the vacuum-arc discharge current to the minimal possible value and to choose the optimal microwave power. The maximal average chargeability, which is equal to 4.3 for platinum ions, was attained for a vacuum-arc current of 80 A, a magnetic field of 2.6 T at the magnetic trap mirrors, and a microwave power at a level of 60 kW (Fig. 7). For convenience of comparison, Fig. 8 shows a histogram on which the two spectra are combined.

DISCUSSION

The ECR heating of electrons in a metal plasma by microwave radiation leads to additional stripping of ions and elevates the plasma density. The above estimates show that for an arc current of 115 A, the plasma generator fills the magnetic trap with a plasma with a density at a level of 4×10^{12} cm^{-3}; the ion charge can be increased in this case by a factor of four, the electron density in the plasma increasing in the same proportion. As a result, the plasma density in the trap may exceed the critical value corresponding to the microwave pumping frequency (1.7×10^{13} cm^{-3}), and the heating of the electron component of the plasma becomes less effective than in the case of a subcritical density [14]. Consequently, the reduction of the vacuum-arc dis-

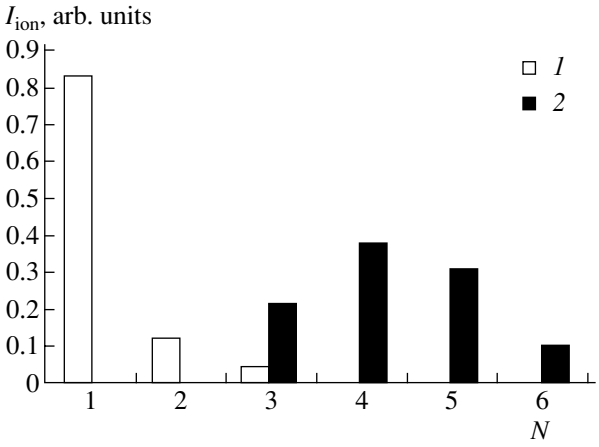

Fig. 8. Charge spectra of platinum ions in vacuum-arc discharge plasma: without microwave pumping (*1*) and with it (*2*); *N* is the degree of ionization.

charge current to a level of 80 A is optimal for the formation of multiply charged metallic ions.

On the one hand, an increase in the microwave pumping power increases the electron temperature and thus improves the conditions for the formation of multiply charged ions. On the other hand, the discharge begins to develop in magnetic trap regions more and more remote from the axis; this in turn leads to a strong increase in the plasma density due to impurities desorbed from the vacuum chamber walls, which may result in a decrease in the electron temperature. This is probably the reason for the existence of optimal microwave radiation power in experiments.

Analysis of mass-charge spectra shows that the plasma contains a large amount of impurities. These are mainly Fe, Ni, and Cr ions present in the stainless steel from which the anode of the plasma generator is made as well as gas ions (H, O, and N). The Fe, Ni, and Cr ions get into the plasma mainly as a result of erosion of the anode, while gases come from the residual atmosphere due to adsorption at the cathode surface between the discharge pulses as a result of a relatively low discharge pulse repetition rate [15], which was 1/20 s^{-1} in the experiments.

At the same time, the experimentally attained value of confinement parameter $N_e\tau_i = 3 \times 10^8$ cm^{-3} s^{-1} approximately corresponds to the maximal ion charge [10]. The current density of the ion beam that can be extracted from such a plasma is $J_e = eN_eV_{Pt} \approx 4$ eA/cm^2. At present, we are not aware of a source capable of generating multiply charged ions of refractory metals with the degree of ionization attained in our experiments, and the current density of the ion beam that can be extracted from such a plasma is several orders of magnitude higher than the corresponding value for the available sources of multiply charged ions.

ACKNOWLEDGMENTS

This study was partly supported by the grants from AFGIR (no. TO-016-02) and from the President of the Russian Federation (no. MD-148.2203.02).

REFERENCES

1. T. Thuillier, J. Bouly, J. Curdy, *et al.*, in *Proceedings of the 15th International Workshop on Electron Cyclotron Resonance (ECR) Ion Sources, Jyväskylä, Finland, 2002*, pp. 13–16.
2. S. Gammino, L. Torrisi, G. Giavola, *et al.*, J. Appl. Phys. **96**, 2961 (2004).
3. G. A. Mesyats and S. A. Barengol'ts, Usp. Fiz. Nauk **172**, 1113 (2002) [Phys. Usp. **45**, 1001 (2002)].
4. E. M. Oks, IEEE Trans. Plasma Sci. **30**, 202 (2002).
5. V. A. Batalin, A. S. Bugaev, V. I. Gushenets, *et al.*, J. Appl. Phys. **92**, 2884 (2002).
6. M. Cavenago, T. Kulevoy, and A. Vassiliev, Rev. Sci. Instrum. **69**, 795 (1998).
7. P. Spadtke, private communication.
8. R. Geller, *Electron Cyclotron Resonance Ion Sources and ECR Plasmas* (Inst. Phys. Publ., Bristol, 1996).
9. R. Geller, Rev. Sci. Instrum. **69**, 1302 (1998).
10. K. S. Golovanivskiĭ, Prib. Tekh. Éksp., No. 5, 7 (1985).
11. V. Semenov, V. Skalyga, A. Smirnov, and V. Zorin, Rev. Sci. Instrum. **73**, 635 (2002).
12. A. L. Goldenberg and A. G. Litvak, Phys. Plasmas **2** (Part 2), 2562 (1995).
13. A. Anders and G. Yu. Yushkov, J. Appl. Phys. **91**, 4824 (2002).
14. T. H. Stix, *The Theory of Plasma Waves* (McGraw-Hill, New York, 1962; Atomizdat, Moscow, 1965).
15. G. Yu. Yushkov and A. Anders, IEEE Trans. Plasma Sci. **26**, 220 (1998).

Translated by N. Wadhwa

Technical Physics, Vol. 50, No. 9, 2005, pp. 1212–1216. Translated from Zhurnal Tekhnicheskoĭ Fiziki, Vol. 75, No. 9, 2005, pp. 106–110.

SURFACE, ELECTRON AND ION EMISSION

Interaction of Iron Atoms with the Si(100)-2 × 1 Surface

M. V. Gomoyunova*, I. I. Pronin*, D. E. Malygin*, S. M. Solov'ev*, D. V. Vyalykh, and S. L. Molodtsov****

** Ioffe Physicotechnical Institute, Russian Academy of Sciences, ul. Politekhnicheskaya 26, St. Petersburg, 194021 Russia*

e-mail: Marina.Gomoyunova@mail.ioffe.ru

*** Institut für Oberflächen- und Mikrosructurphysik, Technische Universität Dresden, Dresden, D-01062 Germany*

Received January 27, 2005

Abstract—Interaction of iron atoms with the Si(100)-2 × 1 surface at room temperature is studied by core-level photoelectron spectroscopy using synchrotron radiation for Fe coverages ranging from a fraction of a monolayer to six monolayers. It is shown that the Fe/Si(100)-2 × 1 interface is chemically active: the Fe–Si solid solution forms early in deposition of iron on silicon. When the Fe coverage reaches four to five monolayers, the state of the system is changed and Fe_3Si silicide arises. © *2005 Pleiades Publishing, Inc.*

INTRODUCTION

Low-dimensional structures emerging when iron atoms interact with a single-crystalline silicon surface are of great interest both for depositing thin metal films with unusual magnetic properties and for growing β-$FeSi_2$/Si epitaxial layers, which are promising for advanced optoelectronic silicon devices [1]. However, the data obtained up to now are contradictory in many ways: results obtained under similar experimental conditions differ. This is especially true for initial stages of Fe–Si(100)-2 × 1 interaction at room temperature [2–8]. It was argued [2, 3] that, when the coverage is less than several monolayers (MLs) at room temperature, an iron film grows almost layer by layer and iron silicides do not form. Contrary to this, it was reported [4] that Fe atoms react with the substrate to produce iron-enriched Fe_3Si silicide even at the early stage of iron deposition, whereas a metal film forms once the iron coverage exceeds five MLs. At the same time, according to [5], a Fe_3Si film appears once the iron coverage exceeds four MLs and continues growing to coverages of 10 MLs. In [6], it is stated that Fe and Si atoms merely mix up when the iron coverage is within several MLs. Intermixing of adsorbate and substrate atoms giving rise to the formation of a film with an average composition of FeSi was also reported in [7]. Finally, the growth of Fe_5Si_3 silicide very early at iron deposition was observed in [8]. These discrepancies testify that investigation into the interaction of iron atoms with the silicon surface is a challenge, since this process is highly sensitive both to the conditions of adsorbate deposition and to the procedure of substrate preparation.

An effective method of studying this process is high-resolution photoelectron spectroscopy using synchrotron radiation [9]. To the Fe/Si(100)-2 × 1 system, this method was applied only in [10]. However, the Si 2*p* spectra were not resolved into components: the conclusions drawn in that work were based only on visual analysis of the data.

Here, this method is used to study iron–Si(100)-2 × 1 interaction at room temperature. The experiments were performed for iron coverages ranged from a fraction of an ML to 6 MLs. The spectra of valence and core 2*p* electron spectra are measured and analyzed.

1. EXPERIMENTAL

The measurements were performed at the Russian–German channel of the BESSY II storage ring (Berlin). An ultra-high-vacuum photoelectron spectrometer with an energy resolution of 130 meV (with allowance for the nonmonochromaticity of the photon beam) was employed. The photoelectrons leaving the cone placed normally to the surface were recorded. The samples to be tested were prepared of KÉF-1 (phosphorus-doped with a resistivity of 1 Ω cm) single-crystalline silicon wafers with their surfaces misoriented relative to the (100) face by less than 0.1°. Prior to loading into the chamber of the spectrometer, the samples were chemically treated according to the Shiraki procedure [11]. Then, they were rapidly heated in an ultrahigh vacuum to 1200°C and slowly cooled down with a rate not exceeding 50°C/min. Such a procedure provides a reconstructed Si(100)-2 × 1 surface free of carbon and oxygen contaminants. The elemental composition of the sample surface was monitored by photoelectron spectroscopy.

Room-temperature evaporation of iron on the surface of the crystal was carried out using a thoroughly degassed source in which the evaporating material (a

rod of high-purity iron) was heated by electron bombardment. The rate of evaporation was about 1 ML/min. An iron layer with an atom surface density of 6.8×10^{14} at/cm^2, which corresponds to the density of silicon atoms on the substrate surface, was taken for one monolayer. All photoemission spectra were taken at room temperature at a residual pressure not exceeding 1.2×10^{-8} Pa. Most of Si 2*p* spectra were taken at photon energy $h\nu$ = 130 eV. At this energy, the spectra are the most sensitive to surface conditions [12]. The fact is that, under such conditions, silicon 2*p* photoelectrons gain a kinetic energy of ≈30 eV, at which their inelastic scattering mean free path is the lowest (λ = 3–4 Å [12–14]) and, thus, so is their escape depth from the crystal. However, to properly estimate the thickness of the surface layer where iron-induced changes take place, a series of volume-sensitive spectra were also taken at a photon energy of 112 eV.

2. RESULTS AND DISCUSSION

2.1. Photoemission of Valence Electrons

Figure 1 shows typical spectra of photoexcited valence electrons taken at $h\nu$ = 130 eV during iron evaporation on the Si(100)-2 × 1 surface at room temperature. All the curves are normalized to their maximal intensity. The spectra are seen to change considerably with the adsorbate dose. At the first stage of evaporation (submonolayer coverage), the structure characteristic of the pure silicon surface gradually disappears. As the coverage reaches 1 ML, the sample surface becomes metallized and remains such during subsequent evaporation. Simultaneously, a new peak arises near an electron binding energy of ≈0.6 eV. Its intensity sharply grows with coverage, and this feature dominates in the spectrum. This peak is similar in shape to that observed in the spectrum of bulk iron [4, 5].

When the coverage exceeds 4 MLs, the spectrum changes radically again. Instead of the intense sharp maximum at 0.6 eV, a broad flat maximum appears, covering the binding energy interval between 0.5 and 2 eV (Fig. 1, curve *7*). This indicates a modification of the electronic structure of the sample surface as the iron coverage varies between 4 and 6 MLs.

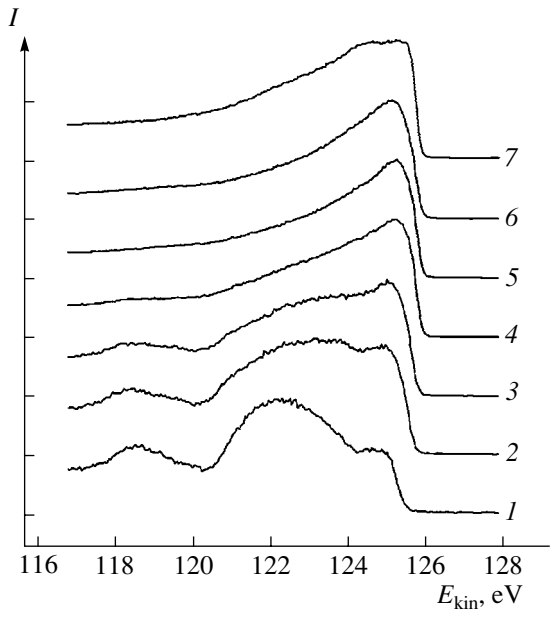

Fig. 1. Valence electron spectra taken at excitation energy $h\nu$ = 130 eV after deposition of iron on the Si(100)-2 × 1 surface. The iron coverage is (*1*) 0 (as-prepared Si(100)-2 × 1 surface), (*2*) 0.25, (*3*) 0.5, (*4*) 1, (*5*) 2.5, (*6*) 4, and (*7*) 6 MLs.

2.2. Photoemission of Silicon Core 2p Electrons

The changes occurring in the Si 2*p* electron spectra during adsorbate deposition are illustrated in Fig. 2. Since the intensity of the substrate lines noticeably drops with amount of the metal deposited, the spectra are normalized to their maximal intensity for convenience of comparison. As follows from Fig. 2, when the iron coverage reaches ≈0.5 ML, the feature observed in the spectrum of pure silicon at $E_{kin} \approx 27$ eV disappears. In [15], this feature was assigned to the upper atoms of dimers on the reconstructed Si(100)-2 × 1 surface [15]. By analogy with cobalt deposition on the same silicon

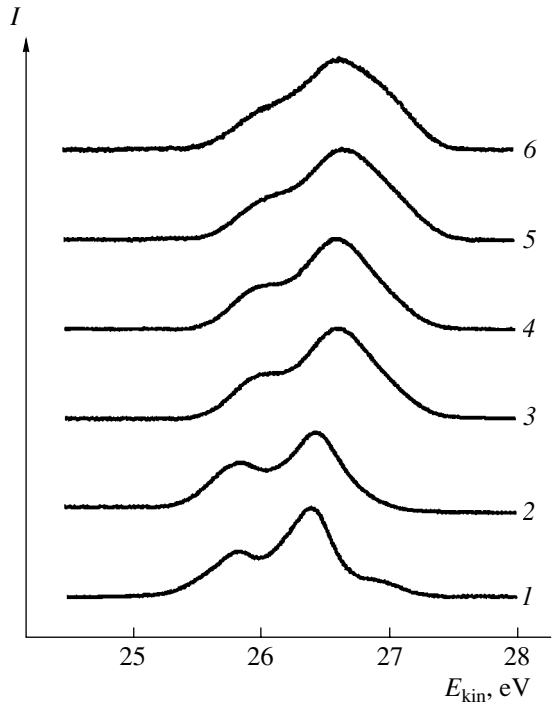

Fig. 2. Si 2*p* photoelectron spectra taken at $h\nu$ = 130 eV after deposition of iron on the Si(100)-2 × 1 surface. The iron coverage is (*1*) 0 (as-prepared Si(100)-2 × 1 surface), (*2*) 0.5, (*3*) 1.0, (*4*) 2.5, (*5*) 4, and (*6*) 6 MLs.

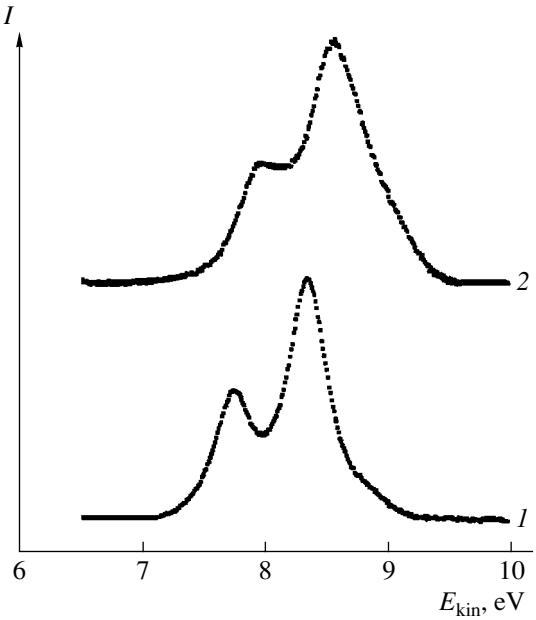

Fig. 3. Si 2*p* photoelectron spectra taken at $h\nu$ = 112 eV (*1*) for the as-prepared Si(100)-2 × 1 surface and (*2*) for the surface covered by 6 ML of Fe.

surface [16], we can conclude that the adsorption of iron atoms prevents the reconstruction of the Si(100)-2 × 1 surface.

The deposition of 1 ML of Fe atoms causes a significant broadening of both sublevels in the Si 2*p* doublet. With an increase in the metal dose, the doublet broadens further and the splitting of the levels becomes less pronounced. Also, the maxima of the spectrum shift toward higher kinetic energies (lower binding energies) of electrons. The most profound changes in the spectrum appear after the deposition of 6 MLs of iron (Fig. 2, curve *6*). The same dynamics is observed in the case of the Si 2*p* spectra taken at excitation energy $h\nu$ = 112 eV (Fig. 3). It is evident from Fig. 3 that iron deposition also changes, although in a smaller extent, the volume-sensitive spectrum of the sample. Hence, not only the surface of the sample but also deeper seated layers are modified.

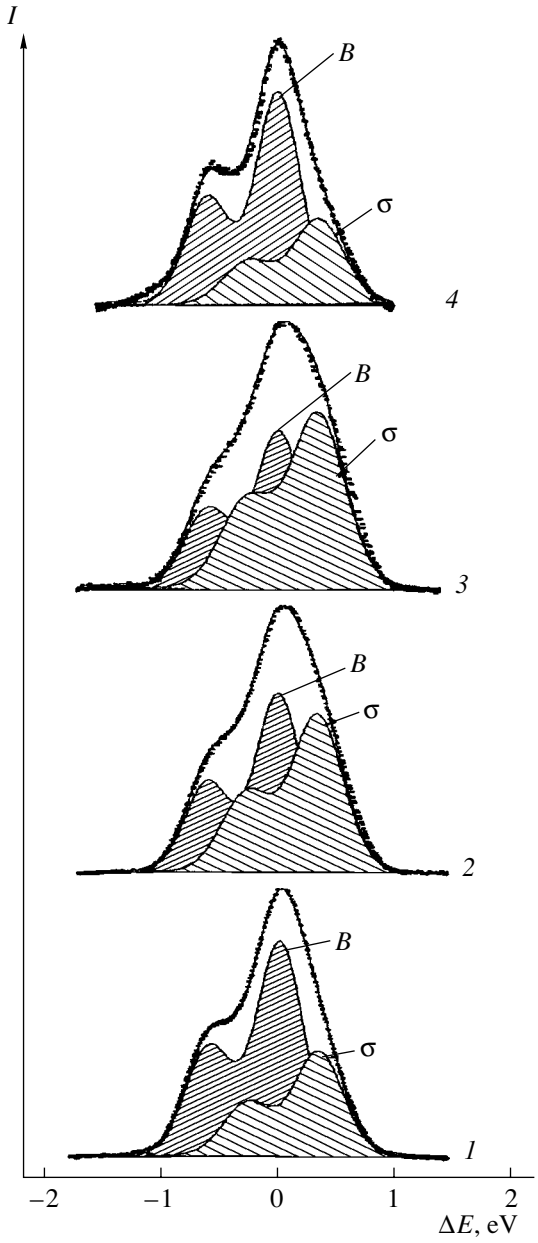

Fig. 4. Results of computer simulation of the Si 2*p* spectra for the Si(100)-2 × 1 surface after deposition of iron atoms. The iron coverage is (*1*) 2.5, (*2*) 4, and (*3*, *4*) 6 MLs. Curves *1–3* are measured at $h\nu$ = 130 eV; curve *4*, at $h\nu$ = 112 eV.

DISCUSSION

To gain information on atomic processes taking place on the Si(100)-2 × 1 surface during iron evaporation, we resolved the Si 2*p* spectra by computer simulation. It was assumed that each spectrum is a sum of the bulk and surface spin–orbit doublets with a splitting of 608 meV between the $2p_{3/2}$ and $2p_{1/2}$ sublevels. The intensity ratio for these sublevels was set equal to two, in accordance with their occupations. The modes of the spectra were described in terms of the Voigt functions, which are usually applied in core-level spectroscopy [12]. These functions represent the convolutions of the Lorentz functions, which take into account the hole lifetime on a core level, and Gaussian distributions, which describe the phonon broadening of the lines and the energy resolution of an instrument. In simulation of the spectra, we varied the energy positions, widths, and relative intensities of the lines.

Figure 4 shows three surface Si 2*p* spectra taken at three iron coverages (curves *1–3*) and the volume spectrum corresponding to the maximal amount of the deposited iron (curve *4*). All the spectra are normalized

to their maxima. It is seen that the spectra consist of two components: volume component *B* of silicon, which decays with coverage, and new component σ with a negative energy shift of –0.32 eV, which remains virtually unchanged throughout the range of coverages. Component σ increases with iron coverage, with its intensity exceeding that of component *B* in the surface-sensitive spectrum after deposition of 6 Fe ML. It should be emphasized that this increase is not only relative but also absolute. As for the contribution of component σ to the volume-sensitive spectrum (Fig. 4d), its intensity exceeds the sum of the contributions from all the surface components to the spectrum of the Si(100)-2×1 surface, which are attributed to the atoms of three upper silicon monolayers, although σ component in the volume-sensitive spectrum is less intense than in the surface-sensitive one.

From the above, it unambiguously follows that the growth of a metal film on the Si(100)-2×1 surface does not follow the layer-by-layer mechanism during iron deposition. Indeed, if such were the case, the intensity from the Fe/Si intermediate layer (appearing after the formation of a 1-ML-thick coating) would have decreased in the same manner as the intensity of the volume component at subsequent deposition of the metal. Above, however, it was noted that the intensity of component σ, on the contrary, increases, indicating the growth of a new silicon phase on the crystal surface. Thus, Fe atoms deposited on the Si(100)-2×1 surface interact with it to form a new phase consisting of silicon and iron atoms. Since the contribution of this phase to the volume-sensitive spectrum is somewhat higher than the total contribution of three upper silicon monolayers on the clean Si(100)-2×1 surface, the thickness of the Fe/Si layer formed after deposition of 6 Fe MLs is bound to far exceed three monolayers; therefore, this phase is not a surface phase.

As was indicated above, when the iron coverage is between 2 and 4 MLs, the intense peak at a binding energy of 0.6 eV prevails in the valence electron spectra. This peak is very much alike the one due to the 3*d* iron states that is observed in the pure iron spectrum. In our spectra, this feature seems to be associated with the same states. If so, the new phase could be reasonably identified with an iron-enriched Fe–Si solid solution. The fact that the energy shift of component σ is close to the value found for the Co–Si solid solution [17–20] also counts in favor of this assumption, especially with regard to similarity between the chemical properties of Fe and Co. The negative sign of the shift can be explained by an increase in the relaxation shift (contribution of interatomic relaxation) at the semiconductor–metal transition (by analogy with the formation of the Co–Si solid solution [20]).

As indicated above, the valence electron spectrum taken after deposition of 6 Fe ML undergoes significant changes, suggesting the onset of a new stage in the formation of the system. At this stage, the valence electron spectrum (Fig. 1, curve *7*) closely approximates that of Fe_3Si [5, 21]. Based on this similarity, we assign the phase formed at this stage to Fe_3Si silicide, which, as well as the Fe–Si solid solution, is enriched by iron. However, this means that, during iron deposition on the Si(100)-2×1 surface, Fe_3Si silicide starts forming once a certain critical dose of iron atoms has been accumulated. The idea that silicon and metal atoms mix up only after a critical amount of the deposited metal has been reached was put forward even in [22]. According to [22], this dose is necessary for surface metallization when delocalized conduction electrons start screening Si–Si bonds, loosening them and, thereby, facilitating intermixing of the elements in the system. However, in our case, metallization begins considerably earlier than the formation of silicides. In this respect, our results correlate with data in [5], where (see the introduction) the silicide formation was observed after deposition of 4 Fe MLs. It should also be borne in mind that, in [5], a monolayer was calculated as the atomic density on the Fe(100) face, i.e., corresponded to 1.21×10^{15} at/cm^2. Therefore, our results are in good agreement with the data in [5]. It seems likely that, at such amount of the iron deposit, the transition of the disordered Fe–Si solid solution to a more ordered state with a certain local stoichiometry is energetically favorable.

It should also be mentioned that no shift of component σ was observed during the formation of Fe_3Si silicide. A possible explanation is that the Si 2*p* components in the spectra of the Fe–Si solid solution and Fe_3Si silicide are closely spaced. As far as we know, no reliable (reference) publications concerning the energy shift of this silicide mode are available. Next, the absence of the shift can be related to different depths from which analytical data for core-level and valence electrons are extracted. Indeed, the escape depth of valence electrons far exceeds that for Si 2*p* core electrons. However, the transformation of the resulting Fe–Si solid solution into Fe_3Si silicide seems to originate at the interfacial layer. Therefore, it is not improbable that the surface modification covers the near-surface region of the solid solution only partly and 2*p* core electrons that have a very small escape depth do not as yet "sense" the modified part, whereas the contribution of this part to the valence electron photoemission already prevails.

CONCLUSIONS

Our results obtained by photoelectron spectroscopy using synchrotron radiation agree with the conclusions made in [5]; namely, during deposition of iron atoms on the Si(100)-2×1 surface, Fe_3Si silicide starts forming only after a certain critical dose of iron atoms (5–6 MLs) has been reached. However, the reactivity of the Fe/Si interface shows up at lower iron coverages, when the formation of the Fe–Si solid solution begins. Its associated negative energy shift in the Si 2*p* spectrum is

found to be –0.32 eV and, according to the published data, falls into the range of values determined for the Co–Si solid solution. However, since in the case of room-temperature cobalt deposition on the Si(100)-2 × 1 surface the silicides do not form, the reactivity of the Fe/Si interface is higher than that of the Co/Si one.

ACKNOWLEDGMENTS

This work was supported in part by the Russian Foundation for Basic Research (project no. 04-02-17651) and the program "Russian–German Laboratory Based on BESSY."

REFERENCES

1. E. G. Michel, Appl. Surf. Sci. **117–118**, 294 (1997).
2. J. Alvarez, J. J. Hinarejos, E. G. Michel, *et al.*, Surf. Sci. **251–252**, 59 (1991).
3. J. M. Gallego and R. Miranda, J. Appl. Phys. **69**, 1377 (1991).
4. J. Alvarez, J. J. Hinarejos, E. G. Michel, *et al.*, Phys. Rev. B **45**, 14042 (1992).
5. R. K. Kläsges, C. Carbone, W. Everhardt, *et al.*, Phys. Rev. B **56**, 10801 (1997).
6. P. Bertoncini, P. Wetzel, D. Berling, *et al.*, Phys. Rev. B **60**, 11123 (1999).
7. K. Konuma, J. Vrijmoeth, P. M. Zagwijn, *et al.*, J. Appl. Phys. **73**, 1104 (1993).
8. M. Hasegama, N. Kobayeshi, N. Hayashi, *et al.*, Surf. Sci. **357–358**, 931 (1996).
9. M. V. Gomoyunova and I. I. Pronin, Zh. Tekh. Fiz. **74** (10), 1 (2004) [Tech. Phys. **49**, 1249 (2004)].
10. J. M. Gallego, J. M. Garcia, J. Alvarez, *et al.*, Phys. Rev. B **46**, 13339 (1992).
11. A. Ishizaka and Y. Shiraki, J. Electrochem. Soc. **133**, 666 (1986).
12. E. Landemark, C. J. Karlsson, Y.-C. Chao, *et al.*, Phys. Rev. Lett. **69**, 1588 (1992).
13. F. J. Himpsel, F. R. McFeely, A. Taleb-Ibrahimi, *et al.*, Phys. Rev. B **38**, 6084 (1988).
14. G. K. Wertheim, D. M. Riffe, J. E. Rowe, *et al.*, Phys. Rev. Lett. **67**, 120 (1991).
15. H. I. Meyrheim, U. Dobler, and A. Puschmann, Phys. Rev. B **44**, 5738 (1991).
16. M. V. Gomoyunova, I. I. Pronin, N. R. Gall', *et al.*, Pis'ma Zh. Tekh. Fiz. **29** (12), 25 (2003) [Tech. Phys. Lett. **29**, 496 (2003)].
17. J. M. Gallego, R. Miranda, S. Molodtsov, *et al.*, Surf. Sci. **239**, 203 (1990).
18. J. M. Rangelov, P. Augustin, J. Stober, *et al.*, Phys. Rev. B **49**, 7535 (1994).
19. F. Boscherini, J. J. Joyce, and M. W. Ruckman, Phys. Rev. B **35**, 4216 (1987).
20. M. V. Gomoyunova, I. I. Pronin, and N. R. Gall', Fiz. Tverd. Tela (St. Petersburg) **45**, 1519 (2003) [Phys. Solid State **45**, 1596 (2003)].
21. B. Egert and G. Panzner, Phys. Rev. B **29**, 2091 (1984).
22. A. Hiraki, Surf. Sci. Rep. **3**, 357 (1984).

Translated by M. Lebedev

Technical Physics, Vol. 50, No. 9, 2005, pp. 1217–1222. Translated from Zhurnal Tekhnicheskoĭ Fiziki, Vol. 75, No. 9, 2005, pp. 111–116.

SURFACE, ELECTRON AND ION EMISSION

Preequilibrium Thermofield Microprotrusions as Effective Field Point Sources of Electrons and Ions

O. L. Golubev and V. N. Shrednik[†]

Ioffe Physicotechnical Institute, Russian Academy of Sciences, St. Petersburg, 194021 Russia

e-mail: O.Golubev@mail.ioffe.ru

Received February 3, 2005

Abstract—Field emission methods are employed for studying the conditions of formation, crystallographic localization, and emissive properties of preequilibrium thermofield microprotrusions for a number of refractory metals. Individual preequilibrium microprotrusions can be easily obtained using a W emitter of the ordinary ⟨110⟩ orientation; however, the number of such protrusions on the surface changes with time in the course of ionic emission, as well as their emission parameters (the parameters and the number of microprotrusions do not change in the case of electron emission). Trihedral angles of the rearranged tip, which are formed in the {111} regions, exhibit higher stability to ionic emission. A single trihedral angle stably emitting ions and located on the geometrical axis of the emitter can easily be obtained with the help of a W emitter with the ⟨111⟩ orientation. Two stable preequilibrium microprotrusions arranged symmetrically about the axis of the emitter in the {111} regions can be obtained using a Ta emitter of the conventional ⟨110⟩ orientation. Such microprotrusions virtually do not change the emission parameters during long-term extraction of ionic current. *© 2005 Pleiades Publishing, Inc.*

INTRODUCTION

Modification of surfaces and pattern drawing on the micrometer and nanometer scales require controllable narrow beams of charged particles. For this purpose, it is convenient to use emission of ions under high-temperature field evaporation [1]. In this case, conventional sources of ions are thermofield microprotrusions, which usually grow on the surface of a field emitter at high temperatures T and electric field strengths F and which can emit for a long time under certain conditions [1, 2]. Ionic currents i of the material of the emitter tip on which microprotrusions grow may reach values $\sim 10^{-14}$–10^{-12} A from a single microprotrusion [3, 4]; the number of such microprotrusions on the surface of the tip may exceed one hundred. Upon a change in the polarity of applied voltage U at room temperature T of the tip, the same microprotrusions can also be used as sources of field emission with much higher values of $i \sim 10^6$ A and even more from a single protrusion. The size of such microprotrusions is usually on the order of 10 nm and their vertices (which actually emit) are even smaller (down to a single atom at the vertex of a protrusion); for this reason, such sources of charged particles are qualified as point sources [2]. In some cases, ionic beams from such sources are convenient for focusing; when used in a scanning tunnel microscope, such beams play the role of recording instruments on the micrometer and nanometer scales, which do not require focusing. Microprotrusions form a stage in the thermofield deformation of a point emitter under simultaneous action of high T and F. First, the tip rearrangement stage is observed, during which the initial smoothed shape is transformed into a ribbed polyhedron. Then, at higher values of T and F, microprotrusions grow. Finally, for the highest values of T and F, large outgrowths (macrooutgrowths) appear mainly on closely packed faces, whose size is commensurate with the size of the faces themselves; the vertices and edges of these macrooutgrowths are covered by microprotrusions [5].

For the finest patterns, quite weak (but concentrated) currents are required so that the thickness of the line being drawn does not exceed one or a few nanometers. In the electronic mode, such currents can be easily obtained since the current is controlled by applied voltage U and can easily be reduced to very small values. As regards ionic currents, steady-state ionic beams are usually emitted by the vertices of microprotrusions existing due to dynamic equilibrium between the diffusive inflow of particles to the vertex of a microprotrusion and the field evaporation flow from the vertex of this protrusion. Such microprotrusions are relatively stable, but emission in this case is subjected to noticeable fluctuations and effluent currents ($i = 10^5$–10^7 ions per second) are too strong for many problems of nanotechnology. However, the control of the current by varying the applied voltage U is problematic in this case since the reduction of U leads only to blunting of the microprotrusion due to surface tension forces and to cessation of emission [5]. The new and rather complicated problem is to construct a point source of ions, which could stably emit weak currents (from 1 to

[†] Deceased.

100 particles per second), and the value of the current could be controlled by applied voltage U.

Thermofield microprotrusions grow on the emitter surface when the ponderomotive pressure $P_F = F^2/8\pi$ of electrostatic forces exceeds the Laplace pressure $P_\gamma = 2\gamma/r$ of capillary forces (γ is the surface tension of the emitter material and r is the radius of curvature of the emitter). Consequently, thermofield microprotrusions can be conditionally divided into three groups: stationary, equilibrium, and preequilibrium. Stationary microprotrusions for which P_F is noticeably greater than P_γ exist due to dynamic equilibrium between the diffusion inflow of atoms to the vertex of a microprotrusion and the outflow of field evaporation of ions from the vertex of the protrusion. Equilibrium microprotrusions for which $P_F = P_\gamma$ are rather stable formations; however, these formations must not evaporate ions. Finally, preequilibrium microprotrusions are microprotrusions for which $P_F > P_\gamma$, but the value of this excess is extremely small; i.e., the field influx of atoms to the vertex slightly exceeds the reverse flow, but the microprotrusion is not sharpened in this case. Precisely such microprotrusions must ensure ionic currents from 1 to 10^2–10^3 particles per second, which can be controlled by applied voltage U.

EXPERIMENTAL TECHNIQUE

Experiments were made using the classical methods of field emission microscopy. The objects of investigation were point emitters made of W or Ta with an ordinary ⟨110⟩ orientation, as well as those cut from a (111) W single crystal. Experiments with preequilibrium microprotrusions must be carried out in perfect ultrahigh vacuum since even a very small amount of adsorbed impurity can strongly affect the parameters of ion field evaporation in the presence of a strong electric field (effect of the so-called field etching [6]). For such experiments, sealed field electron microscopes are quite convenient since a vacuum on the order of 10^{-12} Torr in adsorbed gases can easily be obtained in them.

In the case of thermofield action, the initial treatment field F_{tr}, which is always determined relative to the initial shape of tip annealing, should be distinguished from the final field F_{fin}, which is formed at the emitter surface after the change in its shape. When field emission is observed in the final state, quantity F_{fin} is defined as evaporating field F_{ev}. Thermofield treatment of the emitter at certain values of T and F_{tr} was always carried out during a standard time $t = 1$ min. The values of F and work function φ were determined by the conventional method from the slope of the Fowler–Nordheim characteristics. In determining F, the value of φ was assumed to be equal to 4.5 eV for (110) W, 4.1 eV for Ta, and 4.4 eV for (111) W [7].

EXPERIMENTAL RESULTS AND DISCUSSION

In the case of equality of acting pressures ($P_\gamma = P_F$), a long-lived (in the heated state) equilibrium microprotrusion can easily be grown [5]. The value of P_γ is set by the tip geometry and the properties of the material, while the value of P_F can easily be controlled by varying applied voltage U. Equilibrium thermofield microprotrusions were grown and studied (e.g., while determining the value of γ for W [8]). Such protrusions can be used as electron emitters during cooling of the tip and in the case of a change in the polarity of applied voltage U. Naturally, they are not strictly equilibrium any longer, but their advantage as emitters is that overloading by current will not lead to catastrophic explosion of the emitter. As a matter of fact, the inequality $P_\gamma > P_F$ is always observed for such emitters and the slightest heating of the emitter causes blunting of such microprotrusions and a decrease in the emission current (negative feedback operates in this case). Consequently, electron currents of extremely high density up to 10^9–10^{10} A/cm^2 [9] can be extracted from such microprotrusions.

As regards the ionic currents, equilibrium microprotrusions do not emit ions. The emission of ions is induced by the third flux of particles evaporated from the surface in addition to the other two fluxes, viz., the field influx of particles to the tip of the point and the diffusion flux of particles from the vertex of the tip. This third flux reduces the number of particles at the vertex and is added to the flux determined by P_γ and blunting the tip. The equilibrium will be violated, the microprotrusion will be blunted, and the ionic current will decrease; however, the blunting flux will also become smaller.

We denote the particle fluxes as follows: j_F is the sharpening flux, j_γ is the blunting flux, and j_e is the evaporation flux. The preequilibrium microprotrusion corresponds to the situation when $j_F = j_\gamma + j_e$, i.e., when the field influx to the vertex slightly exceeds the reverse blunting flux, but the point is not sharpened since the entire excess flux to the vertex flows away in the form of the evaporation flux [10]. Controlling the value of F by applied voltage U (and setting various values of emitter temperature T), it is not difficult to obtain not only various equilibrium states (when $j_F = j_\gamma$), but also various preequilibrium states with $j_e = j_F - j_\gamma$ from the flux of individual ions to higher values.

In contrast to stationary dynamically balanced microprotrusions only in fluxes j_e and j_F (in these cases, the value of j_γ is much smaller than the former two flows and is the smaller, the larger the distance between the working point and the critical point of termination of emission), a preequilibrium microprotrusion is substantially more stable. In the presence of fluctuations of F, j_e, and r, it exhibits a tendency to return to its former working point (exactly in the same way as an equilib-

rium microprotrusion returns to its initial shape in the case of fluctuation of r [5]). The main property of a preequilibrium microprotrusion is the possibility of its tuning, which makes it possible to controllably select quite small currents convenient for drawing on the nanometer scale. Fluctuations of current for such a microprotrusion are smaller than fluctuations for a stationary microprotrusion, for which $j_e = j_F$. In addition, the stationary microprotrusion may "creep" along the curvature line $K \sim 1/r$ of the curve $P = f(K)$ [5] in the course of emission in a certain direction; its working point is less stable, not to mention the disruption hazard. A preequilibrium microprotrusion preserves its properties as such (preequilibrium) over a wide range of variation of evaporation flux j_e and, accordingly, the radius of curvature r (i.e., K). However, with increasing U, the preequilibrium microprotrusion can also reach the critical point, behind which we always have $P_F > P_\gamma$, and it will rapidly pass to the state of a stationary microprotrusion. The possibility of varying temperature provides a substantial margin for controlling in this case.

To find out whether the microprotrusions formed in the experiment are equilibrium (as well as preequilibrium) or stationary ($j_e = j_F$) microprotrusions, a simple test can be used. For a slight increase in the value of U to $U + \delta U$, curvature K of the vertex of a microprotrusion increases if it is in equilibrium or a preequilibrium microprotrusion; however, the value of this quantity decreases if the protrusion is stationary. As the value of U decreases to $U - \delta U$, the changes will be reversed. The difference between equilibrium and preequilibrium microprotrusions lies in the extent of variation of K, which is considerable for equilibrium and insignificant for preequilibrium microprotrusions. The variation of K can be judged from the change in the emission current for a fixed U (the larger the current, the higher the value of K) or from the magnitude of the field factor $\beta = 1/kr$, where k is a coefficient depending on the shape of the tip (the larger the value of β, the higher the value of K).

Figure 1 shows field electron images of the surface of a sharp-tipped W single crystal during thermofield action. Figure 1a shows the initial classical shape of the emitter annealing, which is obtained after heating at $T \sim$ 2500 K, for which the field factor $\beta = 5912$ cm^{-1}, radius $r = 0.6$ μm, and the value of U_{10} is 4690 V (U_{10} is the voltage required to obtain the chosen value of emission current $i = 10$ nA; i.e., 10^{-8} A). After the action at $T =$ 1420 K, $U_{tr} = 8.5$ kV, and $F_{tr} = 0.51$ V/Å, several microprotrusions were formed in the vicinity of the (001) faces, for which $U_{10} = 2021$ V and $\beta = 19473$ cm^{-1}. These are stationary microprotrusions at the given T, which evaporate W ions; the value of F_{eV} is 1.66 V/Å. To obtain preequilibrium microprotrusions, we must gradually reduce the value of U_{tr} under thermofield action, tracing the values of U_{10} and β. First, the value of β increases and U_{10} decreases since microprotrusions become sharper with increasing curvature K. In the course of sharpening, the value of U_{10} becomes 1900 V and $\beta = 20100$ cm^{-1} as the value of U_{tr} decreases to 7.8 kV. Finally, when U_{tr} decreases to 7.5 kV, the value of U_{10} slightly increases to 1960 V, while β decreases to 19240 cm^{-1}, which precisely corresponds to preequilibrium microprotrusions.

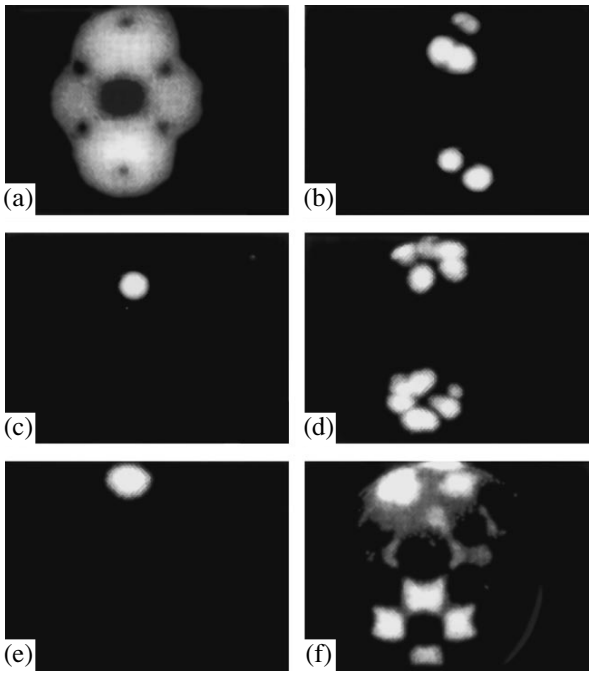

Fig. 1. Field electron images of the surface of a (110) W emitter during thermofield action at $T = 1420$ K for various values of F_{tr}: (a) initial annealing shape; (b) after heating of the emitter at $F_{tr} = 0.52$ V/Å followed by a decrease of F_{tr} to 0.44 V/Å; (c) after further reduction of F_{tr} to 0.42 V/Å; (d) after holding the emitter at $F_{tr} = 0.42$ V/Å and $T =$ 1420 K for 20 min; (e) after heating at $F_{tr} = 0.37$ V/Å; (f) after holding the emitter at $T = 1420$ K and $F_{tr} =$ 0.37 V/Å for 20 min.

Any microprotrusion may serve as a point source of electrons and ions; however, the most interesting is the situation when a single microprotrusion remains on the surface of the emitter. For this purpose, we must reduce the value of F_{tr}. Microprotrusions will become stationary again and will be sharpened, consecutively intersecting the straight line $P_\gamma(K)$ on the P_F, $P_\gamma(K)$ graph [5]. After this, they will be strongly blunted and will vanish from the emitter surface. Thus, it is possible to retain only one protrusion on the emitter surface (this situation is depicted in Fig. 1c) after the value of U_{tr} is reduced to 8.25 kV. This protrusion ensures that $U_{10} =$ 2108 V and $\beta = 19100$ cm^{-1}. Such a microprotrusion is a stable point source of electrons (at least, such an emitter ensures a current of $i = 1000$ nA for 1 h); the value of U required for this effect has changed from 2664 to 2687 V. However, in the case of emission of ions (i.e., upon simultaneous action of T and F), stability of this

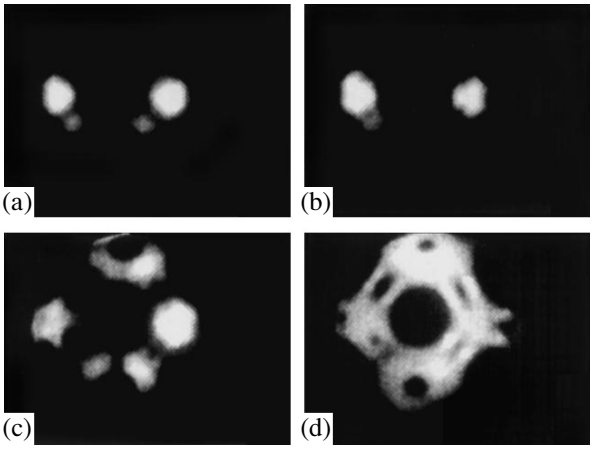

Fig. 2. Field electron images of the surface of a (110) W emitter during thermofield action at T = 1800 K: (a) after heating of the emitter at T = 1800 K and F_{tr} = 0.32 V/Å; (b) after holding the emitter at T = 1800 K and F_{tr} = 0.32 V/Å for 30 min; (c) after short-term heating of state (b) at T = 1200 K in zero field; (d) after short-term heating of state (c) at T = 1400 K in zero field.

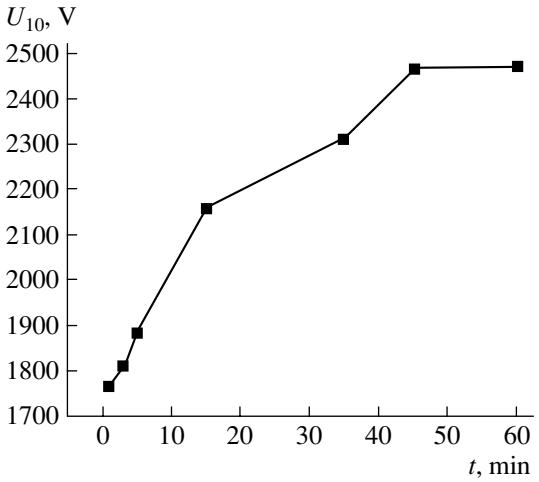

Fig. 3. Time variation of quantity U_{10} under simultaneous action on a W emitter; T = 1800 K and F_{tr} = 0.32 V/Å.

kind is not observed. Figure 1d illustrates the situation when a single microprotrusion shown in Fig. 1c emitted ions for 20 min. It can be seen that five microprotrusions have grown in the regions of {001} in the course of thermofield action and the value of U_{10} = 1740 V, although the value of β virtually remained unchanged. During the thermofield action, processes of field crystal growth continuously occur on the emitter surface, which leads to the emergence of new microprotrusions.

An attempt can be made to retain a solitary preequilibrium microprotrusion on the emitter surface by applying to it very weak fields and extracting very small currents to reduce the microprotrusion growth rate; however, this may also be futile. Figure 1e shows a solitary preequilibrium microprotrusion obtained at U_{tr} = 6.25 kV, F_{tr} = 0.37 V/Å, and T = 1400 K. The parameters of the protrusion are as follows: U_{10} = 2020 V and β = 20 410 cm^{-1}. After ten minutes of continuous ionic emission, the protrusion parameters virtually did not change; however, after 20 min, the emission pattern shown in Fig. 1f was formed. This pattern corresponds to a tip reconstructed in an electric field with U_{10} = 3095 V and β = 10 920 cm^{-1}; i.e., the microprotrusion simply disappeared and was "dissolved" since it attained a state in which $P_\gamma > P_F$. Thus, carrying out thermofield treatment at low temperatures $T \le 1500$ K, we can easily obtain preequilibrium microprotrusions without blunting the emitter; the situation is completely reproducible, but it is practically impossible to retain a single microprotrusion on the surface. Either new microprotrusions are formed in the course of ionic emission, or the microprotrusion is dissolved.

At a higher temperature T of treatment and, accordingly, lower values of U and F, another type of rearrangement of the W emitter can be obtained [11], in which {112} faces do not expand but, conversely, are healed, while in {111} regions trihedral angles are formed due to expansion of the most closely packed {011} faces. In these regions, one can try to grow preequilibrium microprotrusions. Figure 2a shows the emission pattern of the emitter surface after treatment at T = 1800 K, U_{tr} = 5.0 kV, and F_{tr} = 0.3 V/Å. It can be seen that two microprotrusions were formed in the region of {111} faces; the results of tests show that these are preequilibrium microprotrusions for which U_{10} = 1760 V and β = 19 856 cm^{-1}. If such an emitter is held at the same values of T and F_{tr} for some time, the value of U_{10} gradually increases and β decreases. Figure 3 shows the time variation of U_{10}. It can be seen that the value of this quantity smoothly increases from 1760 to 2426 V over 45 min and then remains unchanged. The value of β behaves conversely (i.e., it smoothly decreases from 19 856 to 14978 cm^{-1} and then remains unchanged). Emission images in Figs. 2b–2d show that microprotrusions in this case become blunted and disappear, while trihedral angles on which microprotrusions have grown are preserved. These angles in {111} regions were formed as a result of expansion of three closely packed {011} faces and, hence, the angles have trigonal symmetry (see Fig. 2b). Thermal smoothing of the emitter by heating at T = 1200 K in the absence of applied field reveals the bases of these angles (see Fig. 2c) and the shape of the rearranged tip (Fig. 2d). Thus, trihedral angles are perfect emitters of ions as well as electrons. These angles have all the advantages of preequilibrium microprotrusions, but are more stable on the surface. The disadvantages of such angles as compared to the microprotrusions is that these angles can be obtained only in definite crystallographic regions for a definite structure of the emitter, while preequilibrium microprotrusions can be obtained practically at any point of the surface for any structure of the

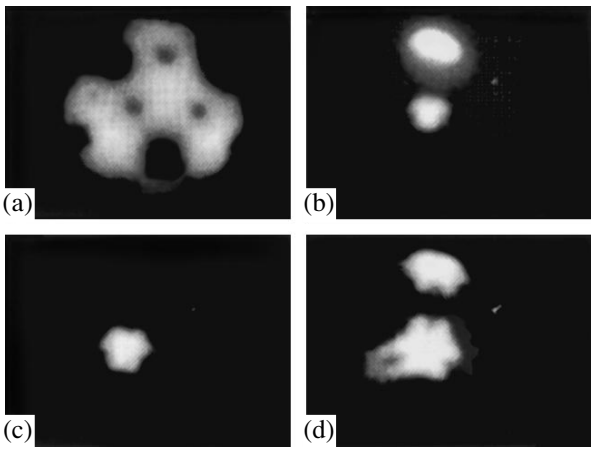

Fig. 4. Field emission images of the surface of a (111) W emitter during thermofield action: (a) initial annealing shape; (b) after heating of the emitter at T = 2100 K and F_{tr} = 0.32 V/Å; (c) after reducing the value of F_{tr} to 0.29 V/Å at the same temperature; (d) after heating of state (c) at T = 1200 K in zero field.

emitter; there are no physical limitations in this case. Trihedral angles are more "blunted" objects as compared to microprotrusions (the value β for microprotrusions ranges between 18000 and 24 000 cm^{-1}, while in the case of angles we have β = 14 000–16 000 cm^{-1}); i.e., higher values of U and, accordingly, F are required for obtaining the same value of the current.

To obtain an emitter of ions and electrons with only one emitting trihedral angle (or microprotrusion) located at the center on the geometrical axis of the tip, it is convenient to use (111) W. Such an emitter was obtained from a sample cut at a definite angle from a W single crystal. Figure 4a shows the initial image of the emitter annealing shape, for which U_{10} = 7121 V and β = 4317 cm^{-1}; i.e., the point has a radius of $r \sim 0.8$ μm. An emitter cut from a single crystal requires slightly higher values of treatment temperature as compared to an emitter made from a wire. The thermofield treatment at T = 2100 K, U_{tr} = 7.5 kV, and F_{tr} = 0.32 V/Å leads to the formation of a microprotrusion in stepped regions of {001} faces and a trihedral angle in the (111) region at the vertex of the emitter (Fig. 4b). The decrease in U_{tr} to 6.75 kV at the same temperature leads to dissolution of the microprotrusion; only the trihedral angle remains at the center of the emitter (Fig. 4c), for which U_{10} = 3616 V and β = 13824 cm^{-1}. This angle virtually does not change its emission parameters as a result of extraction of the ionic current for several hours. Finally, Fig. 4d shows the emission pattern after thermal smoothing; the base of the trihedral angle at the center and a small macrooutgrowth in the (001) region, on which the microprotrusion has grown, can be seen in the figure.

Figure 5 shows the evolution of the surface of a Ta tip under thermofield action. The crystallographic structure of Ta is the same body-centered cube as for W, but with a slightly different faceting of the surface, a larger size of {011} faces, and the absence of {112} faces. It is well known [12] that, in contrast to W, Ta is easily rearranged under thermofield treatment, forming angles in {111} regions; this is precisely due to specific faceting of the surface. Such an emitter is rather blunt since $r \sim 1.1$ μm, U_{10} = 7050 V, and β = 3100 cm^{-1}. Figure 5a shows the rearrangement of the emitter at T = 1450 K, U_{tr} = 7.5 kV, and F_{tr} = 0.22 V/Å; the tip is noticeably sharpened due to emission, forming two acute angles near {111} faces due to expansion of {011} faces and angles near {113} faces, which have been formed due to expansion of {001} and {011} faces. For such an emitter, U_{10} = 3810 V and β = 8685 cm^{-1}. An increase in F_{tr} to 0.32 V/Å and in T to 1550 K leads to the growth of microprotrusions at the angles in {111} regions; these microprotrusions can be made preequilibrium by reducing the value of F_{tr}. Figure 5b shows two such preequilibrium microprotrusions, for which U_{10} = 3263 V and β = 10 263 cm^{-1}. The operation of such an emitter in the ionic emission mode for the same values of T and F_{tr} during the first 20 min causes a weak sharpening of microprotrusions to U_{10} = 2538 V and β = 12 694 cm^{-1}, after which the parameters of microprotrusions virtually remain unchanged. Finally, Fig. 5c shows the situation after thermal smoothing of microprotrusions. Bright spots observed in {111} regions correspond to the nucleation centers of microprotrusions. It can be seen that there are several centers of this kind and that the sharpest microprotrusion emits; for this reason, the image of a microprotrusion is some-

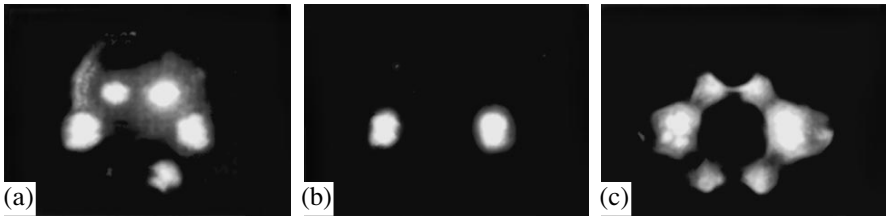

Fig. 5. Field emission images of the surface of a Ta emitter during thermofield action: (a) after heating of the emitter at T = 1450 K and F_{tr} = 0.22 V/Å; (b) after heating the emitter at T = 1550 K and F_{tr} = 0.32 V/Å; (c) after heating of state (b) at T = 1200 K in zero field.

times double since two identical protrusions grow side by side (Fig. 5c). Consequently, in contrast to a W emitter, a Ta emitter makes it possible to obtain stably emitting preequilibrium microprotrusions in {111} regions; trihedral angles can also be used in this case.

CONCLUSIONS

Using a conventional (110) W emitter, it is possible to obtain solitary preequilibrium microprotrusion at relatively low temperatures T = 1400–1600 K for F_{tr} = 0.4–0.6 V/Å practically at any point at the vertex of the tip. However, parameters of the microprotrusion may change with time in the course of thermofield action; the number of microprotrusions on the surface may also change as a result of field crystal growth.

Two solitary preequilibrium microprotrusions can still be obtained, but only in {111} regions, where sharp trihedral angles are formed as a result of thermofield action, and for higher values of T = 1700–2000 K but approximately the same values of F_{tr}. However, these microprotrusions gradually become blunted and dissolve as a result of emission, preserving all the advantages of preequilibrium microprotrusions.

A solitary stably emitting trihedral angle located at the center on the geometrical axis of the tip can be obtained relatively easily using a (111) W emitter. Such a microprotrusion is an ideal stably operating point source of ions and electrons.

A conventional (110) Ta emitter makes it possible to obtain relatively easily two stably emitting preequilibrium microprotrusions, arranged symmetrically relative to the geometrical axis of the tip in {111} regions, by using thermofield treatment at F_{tr} = 0.3–0.5 V/Å and T = 1300–1500 K. In contrast to W, the Ta emitter makes it possible to grow quite stable preequilibrium microprotrusions.

Trihedral angles of a rearranged tip have a number of advantages over microprotrusions when used as stable sources of ions; however, such angles can be obtained only in certain crystallographic regions for a definite structure of the emitter. In this respect, preequilibrium microprotrusions are universal.

ACKNOWLEDGMENTS

This study was supported by the Russian Foundation for Basic Research (project no. 04-02-17658) and by the program of the Ministry of Science and Technology of the Russian Federation (contract no. 40.012.1.1.1152).

REFERENCES

1. Yu. A. Vlasov, V. G. Pavlov, and V. N. Shrednik, Pis'ma Zh. Tekh. Fiz. **12**, 548 (1986) [Sov. Tech. Phys. Lett. **12**, 224 (1986)].
2. V. N. Shrednik, Poverkhnost, No. 2, 102 (1998).
3. O. L. Golubev and V. N. Shrednik, Zh. Tekh. Fiz. **72** (8), 109 (2002) [Tech. Phys. **47**, 1038 (2002)].
4. O. L. Golubev and V. N. Shrednik, Zh. Tekh. Fiz. **73** (6), 118 (2003) [Tech. Phys. **48**, 776 (2003)].
5. Yu. A. Vlasov, O. L. Golubev, and V. N. Shrednik, in *Crystal Growth* (Nauka, Moscow, 1991), Vol. 19, pp. 5–21 [in Russian].
6. E. W. Muller and T. T. Tsong, *Field Ion Microscopy, Field Ionization, and Field Evaporation* (Pergamon, Oxford, 1973; Nauka, Moscow, 1980).
7. V. S. Fomenko, *Emission Properties of Materials: A Handbook* (Naukova Dumka, Kiev, 1981) [in Russian].
8. Yu. A. Vlasov, O. L. Golubev, and V. N. Shrednik, Izv. Akad. Nauk SSSR, Ser. Fiz. **52**, 1538 (1988).
9. V. G. Pavlov, A. A. Rabinovich, and V. N. Shrednik, Zh. Tekh. Fiz. **45**, 2126 (1975) [Sov. Phys. Tech. Phys. **20**, 1337 (1975)].
10. V. N. Shrednik, D. V. Glazanov, and E. L. Kontorovich, Zh. Tekh. Fiz. **73** (9), 120 (2003) [Tech. Phys. **48**, 1199 (2003)].
11. M. Benjamin and R. O. Jenkins, Proc. R. Soc. London, Ser. A **176**, 262 (1940).
12. M. Drechsler, Z. Elektrochem. **58**, 327 (1954).

Translated by N. Wadhwa

Technical Physics, Vol. 50, No. 9, 2005, pp. 1223–1229. Translated from Zhurnal Tekhnicheskoĭ Fiziki, Vol. 75, No. 9, 2005, pp. 117–122.

EXPERIMENTAL INSTRUMENTS AND TECHNIQUES

Influence of Dispersion on Rogowski Loop Operation in the Short-Pulse Regime

M. B. Goykhman*, V. V. Kladukhin, and N. F. Kovalev***

** Institute of Applied Physics, Russian Academy of Sciences, ul. Ul'yanova 46, Nizhni Novgorod, 603950 Russia*

*** Design Bureau of Scientific Instrument Making, Ural Division, Russian Academy of Sciences, Yekaterinburg, 620049 Russia*

e-mail: skbnp@uran.ru

Received February 4, 2005

Abstract—Basic effects and conditions limiting application of the Rogowski loop in ultrashort current pulse measurements are considered. A technique for partial reconstruction of the current pulse shape is suggested that substantially extends the potential of related sensors. © *2005 Pleiades Publishing, Inc.*

(1) It has been shown [1–4] that the Rogowski loop (Fig. 1) may well be used for measuring high-amplitude current pulses of width τ_0 as short as several nanoseconds without radically modifying its design. However, the operation of the loop under such conditions changes significantly. The winding (Fig. 1), as well as the protective shield with a narrow slot, becomes a current-carrying system, where the variable magnetic field of current $\hat{J}_0(t)$ being measured generates slow waves. If, in this case, pulse width τ_0 is shorter than time t_g of pulse propagation along the loop ($\tau_0 < t_g$), a train of pulses generally arises on the load, the first of them $\hat{U}_1(t)$ being close to $\hat{J}_0(t)$ in shape without integration.

Distortion of the voltage pulse $\hat{U}_1(t)$, which is believed to be minor at small τ_0 [2], is usually associated with the spurious capacitance and inductance of the load and with losses in the winding [1–3]. It is, however, obvious that, as τ_0 decreases, the dispersion of the waveguiding system of the loop has a progressively increasing effect, since the spectrum of pulses being measured widens ($\omega_{max} \sim 2\pi/\tau_0$) and the low-frequency dispersion in helix waveguides is hard to eliminate [5].[1] In this paper, we present estimates of dispersion-related errors and suggest a correction calculation technique that improves the accuracy of measuring short current pulses with the Rogowski loop.

(2) In calculations, the waveguiding system of the loop is replaced [1, 3] by an equivalent circuit comprising a chain of simple cells (Fig. 2), which even outwardly resembles the helix waveguide in the shield (Fig. 1). To allow for dispersion, we use the Fourier transformation and, accordingly, write relevant equations for the complex amplitudes,

$$\frac{dU}{dx} = -ZJ + i\omega\kappa J_0, \qquad \frac{dJ}{dx} = -YU. \tag{1}$$

Here, U is the complex amplitude of the voltage between the winding and shield; J is the current in the winding; Z is the winding impedance per unit length; Y is the admittance per unit length, which is related to the winding–shield capacitance (admittance Y and impedance Z are assumed to be independent of longitu-

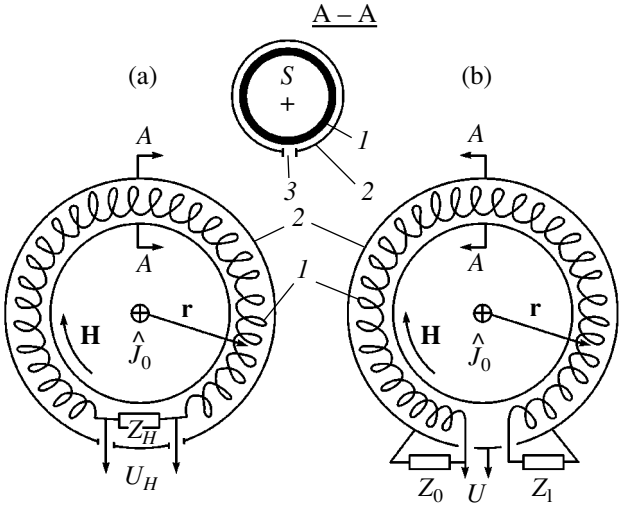

Fig. 1. Simplified representations of the Rogowski loop with (a) series- and (b) parallel-connected load: (*1*) winding, (*2*) protective shield, and (*3*) narrow slot in the shield.

[1] Here, as is customary in radio engineering, a helix waveguide represents a helically wound metallic wire.

1063-7842/05/5009-1223$26.00 © 2005 Pleiades Publishing, Inc.

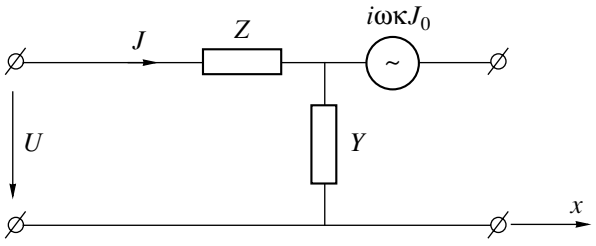

Fig. 2. Cell of the equivalent circuit of the Rogowski loop's waveguide.

dinal coordinate x); J_0 is the complex amplitude of the current being measured;

$$\kappa = \bar{\kappa}(x)\frac{N\mu_0 S}{2\pi r}; \tag{2}$$

μ_0 is the free-space permeability; N is the density of turns in the winding; S is the effective surface area of the turns; r is the radius of the midline of the winding (which is assumed to have the shape of a torus, Fig. 1); and

$$\bar{\kappa}(x) = \frac{2\pi r H_x(x)}{\oint H_x dx} \tag{3}$$

is the normalized magnetic field produced by current J_0 being measured at the midline of the winding.

A change in field H_x over the cross section of the turns is assumed to be insignificant, and its variation along the midline (i.e., along the x axis) is taken into account only in general relationships. Field H_x depends on x if current J_0 is asymmetrically distributed over the cross section of the torus ($\partial J_0/\partial\varphi \neq 0$) and also if the screen is placed nonaxially. The field is assumed to depend on time exponentially, $H_x \sim \exp(i\omega t)$.

The general solution to system (1) is trivial,

$$\begin{aligned} U &= \rho A e^{-ihx} + \rho B e^{ihx} + i\omega J_0 \int_0^x \kappa \cosh(x-x')dx', \\ J &= A e^{-ihx} - B e^{ihx} + J_0 \frac{\omega}{\rho}\int_0^x \kappa \sinh(x-x')dx', \end{aligned} \tag{4}$$

where A and B are constants of integration,

$$\rho = \sqrt{Z/Y} \tag{5}$$

is the wave impedance measured at the terminals of the cells (Fig. 2),

$$h = -i\sqrt{ZY} \tag{6}$$

are the wavenumber, and h and ρ are constants related to the fundamental mode of the shielded helix waveguide (in general, they are complex).

A load can be connected to the Rogowski loop in series, i.e., be inserted into a gap in the conductor (Fig. 1a), or in parallel, when one of the ends of the conductor ($x = 0$) is connected to the shield through load resistance Z_0 and the other through load resistance Z_l (Fig. 1b).[2]

For the series connection (Fig. 1a), solution (4) with boundary conditions

$$J(l) = J(0), \quad U(l) = U(0) + Z_H J(0) \tag{7}$$

yields an integral expression for voltage U_H across load Z_H,

$$U_H = \omega J_0 \frac{Z_H}{2\rho}\frac{\int_0^l \kappa[\sinh(l-x') + \sinh hk']dx'}{1 - \cosh hl - i\frac{Z_H}{2\rho}\sinh hl}. \tag{8}$$

For the parallel connection (Fig. 1b), the boundary conditions are

$$U(0) = -Z_0 J(0), \quad U(l) = Z_l J(l), \tag{9}$$

and solution (4) yields another expression for the voltage across load Z_0,

$$\begin{aligned} U &= 2i\omega J_0 \rho Z_0 \\ &\times \frac{\int_0^l \kappa\left[\cosh h(l-x') + i\frac{Z_l}{\rho}\sinh h(l-x')\right]dx'}{(Z_0-\rho)(Z_l-\rho)e^{-ihl} - (Z_0+\rho)(Z_l+\rho)e^{ihl}}. \end{aligned} \tag{10}$$

In experiments, the first connection is uncommon, in particular, because of the possibility of excitation of high-Q oscillations with eigenfrequencies defined by the dispersion relation following from (8),

$$\sinh\frac{l}{2} = 0. \tag{11}$$

The complex frequencies of lower Q oscillations are found from another dispersion relaxation,

$$\sinh\frac{l}{2} - i\frac{Z_H}{2\rho}\cosh\frac{l}{2} = 0.$$

A reason for excitation of oscillations (11) may be the above-mentioned nonuniformity of magnetic field (3) along the loop ($d\kappa/dx \neq 0$). This nonuniformity generally arises when current $\hat{J}_0(t)$ is distributed asymmetrically about the loop axis (Fig. 1a). The second connection scheme (Fig. 1b) is less sensitive to violation of

[2] Other connection schemes can also be used: for example, a return wire passing along the axis of the helical winding. However, the waveguide then becomes two-mode and system (1) does not suffice to describe its behavior. Importantly, the mutual reradiation of modes at the ends of the loop becomes essential in this situation.

the condition

$$\frac{d\kappa}{dx} = 0; \tag{12}$$

therefore, one can assume that, for the second connection, condition (12) is met in a first approximation. Then, expression (10) can be transformed into the functional equation

$$U = -\frac{\alpha}{2}J_0(\beta_0 + 1)[1 - (\beta_1 + 1)e^{-ihl} + \beta_1 e^{-2ihl}] + U\beta_0\beta_1 e^{-2ihl}, \tag{13}$$

where $\alpha = (\omega\kappa)/h$ is the coupling parameter and

$$\beta_0 = \frac{Z_0 - \rho}{Z_0 + \rho}, \quad \beta_1 = \frac{Z_1 - \rho}{Z_1 + \rho} \tag{14}$$

are the coefficients of reflection from terminations Z_0 and Z_1.

Solution (13) can be represented in the form of two series,

$$U = -\frac{\alpha}{2}J_0(\beta_0 + 1) + \frac{\alpha}{2}J_0(\beta_0 + 1)(\beta_1 + 1)\sum_{n=0}^{\infty}\beta_0^n\beta_1^n e^{-i(2n+1)hl} - \frac{\alpha}{2}J_0(\beta_0 + 1)^2\sum_{n=1}^{\infty}\beta_0^{n-1}\beta_1^n e^{-2inhl}, \tag{15}$$

which converge at $|\beta_0\beta_1| < 1$. Expression (8) can also be represented in a similar form provided that condition (12) is met,

$$U_H = \alpha J_0(\beta + 1) + \alpha J_0(\beta + 1)^2\sum_{n=1}^{\infty}(-1)^n\beta^{n-1}e^{-inhl}, \quad \beta = \frac{Z_H - 2\rho}{Z_H + 2\rho}. \tag{16}$$

Upon the inverse Fourier transformation, each term of the sums in (15) and (16) can be assigned individual pulses that are variously delayed according to the exponential factors,[3]

$$t \approx nt_g, \quad t \approx (2n + 1)t_g, \quad t \approx 2nt_g,$$

where

$$t_g = \lim_{\omega\to 0}\left(\frac{h}{\omega}l\right). \tag{17}$$

If width τ_0 of current pulse $\hat{J}_0(t)$ is shorter than the time the pulse takes to propagate along the loop (i.e., $\tau_0 < t_g$) and if the distortion of the pulse is moderate, at least several initial pulses in sequences $\hat{U}_n(t)$ or $\hat{U}_{H,n}(t)$ are separated in time. Therein lies the advantage of using the sums in (15) and (16) when the short-pulse regime of Rogowski loop operation is analyzed.

To proceed further, we will simplify the dispersion relation $h = h(\omega)$ for the fundamental mode of the shielded helix waveguide to the polynomial form (provided that singularities at the zero frequency $\omega = 0$ are absent),

$$h = -i\sigma + \frac{\omega}{v} + \gamma\frac{\omega^3}{v}, \tag{18}$$

where $\sigma = \lim_{\omega\to 0} ih$ is the damping rate, $v = \lim_{\omega\to 0}(d\omega/dh)$ is the group velocity at the zero frequency, and

$$\gamma = \frac{v}{6}\lim_{\omega\to 0}(d^3h/d\omega^3)$$

is the dispersion parameter.[4]

For simplicity, we assume that reflection coefficient β_0 is real and frequency-independent,

$$d\beta_0/d\omega = 0, \tag{19}$$

although the general case is also simple to analyze. Applying the inverse Fourier transformation to the first term in (15), we easily come to an expression that relates current pulse $\hat{J}_0(t)$ to the first pulse $\hat{U}_1(t)$ picked up from the load,

$$\hat{U}_1(t) + \sigma v\int_0^t\hat{U}_1(t')dt' - \gamma\frac{d^2\hat{U}_1}{dt^2} = -\kappa v\frac{\beta_0 + 1}{2}\hat{J}_0(t). \tag{20}$$

This formula without the dispersion-related term

$$\gamma\frac{d^2\hat{U}_1}{dt^2} \tag{21}$$

was found and analyzed in [2]. The absence of (21) in the formula derived in [2] is due to the fact that the expression used in [2] for the current in the short-circuited winding at high frequencies was incorrect.

Relationship (20) allows us to estimate the discrepancy between the shapes of pulses $\hat{U}_1(t)$ and $\hat{J}_0(t)$ and compare the effect of different factors on the formation of $\hat{U}_1(t)$. The integral term in (20) is a correction due to losses in the waveguiding system, and (21) evaluates the effect of dispersion. It is seen that the effect of dispersion is essential at the leading and trailing edges of the pulse; that is, fast processes are subject to more severe distortions, contrary to assertions in [1–3]. As τ_0 diminishes, the effect of dispersion, according to (20), starts prevailing and the dispersion, in essence,

[3] A similar series could be obtained using the results given in [4].

[4] The commonly accepted expression for the group velocity is justified here, since the condition $\mathrm{Im}(dh/d\omega) = 0$ (see (18)) is assumed to hold.

becomes the factor that imposes basic restrictions on τ_0.

On the other hand, relationship (20) can be used to reconstruct the shape of pulse $\hat{J}_0(t)$ from the waveform of pulse $\hat{U}_1(t)$ picked up from the load and observed on an oscilloscope, i.e., to calculate corrections to $\hat{U}_1$ and, thereby, extend the spectrum of applications of the Rogowski loop. Note, however, that the process of reconstruction involves differentiation of functional dependences found experimentally, which is a possible reason for progressively increasing errors.

(3) Parameters σ, v, and γ of polynomial (18) that are necessary for reconstruction of pulses $\hat{J}_0(t)$ are found by processing the pulse waveforms. The condition $\beta_l = 0$ (weak reflections from termination Z_l) is best suited for this purpose. At such matching, only the two first terms of infinite sums (15) are left,

$$U = U_1 + U_2 = -\frac{\alpha}{2}J_0(\beta_0 + 1) + \frac{\alpha}{2}J_0(\beta_0 + 1)e^{-ihl}, \quad (22)$$

at any load Z_0. Experimentally, such a situation is simulated well by closing part of the slot on the side $x = l$. However, a number of extra pulses may appear after $\hat{U}_1$ and $\hat{U}_2$ in this case.

Functions $U_1(\omega)$ and $U(\omega) = U_1 + U_2$ entering into (22) are the Fourier transforms of the first single, $\hat{U}_1(t)$, and composite, $\hat{U}_1(t) + \hat{U}_2(t)$, pulses picked up from the load. The procedure of separating out $\hat{U}_1(t)$ from the waveform on the oscillogram is uncertain. To minimize errors due to this uncertainty, one should increase ratio t_g/τ_0. Obviously, this requirement, along with dispersion-related term (21), limits the potentiality of the reconstruction procedure.

Formula (22) and representation (18) make it possible to derive the functionals

$$\sigma l = -\mathrm{Re}\left[\ln\left(1 + \frac{U}{U_1}\right)\right]\Bigg|_{\omega = 0},$$

$$t_g = -\mathrm{Im}\left[\frac{d}{d\omega}\ln\left(1 + \frac{U}{U_1}\right)\right]\Bigg|_{\omega = 0}, \quad (23)$$

$$6\gamma t_g = -\mathrm{Im}\left[\frac{d^3}{d\omega^3}\ln\left(1 + \frac{U}{U_1}\right)\right]\Bigg|_{\omega = 0},$$

which are suitable for calculating the parameters of the dispersion dependence $h(\omega)$ from the Fourier transforms of the waveforms of the two initial pulses picked up from the load. Since the derivatives in (23) are taken at the zero frequency ($\omega \longrightarrow 0$), functionals (23) have the filtration property; that is, they are stationary relative to rapidly oscillating processes and, hence, can be applied in experimental data processing.

According to (23), if pulses $\hat{U}_1$ and $\hat{U}_2$ are similar in shape and amplitude, we have $\sigma l \ll 1$ and $8\pi^2\gamma t_g/\tau_0^3 \ll 1$; so, the design of the shielded helix waveguide can be considered adequate. Distortions in this case are caused by the reactance of the load, specifically, by the frequency dependence of the reactance.

The accuracy of the results can be additionally checked by comparing t_g calculated by the related formula in (23) with

$$t_g = \sqrt{L_\Sigma C_\Sigma}, \quad (24)$$

where L_Σ and C_Σ are the total inductance of the winding and its capacitance relative to the shield that are measured at low frequencies.

(4) In the short-pulse operating regime of the Rogowski loop, the shield around the winding (Fig. 1) becomes a functional component of the waveguiding system. Its design and dimensions have an influence on the low-frequency dispersion properties of the loop, i.e., on parameters γ and v, and ultimately on the measurement accuracy. Because of this, let us consider the properties of the helix waveguide in the shield.

The problem of helix (helical winding) in a shield with a single narrow longitudinal slot is very complicated. Here, we replace it by a simpler problem of a helically conducting cylinder of diameter $2a$ placed in a coaxial circular screen of diameter $2b$ with several longitudinal slots (Fig. 3). We assume that the simple boundary conditions

$$E_s(r = a - 0) = 0, \quad E_s(r = a + 0) = 0, \quad (25a)$$

$$E_t(r = a - 0) - E_t(r = a + 0) = 0, \quad (25b)$$

$$H_s(r = a - 0) - H_s(r = a + 0) = 0 \quad (25c)$$

are fulfilled on the surface $r = a$ and the boundary conditions

$$E_z(r = b - 0), \quad E_s(r = b + 0) = 0, \quad (26a)$$

$$E_\varphi(r = b - 0) - E_\varphi(r = b + 0) = 0, \quad (26b)$$

$$H_z(r = b - 0) - H_z(r = b + 0) = 2\pi i\omega b C E_\varphi(r = b) \quad (26c)$$

on the surface $r = b > a$ take into account the shunting capacitance of the slots per unit length,

$$C \simeq \varepsilon_0\Delta/d, \quad (27)$$

since total width $d = \sum_i d_i$ of the slots (d_i is the width of an ith slot) is assumed to be much smaller than the perimeter of the shield,

$$d \ll 2\pi b. \quad (28)$$

In formulas (25) and (26), subscript s denotes the direction along the spiral-wound conductor; subscript t denotes the direction (orthogonal to s) of the tangent to

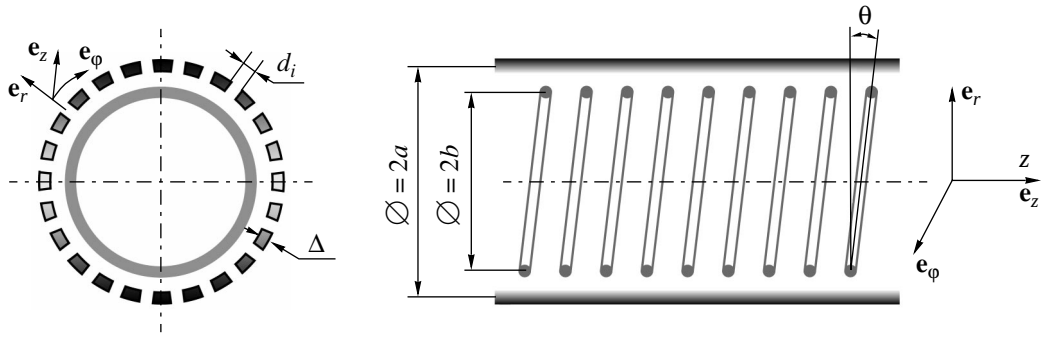

Fig. 3. Coaxial waveguide with a longitudinally conducting outer cylinder and helically conducting inner cylinder.

the plane $r = a$ (Fig. 3); ε_0 is the permittivity of free space; and unit vectors $\mathbf{e}_r$, $\mathbf{r}_s$, and $\mathbf{r}_t$ constitute a right-hand triplet.

With the routine calculation procedure used for such models (see, e.g., [5]), one easily arrives at a dispersion relation for the fundamental axisymmetric mode, which is a slow ($k/h = v_\varphi/c < 1$) hybrid wave,

$$\frac{p^2}{k^2}\tan^2\vartheta\frac{I_0(pa)K_0(pa)}{I_1(pa)K_1(pa)}$$

$$\times\left[1-\frac{I_0(pa)K_0(pb)}{K_0(pa)I_0(pb)}\right][1-\chi K_1(pb)I_1(pb)] \quad (29)$$

$$= 1-\chi K_1(pb)I_1(pb)\left[1-\frac{I_1(pa)K_1(pb)}{K_1(pa)I_1(pb)}\right].$$

Here, $p = \sqrt{h^2-k^2}$ and h are transverse and longitudinal wavenumbers; $k = \omega\sqrt{\varepsilon_0\mu_0}$; ϑ is the angle of winding (Fig. 3); I_m and K_m are the modified Bessel and Macdonald functions of order m, respectively; and

$$\chi = \frac{2\pi}{\varepsilon_0}k^2b^2C \quad (30)$$

is the shunting coefficient, which is proportional to capacity per unit length C and frequency squared (ω^2).

If slot width d is so small that the shunting coefficient becomes high ($\chi \gg 1$), expression (29) turns into the dispersion relation for a helix in a continuous perfectly conducting shield that is well known from the theory of slow-wave systems [5]. If $\chi \ll 1$ (that is, for example, shield wall thickness Δ is small, $\Delta/d \ll 1$), expression (29) turns into the simplified dispersion relation

$$\frac{p^2}{k^2}\tan^2\vartheta\frac{I_0(pa)K_0(pa)}{I_1(pa)K_1(pa)}\left[1-\frac{I_0(pa)K_0(pb)}{K_0(pa)I_0(pb)}\right] = 1, \quad (31)$$

which was obtained in another work [6] concerned with the Rogowski loop.

A number of simple dependences given below illustrate the dispersion properties of the electrodynamic system of the Rogowski loop and the effect of a shield on these properties. Figure 4 plots slowing-down k/h versus frequency ω for a helix without a shield ($pb \longrightarrow \infty$) and for the same helix placed in a continuous ($\chi \gg 1$) shield. In the low-frequency range, the shield is seen to have a significant effect on the slowing-down and, importantly, the role of longitudinal slots is high. It is remarkable that, as the transverse conduction of the shield declines, the low-frequency slowing-down increases and may even exceed its asymptotic value at $\omega \longrightarrow \infty$.

Detailed slowing-down curves taken at two different ratios between the radii of turns and longitudinal-conductance ($\chi \ll 1$) shield are presented in Fig. 5. By appropriately selecting the geometric parameters (Fig. 5b), the dispersion characteristics of waveguides with different shields may be rendered the same. This

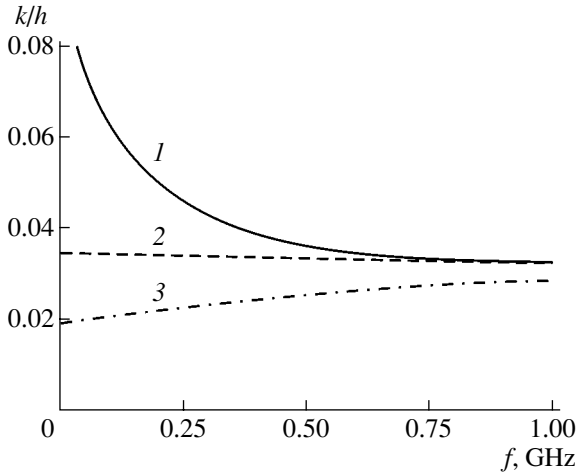

Fig. 4. Dispersion characteristics of helix waveguides with coil pitch $d = 1$ mm, turn diameter $2a = 10d$, and outer shield diameter $2b = 2.4a$. (*1*) Helix without a shield, $(k/h)_{f=0} = 1$; (*2*) helix inside a continuous shield; and (*3*) helix inside a longitudinally conducting shield. For all the waveguides, $\lim_{f\to\infty} k/h = 0.032$.

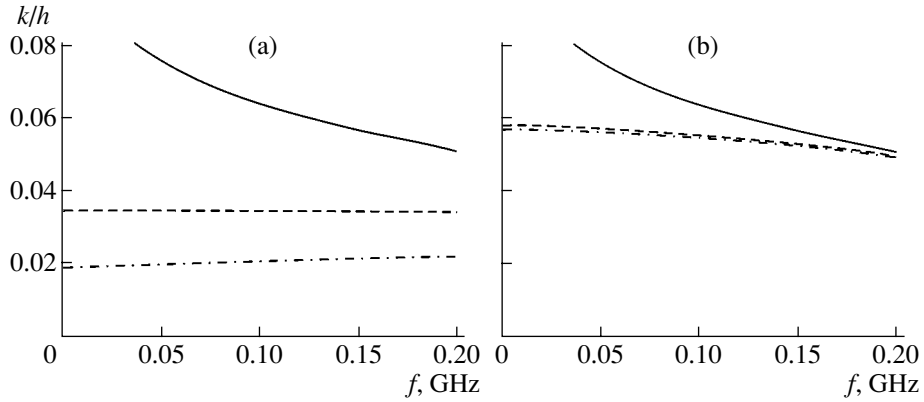

Fig. 5. Low-frequency parts of the dispersion characteristics of helix waveguides with coil pitch $d = 1$ mm. The dashed line, a helix inside a continuous shield; dash-and-dot line, a helix inside a longitudinally conducting shield; and continuous line, unshielded helix. (a) $2a = 10d$, $2b = 2.4a$ and (b) $2a = 10d$, $2b = 10a$. For all the waveguides, $\lim_{f \to \infty} k/h = 0.032$.

fact may be put to good use in designing irregular loops and matching the loop with a continuous shield (see (22)).

According to (18), the dispersion-related relative error in the shape of $\hat{U}_1(t)$ can be found by the formula

$$\delta\hat{U}_1 = \left|\frac{\Delta\hat{U}_1}{\hat{U}_1}\right| = \left|\frac{\Delta v}{v_{cr}}\right|, \quad (32)$$

where $\Delta v = v - v_{cr}$, $v_{cr} = \left.\frac{\omega}{h}\right|_{\omega = \omega_{cr}}$ is the phase velocity of the fundamental mode of the loop at frequency $\omega_{cr} = 1/\tau_r$ and τ_r is the current pulse rise time.

For the dispersion curves shown in Fig. 5a,

$$\delta\hat{U}_1^{(1)} = 17.1, \quad \delta\hat{U}_1^{(2)} = 0.006, \quad \delta\hat{U}_1^{(3)} = 0.11; \quad (33)$$

for those shown in Fig. 5b,

$$\delta\hat{U}_1^{(1)} = 17.1, \quad \delta\hat{U}_1^{(2)} = 0.11, \quad \delta\hat{U}_1^{(3)} = 0.09. \quad (34)$$

As follows from the above estimates, dispersion may heavily distort the pulse shape; however, the distortion may be decreased to a reasonable value by modifying the shield design.

Without pretending to completeness, these results do illustrate not only the strong effect of shields on the dispersion characteristics but also the feasibility of varying parameters γ and v by properly selecting the size of the shield and the slot. One can also try to find conditions that provide a minimal value of dispersion parameter γ and, hence, to minimize distortions; however, to do this requires a more rigorous waveguide model than the one considered here.

(5) Taking into account shunting capacitance C (see (26c)) makes it possible to more correctly estimate the dispersion properties of the fundamental mode and find excitation conditions for higher frequency modes, which contribute to the error in measuring short current pulses.

Consideration of shunting capacitance C also allows one to estimate the difference between the current measured, J_{00}, and current J_0 entering into formulas (4). This difference, associated with azimuth currents passing through the shield, can be included by substituting the Faraday induction law

$$\varepsilon = -\pi b^2 \mu_0 \partial H_z/\partial t \quad (35)$$

into boundary condition (26c) written for the physical quantities,

$$J_{00} = J_0 + \frac{1}{\omega_0^2}\frac{\partial^2 J_0}{\partial t^2}, \quad (36)$$

$$\omega_0^2 \simeq 1/\pi b^2 \mu_0 C. \quad (37)$$

If the capacitance is small,

$$(\omega_0 \tau_0)^2 \gg 1 \quad (38)$$

the difference between currents J_{00} and J_0 is also small and the correction can be calculated directly from (36). Note that frequency ω_0 is more convenient to calculate not from (37) but from the period of ringing, which is often observed in voltage waveforms at the output of the loop [2]. At moderate frequencies, $(\omega_0\tau_0)^2 \simeq 1$, formula (36) fails in reconstructing the shape of a current pulse being measured and, accordingly, the configuration of the loop should be refined.

CONCLUSIONS

Under the simplifications and assumptions made in this work, our tentative analysis of the Rogowski loop operation in the short-pulse regime indicates the following.

(i) Dispersion should be taken into account both in elaborating a correct theory and in experimental data processing.

(ii) The configuration of the shield to a great extent specifies the dispersion characteristics of the electrodynamic system of the loop.

(iii) The basic parameters of the dispersion relation and the resonance frequencies can be determined by processing a number of sequential voltage pulses picked up from the load.

The analytical relationships obtained in this work apparently have a limited range of applicability. To generalize them, it is desirable to dismiss the approach based on the equivalent circuit and use a more general electrodynamic theory of waveguide excitation by nonstationary currents. This would allow us to more correctly consider the effects of shielding and multimodality, as well as nonuniformities in the induced emf distribution (i.e., in distribution $\kappa = \kappa(x)$). In addition, we could have a chance to locate the current being measured in the loop's cross section and to take into account the inverse effect of the loop on the current being measured.

It is also worth noting that, when slightly refined, the solutions obtained are applicable to the problem of excitation and reception of surface acoustic waves by piezoelectric transducers and to analysis of fiber sensors.

REFERENCES

1. J. Cooper, Plasma Phys. **5**, 285 (1963).
2. S. B. Vasserman, Prib. Tekh. Éksp., No. 2, 99 (1972).
3. V. Nassisi and A. Luches, Rev. Sci. Instrum. **50**, 900 (1979).
4. A. I. Pavlovskiĭ *et al.*, Prib. Tekh. Éksp., No. 3, 111 (1991).
5. R. V. Silin and V. P. Sazonov, *Slow-Wave Systems* (Nauka, Moscow, 1966) [in Russian].
6. H. Krompholz, K. Schoenbach, and G. Schaefer, in *Proceedings of the IEEE Instrumentation and Measurement Technology Conference (IMTC'85), Tampa, 1985*, pp. 224–227.

Translated by V. Isaakyan

Technical Physics, Vol. 50, No. 9, 2005, pp. 1230–1232. Translated from Zhurnal Tekhnicheskoĭ Fiziki, Vol. 75, No. 9, 2005, pp. 123–125.

SHORT COMMUNICATIONS

Sliding *Z*-Pinch

V. D. Selemir, A. E. Dubinov, E. A. Ryaslov, V. I. Kargin, and B. G. Ptitsyn

All-Russia Research Institute of Experimental Physics, Federal State Unitary Enterprise Russian Federal Nuclear Center, Sarov, Nizhegorodskaya Oblast, 607190 Russia

e-mail: dubinov@ntc.vniief.ru

Received July 5, 2004

Abstract—New devices are proposed for producing self-contracting discharges. The operation principle of these devices is based on focusing of plasma sliding over the insulator surface, when the magnetic field of the sliding discharge itself presses the plasma channel to the surface and focuses it. One of the proposed devices with an insulator in the form of a dihedral angle is studied experimentally. X-rays are detected and an X-ray image of the focused plasma is formed. © *2005 Pleiades Publishing, Inc.*

Pinch-type devices such as the cylindrical Z-pinch [1], crossing X-pinch [2], and plasma focus [3] are often used for obtaining dense high-temperature plasmas and for generating thermal X-ray pulses and neutrons, as well as for pulsed thermonuclear fusion research. In all such devices, the magnetic field of the discharge executes bulk focusing of a current-carrying plasma.

In patent [4], new devices were proposed for obtaining such discharges with focusing and with a plasma sliding over the insulator surface, when the magnetic field of the sliding discharge itself presses the plasma channel against the surface and focuses it. This leads to suppression of kink and snake instability by the solid surface of the insulator; ensures convenient visualization of the plasma focusing owing to open geometry of the system; and results in exact localization of the plasma focus at the bent or in the corner on the insulator surface, which makes it possible to install the required sensors for diagnostics of dense plasmas beforehand.

In accordance with [4], several different devices can be designed, such as a device for generating a longitudinal sliding Z-pinch (book-type configuration in Fig. 1a) with plasma focusing at the bend of the insulator; a device for obtaining a sliding X-pinch (pyramid-type configuration in Fig. 1b) with plasma focusing at the tetrahedral angle of the insulator; and a Meiser sliding focus (book-type configuration in Fig. 1c) with plasma focusing at the bend of the insulator. In all cases, a special arrangement of the current source and power buses is required to ensure plasma pressing against the insulator and plasma focusing.

It should be noted that the sliding discharge mode is often used to form a plasma shell in traditional devices for obtaining a cylindrical Z-pinch [5] and plasma focus [6]; however, the discharge contours in these devices are organized so that the magnetic field of the discharge detaches the plasma from the insulator surface and produces bulk focusing.

Here, we report the results of first experiments with a Z-pinch in a device with a book-type configuration, which demonstrate the operating capacity of this device. Figure 2 shows such a device. The insulator was made of caprolan in the form of a 90°-dihedral angle with 2×2-cm square faces; the thickness of the insulator wall was 0.5 cm. The electrodes were made of steel; at a distance of 1.5 cm from the book edge, the electrodes were equipped with tips initiating the surface discharge. The device was placed in a vacuum chamber in which the air pressure was maintained at 10^{-1} Torr.

We used a power source with the following characteristics: capacitance 0.8 μF, inductance 0.55 μH, and charging voltage 75 kV. Power was supplied to the device via RK-75-9-13 coaxial cables. The total inductance of the discharge loop was 0.95 μH.

In our experiments, we recorded discharge current pulses in the loop, light pulses, UV radiation pulses, and soft X-ray pulses (SXPs). A pinhole camera was used for obtaining an X-ray image of the discharge.

Light pulses were registered with the help of a photocell F-22, while a photocell F-32 registered UV radi-

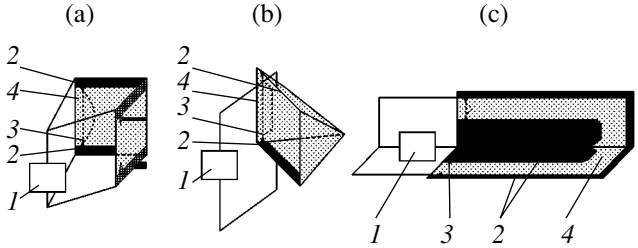

Fig. 1. Proposed configurations of devices for studying sliding pinches: (a) *Z*-pinch of the "book" type; (b) X-pinch of the "pyramid" type; (c) plasma focus of the "book" type: *1*—current source; *2*—electrodes; *3*—tips for initiating a discharge; *4*—surface of the insulator against which the discharge is pressed; dashed curves show discharge channels.

1063-7842/05/5009-1230$26.00

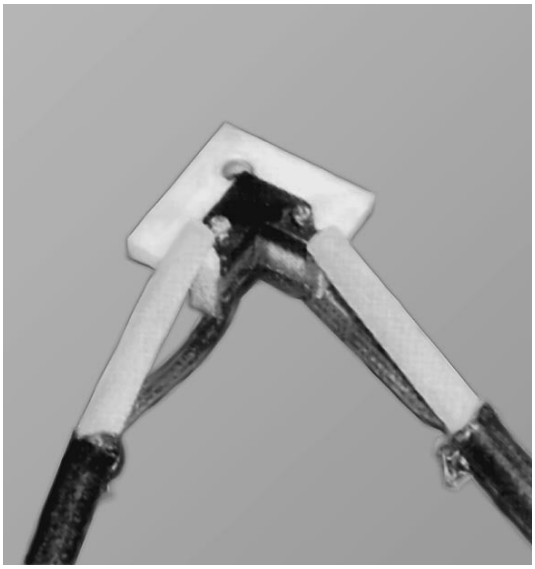

Fig. 2. Device for studying the sliding *Z*-pinch of the "book" type.

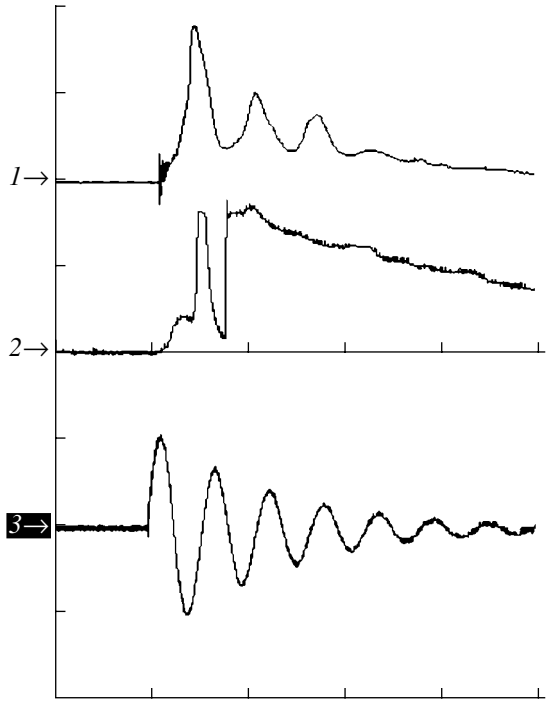

Fig. 3. Oscillograms of current and radiation: *1*—light pulse; *2*—UV pulse; *3*—discharge current; sweep is 10 μs/div.

ation pulses. The diaphragms on photocells F-22 and F-32 were chosen so that the amplitudes of their signals induced by the flash of a calibration lamp IFK-120 were equal. SXP pulses were registered using three semiconductor detectors SPPD-11. The first detector was not equipped with a filter and detected radiation with a quantum energy $E_\gamma > 400$ eV; the second detector was equipped with a 10-μm-thick Dacron filter with a 1-μm-thick aluminum coating. This detector registered radiation with a quantum energy $E_\gamma > 2$ keV. The third detector with an aluminum foil filter (10 μm in thickness) registered radiation with a quantum energy $E_\gamma > 5$ keV. All detectors were mounted in the vacuum part of the device at a distance of 100 mm from the discharge. The pinhole camera had the same filter as in the second detector and was placed at a distance of 180 mm from the edge of the dihedral angle.

Figures 3 and 4 show oscillograms of the pulses obtained for the discharge current amplitude of 70 kA in the loop. The UV pulse amplitude was an order of magnitude larger than the amplitude of the light pulse. The amplitudes of the pulse from the first, second, and third detectors were 2.8, 0.4, and 0.07 V, respectively.

It is well known that the sensitivity of semiconductor detectors SPPD-11 is 5.5×10^{-18} A s cm^2/quantum for $E_\gamma = 400$ eV, 56×10^{-18} A s cm^2/quantum for $E_\gamma = 2$ keV, and 155×10^{-18} A s cm^2/quantum for $E_\gamma = 5$ keV. The filters of the second and third detectors suppresses radiation with $E_\gamma = 2$ and 5 keV by factors of 3 and 1.7, respectively. For this reason, the radiation flux with $E_\gamma > 400$ eV is 23 times that for radiation with $E_\gamma >$

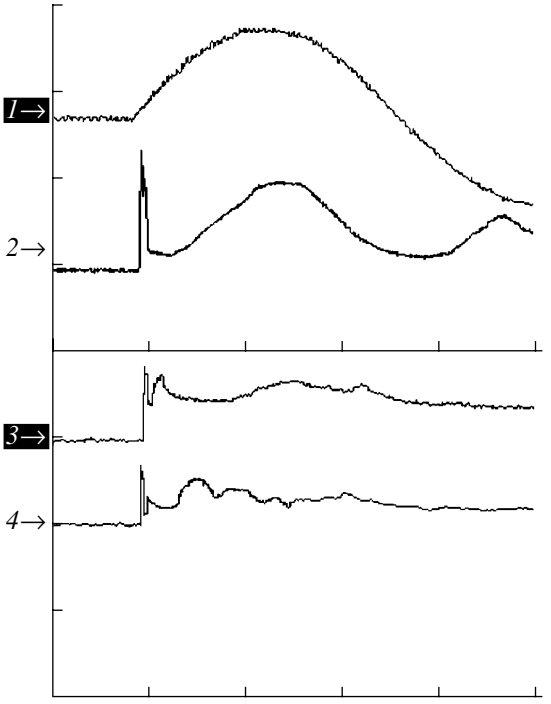

Fig. 4. Oscillograms of current and X-ray radiation: *1*—discharge current; *2*—SXP from the first detector ($E_\gamma >$ 400 eV); *3*—SXP from the second detector ($E_\gamma > 2$ keV); *4*—SXP from the third detector ($E_\gamma > 5$ keV); sweep is 1 μs/div.

Fig. 5. X-ray image of the plasma in the focus region, integrated over the pulse.

2 keV, while the radiation flux with $E_\gamma > 2$ keV is 27 times that for radiation with $E_\gamma > 5$ keV.

The image of the pinch obtained with the help of an X-ray pinhole camera is shown in Fig. 5. This image is integrated in time; consequently, we can state that radiation with the highest intensity corresponds to the instant of discharge pinching. The characteristic transverse dimensions of the X-ray source formed in the region of the edge of the dihedral angle were ~1 mm.

Thus, preliminary experiments indicate the effectiveness and promise of the devices proposed here for studying magnetic focusing of high-temperature plasmas.

REFERENCES

1. V. D. Selemir, V. A. Demidov, A. V. Ivanovskiĭ, *et al.*, Fiz. Plazmy **25**, 1085 (1999) [Plasma Phys. Rep. **25**, 1000 (1999)].
2. G. V. Ivanenkov, S. A. Pikuz, D. B. Sinars, *et al.*, Fiz. Plazmy **26**, 927 (2000) [Plasma Phys. Rep. **26**, 868 (2000)].
3. J. O. Pouzo and M. M. Milanese, IEEE Trans. Plasma Sci. **31**, 1237 (2003).
4. A. E. Dubinov, B. G. Ptitsyn, and V. D. Selemir, RF Patent No. 2200372, Byull. Izobret., No. 7 (2003).
5. S. I. Andreev, O. G. Baikov, P. N. Dashuk, and P. G. Popov, Zh. Tekh. Fiz. **47**, 1205 (1977) [Sov. Phys. Tech. Phys. **22**, 691 (1977)].
6. B. G. Ptitsyn and E. N. Smirnov, in *Studies on the Physics of the Gas Discharge: Collection of Scientific Works*, Ed. by V. D. Selemir and A. E. Dubinov (RFYaTs-VNIIÉF, Sarov, 2003), pp. 6–47.

Translated by N. Wadhwa

Technical Physics, Vol. 50, No. 9, 2005, pp. 1233–1235. Translated from Zhurnal Tekhnicheskoĭ Fiziki, Vol. 75, No. 9, 2005, pp. 126–128.

SHORT COMMUNICATIONS

Electron Emission from a Cathode Doped by Fast Particles of a Working Gas

A. P. Bokhan, P. A. Bokhan, and Dm. É. Zakrevsky

Institute of Semiconductor Physics, Siberian Division, Russian Academy of Sciences, pr. Akademika Lavrent'eva 13, Novosibirsk, 630090 Russia

e-mail: bokhan@isp.nsc.ru

Received July 20, 2004

Abstract—The effect of fast charged and neutral particles on the emission properties of different materials is investigated. In many plasma devices, a flux of fast atoms and ions produces a specific self-sustained state of the layer near the cathode surface. In particular, this layer is saturated by working gas atoms to a depth of several monolayers. This state variously modifies different types of emission. Potential emission, taking place under the action of metastable atoms and ions, weakens because of a rise in the work function. On the contrary, kinetic emission, which is due to fast heavy particles, is enhanced, since energy losses in the modified near-surface layer increase. Photoemission resulting under the action of resonance radiation increases considerably, and its mechanism changes. © *2005 Pleiades Publishing, Inc.*

(1) Plasma devices, in which fluxes of charged and neutral particles (electrons, ions, and atoms) are generated, are being widely used in contemporary science and technology (their application ranges from devices intended for magnetic plasma confinement to etchers used in semiconductor technology). The key factor governing the properties of the devices is the emissivity of structural materials exposed to fast heavy particles and photons in the vacuum UV (VUV) range. Emission caused by particle bombardment has been studied for about a century. To date, a huge body of both theoretical and experimental data on this issue has been collected. However, attempts to employ these data in simulating, for example, the anomalous gas discharge often applied in plasma technologies have led to the conclusion that the behavior of electrical characteristics (in particular, decreasing *I–V* characteristics [1, 2]) is physically meaningless [1]. Despite significant efforts made in this field, the authors of [3–5] inferred that emission under the conditions considered is basically unpredictable.

To resolve this contradiction requires that other approaches to the problem be applied. In particular, one should assume that the material in the near-surface layer is characterized by a specific state with considerably modified emission properties. The aim of this study is to elucidate a mechanism of such modifications and how they influence the emissivity.

(2) Implantation of particles with energies ranging from a fraction of a kilo-electron-volt to several kilo-electron-volts into the material as a mechanism of surface modification has not yet been considered. Note that, when a gas discharge occurs in argon with a Cu cathode at a field intensity in the cathode region E/N = 100 kTd or at an average energy of ions and fast atoms of 500 eV, the penetration depth calculated according to [6] equals ≈25 Å (E is the field intensity, N is the particle concentration, and 1 Td = 10^{-21} V m^2). The radius of an Ar atom for an interaction energy of ≈5 eV (which is equal to the work function) is 1.85 Å [7]. Consequently, more than six Ar monolayers form in the near-surface layer if the atom density in a monolayer is taken to be equal to ~10^{19} m^{-2}. At a current density of 10 A/m^2, the flux of fast atoms and ions into the material is ≈2 × 10^{20} m^{-2} s^{-1}, while the diffusion flux in the opposite direction is weaker by several orders of magnitude. The energy of electron detachment from atoms, such as hydrogen atoms in tokamaks or high-temperature traps and noble gas atoms in discharges, significantly exceeds the free energy of structural materials. Therefore, working gas particles implanted into the target stay in the atomic state and the near-surface layer remains saturated.

Exchange interaction, greatly expanding the cross section of inelastic collisions between identical atoms, raises the probability of ionizing the implants. Since the kinetic part of the coefficient of ion–electron emission is proportional to energy losses due to particle–particle inelastic collisions in the cathode [8], $\gamma_{ic} \sim (dw/dx)_i$, the emission threshold lowers and the emission yield grows. The mean free path of the resulting electrons is several tens of angstroms [9], and so the entire modified layer contributes to emission. For potential emission, the implants, which have a high ionization energy, produce an additional barrier raising the work function [8]. Therefore, the yield of electrons drops.

Figure 1 (curve *a*) shows coefficient γ_{ap} of apparent emission for a Cu cathode exposed to argon atoms and argon ions in an anomalous discharge. The curve was calculated for a wide range of E/N based on the model

1063-7842/05/5009-1233$26.00

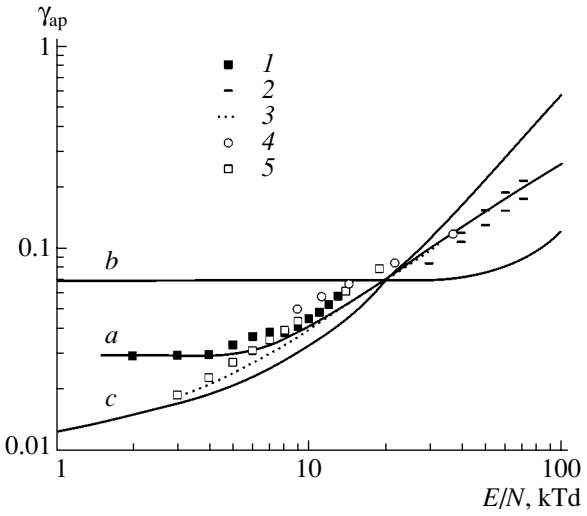

Fig. 1. Apparent emission coefficient γ_{ap} vs. reduced field intensity at the cathode: (*a*) the model used in this study, (*b*) the model of pure surface, and (*c*) the model of contaminated surface. The data points are taken from (*1*) [1], (*2*) [10], (*3*) [11], (*4*) [12], and (*5*) [13].

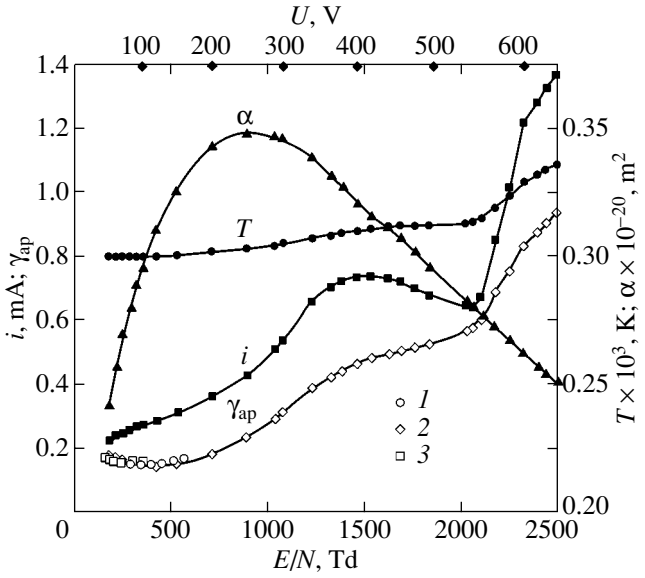

Fig. 2. Current *i* in the accelerating gap, apparent emission coefficient γ_{ap} (P = (*1*) 5, (*2*) 8.8, and (*3*) 15 Torr), Townsend coefficient α, and operating temperature *T* vs. reduced field intensity *E*/*N*.

considered. For the coefficient of potential emission, we took $\gamma_{ip} = 0.03$, as follows from measurements made under actual gas-discharge conditions [1]. Kinetic emission is related to the interaction of fast heavy particles with the cathode and the argon atoms implanted in it. The emission from the Cu cathode under the action of argon ions and argon atoms was calculated using the approximation [3] for the material cleaned by discharge sputtering, $\gamma^c_{i,a} = 5 \times 10^{-5} kT^{1.2}_{i,a}(-300/kT_{i,a})$, where k is the Boltzmann constant and $T_{i,a}$ is the temperature of heavy argon particles. In turn, $kT_{i,a} = 1.9(E/N)^{1.1}$, where kT and E/N are expressed in eV and kTd, respectively. It was taken into account that there were two fast atoms for an ion [10]. The emission caused by interaction with the implanted argon was calculated by the general relationship $\gamma_{ic} = \Lambda(dw/dx)_i$ [8], where $\Lambda = 10^{-11}$ m/eV. The energy losses were evaluated from the ionization coefficient and coefficient of resonance state excitation [3]; the elastic losses, according to [6].

Today, the available techniques for calculating the secondary electron extraction coefficient lack accuracy; therefore, curve *1* in Fig. 1 was calibrated at one point: at E/N = 100 kTd, $\gamma_{ap} = 0.27$ according to [4]. The experimental data known to date are also presented in Fig. 1. For comparison, curves *b* and *c* show the data for γ_{ap} calculated in terms of the "pure" and "contaminated" surface models, respectively [3]. The observed spread in γ_{ap} characterizes the surface condition. It is seen that the model proposed eliminates this spread and is in good agreement with the experimental data. Specifically, in terms of this model, the significant decrease in the energy threshold for kinetic emission, which is observed in the experiments, is accounted for by excitation and ionization of implanted atoms when fast particles of the working gas bombard the cathode.

(3) Implantation of working atoms into near-surface layers radically modifies the photoemission mechanism. For radiation in the VUV range ($\lambda < 100$ nm), the absorption coefficient in metals decreases rapidly, which leads to a sharp drop in electron yield γ_p under the action of photons [2, 14, 15]. For implanted helium atoms, the resonance radiation absorption cross section calculated for the Doppler profile is on the order of 10^{-17} m^2. This corresponds to the total absorption over 10^{-2} of a helium atom monolayer. Under these conditions, the resonant state is rapidly deactivated due to Auger processes. The rate of deactivation is comparable to, or even exceeds, the rate of radioactive decay [8]. As far as we know, emission coefficient γ_p corresponding to this mechanism has not been measured.

Experiments with photoemission from near-surface atoms were carried out using the setup described in [16]. The measuring cell contains an accelerating gap ($l = 10^{-3}$ m) formed by a gridlike anode and a massive Fe cathode. The electrons accelerated are gathered by a collector. The current in the accelerating gap is described by the relationship [5]

$$i = i_0 \exp\alpha Nl/(1 - \gamma_{ap}(\exp\alpha Nl - 1)),$$

where i_0 is the emission current produced by optical illumination from the drift space and α is the Townsend coefficient of electron multiplication.

I–V characteristics of such a discharge in helium are exemplified in Fig. 2. From a family of *I–V* curves obtained at different pressures and i_0, one can find γ_{ap} and α entering into the expression for *i*. In the range of small *E*/*N* (down to *E*/*N* ≈ 700 Td), where γ_{ap} depends on *E*/*N* only slightly, potential emission with coefficient $\gamma_{ip} = 0.158 \pm 0.007$ prevails. According to the formula $\gamma_{ip} = 0.032(0.78E_i - 2\Phi)$ [17], this corresponds to work function $\Phi = 7.1$ eV versus $\Phi_0 = 4.3$ eV for the pure cathode surface (here, E_i is the ionization energy of an atom striking the cathode). As follows from Fig. 1, for the discharge in Ar, $\Phi = 5.67$ eV versus 4.4 eV for pure Cu. Consequently, implanted He atoms create a higher threshold for electron escape than Ar atoms in full accordance with the theory of potential emission [8].

As ratio *E*/*N* increases, other mechanisms of emission come into play. At voltages *U* > 600 V, when the processes of excitation and ionization in the gap weaken considerably because of a decrease in α (see [18] and Fig. 2), optical illumination from the drift space due to deceleration of fast electrons becomes a key factor. Kinetic emission of electrons contributes insignificantly ($\Delta\gamma_{i,a} = 0.008$ at *U* = 630 V) according to the data on $\gamma_{i,a}$ for helium [19]. Consequently, contribution γ_{ph} of photoemission to γ_{ap} is $\gamma_{ph} = \gamma_{ap} - \gamma_{ip} - \Delta\gamma_{i,a} = 0.78$. The amount of photons that reached the cathode, N_{ph}, was calculated with allowance for excitation due to (i) the avalanche multiplication of electrons in the gap; (ii) fast electrons scattered by the anode; (iii) the field extending outside the anode; and (iv) accelerated electrons emitted from the cathode, forming in the gap, and escaping into the drift space. The total amount of photons per emitted electron was found to be $N_{ph} = 3.5$ at *U* = 630 V. This yields emission coefficient $\gamma_p = \gamma_{ph}/N_{ph} = 0.22$ versus $\gamma_p \approx 0.03$ for the pure surface [3]. The theoretical coefficient of emission from excited atoms calculated by the formula $\gamma_r = 0.032(0.78E_r - \Phi)$ [8, 17] is $\gamma_r = 0.3$ (E_r is the excitation energy of resonance states). Hence, it follows that more than 70% of helium atoms excited in the surface layer are deactivated in Auger processes and generate electrons.

Thus, modification of the near-surface region (several monoatomic layers in thickness) under the action of fast working particles leads to a radical change in the emissivity of materials. The mechanisms of potential emission (due to ions) and of kinetic emission (due to fast heavy particles) remain the same: the changes are of only quantitative character. The potential emission weakens, whereas the kinetic one is enhanced, with a simultaneous decrease in the energy threshold. At the same time, the mechanism of photoemission changes completely and the process passes through two stages: the excitation of the resonant state of implanted atoms and the deactivation of the atoms through Auger processes with electron generation. In this case, the emission coefficient increases considerably as compared with that for the pure surface. Our results are in good agreement with the available data obtained under controlled experimental conditions.

ACKNOWLEDGMENTS

This work was supported in part by the Russian Foundation for Basic Research, grant no. 04-02-17407.

REFERENCES

1. D. Maric, K. Kutasi, G. Malovic, *et al.*, Eur. Phys. J. D. **21**, 73 (2002).
2. A. V. Phelps, L. C. Pichford, C. Pedoussat, *et al.*, Plasma Sources Sci. Technol. **8** (4), B1 (1999).
3. A. V. Phelps and Z. L. Petrovic, Plasma Sources Sci. Technol. **8** (3), R21 (1999).
4. A. V. Phelps, Plasma Sources Sci. Technol. **10**, 329 (2001).
5. Yu. P. Raizer, *Gas Discharge Physics* (Nauka, Moscow, 1992; Springer, Berlin, 1991).
6. W. D. Wilson, L. G. Haggmark, and J. P. Biersack, Phys. Rev. B **15**, 2458 (1977).
7. V. K. Nikulin, Zh. Tekh. Fiz. **41**, 41 (1971) [Sov. Phys. Tech. Phys. **16**, 28 (1971)].
8. P. Varga and H. Winter, in *Particle Induced Electron Emission II*, Ed. by G. Hohler (Springer, New York, 1992); Springer Tracts Mod. Phys. **123**, 149 (1992).
9. J. Devooght, J.-C. Dehaes, A. Dubus, *et al.*, Springer Tracts Mod. Phys. **122**, 67 (1991).
10. A. Bogaerts and R. Gijbels, Plasma Sources Sci. Technol. **11**, 27 (2002).
11. Z. J. Donko, J. Appl. Phys. **88**, 2226 (2000).
12. K. Kutasi and Z. Donko, J. Phys. D **33**, 1081 (2000).
13. Z. Donko, Phys. Rev. E **64,** 026401 (2001).
14. W. C. Walker, O. P. Rustgi, and G. L. Weissler, J. Opt. Soc. Am. **49**, 471 (1959).
15. R. B. Cairns and J. A. R. Samson, J. Opt. Soc. Am. **56**, 1568 (1966).
16. A. P. Bokhan and P. A. Bokhan, Pis'ma Zh. Tekh. Fiz. **27** (6), 7 (2001) [Tech. Phys. Lett. **27**, 220 (2001)].
17. R. A. Baragiola, E. V. Alonso, J. Ferron, and A. Oliva-Florio, Surf. Sci. **90**, 240 (1979).
18. A. N. Tkachev and S. I. Yakovlenko, Pis'ma Zh. Éksp. Teor. Fiz. **77**, 264 (2003) [JETP Lett. **77**, 221 (2003)].
19. P. Hartmann, H. Matsuo, Y. Ohtsuka, *et al.*, Jpn. J. Appl. Phys. **42**, 3633 (2003).

Translated by Yu. Vishnyakov

Technical Physics, Vol. 50, No. 9, 2005, pp. 1236–1238. Translated from Zhurnal Tekhnicheskoĭ Fiziki, Vol. 75, No. 9, 2005, pp. 129–131.

SHORT COMMUNICATIONS

Relaxation of the Energy of the Protein Colloidal Solution Arising at Drying in Open and Closed Systems

E. Rapis

Laboratory of Applied Physics, Tel-Aviv University, Ramat-Aviv, Tel Aviv, 64239 Israel

Received December 27, 2004

Abstract—Experiments show that drying of the same protein colloidal solution in open (air) and closed systems results in two thermodynamically nonequilibrium processes differing in character of energy relaxation. It has been shown that fast removal of the water (evaporation in this case) from the protein–water system is crucial for the protein to stay in the nonequilibrium state. To a certain extent, this fact can be considered as a simplified experimental equivalent of fast adenosine triphosphoric acid (ATF) hydrolysis, a reaction common to living organisms, since fast removal of the water from the water–protein system is also typical of this reaction. This analogy, as well as the similarity (in appearance and types and scales of symmetry) of the protein structures resulting upon drying the protein colloidal solution *in vitro* and *in vivo*, suggests that the relaxation processes taking place at nonequilibrium protein self-organization are similar in thermodynamic parameters in both cases. Thus, there appears the possibility of studying the protein in both the equilibrium and nonequilibrium (as yet poorly understood) state. © *2005 Pleiades Publishing, Inc.*

Long-standing experiments published elsewhere give impetus to discussion concerning the energy relaxation process during drying of the protein colloidal solution under different conditions (in open and closed systems, in a state with a different degree of nonequilibrium, etc.). It has been convincingly (with 100% reproducibility) demonstrated that room-temperature drying of the same protein–water colloidal solution in an open and closed system on a hard substrate is accompanied with different energy relaxation processes.

At slow dehydration in the closed system, the protein crystallizes into an equilibrium structure with long-range order on the angstrom scale. In the open system, evaporation proceeds much more rapidly, the conditions are far from equilibrium, and the character of energy relaxation differs. The medium is activated, exhibiting autowave processes and self-organization properties. The latter show up in self-similarity, replication, and multiplication of 3D helical vortical structures with orderly arranged defects. The defects become macroscopic; the homogeneous mass is divided into blocks (domains or cells with a nucleus at the center); and attributes of autocatalysis, of which a high-energy state is typical, arise.

Thus, the protein in the open system exhibits properties typical of nonequilibrium systems (the Belousov–Zhabotinsky reaction, Benard phenomenon, etc.), where self-organization features nonlinear dynamics and a transition to a high-energy state with free-energy dissipation. In the case at hand, drying of the protein solution causes structuring, whose dynamics, in essence, represents the route of energy stabilization.

The two types of energy relaxation observed at drying of the same protein solution in less and more nonequilibrium (close and open) systems are due to the second law of nonequilibrium thermodynamics. Note that one route of drying is energy-consuming, while the other is conservative. The question arises as to whether the phenomenon observed is pertinent to what happens with protein in the living organism and whether there is at least a bit in common in seemingly radically different processes as vital functions and protein solution drying.

The revealed analogy and the similarity of the structures (in appearance and types and scales of symmetry) resulting upon drying *in vivo* and *in vitro* lead us to look for reasons for such likeness. It is certain that life, with its activity, high energy, mobility, nonequilibrium, and nonlinearity, originates if that form of protein among the above two which offers the attributes of activity serves as a driving force of evolution. It is logical to assume that nature uses the protein in the more nonequilibrium state as a building block of animate matter. Therefore, this form of protein is of special interest in investigating living systems. Significantly, it is precisely this state that has been found to occur upon drying the protein solution *in vitro* in the open system (in air). It seems that a factor common to the processes *in vitro* and *in vivo* is that the protein in the open system is active or, in other words, nonequilibrium; that is, nonequilibrium is pronounced both *in vitro* and *in vivo.* In view of the aforesaid, let us consider the energy relaxation process from another standpoint.

Today, it is generally accepted in biology that the basic source of the energy needed for synthesis and functioning of the protein (for its conformation transitions) is fast ATF hydrolysis with subsequent phospho-

1063-7842/05/5009-1236$26.00

rylation of the protein [1–7]. Yet, the source of the catalytic strength of the protein (enzyme), the reason for its transition to the high-energy state, and the character of energy relaxation still remain a mystery. It has been shown, however, that self-organization, the inherently nonequilibrium process [8, 10], is central to all phenomena taking place in animate matter, including protein. At the same time, the experimental data currently available demonstrate that, when drying out under nonequilibrium conditions in an open system on a hard substrate, the protein passes to a distinctly nonequilibrium state, which is in the process of self-organization [11–16]. Apparently, therein lies the fundamental similarity of the processes *in vitro* and *in vivo.*

The experiments described above are hoped to draw researchers' attention to spontaneous self-organization in an attempt to somehow separate this process out of the complex inseparable processes occurring in the living organism. To do this certainly calls for a deeper insight into the condensation dynamics and structuring of the protein in its nonequilibrium state under highly nonequilibrium thermodynamic conditions. These processes can be simulated singly only *in vitro.* To date, sparse experiments of this sort have been carried out. Emphasis has been on examining the equilibrium crystal structure (lattice with long-range order) of the protein (by X-ray diffraction analysis and similar techniques).

Yet, early steps on the road to studying the nonequilibrium state of the protein have already been made [11–16]. Even they strongly suggest that *in vitro* structuring and autocatalysis in the nonequilibrium state of the protein may proceed without participation of ATF: it is absent upon drying the protein.

The experiments *in vitro* have demonstrated that fast removal of the water (evaporation in our case) from the protein–water system is crucial for the state of the protein to be highly nonequilibrium. These experiments may be viewed as a simplified equivalent of the reaction actually proceeding in the living organism: fast ATF hydrolysis (water capture). Thereby, there has appeared a chance to separate out one stage, fast dehydration of the protein in the water–protein system, from the complex process of functioning of the living organism and visualize its role in the process of protein polymerization (synthesis) in a simplified form *in vitro.* Despite the simplicity of the experimental conditions, it has been proved that fast removal of the water makes the system highly nonequilibrium, i.e., the protein takes the nonequilibrium state upon condensation and self-organization.

These findings allowed us to clarify the source of energy potential at drying (condensation) of the protein colloidal solution *in vitro* in the absence of ATF. It is known that self-organization releases (minimizes) free energy of the system through relaxation during stabilization of the nonequilibrium state [8–10]. It is this mechanism that provides functioning (structuring and conformation reconfiguration) of the protein in our experiments.

Such a viewpoint is totally consistent with the idea put forward in [17], where it was assumed that spontaneous self-organization is the climax of condensation, which executes the intrinsic program of a given system. The author believes that this process alone may be responsible for nonlinear dynamics featuring the presence of organized algorithmically repetitive supramolecular dissipative structures from the nano- to macroscale *in vitro* and *in vivo.* This program forbids the system from evolving in another direction. Based on the data mentioned above, the functioning of ATF may schematically be represented as fast capture of the water using a phosphate chemical system that triggers the fast reaction of protein dehydration (in ATF hydrolysis) and energy release during protein phosphorylation. One may extend the results of the experiments *in vitro*, thinking that fast dehydration *in vivo* also sets nonequilibrium conditions in the water–protein system, which are a prerequisite for the self-organization of the nonequilibrium protein.

One can assume that, in the living organism, both sources of the energy that arises during the self-organization of the protein and depends on its phosphorylation compete, providing the maximal activity and mobility typical of biological systems. It is not improbable, however, that self-organization *in vivo* may proceed without participation of ATF.

The aforesaid can be supported by a set of theoretical and experimental data and also by the results of biological studies.

(1) It is common knowledge that the functioning (self-organization) of the living organism is possible only in open systems, which are far from thermodynamic equilibrium: the equilibrium state of the living organism means its death [1–9, 18, 19].

(2) The experimental data obtained by the author show that self-organization of the protein with conformation reconfigurations in the nonequilibrium state occurs only upon drying the protein colloidal solution in the open (far from thermodynamic equilibrium) system naturally in the absence of ATF [11–16].

(3) It should be noted that there exists a body of experimental and clinical data indicating the functioning of the protein in the absence of ATF, such as the functioning of the protein *in vitro* without ATF [18, 19], the antigen–antibody reaction widely applied in medical practice, and the functioning of pure hydrated (freeze-dried) protein.

(4) Next, recent biological observations that indirectly support the effect of nonequilibrium and nanostructures on the functioning of the protein in the living organism are noteworthy. It has been shown, for example, that enzymes function with a high rate, offering a unique ability of synchronization. Such behavior, which is termed the unstable dynamics of the protein, is characteristic, in particular, of microtubules of the pro-

tein [20]. ATF hydrolysis, causing fast polymerization, is today considered as a reason for the coherent behavior of the protein [21, 23]. This concept is most impressively corroborated by mitosis, when the microtubules are assembled and diassembled with a very high rate. Importantly, all vital processes in the living organism (division, multiplication, functioning, etc.) originate at the nanolevel and evolve to the macrolevel.

CONCLUSIONS

Thus, the experiments with the protein *in vitro* discovered the universal thermodynamic energy properties of matter: self-organization from the nano- to macrolevel. These properties are known to be inherent to inorganic, organic, and animated matter [8–10, 17, 19]. It may be inferred that dissipative structures also occur in the protein under the nonequilibrium conditions of stabilization of its nonequilibrium high-energy state. In other words, the source of activity and mechanical work of the protein may be related to the intrinsic dynamics of its self-organization, i.e., structural (conformation) reconfigurations reaching the macrolevel.

The analogies in the protein behavior discussed above, as well as the similarity (in appearance and types and scales of symmetry) of the protein structures resulting upon drying the protein colloidal solution *in vitro* and *in vivo* [11–16], suggest that the relaxation processes taking place at the self-organization of the nonequilibrium protein are similar in thermodynamic parameters in both cases. Thus, there appears the possibility of studying the protein in both the equilibrium and nonequilibrium (as yet poorly understood) state.

A more detailed investigation into the nonequilibrium state of the protein and its role in the living organism could favor further advances in proteomics (the science of protein); biology; biotechnology; pharmacology; medicine (diagnostics and treatment); and technology, where organic polymers, in particular, protein nanostructures, are today playing a progressively important role.

ACKNOWLEDGMENTS

The author thanks M. Amus'ya, A. Arel, E. Braudo, V. Buravtsev, V. Volkov, A. Zaikin, M. Klinger, L. Manevich, Yu. Neeman, and I. Prigogine for encouragement, fruitful discussion, and valuable remarks.

REFERENCES

1. B. M. Alberts, D. Bray, J. Lewis, *et al.*, *Molecular Biology of the Cell* (Garland, New York, 1989; Mir, Moscow, 1994).
2. E. D. P. De Robertis, W. W. Nowinski, and F. A. Saez, *Cell Biology*, 5th ed. (Saunders, Philadelphia, 1970; Mir, Moscow, 1973).
3. B. M. Alberts, D. Bray, J. Lewis, M. Raff, K. Roberts, and J. D. Watson, *Molecular Biology of the Cell* (Garland, New York, 1983; Mir, Moscow, 1994), Chap. 5.
4. B. M. Alberts, D. Bray, J. Lewis, *et al.*, *Molecular Biology of the Cell* (Garland, New York, 1994; Mir, Moscow, 1994).
5. K. Kimura *et al.*, Science **282**, 487 (1998).
6. D. Evans *et al.*, Nature **394**, 23 (1998).
7. M. B. Yaffe *et al.*, Science **278**, 1957 (1997).
8. I. Prigogine and I. Stengers, *Order Out of Chaos: Man's New Dialogue with Nature* (Heinemann, London, 1984; Progress, Moscow, 1986).
9. A. Winfree, *The Geometry of Biological Time* (Springer, Berlin, 1980).
10. D. Avnir *et al.*, Chem. Phys. Lett. **135**, 177 (1987).
11. E. Rapis, Pis'ma Zh. Tekh. Fiz. **14**, 1561 (1988) [Sov. Tech. Phys. Lett. **14**, 679 (1988)].
12. E. Rapis, Pis'ma Zh. Tekh. Fiz. **21** (5), 13 (1995) [Tech. Phys. Lett. **21**, 321 (1995)].
13. E. Rapis, Pis'ma Zh. Tekh. Fiz. **23** (4), 28 (1997) [Tech. Phys. Lett. **23**, 263 (1997)].
14. E. Rapis, Zh. Tekh. Fiz. **70** (1), 122 (2000) [Tech. Phys. **45**, 121 (2000)].
15. E. Rapis, Zh. Tekh. Fiz. **71** (10), 104 (2001) [Tech. Phys. **46**, 1307 (2001)].
16. E. Rapis, *Protein and Life: Self-Assembling and Symmetry of Protein Nanostructures* (MiltaPKPTIT, Moscow, 2003; Filobiblon, Yerusalem, 2003), p. 257.
17. J. M. Lehn, Proc. Natl. Acad. Sci. USA **99**, 4763 (2002).
18. T. Nishizaka *et al.*, Nature **377**, 251 (1995).
19. J. Dobbie *et al.*, Nature **396**, 383 (1998).
20. J. Howard and A. Hyman, Nature **422**, 753 (2003).
21. Th. Pollard, Nature **422**, 741 (2003).
22. M. Schliwa and G. Wochlke, Nature **422**, 759 (2003).
23. A. Groisman and V. Stainberg, Nature **405**, 53 (2000).

Translated by V. Isaakyan

Technical Physics, Vol. 50, No. 9, 2005, pp. 1239–1242. Translated from Zhurnal Tekhnicheskoĭ Fiziki, Vol. 75, No. 9, 2005, pp. 132–135.

SHORT COMMUNICATIONS

Fractal Model of the Frequency Dependence of Electromagnetic Wave Attenuation by Vegetation Fragments

V. K. Balkhanov and Yu. B. Bashkuev

Buryat Research Center, Siberian Division, Russian Academy of Sciences, ul. Sakhynovoĭ 6, Ulan Ude, 670047 Russia

e-mail: lab@rgp.bsc.buryatia.ru

Received September 20, 2004

Abstract—An approach to describing the earlier discovered power-type frequency dependence of microwave attenuation Y by vegetation fragments is developed. It is established that $Y \sim \omega^{3-D}$, where ω is the circular frequency, 3 is the dimension of the Euclidean space, and D is the fractal dimension of the structure related to vegetation fragments. © *2005 Pleiades Publishing, Inc.*

INTRODUCTION

In [1], the power-type frequency dependence of the attenuation of microwaves by vegetation fragments was found experimentally (Fig. 1). The most natural way of explaining this dependence is invoking the fractal approach and using an equivalent electrical circuit. With such an approach, it becomes possible to express the exponent in the frequency dependence of the attenuation through fractal dimension D and the dimension of the Euclidean space, in which the fragments are embedded. In this work, the attenuation will first be expressed though reduced impedance δ, which is a commonly used physical quantity [2]. Then, we will construct a fractal set describing vegetation fragments and simulate the electrical properties of the fragments by equivalent electrical circuits to make up a hierarchical system and find a desired frequency dependence of the attenuation. Finally, we will show how the dependence found can be determined by qualitative fractal analysis.

1. RELATIONSHIP BETWEEN THE ATTENUATION AND REDUCED IMPEDANCE

The measuring setup used in this work is depicted in Fig. 2 [1]. As was noted in [1] and is seen from Fig. 2, the experimental conditions allow us to assume that a plane wave is incident on the 3D layer formed by vegetation fragments. The aim of the experiment is to measure the wave of intensity $(1/Y)e^{ikx}$ that passes through the 3D layer. Here, Y is the desired attenuation, k is the wavenumber, and x is the propagation direction of the plane wave. For a homogeneous medium, the microwave wavenumber squared is

$$k^2 = \frac{\omega^2}{C^2}\varepsilon,$$

where ω is the circular frequency, C is the speed of light, and ε is the complex permittivity. The attenuation is found by solving the wave problem for a three-layer (free space–3D layer filled with vegetation fragments–free space) medium. With regard to the existence of the forward and backward waves in the 3D layer, factor Y (attenuation) can be expressed as follows:

$$Y = \frac{1}{4}\delta^{-1}. \quad (1)$$

The reduced impedances in inhomogeneous and homogeneous media differ. We will assume that a linear relationship between the attenuation and the reciprocal of the reduced impedance holds in inhomogeneous media like vegetation fragments too. A simplest model that can relate the reduced impedance to the inhomogeneity of the medium handles a fractal set.

2. FRACTAL SET

A fractal model of vegetation fragments will be constructed by invoking the principles of fractal geometry [3, 4]. Similar models were used, for example, in roughness analysis [5].

Let us have a single branch. The length of the branch can be measured on scale χ applying it only once, $N(\chi) = 1$. We divide the branch into three parts so that the side parts account for $1/\alpha$ of the initial length and discard the middle part. Now, taking scale χ/α and applying it twice, one can measure the length of the two remaining parts, $N(\chi/\alpha) = 2$. Substituting $2N(\chi)$ for 2, we obtain the functional equation $N(\chi/\alpha) = 2N(\chi)$. Its solution is $N(\chi) \sim \chi^{-D}$, where exponent $D = \ln 2/\ln\alpha$ is called the fractal dimension. For several branches placed on a plane, the construction described above will

1063-7842/05/5009-1239$26.00

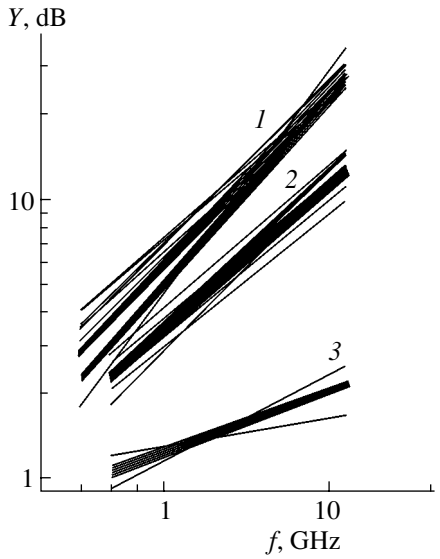

Fig. 1. Frequency dependence of electromagnetic wave attenuation by primary branches: (*1*) $Y = 5.92f^{2.046}$, (*2*) $9.47f^{1.694}$, and (*3*) $1.26f^{0.7186}$.

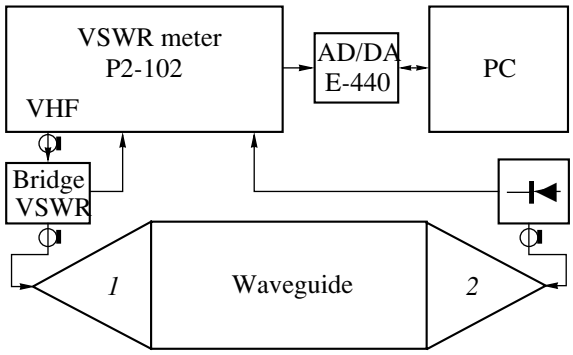

Fig. 2. Schematic of the measuring setup: (*1*) horn generating a plane wave and (*2*) receiving horn.

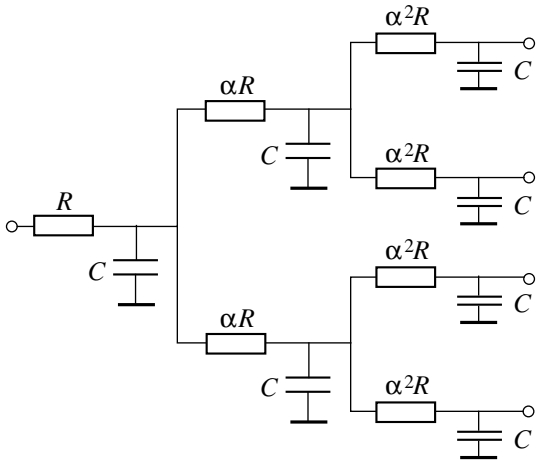

Fig. 3. Equivalent hierarchical circuit used to simulate vegetation fragments.

give the fractal dimension $D = \ln 4/\ln\alpha$. For branches filling a volume, the fractal dimension is

$$D = \frac{\ln 8}{\ln\alpha}. \qquad (2)$$

3. EQUIVALENT ELECTRICAL CIRCUIT

To analyze wave processes in inhomogeneous media, it is necessary to know analytical frequency dependences of basic electrical parameters. These dependences may be found using equivalent electrical circuits, which "highlight" them [6]. The essence of graphical representation of the Maxwell equations is that electromagnetic fields in a domain considered are mapped onto a spatial electric circuit with limped or distributed elements [7]. Correlation between a phenomenon under study and its related electrical circuit (i.e., construction of an equivalent circuit) means that the parameters of the equivalent circuit and those of the phenomenon follow the same relationships. Here, we assume that vegetation fragments form a capacitive medium and so can be simulated by resistance R and capacitance C in a wide frequency range.

It is remembered that we are dealing with the reduced impedance. The reduced impedance of an electrical circuit can be determined by dividing the resistance of all its elements by the free-space resistance, which equals 377 Ω (the awkward formula for the free-space resistance is omitted).

Let us now proceed to simulating the electrical properties of vegetation fragments by an equivalent hierarchical electric circuit consisting of resistance R and capacitance C (Fig. 3). The circuit in Fig. 3 is the same as that used in [5]. The reduced impedance of the first (initial) branch is

$$\delta(\omega) = R + \frac{1}{i\omega C}.$$

Resistance r of either of the next two parallel branches emerging from the initial one is taken to be $r = \alpha R$ with capacitance C remaining the same. The impedance of these two parallel dielectric branches is given by

$$\delta(\omega) = \frac{1}{2}\left(\alpha R + \frac{1}{i\omega C}\right).$$

We recast this formula in the form that clarifies the scheme of constructing the total impedance,

$$\delta(\omega) = \frac{1}{\dfrac{2}{\dfrac{1}{1/\alpha R} + \dfrac{1}{i\omega C}}}.$$

Similarly, the resistance of either of the two parallel branches emerging from each of the former two is taken to be $\alpha = R\alpha^2$ and their capacitance remains unchanged.

Eventually, the total impedance has the form of an infinite fraction,

$$\delta(\omega) = R + \cfrac{1}{i\omega C + \cfrac{2}{\alpha R + \cfrac{1}{i\omega C + \cfrac{2}{\alpha^2 R + \ldots}}}}.$$

Factoring out α from the expression

$$\left(\alpha R + \frac{1}{i\omega C + \ldots}\right)$$

yields

$$\delta(\omega) = R + \cfrac{\alpha}{i\omega C + \cfrac{2}{\delta(\omega\alpha)}}. \quad (3)$$

In the limit $\delta(\omega) \ll 1$, it follows from (3) that

$$\delta(\omega) = \frac{\alpha}{2}\delta(\alpha\omega). \quad (4)$$

The spatial form of expression (4) is

$$\delta(\omega) = \frac{\alpha^3}{8}\delta(\alpha\omega).$$

This is a functional equation that has, in view of (2), the solution

$$\delta(\omega) \sim \omega^{-3+D}. \quad (5)$$

Substituting (5) into (1) yields the desired frequency dependence of the attenuation,

$$Y \sim \omega^{3-D}. \quad (6)$$

Using the data obtained in [1], we find the fractal dimension for three values of the relative humidity of vegetation (see [1], Fig. 3): $D(1) = 0.95$, $D(2) = 1.3$, and $D(3) = 2.3$. These fractal dimensions seem to be typical of vegetation fragments and, possibly, large forests.

4. QUALITATIVE FRACTAL PATTERN

As was noted in [1], "a near-linear dependence of the attenuation on the vegetation biomass is observed." Since the volume of the measuring chamber was fixed, the attenuation varied in proportion with biomass density ρ. The biomass density, in turn, is related to the linear size [8]. Let the linear size be λ. Then, by virtue of the relationship $Y \sim \rho$, we have $Y \sim 1/\lambda^{3-D}$. According to the basic statements of the fractal geometry, one must have a ruler to study inhomogeneous objects. With a ruler, one can study the objects on different scales. If electromagnetic waves are taken as a measuring tool, the wavelength can be naturally used as a scale. In other words, quantity λ mentioned above should be taken as the electromagnetic wave length. Substituting $1/\omega$ for λ, we again arrive at relationship (6).

Some closing remarks are necessary. The fractal dimension reflects the geometric properties of inhomogeneous media. However, Fig. 1 clearly indicates that fractal dimension D depends on the humidity: as follows from (7) and the conclusions drawn in [1], it decreases with increasing humidity. Such a variation of the fractal dimension implies that humidity has a considerable effect on the geometric characteristics of vegetation fragments. This issue will be studied at length in subsequent publications. Here, we only note that

$$D = 0.582m^{-0.885},$$

where m is the gravimetric humidity of vegetation, as follows from the data in [1].

CONCLUSIONS

By virtue of self-similarity, the basic property of the fractal geometry, physical quantities represented on different scales are related to each other via a power-type dependence. In general, however, exponents in these dependences cannot be expressed through the fractal dimension using only the self-similarity of the objects, which necessitates other approaches. As applied to electromagnetic wave attenuation by vegetation fragments, we suggest an approach in which the geometry of the fragments is represented by a fractal set.

The frequency dependence of the attenuation is determined with the reduced impedance, and the inhomogeneous medium (vegetation fragments) is represented as a fractal structure. The electrical properties of the fragments are simulated by an equivalent hierarchical circuit consisting of resistances and capacitances. Such a circuit makes it possible to express the exponent in the frequency dependence of the attenuation through the fractal dimension.

The same frequency dependence of the attenuation is obtained by means of independent qualitative fractal analysis. Based on the data reported in [1], a formula relating fractal dimension D to the gravimetric humidity of vegetation fragments is suggested.

ACKNOWLEDGMENTS

This work was supported by the Russian Foundation for Basic Research, grant nos. 03-05-96029, 05-01-97200, and 05-02-97202.

REFERENCES

1. A. A. Chukhlantsev, S. V. Marechek, E. P. Novichikhin, *et al.*, Radiotekh. Élektronika **49**, 677 (2004).

2. Yu. B. Bashkuev, *Electrical Properties of Natural Layered Media* (Izd. SO RAN, Novosibirsk, 1996) [in Russian].
3. B. B. Mandelbrot, *Les Objets Fractals: Forme, Hazard et Dimension* (Flammarion, Paris, 1975).
4. B. B. Mandelbrot, *The Fractal Geometry of Nature* (Freeman, New York, 1983; Izd. Inst. Komp'yut. Issled., 2002).
5. S. H. Liu, T. Kaplan, and P. Gray, in *Fractals in Physics*, Ed. by L. Pietronero *et al.* (North-Holland, Amsterdam, 1986; Mir, Moscow, 1988), pp. 543–552.
6. V. V. Rzhevskiĭ and E. B. Korenberg, *Radio Introscopy and Radio Communication in Mining* (Nedra, Moscow, 1978) [in Russian].
7. A. S. Petrov, S. A. Ivanov, S. A. Korolev, *et al.*, Usp. Sovr. Radioelektron., No. 1, 3 (2002).
8. J. Feder, *Fractals* (Plenum, New York, 1988; Mir, Moscow, 1991).

Translated by V. Isaakyan

Technical Physics, Vol. 50, No. 9, 2005, pp. 1243–1245. Translated from Zhurnal Tekhnicheskoĭ Fiziki, Vol. 75, No. 9, 2005, pp. 136–138.

SHORT COMMUNICATIONS

Effect of Delay of the Thermocapillary Response of a Transparent Liquid Layer during Laser Heating of the Absorbing Substrate

B. A. Bezuglyi and S. I. Chemodanov

Tyumen State University, Tyumen, 625003 Russia

e-mail: bezuglyi@utmn.ru

Received October 4, 2004; revision received January 25, 2005

Abstract—The effect of delay in the thermocapillary response of a transparent liquid layer on an absorbing substrate during its heating by a laser beam is discovered. The response is an interference pattern formed on a screen placed in the beam cross section by the beam reflected from a thermocapillary dip. It is found that the delay time of the response of a thin ($h < 1.8$ mm) layer of a liquid in a viscosity range of 3–6 mPa s to a 20.9-mW exciting beam from a He–Ne laser ($\lambda = 633$ nm) is proportional to the squared layer thickness with a proportionality factor depending on the viscosity and thermal diffusivity of the liquid. © *2005 Pleiades Publishing, Inc.*

Until recently, photoinduced thermocapillary (TC) convection has been studied predominantly in layers of strongly absorbing liquids of thickness $h > 2$ mm [1–3]. The application of phenomenon in laser diagnostics of liquids [4, 5] requires its study in a transparent liquid layer with $h < 2$ mm on an absorbing substrate. We detected the effect of TC response delay for the first time in such investigations.

It is well known [6] that if a heat source is instantaneously formed on a substrate covered with a layer of liquid so that the temperature of the liquid increases by ΔT, the isotherm ΔTe^{-n} will reach the free surface of the liquid after a time of

$$\tau = h^2/4n\kappa, \quad (1)$$

where κ is the thermal diffusivity and n is a positive number.

This simple idea forms the basis of a number of methods for measuring the thermal diffusivity of solids [6].

It is also known that liquids exhibit a high sensitivity to shear stresses, including those of TC origin. It is this property that formed the basis of a number of liquid-layer systems for information recording [7–9].

The sensitivity of a liquid to shear stresses, which is characterized by number n, obviously depends on viscosity μ. The value of the tangential stress,

$$-\gamma\frac{\partial T}{\partial r} = \mu\frac{\partial v_r}{\partial z}, \quad (2)$$

producing the observed effect increases with viscosity and vice versa. Here, γ is the thermal coefficient of surface tension, T is the temperature, and v_r is the radial velocity field. This study is devoted to verification of the existence of the predicted delay and to determining its dependence on the layer thickness and the liquid viscosity.

The schematic diagram of the experiment is shown in Fig. 1. Laser beam *1* induced TC convection in layer *13*. Since the diameter of the emerging TC deformation of the surface exceeded the diameter of the inducing

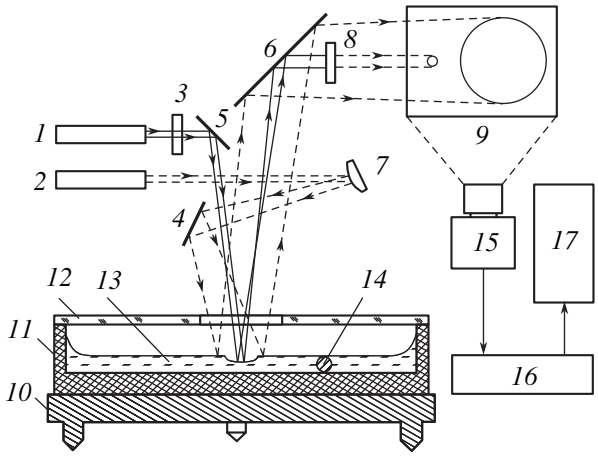

Fig 1. Experimental setup: single-mode He–Ne laser LG-25-1 inducing laser ($\lambda = 633$ nm, $P = 20.9$ mW) (*1*) and test laser LGN-207a ($P = 0.5$ mW) (*2*); shutter (*3*); mirrors (*4–6*); spherical mirror (*7*); light filter (*8*); screen (*9*); micrometer tripod (*10*); ebonite cuvette of diameter 65 mm (*11*); glass lid with a hole of diameter 10 mm (*12*); liquid layer (*13*); gauge wire (*14*); CCD video camera ACE-S560CH (600 lines, 25 frames/s) with Helios-44 objective (*15*); videotape recorder AIWA HV-GX1100 (*16*); and computer Pentium-4 with TV tuner Aver Media VC-8139 (*17*).

Physical characteristics of liquids

Liquid	Viscosity μ, mPa s	Volume expansion coefficient β, K^{-1}	$\frac{Ra}{gh^3\Delta T} \times 10^{-9}$, s^2/m^4 K	*n*
Ethylene glycol	19.9	0.64	0.36	1.4
Benzyl alcohol	5.8	0.75	1.87	2.6
Butanol-1	2.95	0.95	3.35	3.1
n-octane	0.546	1.14	15.7	3.5

beam in the layer (2.5 mm), the boundaries of the TC response were blurred. For complete coverage of the deformation zone of the free surface, a test beam from laser *2* (with a diameter of 10 mm in the layer), which was expanded by spherical mirror *7*, was used; this beam did not introduce any noticeable perturbations. The setup was adjusted with the help of mirrors *4–7* so that the responses to both beams were present on screen *9* in the field of vision of video camera *15*, the inducing beam being suppressed by attenuator *8* to the brightness of the test beam. Gauge wire *14* was used to adjust the preset layer thickness [9], and horizontality of the cuvette bottom was attained with the help of micrometer tripod *10*. The characteristics of liquids studied are given in the table.

The experiments were made at a temperature of 21 ± 1°C in the following manner. Liquid was poured into cuvette *11* with the help of a micropipette and was covered with glass lid *12* with a central hole of diameter 10 mm. The lid noticeably reduces evaporation and protects the layer from the action of convective air flows. The hole ensures the access to the layer for measuring its thickness without affecting the conditions in the bulk of the gaseous phase in the cuvette and ruling out multiple reflection of light from two glass surfaces and from the surface of the liquid. After adjusting the layer thickness, videotape recorder *16* was switched on for recording; shutter *3* was opened, and the response evolution was recorded. The diameter of the response was determined from the frames of video material with the help of the software Photoshop.

Between measurements, a pause was made for the substrate-layer system to return to the initial state. The time of action of the beam on the substrate was a few seconds, while the relaxation time of the system was several minutes. The latter was determined from the effect of the pause between measurements on the experimental results. In experiments, deliberately longer pauses (4-5 min) were made.

After switching on the inducing beam, the pattern of the test beam did not change for a certain time interval.

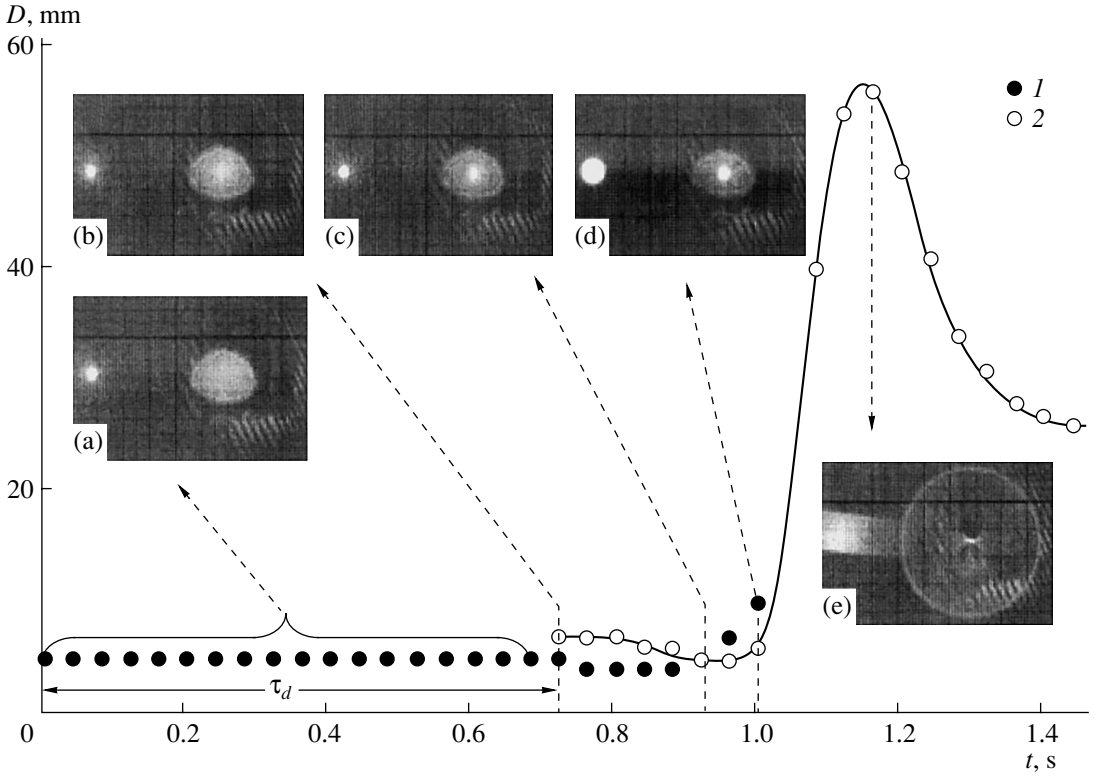

Fig. 2. Evolution of the TC response. Inducing (*1* left) and test (*2* right) beams: (a) response; (b) beginning of deformation, $t = \tau_d$; (c) focusing of test beam; (d) beginning of refocusing; (e) spike.

This pause will be referred to as the TC delay time τ_d of the response, while the beam reflected from the plane surface of the liquid (inducing or test beam) and appearing on the screen will be termed just as the response (Fig. 2a). On the other hand, it is convenient to apply the term the TC response to the beam reflected from the liquid surface that has already been deformed by TC convection (Figs. 2b–2e). The beginning of deformation was registered from the deviation of the free surface from the plane surface observed from the emergence of a light spot at the center of the test beam (Fig. 2b); the spot diameter becomes minimal at the instant of focusing (Fig. 2c). Further, as the deformation depth increases, the diameters of both inducing and test beams become larger (Fig. 2d), culminating in a refocusing spike (Fig. 2e); this is reflected in a sharp increase in the TC response followed by its decrease. The reason for the spike is the accumulation of thermal energy in the liquid layer prior to convection (we omit here the corresponding analysis).

Among the liquids investigated here, only butanol and benzyl alcohol exhibit the predicted quadratic dependence (1) of τ_d on the layer thickness (Fig. 3). For a more viscous ethylene glycol with a larger thickness, the value of τ_d is larger than expected, while for low-viscosity octane it is smaller.

Experimental data suggest that the $\tau_d(h)$ dependence is quadratic in the viscosity range 3–6 mPa s for a layer thickness of $h < 1.8$ mm.

Since the surface itself serves as a detector of thermal perturbation reaching the free surface, a higher shear stress (i.e., a higher temperature gradient (2) and, hence, a longer heating time) is required for producing a detectable deformation for higher values of viscosity. This assumption is confirmed by the arrangement of the $\tau_d(h)$ curves for liquids with different viscosities (Fig. 3).

The departure from the quadratic dependence for octane can be explained by at least three reasons. First, owing to the high mobility of octane, the TC spread of the layer can be initiated by absorption of thermal radiation from the substrate being heated in the layer. This effect must be enhanced with increasing thickness of the layer and, apparently, is the reason for the departure of experimental points for butanol and benzyl alcohol layers of large thickness. Second, a buoyancy force whose role is enhanced with increasing thickness of the layer cannot be ruled out. This hypothesis is confirmed by the order of the Rayleigh numbers for the corresponding curves in Fig. 3 ($Ra_1 < Ra_2 < Ra_3 < Ra_4$). Finally, beginning from the instant of heating of the liquid, its expansion takes place and a hump is formed, which spreads out under the action of the Laplace pressure. This process is sustained during propagation of the thermal front. The centrifugal flow initiated by the Laplace pressure at the surface of the layer might enhance its sensitivity to centrifugal TC flow. This process is characterized by the volume expansion coefficient β. Strange as it may seem, the order of arrangement of the curves also corresponds to the latter assumption (i.e., $\beta_1 < \beta_2 < \beta_3 < \beta_4$). To determine the contribution from each of the mechanisms listed above, more detailed studies are required.

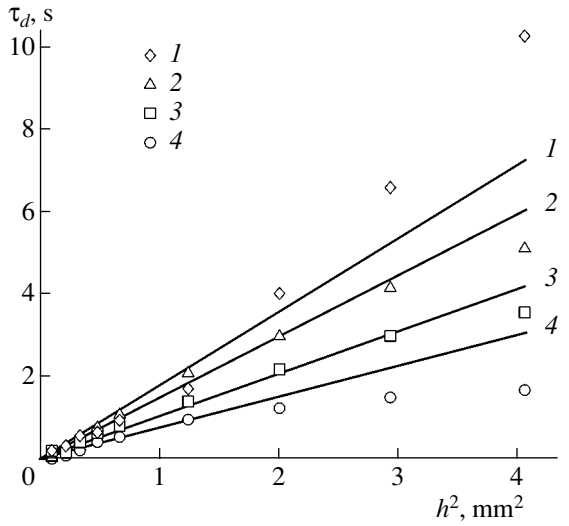

Fig. 3. Dependence of the delay time of the TC response on the squared thickness of the layer. Solid curves describe the dependence $\tau_d = h^2/4nk$: ethylene glycol (*1*), benzyl alcohol (*2*), butanol-1 (*3*), and n-octane (*4*). The values of *n* are given in the table.

This work was supported by the Russian Foundation for Basic Research, project no. 04-01-00493.

REFERENCES

1. H. Helmers and W. Witte, Opt. Commun. **49**, 21 (1984).
2. G. DaCosta and R. Escalona, Appl. Opt. **29**, 1023 (1990).
3. M. Gugliotti, M. S. Baptista, and M. J. Politi, Langmuir **18**, 9792 (2002).
4. B. A. Bezuglyi, O. A. Tarasov, and A. A. Fedorets, Kolloid. Zh. **63**, 735 (2001).
5. B. A. Bezuglyi and O. A. Tarasov, Pis'ma Zh. Tekh. Fiz. **30** (4), 20 (2004) [Tech. Phys. Lett. **30**, 138 (2004)].
6. H. S. Carslaw and J. C. Jaeger, *Conduction of Heat in Solids* (Clarendon, Oxford, 1959; Nauka, Moscow, 1962).
7. W. McDaniel and D. Z. Robinson, Appl. Opt. **1**, 311 (1962).
8. J. C. Loulergue and S. L. Xu, Int. J. Infrared Millim. Waves **7**, 171 (1986).
9. B. A. Bezuglyi, Candidate's Dissertation (Mos. State Univ., Moscow, 1983).

Translated by N. Wadhwa

Technical Physics, Vol. 50, No. 9, 2005, pp. 1246–1249. Translated from Zhurnal Tekhnicheskoĭ Fiziki, Vol. 75, No. 9, 2005, pp. 139–142.

SHORT COMMUNICATIONS

On the Limiting Physical Adsorption of Hydrogen in Carbon Materials

A. A. Bogdanov

Ioffe Physicotechnical Institute, Russian Academy of Sciences, Politekhnicheskaya ul. 26, St. Petersburg, 194021 Russia

e-mail: a.bogdanov@ioffe.mail.ru

Received November 10, 2004

Abstract—The specific features of hydrogen adsorption (and adsorption of other gases) at supercritical temperatures (specifically, the absence of capillary condensation and polymolecular adsorption and the appearance of a maximum in the adsorption isotherm in the pressure range 1–10 MPa) are discussed. Hydrogen adsorption decreases by an order of magnitude as the temperature increases from the critical temperature to the room value. The experimental adsorption isotherms in the supercritical range found in the literature are used to deduce a criterion of limiting hydrogen adsorption at various temperatures. Carbon adsorbents of different types (individual single-wall nanotubes, bundles of such nanotubes, multiwall nanotubes, and carbon fibers) are considered. A model of single graphite plane shows that the limiting hydrogen adsorption is 5 wt % at 77 K and 1 wt % at 293 K. These values can only be approached by adsorption in a material made of individual single-wall nanotubes. Methods to increase the adsorption are proposed. © *2005 Pleiades Publishing, Inc.*

Hydrogen adsorption in various materials is one of the methods for hydrogen storage and can be used to design hydrogen storage systems for transport power installations [1]. With the advent of new carbon materials (fullerenes, nanotubes, and nanofibers), the annual number of experimental and theoretical works dealing with hydrogen adsorption has increased sharply [2–5]. However, the results and conclusions of these works are often conflicting. The purpose of this work is to obtain a simple and reliable criterion for determination of the limiting adsorbability of various carbon materials. We obtain this criterion using experimental adsorption isotherms for hydrogen and other gases in the supercritical region.

From the economic and technological standpoints, hydrogen storage using physical adsorption is profitable only at temperatures $T > 77$ K, which is significantly higher than the critical hydrogen temperature $T_{cr}(H_2) = 33$ K; the reduced temperature is $T^* = T/T_{cr}(H_2) > 2.3$. When temperature increases above T_{cr}, adsorption isotherms of different gases lose a polymolecular adsorption branch and acquire a maximum in the range 1–10 MPa [6–10]. As the temperature T increases further, the isotherms lower monotonically toward the pressure axis and the maximum shifts toward high pressures [6–10]. It is natural that, at such temperatures, there is no capillary hydrogen condensation in mesopores.

The volumetric filling of micropores at $T^* < 1$ is caused by a significant increase in the interaction potential between molecules and the walls of narrow pores. In slotlike pores, such an increase is detectable up to $d/\sigma = 1.5$–2, and that in cylindrical pores, up to $d/\sigma = 3$ (where d is the micropore size across and σ is the van der Waals molecular size) [11, 12]. In wider micropores (supermicropores) with $d/\sigma = 5$–6, volumetric filling is explained by the cooperative effect [12–14], namely, by intensification of molecular clustering in the space of a supermicropore after the first monolayer has been adsorbed. At $T^* > 1$, or the more so at $T^* > 2.3$, clustering is almost absent, and, hence, volumetric filling of micropores is also absent; as the pressure increases, only the first monolayer is gradually filled. As for the limiting adsorption capacity, the volumetric filling of narrow micropores, where the interaction potential is enhanced, is virtually identical to surface adsorption.

For monolayer filling, specific adsorption a_m, mol/g, is connected with the adsorbent specific area A by the relation [12, 15, 16]

$$A = a_m N \omega_m. \quad (1)$$

Here, N is the Avogadro number and ω_m is the area per adsorbate molecule in the monolayer. It was noted in [15, 17] that the molecular density in real liquids and monolayers is significantly lower than that in the case of close packing. This means that the fraction of molecule-free surface in a monolayer ε_S is much higher than the value ($\varepsilon_{S0} = 0.093$) characteristic of the case of spherical molecules closely packed on a surface. For a number of gases (Ar, Kr, Xe, CO_2, C_6H_6, C_6H_{14}, CH_3OH, CCl_4, H_2O), the authors of [17] found that $\varepsilon_S = 1 - S_{VdV}/\omega_m$, where S_{VdV} is the projection area of molecules of a certain adsorbate (S_{VdV} is calculated using the van der Waals radius of the corresponding molecule).

For these gases, ε_S was found to range from 0.32 to 0.38 with an average value of 0.35. Note that all measurements for these gases were performed at temperatures close to T = 77 K, i.e., well below their critical temperatures T_{cr}.

In [6, 8, 9], the adsorption isotherms of various gases, including hydrogen, in carbon materials and synthetic zeolite were measured in the supercritical temperature range. For these materials, the specific surface area A was known. Using these isotherms and Eq. (1), we calculated $\omega_m(T^*)$ at their maxima and determined the values of $S_{VdV}/\omega_m(T^*)$ (Fig. 1). The particle projection areas S_{VdV} were calculated using the van der Waals atomic radii recommended in [18–20]: 0.202, 0.188, 0.154, 0.171, 0.150, and 0.116 nm for Kr, Ar, Ne, C, N, and H, respectively. The S_{VdV} areas were found to be 0.128, 0.139, 0.111, 0.104, 0.074, and 0.059 nm^2 for Kr, CH_4, Ar, N_2, Ne, and H_2, respectively. Note that, in our estimations based on the results of [8], we took into account that those authors used powdered active AKh-21 carbon with A = 2800 m^2/g and a density ρ = 0.3 g/cm^3 [21]. Using points for hydrogen, we plotted the $f(T^*)$ curve, which decreases monotonically with increasing T^* (see figure). Points for other gases (Ne, Ar, Kr, H_2, CH_4) deviate only weakly from this curve. We also estimated S_{VdV}/ω_m using the results of [22] for hydrogen adsorption on a number of carbon materials and zeolite at 77 K and a hydrogen pressure of 0.1 MPa. The specific surface areas S_{BET} for the materials under study were in the range 431–2029 m^2/g. To obtain a_m, we use extrapolation at maxima in the isotherms: the experimental values of a_m were increased by 30% according to the isotherms of [8]. The values of S_{VdV}/ω_m for all materials were found to fall in the range 0.24–0.47. By making allowance for the extrapolation roughness, we may conclude that these values agree well with the value (0.35) calculated from the complete isotherm of [8].

The function $f(T^*) = S_{VdV}/\omega_m(T^*)$ allows us to estimate the limiting capacity of various adsorbents using Eq. (1). For hydrogen, S_{VdV} = 0.059 nm^2; therefore, $a_m = 5.67 \times 10^{-2} f(T^*)A[g(H_2)/g]$, $A[10^3$ m^2/g]. For carbon adsorbents based on a certain combination of fragments of the graphite plane (more specifically, the graphite network), the maximum specific surface area A_{max} can be estimated from the consideration of the ideal case of hydrogen adsorption on both sides of the graphite plane. In this case, A_{max} = 2630 m^2/g; therefore, at T = 77 K ($f(T^*)$ = 0.35), the maximum adsorption is $a_{max}(77)$ = 0.052 g/g, or 5 wt %. At T = 293 K ($f(T^*)$ = 0.072), it is $a_{max}(293)$ = 0.0107 g/g, or 1.06 wt %. The limiting volume hydrogen content is 50 and 10 g/l, respectively.

If the van der Waals sizes of the hydrogen molecule (0.31 × 0.232 nm) and the carbon atom (0.34 nm) are taken into account, the interaction potential increases in carbon nanotubes having a diameter less than 1.1 nm. For tubes with a larger diameter, the increase in the potential is insignificant, and the character of adsorption in these tubes at supercritical temperatures is virtually identical to adsorption on the graphite plane. The same is true of most single-wall carbon nanotubes (SWNTs) synthesized with an electric arc or a laser beam, since their diameters lie in the range 1.0–1.5 nm [23–25].

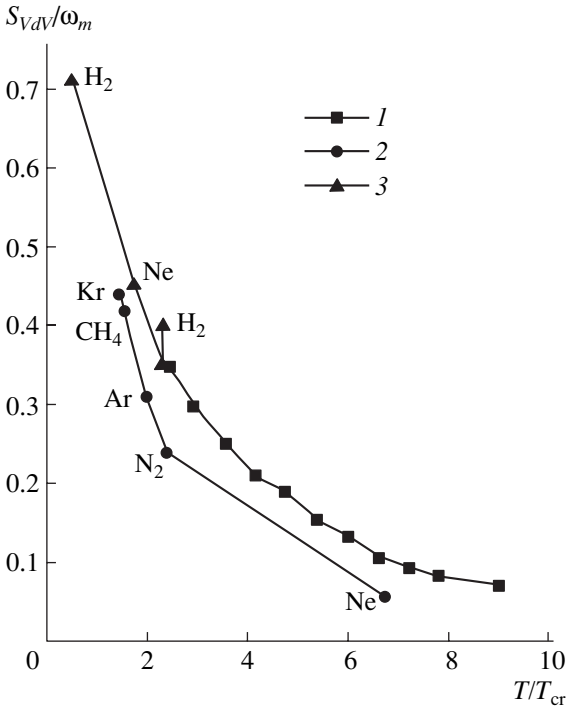

Experimental curves plotted using experimental values of S_{VdV}/ω_m taken from (*1*) [8], (*2*) [9], and (*3*) [6].

For single SWNTs, the total specific surface (both inner and outer surface) is identical to that of the graphite plane [26]. Therefore, the estimates of a_{max} made above hold true for single SWNTs. In single SWNTs, the volume hydrogen content is lower than that for adsorption on the graphite plane, and it depends on the density of packing such tubes in a sample and the ratio of the average tube diameter in the sample to the hydrogen molecular diameter. However, cables of several tens of nanotubes stuck together form during synthesis and can hardly be separated. The total specific surface area of the cables of SWNTs is well below A_{max} (by a factor of up to two) [26]; correspondingly, the limiting value of a_m for them is lower in proportion.

The distance between neighboring coaxial tubes in a multiwall nanotube is specified by the van der Waals interaction of carbon atoms in them: it is 0.34 nm, which is close to the graphite interplanar spacing (0.335 nm). Naturally, hydrogen molecules cannot penetrate into the space between the coaxial tubes (just as in the space between planes in graphite) as a result of

weak adsorption attraction. Otherwise, they should be located at such short distances from carbon networks that correspond to the range of very strong repulsion. Therefore, adsorption in multiwall carbon nanotubes can occur only on the surface of the inner channel and on the outer surface of a nanotube. This behavior should result in a sharp decrease in the maximum hydrogen adsorption in multiwall tubes (this decrease is inversely proportional to the number of layers in a multiwall carbon nanotube). These considerations can be applied for different-type carbon fibers (tubular, platelet, and herringbone graphite nanofibers) that are made of graphite-plane fragments placed at various angles to the fiber axis. The authors of [27] reported on "fantastic" hydrogen adsorption in such fibers even at room temperature (up to 67 wt %). To explain their results, those authors proposed also "fantastic" hypotheses that, during hydrogen adsorption, graphite-plane fragments move apart and hydrogen is accumulated between these planes in the form of a multilayer configuration and that this process is accompanied by a phase transition and capillary condensation at anomalously high temperatures. The value reported (a_m = 67 wt %) is two to three orders of magnitude higher than our estimates given above for single- and multiwall nanotubes. It is not surprising that this result has not been repeated in other laboratories.

The estimates given above show that all modern carbon adsorbents do not satisfy the generally accepted criteria of practical applicability: the hydrogen weight content must be no less than 6.5 wt %, and the hydrogen volume content must be no less than 62 g/l [28]. Even for the ideal case of the maximum specific surface of 2630 m^2/g, adsorption is estimated to be 0.052 g/g at 77 K, and the hydrogen volume content is 50 g/l. For real adsorbents, including nanotubes and nanofibers, the adsorption characteristics at room temperature are much lower. Moreover, the cost of single-wall carbon nanotubes purified to 60–80% is now 250 $/g (e.g., see [29]). This circumstance makes the application of SWNTs for hydrogen storage problematic in the near future.

We can propose the following methods for increasing the adsorption of carbon adsorbents. The packing density of adsorbed molecules of different gases in a monolayer is known to vary significantly with the nature of an adsorbent surface. This fact has been discussed and experimentally grounded, in particular, in [16], using argon, nitrogen, and krypton as examples at $T^* < 1$. As was shown in [16], the determining factor in this variation is the adsorption energy, which can change due to both qualitative changes in the adsorbate–adsorbent interaction and quantitative adsorbent characteristics (changes in the surface concentration of force centers). Therefore, we can assume that using adsorbents with an optimum micropore cross-sectional dimension, where adsorption potential becomes substantially stronger, can lead to denser hydrogen packing (ω_m becomes lower) even at $T^* > 1$. It is obvious that, in slotlike micropores, this phenomenon is much more pronounced, since the potential in nanotubes can be increased only inside them. It is clear that, to check the possibility of an increase in the adsorption, one has to synthesize adsorbents having the given average cross-sectional dimension of slotlike micropores (0.8–1.5 nm) and a very narrow size distribution of these micropores.

Another method is related to the synthesis of adsorbents (which need not be made of carbon) in which the number of adsorbent atoms per unit pore surface is low as compared to graphite; as a result, their specific surface increases. An example of synthesis of such adsorbents (metal-organic frameworks) is given in [30], where an MOF-177 adsorbent having a specific surface of 4500 m^2/g and a pore diameter of 1.18 and 1.08 nm is described. It should be noted that this method of increasing A leads to a decrease in the adsorption heat, since each adsorbate molecule interacts with a smaller number of adsorbent atoms (the adsorbent atomic density in the pore walls decreases). Because of the absence of a complete set of data, we cannot now exactly calculate the joint effect of the factors given above; therefore, we need experiments to check the hydrogen adsorbability of the new class of adsorbents at supercritical temperatures.

ACKNOWLEDGMENTS

I thank P. Bénard for useful discussion and for informing me about details of experiments [9] and D.F. Quinn for the discussion of problems related to carbon adsorbents.

REFERENCES

1. L. Schlapbach and A. Züttel, Nature **414**, 353 (2001).
2. U. Bünger and W. Zittel, Appl. Phys. A **72**, 147 (2001).
3. A. Züttel, Ch. Nützenadel, P. Sudan, *et al.*, J. Alloys Compd. **330–332**, 676 (2002).
4. M. Hirscher, M. Becher, M. Haluska, *et al.*, J. Alloys Compd. **356–357**, 433 (2003).
5. A. Züttel, P. Sudan, P. Mauron, *et al.*, Appl. Phys. A **78**, 941 (2004).
6. A. J. Kidnay and M. J. Hiza, Adv. Cryog. Eng. **12**, 730 (1967).
7. Li Zhou, Yaping Zhou, Shupei Bai, *et al.*, J. Colloid Interface Sci. **253**, 9 (2002).
8. E. Poirier, R. Chahine, P. Benard, *et al.*, Appl. Phys. A **78**, 961 (2004).
9. P. Malbrunot, D. Vodal, L. Vermesse, *et al.*, Langmuir **8**, 577 (1992).
10. D. F. Quinn, Carbon **40**, 2767 (2002).
11. D. H. Everett and J. C. Powl, J. Chem. Soc., Faraday Trans. 1 **72**, 619 (1976).
12. S. J. Gregg and K. S. Sing, *Adsorption, Surface Area, and Porosity* (Academic, New York, 1982; Mir, Moscow, 1984).

13. A. P. Karnaukhov, *Adsorption: Texture of Disperse and Porous Materials* (Nauka, Novosibirsk, 1999) [in Russian].
14. S. F. Grebennikov, V. V. Serpinskiĭ, Yu. I. Pakhomov, *et al.*, Izv. Akad. Nauk SSSR, Ser. Khim., No. 15, 498 (1983).
15. A. P. Karnaukhov, Kinet. Katal. **23**, 1439 (1982).
16. N. E. Buyanova, R. V. Zagrafskaya, A. P. Karnaukhov, *et al.*, Kinet. Katal. **24**, 1187 (1983).
17. R. V. Zagrafskaya, A. P. Karnaukhov, and V. B. Fenelonov, React. Kinet. Catal. Lett. **16**, 223 (1981).
18. Yu. V. Zefirov and P. M. Zorkiĭ, Usp. Khim. **58**, 713 (1989).
19. Yu. V. Zefirov and P. M. Zorkiĭ, *Van der Waals Radii of Atoms in Crystal Chemistry and Structural Chemistry* (Historical Review); http://www.chem-net.ru/rus/cryst/cryshist/vanderw.htm
20. G. E. Gadd, P. J. Evans, S. Kennedy, *et al.*, Fullerene Sci. Technol. **7**, 1043 (1999).
21. P. Bénard, private communication.
22. M. G. Nijkamp, J. E. M. J. Raaymakers, A. J. van Dillen, and K. P. de Jong, Appl. Phys. A **72**, 619 (2001).
23. S. Bandow, S. Asaka, Y. Saito, *et al.*, Phys. Rev. Lett. **80**, 3779 (1998).
24. O. Jost, A. A. Gorbunov, W. Pompe, *et al.*, Appl. Phys. Lett. **75**, 2217 (1999).
25. S. Farhat, M. L. de La Chapelle, A. Loiseau, *et al.*, J. Chem. Phys. **115**, 6752 (2001).
26. K. A. Williams and P. C. Eklund, Chem. Phys. Lett. **320**, 352 (2000).
27. A. Chambers, C. Park, R. T. K. Baker, and N. M. Rodriguez, J. Phys. Chem. B **102**, 4253 (1998).
28. http://www.eere.energy.gov/hydrogenandfuelcells/hydrogen/pdfs/technical_targets.pdf
29. http://www.carbonsolution.com/index.htm
30. H. K. Chae, D. Y. Siberio-Perez, Y. Kim, *et al.*, Nature **427**, 523 (2004).

Translated by K. Shakhlevich